

Western Australia School of Mines: Minerals, Energy and Chemical Engineering

Investigations of Corrosion Effects at High Temperatures and High Pressure Conditions

Yousuf Abdulwahhab

This thesis is presented for the Degree of

Doctor of Philosophy

of

Curtin University

March 2020

## **Declaration**

To the best of my knowledge and belief this thesis contains no material previously published by any other person except where due acknowledgment has been made.

This thesis contains no material which has been accepted for the award of any other academic degree or diploma in any university.

Yousuf Abdulwahhab

## **Abstract**

The impact of corrosion on the oil and gas industry has been viewed in terms of its effect on both capital and operational expenditures. The wide-ranging environmental conditions prevailing in the oil and gas industry necessitates the appropriate and cost-effective materials choice and corrosion control measures. The implementation of these measures is becoming increasingly important as the corrosion related failures constitute over 25% of failures experienced in the oil and gas industry. More than half of these failures are associated with sweet corrosion (CO<sub>2</sub> corrosion). The use of corrosion resistant alloys, such as 316 stainless steel, are being increasingly used due to its superior mechanical properties and corrosion resistance. Despite the increasing use of stainless steel in oil and gas production where anaerobic CO<sub>2</sub> (carbonic acid) environments exist, not a great deal is known about the nature of the passive film and its protective mechanism in these environments.

The first experimental work chapter in this thesis (chapter 3) has been studied the relationship between the passive film properties in relatively mild CO<sub>2</sub> environments and the susceptibility to pitting corrosion by using different electrochemical techniques, such as cyclic polarization, electrochemical impedance spectroscopy, and Mott-Schottky. The results indicate that the pitting susceptibility of 316L stainless steel increase with increasing temperature and NaCl concentration. In addition, the results provide insight into the possible change in the passive film structure as a result of an increase in temperature. It is interesting that the results for 316L in a deoxygenated CO<sub>2</sub> environment are not dissimilar in behavior expected in oxygen-rich environments which has been the focus on much more research.

The second experimental work chapter (chapter 4) has involved the comparison of the corrosion behavior and passive film properties in CO<sub>2</sub> and N<sub>2</sub> environments using cyclic polarization, electrochemical impedance spectroscopy, Mott-Schottky, and x-ray photoelectron spectroscopy. The results showed no porous layer was found on the passive film formed in N<sub>2</sub> environment at any temperatures tested. In addition, x-ray photoelectron spectroscopy analysis indicates that the variation in the elemental composition of the passive films, a higher concentration of metal hydroxides (potentially Cr(OH)<sub>3</sub>) is observed as temperature increases particularly in the presence of CO<sub>2</sub>.

The third experimental work chapter (chapter 5) was studied the impact of high temperature and high pressure and NaCl concentrations on the pitting corrosion of 316L stainless steel in a CO<sub>2</sub> environment simulating to the oil and gas production systems. The production conditions

tend to become more corrosive hence requiring a more stringent corrosion management strategy. The results revealed a synergistic effect of high temperatures and high NaCl concentration on the change in the passive layer structure. As the temperature increase, the defects in the passive film formed on the 316L increase and makes it more heterogeneous. In addition, this harmful effect is intensified at higher NaCl concentrations. Therefore, the combined effect of these factors decreases the protectiveness of the passive film. Whereas, Mott-Schottky results have shown that the donor and acceptor densities appear to be unaffected by the increasing the temperatures to the same extent as increased NaCl concentrations.

Because the abnormal corrosion phenomenon took place when CO<sub>2</sub> was present. The fourth experimental work chapter (chapter 6) has investigated the effect of different CO<sub>2</sub> partial pressure on the passive film formed on 316L stainless steel at different temperatures. The results indicate that the presence of the high CO<sub>2</sub> partial pressure caused the decrease in the corrosion potential observed over long periods of exposure due to increase the complexity of the electrolyte systems meaning the corrosion rates of 316L stainless steels depend significantly on the partial pressure of CO<sub>2</sub>. The dissolved CO<sub>2</sub> can play an important role, to some extent, in deciding the composition of the metal oxide scale. In addition, the temperature has a profound effect on the corrosion behavior of 316L.

The research presented in this thesis (chapter 7 and Appendix I) involved the effect of temperature on the corrosion rate and the protective layer formed on UNS G101800 and UNS G10300 carbon steel at different corrosion inhibitor concentrations in the present and absence of NaCl. The results showed that the corrosion resistance of carbon steel was improved by the addition of NO<sub>2</sub><sup>-</sup> as evident by the reduction in weight loss corrosion rate and the combined results from electrochemical measurements. In addition, the presence of 500 ppm chloride ion increased the susceptibility to localized corrosion in the form of pits, which was mitigated by the addition of 500 ppm NO<sub>2</sub><sup>-</sup>. The action of nitrite based corrosion inhibitor is due to the oxidation of iron ion to form Fe<sub>2</sub>O<sub>3</sub> on the carbon steel surface.

## **Acknowledgment**

First and foremost, praises and thanks to God, for His showers of blessings throughout my research work to complete the research successfully.

I would like to express my deep and sincere gratitude to my principal research supervisor, Dr.Ahmed Barifcani, for his constrictive guidance, internal motivation, friendship, empathy, and a great sense of care. I am extremely grateful for what he has offered me.

I wish to express my sincere and deepest gratitude to my co-supervisor, Dr.Kod Pojtanabuntoeng, for her unlimited support and for providing invaluable guidance throughout this research. Her dynamism, vision, sincerity, and motivation have deeply inspired me. She has taught me the methodology to carry out the research and to present the research works as clearly as possible.

I would also like to thank Prof. Moses Tade and Prof. Brian Kinsella for their constant encouragement and invaluable suggestions to complete this thesis successfully.

I want to express my sincere gratitude to the Iraqi Government, Higher Education and Scientific Research Ministry, and the presidency of Baghdad University for giving me the opportunity to do research.

I would like to sincerely acknowledge the kind help from the staff and colleagues in the corrosion center, who helped me, advise me, taught me to make my task easier.

I am extremely grateful to my parents for their love, valuable prayers, caring, and sacrifices for educating and preparing me for my future. I am very much thankful to my wife, my son, and my daughter, for their love, understanding, prayers, and continuing support to complete this research work.

Finally, my thanks go to all the people who have supported me to complete the research work directly or indirectly.

## **List of publications included as part of the thesis**

This thesis is assembled as a hybrid consisting of publication papers, submitted manuscript, and manuscript in preparation, which from individual chapters listed below:

### **Chapter 4**

Y Abdulwahhab, T Pojtanabuntoeng, B Kinsella, JP Veder, A Barifcani, Comparison of Corrosion behavior and Passive Film Properties of 316L Austenitic Stainless Steel in CO<sub>2</sub> and N<sub>2</sub> Environments, Corrosion Engineering, Science and Technology, Volume 54, 2019- Issue 1

### **Chapter 5**

Y Abdulwahhab, T Pojtanabuntoeng, B Kinsella, A Barifcani, Study the influence of high temperature and high-pressure conditions on the 316L stainless steel in CO<sub>2</sub> environment, under review in the Journal of Science and Engineering.

### **Chapter 6**

Y Abdulwahhab, T Pojtanabuntoeng, A Barifcani, Effect of CO<sub>2</sub> partial pressure on the pitting susceptibility of UNS S31603 at different temperatures, Corrosion Engineering, Science and Technology, under review.

## **Conference Presentation**

Y Abdulwahhab, T Pojtanabuntoeng, A Barifcani, M Tade, B Kinsella, EIS, and Mott-Schottky to Study the Passive Film Properties of 316L and its Susceptibility to Pitting Corrosion in CO<sub>2</sub> Environments, ACA Conference 15.11.2016, Auckland, Paper No. 144.

## Table of Contents

<b>Declaration</b> .....	ii
<b>Abstract</b> .....	iii
<b>Acknowledgment</b> .....	v
<b>List of publications included as part of the thesis</b> .....	vi
<b>Conference Presentation</b> .....	vii
<b>List of Figures</b> .....	xii
<b>List of Table</b> .....	xv
<b>List of abbreviations</b> .....	xvii
<b>Chapter 1: Introduction</b> .....	1
1.1 Introduction.....	1
1.2 The objective of this work .....	4
1.3 Significance of this work .....	5
1.4 Research Methods .....	5
<b>1.4.1 Immersion Corrosion Test</b> .....	5
<b>1.4.2 Electrochemical Test</b> .....	6
<b>1.4.3 Autoclave cell</b> .....	7
<b>1.4.4 Surface analysis</b> .....	7
1.5 Outline of the thesis.....	8
<b>Chapter 2: Literature Review</b> .....	9
2.1 Introduction.....	9
2.2 Corrosion forms.....	9
<b>2.2.1 Sweet corrosion (CO<sub>2</sub> corrosion)</b> .....	10
<b>2.2.2 Sour corrosion (H<sub>2</sub>S corrosion)</b> .....	12
<b>2.2.3 Oxygen corrosion</b> .....	12
<b>2.2.4 Galvanic Corrosion</b> .....	12
<b>2.2.5 Crevice corrosion</b> .....	12
<b>2.2.6 Erosion corrosion</b> .....	13
<b>2.2.7 Microbiologically induced corrosion</b> .....	13
<b>2.2.8 Stress corrosion cracking</b> .....	13
2.3 Corrosion mitigation.....	14
2.4 Corrosion Inhibitors.....	14
<b>2.4.1 Mechanisms of action of inhibitors</b> .....	15
<b>2.4.2 Inhibitors classifications</b> .....	15
<b>2.4.3 Techniques for analysis of inhibitors</b> .....	16

<b>2.4.4 Inhibitor efficiency</b> .....	16
2.5 Understanding Localized corrosion.....	16
2.6 Pitting corrosion characteristics .....	18
<b>2.6.1 Pitting potential and repassivation potential</b> .....	18
2.7 Passivity breakdown.....	19
<b>2.7.1 Passive film penetration mechanism</b> .....	20
<b>2.7.2 Film breakdown mechanism</b> .....	21
<b>2.7.3 Adsorption mechanisms</b> .....	22
<b>Chapter 3: EIS and Mott-Schottky to Study the Passive Film Properties of 316L and its Susceptibility to Pitting Corrosion in CO<sub>2</sub> Environments</b> .....	24
3.1 Abstract.....	24
3.2 Introduction.....	24
3.3 Experimental procedure.....	27
<b>3.3.1 Materials and specimen preparation</b> .....	27
<b>3.3.2 Test solutions</b> .....	27
<b>3.3.3 Electrochemical measurements</b> .....	28
3.4 Results and discussion.....	29
<b>3.4.1 Cyclic polarization technique</b> .....	29
<b>3.4.2 Electrochemical impedance spectroscopy (EIS) technique</b> .....	31
<b>3.4.3 Mott – Schottky</b> .....	36
3.5 Conclusions.....	41
<b>Chapter 4: Comparison of Corrosion behavior and Passive Film Properties of 316L Austenitic Stainless Steel in CO<sub>2</sub> and N<sub>2</sub> Environments</b> .....	43
4.1 Abstract.....	43
4.2 Introduction.....	43
4.3 Experimental procedure.....	44
<b>4.3.1 Materials and specimen preparation</b> .....	44
<b>4.3.2 Test solutions</b> .....	45
<b>4.3.3 Electrochemical measurements</b> .....	45
<b>4.3.4 Surface characterization</b> .....	46
4.4 Results and dissection.....	47
<b>4.4.1 Cyclic polarization technique</b> .....	47
<b>4.4.2 Electrochemical impedance spectroscopy (EIS) technique</b> .....	49
<b>4.4.3 Mott – Schottky (M-S) technique</b> .....	54
<b>4.4.4 Surface analysis by XPS</b> .....	56

4.5 Conclusions.....	62
<b>Chapter 5: Study the influence of high temperature and high-pressure conditions on the 316L stainless steel in CO<sub>2</sub> environment .....</b>	<b>63</b>
5.1 Abstract.....	63
5.2 Introduction.....	63
5.3 Experimental works.....	64
<b>5.3.1 Materials and specimen preparation .....</b>	<b>64</b>
<b>5.3.2 Test solutions.....</b>	<b>65</b>
<b>5.3.3 Experimental setups .....</b>	<b>66</b>
<b>5.3.4 Experimental procedure.....</b>	<b>66</b>
5.4 Results and discussion.....	67
<b>5.4.1 In-situ pH measurement.....</b>	<b>67</b>
<b>5.4.2 Cyclic polarization technique.....</b>	<b>67</b>
<b>5.4.3 Electrochemical impedance spectroscopy (EIS) technique.....</b>	<b>71</b>
<b>5.4.4 Mott – Schottky.....</b>	<b>76</b>
5.5 Conclusions.....	80
<b>Chapter 6: Effect of CO<sub>2</sub> partial pressure on the pitting susceptibility of UNS S31603 at different temperatures .....</b>	<b>81</b>
6.1 Abstract.....	81
6.2 Introduction.....	81
6.3 Experimental procedure.....	83
<b>6.3.1 Materials and specimen preparation .....</b>	<b>83</b>
<b>6.3.2 In-situ pH measurement.....</b>	<b>83</b>
<b>6.3.3 Test solutions.....</b>	<b>83</b>
<b>6.3.4 Experimental setup.....</b>	<b>84</b>
<b>6.3.5 Electrochemical measurements.....</b>	<b>84</b>
6.4 Results and discussion.....	85
<b>6.4.1 Open circuit potential measurements .....</b>	<b>85</b>
<b>6.4.2 Cyclic polarization technique.....</b>	<b>86</b>
<b>6.4.3 Electrochemical impedance spectroscopy (EIS) technique.....</b>	<b>88</b>
6.5 Conclusions.....	92
<b>Chapter 7: Electrochemical investigation of nitrite ions as a corrosion inhibitor at elevated temperature.....</b>	<b>93</b>
7.1 Abstract.....	93
7.2 Introduction.....	93
7.3 Experimental.....	94

<b>7.3.1 Materials and specimen preparation</b> .....	94
<b>7.3.2 Test solutions</b> .....	95
<b>7.3.3 In-situ pH measurement</b> .....	95
<b>7.3.4 Experimental setups</b> .....	96
<b>7.3.5 Experimental procedure</b> .....	97
<b>7.4 Results and discussion</b> .....	98
<b>7.4.1 HP/HT pH measurements</b> .....	98
<b>7.4.2 Weight loss measurements</b> .....	98
<b>7.4.3 Electrochemical measurements</b> .....	100
<b>7.5 Conclusions</b> .....	107
<b>Chapter 8: Conclusions and Recommendations</b> .....	108
8.1 Conclusion .....	108
8.2 Recommendations for future work.....	110
<b>Appendix 1</b> .....	111
<b>1 Abstract</b> .....	111
<b>2 Introduction</b> .....	111
<b>3 Experimental procedure</b> .....	113
3.1 Materials and solution .....	113
3.2 Immersion tests.....	113
3.3 Post-test analysis.....	114
<b>3.3.1 Water analysis</b> .....	114
<b>3.3.2 Weight loss and localized corrosion</b> .....	114
<b>3.3.3 Surface characterization</b> .....	114
<b>4 Results and discussion</b> .....	115
4.1 Immersion tests.....	115
4.2 Water analysis.....	119
<b>5 Corrosion product characterization</b> .....	120
5.1 Scanning Electron Microscopy (SEM) .....	120
5.2 X-ray diffraction .....	122
5.3 X-ray photoelectron spectroscopy .....	124
<b>6 Conclusion</b> .....	126
<b>References</b> .....	127
<b>Appendix 2: Written Statements of co-authors</b> .....	140
<b>Appendix 3: Copyright Statements</b> .....	145

## List of Figures

Figure 3.1 Cyclic polarization curves of 316L SS in 3% NaCl, pH 4 at different temperatures .....	30
Figure 3.2 Cyclic polarization curves for 316L SS in different NaCl concentrations at 30 °C, pH 4.....	31
Figure 3.3 (A) Nyquist plots and (B) Bode phase diagrams for 316L SS with fitting in 3 wt.% NaCl, pH 4. Temperature was varied from 30 °C to 80 °C.....	34
Figure 3.4 Equivalent circuit for fitting of EIS data (A) one time constant, (B) two time constant.....	34
Figure 3.5 (A) Nyquist plots and (B) Bode diagrams for 316L SS with the fitting in different NaCl concentrations, at 30 °C, pH 4, at a film formation of -1 V <sub>Ag/AgCl</sub> .....	35
Figure 3.6 Capacitance vs. potential curves obtained at different frequencies for 316L SS in 3% NaCl, pH 4 at 30 °C.....	38
Figure 3.7 Mott-Schottky plots for 316L in 3% NaCl, pH 4 at different temperature, 3 kHz, with AC 10mV .....	39
Figure 3.8 Mott-Schottky plots for 316L in different NaCl concentrations, at 30 °C pH 4, 3 kHz, with AC 10mV .....	40
Figure 4.1 Cyclic polarization curves of 316L SS in 3wt.% NaCl, pH 4 saturated with a) CO <sub>2</sub> and b) N <sub>2</sub> at different temperatures. Arrows indicate direction of scans .....	49
Figure 4.2 a) $\Delta E_{pit}$ , and b) $\Delta E_{rep}$ of 316L SS in 3wt.% NaCl, pH 4 saturated with CO <sub>2</sub> and N <sub>2</sub> at different temperatures. Error bars indicate standard deviation from multiple repeats...	49
Figure 4.3 Kramer-Kronig transform of EIS data for 316L SS in 3wt.% NaCl, pH 4 saturated with a) CO <sub>2</sub> and b) N <sub>2</sub> at a different temperatures .....	50
Figure 4.4 a) Nyquist, b) Bode phase angle and c) Bode magnitude diagrams of 316L SS in 3wt.% NaCl, pH 4 saturated with CO <sub>2</sub> gas at different temperatures. Lines represent the fitting with an equivalent circuit depicted in Figure 4.6 .....	51
Figure 4.5 a) Nyquist diagram, b) Bode phase angle plot and c) Bode magnitude plot of 316L SS in 3wt.% NaCl, pH 4 saturated with N <sub>2</sub> gas at different temperature. Lines represent the fitting with an equivalent circuit depicted in Figure 4.6. ....	52
Figure 4.6 Equivalent circuits used for fitting of EIS data exhibiting a) one time constant and b) two time constant .....	53
Figure 4.7 Mott-Schottky plots for 316L SS in 3wt.% NaCl, pH 4 sparged with a) CO <sub>2</sub> and b) N <sub>2</sub> at different temperatures.....	56
Figure 4.8 Survey XPS of the passive film formed on 316L SS a) after exposed to air and in 3wt.% NaCl pH 4 sparged with b) CO <sub>2</sub> and c) N <sub>2</sub> at 2 temperatures.....	59
Figure 4.9 Representative high resolution XPS spectra of the passive film formed on 316L SS in CO <sub>2</sub> environment at 60 °C for a) Cr <sub>2p</sub> , b) Fe <sub>2p</sub> , C) Mo <sub>3d</sub> , and d) O <sub>1s</sub> .....	60

Figure 4.10 XPS depth profiles of, Cr, Fe, Mo, Ni and O elements in the passive film formed on a) 316L SS exposed to air at room temperature and that immersed in 3wt.%NaCl at b) 30 °C in CO <sub>2</sub> , c) 60 °C in CO <sub>2</sub> , d) 30 °C in N <sub>2</sub> , and e) 60 °C in N <sub>2</sub> .....	61
Figure 5.1 Schematic diagram to the working electrode.....	65
Figure 5.2 Cyclic polarization curves of UNS S31603 in a) 0.05 wt.% NaCl, b) 3 wt.% NaCl and c) 8 wt.% NaCl, pH 4 at different temperatures.....	69
Figure 5.3 Cyclic polarization curves for UNS S31603 in different NaCl concentrations, pH 4 at a) 30 °C, b) 100 °C and c) 140 °C .....	71
Figure 5.4 Nyquist plots (left) and Bode phase diagrams (right) of UNS S31603 in a) 0.05 wt.% NaCl, b) 3 wt.% NaCl and c) 8 wt.% NaCl, pH 4 at different temperatures.....	73
Figure 5.5 Nyquist plots (left) and Bode phase diagrams (right) of UNS S31603 in different NaCl concentrations, at a) 30 °C, b) 100 °C and c) 140 °C, pH 4.....	74
Figure 5.6 Equivalent circuit for fitting of EIS data a) one time constant, b) one time constant with diffusion and c) two time constant .....	75
Figure 5.7 Mott-Schottky plots for UNS S31603 in a) 0.05 wt.% NaCl, b) 3 wt.% NaCl and c) 8 wt.% NaCl, pH 4 at different temperature, 3 kHz, with AC 10 mV .....	78
Figure 5.8 Mott-Schottky plots for UNS S31603 in different NaCl concentrations, at a) 30 °C, b) 100 °C and c) 140 °C, pH 4, 3 kHz, with AC 10 mV.....	79
Figure 6.1 Open circuit potential of UNS S31603 stainless steels in 3wt.% NaCl at different CO <sub>2</sub> partial pressure at 100 °C.....	86
Figure 6.2 Open circuit potential of UNS S31603 stainless steels in 3wt.% NaCl at different CO <sub>2</sub> partial pressure at 140 °C .....	86
Figure 6.3 Cyclic polarization curves of UNS S31603 stainless steel in 3wt.% NaCl at different CO <sub>2</sub> partial pressure at 100 °C.....	88
Figure 6.4 Cyclic polarization curves of UNS S31603 stainless steel in 3wt.% NaCl at different CO <sub>2</sub> partial pressure at 140 °C .....	88
Figure 6.5 a) Nyquist plots and Bode diagrams b) variation of the impedance, and c) variation of the phase angle with the frequency of UNS S31603 stainless steel in 3wt.% NaCl and different P <sub>CO2</sub> at 100 °C.....	90
Figure 6.6 a) Nyquist plots and Bode diagrams b) variation of the impedance, and c) variation of the phase angle with the frequency of UNS S31603 stainless steel in 3wt.% NaCl and different P <sub>CO2</sub> at 140 °C. ....	91
Figure 6.7 Two-time constant equivalent circuit for the fitting of EIS data .....	91
Figure 7.1 a) High-Pressure Ag/AgCl reference electrode and b) High-Temperature and High- pressure ZrO <sub>2</sub> based pH electrodes .....	96
Figure 7.2 The experimental setup for a) immersion tests and b) electrochemical tests .....	97
Figure 7.3 UNS G101800 (a) before and (b) after corrosion product removal. The samples were immersed in the baseline solution (0 ppm NO <sub>2</sub> <sup>-</sup> ) at 115 °C for 30 days.....	99

Figure 7.4 Microscope image of a sample UNS G101800 immersed in 700 ppm $\text{NO}_2^-$ solution at 115 °C for 30 days after cleaning with Clarke solution .....	100
Figure 7.5 a) Cyclic polarization curves and b) to d) optical microscopic images of UNS G10300 samples in solutions with varying concentrations of $\text{NO}_2^-$ after cyclic polarisation experiments at 115 °C. ....	101
Figure 7.6 Open circuit potential of UNS G10300 samples in solutions containing 0, 500, and 1100 ppm $\text{NO}_2^-$ and 500 ppm NaCl at 115 °C .....	102
Figure 7.7 UNS G103000 a) Cyclic polarization curves and b) & c) light optical micrographs in a solution containing 500 ppm NaCl at 115 °C at different pH values. ....	103
Figure 7.8 a) Cyclic polarization curves and b) to d) optical microscopic images of UNS G10300 samples in a solution containing different $\text{NO}_2^-$ concentrations with 500 ppm NaCl at 115 °C. ....	104
Figure 7.9 a) Nyquist, b) Bode impedance, and c) Bode phase angle plots of UNS G10300 samples in 500 ppm NaCl and different $\text{NO}_2^-$ concentrations at 115 °C. Initial solution pH was 11. ....	106
Figure 7.10 Two-time constant equivalent circuit for the fitting of EIS data .....	106
Figure 1 LOM images of samples exposed to DI water at a) 230 °C and b) 115 °C after cleaning with Clarke solution .....	117
Figure 2 LOM images of samples exposed to inhibited-DI water at a) 230 °C, 700 ppm $\text{NO}_2^-$ , b) 230 °C, 700 ppm $\text{NO}_2^-$ with neutralized citric acid, c) 230 °C, 1100 ppm $\text{NO}_2^-$ , d) 115 °C 700 ppm $\text{NO}_2^-$ , e) 115 °C, 700 ppm $\text{NO}_2^-$ , with non-neutralized citric acid after cleaning with Clarke solution. ....	118
Figure 3 Secondary Electron (SE) SEM images of carbon steel UNS G10180 samples after a 4-week exposure in DI-water containing various corrosion inhibitor concentrations at 230 °C .....	121
Figure 4 Secondary Electron (SE) SEM images of carbon steel UNS G10180 samples after 4-week exposure in deionized water containing various corrosion inhibitor concentrations at 115 °C. ....	122
Figure 5 Overlaid X-Ray diffraction patterns of samples exposed to a) 230 °C and b) 115 °C .....	123
Figure 6 XPS of Fe 2p (a to c) and of O 1s (d) at the primary loop conditions (230 °C) .....	125
Figure 7 XPS of a) Fe 2p and b) O 1s at the secondary loop conditions (115 °C) .....	125
Figure 8 Examples of X-Ray Photoelectron spectroscopy curve fittings .....	126

## List of Table

Table 3.1 Composition of 316L SS used in this study.....	27
Table 3.2. Summary of test conditions.....	28
Table 3.3. $\Delta E_{\text{pit}}$ and $\Delta E_{\text{rep}}$ of 316L in 3%NaCl saturated with CO <sub>2</sub> at temperature from 30 °C to 80 °C .....	30
Table 3.4. $\Delta E_{\text{pit}}$ and $\Delta E_{\text{rep}}$ of 316L in solution with varying NaCl concentration saturated with CO <sub>2</sub> at temperature at 30 °C .....	31
Table 3.5. Electrical parameters obtained by fitting the EIS data for 316L SS in 3% NaCl, pH 4 at different temperatures.....	34
Table 3.6. Electrical parameters obtained by fitting the EIS data for 316L SS in different NaCl concentrations, at 30 °C.....	36
Table 3.7. Donor and acceptor densities of 316L in 3%NaCl, pH 4 at different temperature.....	39
Table 3.8. Donor and acceptor densities of 316L in different NaCl concentrations at 30 °C, pH 4.....	41
Table 4.1 Summary of test conditions.....	45
Table 4.2 Electrical parameters obtained by fitting the EIS data for 316L SS in 3wt.% NaCl, pH 4 saturated with N <sub>2</sub> gas at different temperatures .....	54
Table 4.3 Electrical parameters obtained by fitting the EIS data for 316L SS in 3wt.% NaCl, pH 4 saturated with CO <sub>2</sub> gas at different temperatures.....	54
Table 4.4 Donor and acceptor densities ( $N_D$ and $N_A$ ) of the passive film formed on 316L SS in 3wt.% NaCl, pH 4 sparged with CO <sub>2</sub> and N <sub>2</sub> at different temperatures. Region 1(-0.5 V to -0.1 V), region 2 (-0.1 V to 0.4 V), and region 3 (0.4 V to 1.0 V).....	56
Table 4.5 Surface concentration (at%) of elements obtained from high-resolution XPS survey on the passive film formed on 316L SS exposed to air and in 3% NaCl, pH 4 at different temperatures in CO <sub>2</sub> and N <sub>2</sub> environments.....	59
Table 4.6 The detailed XPS spectra of the passive film formed on 316L SS in CO <sub>2</sub> media at 2 different temperatures .....	60
Table 4.7 The detailed XPS spectra of the passive film formed on 316L SS in N <sub>2</sub> media at 2 different temperatures .....	60
Table 5.1. Chemical composition of UNS S31600 used in this study.....	65
Table 5.2. Summary of test conditions.....	65
Table 5.3. Electrical parameters obtained by fitting the EIS data for 316L SS in a) 0.05 wt.% NaCl, b) 3 wt.% NaCl and c) 8 wt.% NaCl, pH 4 at different temperatures.....	75
Table 6.1. Chemical composition of UNS S31603 stainless steel.....	83
Table 6.2. Summary of test conditions.....	84
Table 6.3 Electrical parameters obtained by fitting the EIS data for UNS S31603 stainless steel in 3wt.% NaCl and different P <sub>CO2</sub> at 100 °C.....	92

Table 6.4 Electrical parameters obtained by fitting the EIS data for UNS S31603 stainless steel in 3wt.% NaCl and different $P_{CO_2}$ at 140 °C.....	92
Table 7.1. Nominal composition of UNS G101800 and UNS G10300 carbon steel used in this study.....	95
Table 7.2. Summary of the test conditions.....	95
Table 7.3 In-situ pH measurements at 115 °C.....	98
Table 7.4 the effect of different nitrite concentrations on the corrosion rate of UNS G101800 carbon steel after 30 days immersion at 115 °C .....	99
Table 7.5. Electrical parameters obtained by fitting the EIS data for UNS G10300 samples in 500 ppm NaCl and different $NO_2^-$ concentrations at 115 °C, pH 11 .....	107
Table 1 Weight loss corrosion rates, pit depth (if found and quantifiable), and photographs of carbon steel samples after immersion tests .....	116
Table 2 pH, $NO_2^-$ , and $NO_3^-$ concentrations analysis of test solutions before and after exposure.....	120

## List of abbreviations

CRA <sub>s</sub>	Corrosion resistant alloys
Cl <sup>-</sup>	Chloride ion concentration
DO	Dissolved oxygen
PRE	Pitting resistance equivalent
PDM	Point defect model
OCP	Open circuit potential
WE	Working electrode
CE	Counter electrode
RE	Reference electrode
E <sub>pit</sub>	Pitting potential
ΔE <sub>pit</sub>	Driving force pitting potential
E <sub>pp</sub>	Protection potential
E <sub>r</sub>	Repassivating potential
ΔE <sub>rep</sub>	Driving force repassivation potential
CP	Cyclic polarization technique
EIS	Electrochemical impedance spectroscopy technique
M-S	Mott - Schottky technique
JIC	Jet impingement cell
XPS	X-ray photoelectron spectroscopy
XRD	X-ray diffraction spectroscopy
SEM	Scanning electron microscopy
EDS	Energy X-ray spectroscopy
FESEM	Field emission scanning electron microscope
LOM	Light optical microscopy
P <sub>CO<sub>2</sub></sub>	CO <sub>2</sub> partial pressure
N <sub>D</sub>	Donor density
N <sub>A</sub>	Acceptor density
R <sub>s</sub>	Solution resistance
R <sub>ct</sub>	Charge transfer resistance
C <sub>dl</sub>	Double layer capacitance
CPE	Constant phase element

$Y_0$	Constant phase element constant
$\Omega$	Angular frequency
$W_s$	Warburg impedance
$j^2$	Imaginary number
A	Constant phase element exponent
C	Pure capacitance
$C_{SC}$	Capacitance of space charge layer
$C_H$	Capacitance of Helmholtz layer
R	Resistance
$R_{po}$	Pore resistance
F	Frequency
$Z''$	Imaginary part of the impedance
E	Applied potential
$\epsilon$	Dielectric constant
$\epsilon_0$	Permittivity of free space
Q	Electron charge
$E_{FB}$	Flat band potential
K	Boltzmann constant
T	Temperature
$1/C^2$	Space charge layer capacitance
D	Thickness of the passive film
PEEK	Polyether ether ketone
K-K	Kramers-Kronig
HT/HP	High temperature / High pressure
$E_{Corr}$	Corrosion potential
$C_{NO_2^-}$	Nitrite concentration
MEG	Monoethylene glycol

# Chapter 1: Introduction

## 1.1 Introduction

Corrosion is defined as the deterioration of materials by chemical interaction with their surrounding medium. Corrosion is an electrochemical process that occurs because of the presence of anodic and cathodic active sites on the material surfaces in which a current flows from the material surface at the anode site passes through an electrolyte and re-enters the material surface at the cathode site. Current flows because of a potential difference between the anode and cathode. The anode potential is more negative than the cathode potential, and this difference is the driving force for the corrosion current. The combination of all the main corrosion elements (anode, cathode, electrolyte, and the metallic connection between anode and cathode) is termed a corrosion cell.

The effect of corrosion in the oil and gas industry includes dangerous damage in pipelines and leads to the failure of parts which could result in the plant shutdown [1]. The annual cost of corrosion to the oil and gas industry in the United States alone is estimated to be \$1.372 billion (According to NACE International), this prompted specialists to estimate the global annual cost to the oil and gas industry as exceeding \$60 billion [2]. In addition, corrosion may cause serious environmental problems, such as spills and releases of toxic chemicals. Because it is impossible to stop corrosion, it is becoming more apparent that controlling the corrosion rate may be the most economical solution. ‘‘Corrosion Control’’ in the oil and gas industry provides engineers and designers with the tools and methods to design and implement comprehensive corrosion-management programs for oil and gas infrastructures [3].

The impact of carbon dioxide (CO<sub>2</sub>) corrosion in the oil and gas industry is well known [4, 5]. The results from CO<sub>2</sub> saturated water that is produced along with the crude oil and natural gas processing [6]. Approximately 60% of oilfield failures are related to CO<sub>2</sub> corrosion, mainly due to poor resistance of materials to this type of corrosive attack [7]. CO<sub>2</sub> can cause not only general corrosion but also localized corrosion, which is a much more serious problem. In addition, the type of corrosion caused by dissolved CO<sub>2</sub> varies considerably depending on the precise environmental conditions [8]. Many researchers have studied the mechanism of CO<sub>2</sub> corrosion [9, 10], some of them have focused on the partial pressure of CO<sub>2</sub> due to its aggressiveness and its impact on oil production [11]. Generally, corrosion under these conditions occurs in the absence of oxygen.

Until the 1980s, carbon steel is one of the most important metals used in oil and gas operations. The rapid development in these industries has led to the use of corrosion resistant alloys (CRAs), and this trend continues as these industries become involved in deeper and more aggressive environments [12]. These alloys can extend the corrosion resistance more than the other components like carbon steel or mild steel because of their passive film formation, and also offer reliable protection from corrosion, eliminating the need for expensive continuous maintenance and repairs [13, 14].

Generally, the assessment to use CRAs should be conducted as early as the pre-engineering phase. For example, these alloys are now widely employed in piping applications. Metallurgy and production technology have been developed and established to allow the use of corrosion resistant alloys for severe conditions. Many variables influence the performance of CRAs, e.g., temperature, chloride ion concentration ( $\text{Cl}^-$ ), the Partial pressure of  $\text{CO}_2$ , and pH [13-15].

Choosing the right materials is crucial; some factors to be considered include [13, 16]:

- 1- Ranges of alloy composition.
- 2- Heat treatment parameters.
- 3- Complex material mixture metallurgy.

The selection of corrosion resistant alloys for producing and transporting corrosive oil and gas can be a very complex procedure, and if improperly carried out, it could cause negative consequences. Therefore, all factors should be considered.

CRAs are widely used in the oil and gas production containing  $\text{CO}_2$  [17] although the combined effects of different parameters such as temperature, pressure,  $\text{Cl}^-$  ion, and acetic acid may lead to significant effects on the CRAs, due to the potential threat of sudden material failure such as pitting and stress corrosion cracking [18, 19].

Localized corrosion of stainless steel has been extensively studied with the focus on the characterization of passive film and investigation of corrosion mechanisms [12, 20, 21]. In particular, the effect of  $\text{Cl}^-$  on the local breakdown of passivity and stability of surface oxide was proposed [22-24]. Recently, some researchers reported the combined effect of  $\text{Cl}^-$  and  $\text{CO}_2$  on a passive oxide film [25, 26].

Pitting corrosion of metals and alloys is one of the main causes of material failure in industrial systems. It is difficult to control pitting corrosion due to its complex nature. Pitting corrosion comprises two main processes: pit nucleation and pit growth. Some authors have considered that pit initiation is attributed to the breakdown of the passive film layer caused by random fluctuations at local sites. After pit nucleation occurs, depending upon the conditions, the pit can either repassivate immediately or grow and then repassivate. It is generally agreed that pit initiation occurs as a result of breaking down of a passive film rich in chromium oxide, mostly in the presence of chloride, the propagation is an autocatalytic process in which corrosion products are hydrolyzed to provide local enrichment in chloride and proton concentrations. The pits could also provide active crevices sites for a formidable corrosion attack [27].

In recent years, there are studies on the pitting of metals, particularly stainless steel [28-30]. Pitting potential ( $E_{pit}$ ), protection potential ( $E_{pp}$ ), and repassivating potential ( $E_{rep}$ ) are the important electrochemical parameters for studying the likelihood of pitting corrosion of materials. Pitting potential ( $E_{pit}$ ) is the potential above which passive alloys are susceptible to pitting corrosion under certain environments, but below which pits cannot be formed, although existing pits can grow if the potential is greater than the protection potential. On the other hand, the existing pits will remain passive if the open circuit potential (OCP) lies below this repassivating potential. These parameters depend on the environment and the surface condition of the metal. Until recently,  $E_{pit}$  was the fundamental parameter in evaluating the susceptibility of different materials, in a different environment to localized corrosion. However, it is accepted widely that due to similarities between the crevice and pitting corrosion mechanisms, it would be more appropriate to introduce a new parameter called the breakdown potential,  $E_b$ . It is defined as a potential at which the pitting or crevice corrosion initiates. Thus, it is more appropriate to represent localized corrosion by  $E_b$  rather than referring to  $E_{pit}$  or crevice potential separately [31].

Crevice and pitting corrosion are forms of localized corrosion, which means that the corrosion occurs in a limited area on the pipe. The corrosion rate is often high and is generally higher than that for uniform corrosion, due to a large cathode/anode ratio. A severe attack is therefore usually observed, and the pit or crevice may cut through the pipe wall thickness to form a hole.

Crevice corrosion is another type of localized corrosion and commonly occurs where there is a narrow fissure with a width of normally only a few micrometers. These fissures can occur where two surfaces meet or where there are external agents such as paint remnants, tape or

insulation that forms a crevice against the pipe surface. Inside small crevices, the electrolyte exchange is severely disabled, and therefore the corrosion condition can be aggravating over time [12, 30]. In the last several decades, crevice corrosion was extensively researched [12, 30, 32]. The crevice corrosion mechanism is dependent on several parameters, and it may change accordingly with a change in the parameters [33].

Critical factors affecting the crevice corrosion of stainless steel in seawater or similar solutions include the salinity, velocity, temperature, dissolved oxygen level, the chromium and molybdenum contents of the stainless steel. In addition, the behavior of the passive film, crevice type, and chemical reaction also considered significant factors [29]. In most cases, there are obvious similarities between crevice corrosion and pitting corrosion mechanisms.

## **1.2 The objective of this work**

The experiments have been designed to investigate the objectives as listed below:

- ❖ Study the passive film properties of 316L and its susceptibility to pitting corrosion in different environments ( $\text{CO}_2$  and  $\text{N}_2$ ) by using different electrochemical techniques.
- ❖ Investigate the best stability of the passive film that will be formed on 316L Stainless steel for different parameters such as the change in the temperature and the change in concentration of NaCl.
- ❖ Studying the characteristics of the passive film formed on the surface of 316L Stainless steel at different stages of exposure, as well as the re-passivation kinetics.
- ❖ Screening of the corrosion scales of 316L Stainless steel by using different surface analysis techniques.
- ❖ Study the impact of high temperature and high pressure and NaCl concentrations on the pitting corrosion of 316L stainless steel in an environment simulating to the oil and gas production systems.
- ❖ Study the effect of different  $\text{CO}_2$  partial pressure on the passive film formed on 316L stainless steel at different temperatures.
- ❖ Evaluate the performance and thermal stability of  $\text{NO}_2^-$  as a corrosion inhibitor for a different type of carbon steel.

### **1.3 Significance of this work**

Corrosion resistance alloy (CRA), especially 316L Stainless steel has been used in the production of oil & gas for several decades because it provides long-term resistance to aggressive environments involving high CO<sub>2</sub> content, high temperatures, and pressures, where conventional carbon steel is not suitable. However, corrosion problems still represent the most important challenges causing huge losses in the industry. Many annual reports have estimated the cost of corrosion in the industry to be about millions of dollars, for example, the cost of corrosion for the Shell Company has been calculated to be equivalent to \$400 million in 1995 [2].

As mentioned before, this research aims to significantly improve the understanding of the behavior of 316L Stainless steel exposed to severe conditions such as high temperature and pressure and under corrosive environments. The formation of the passive film and its stability under various corrosive conditions will be investigated. In addition, to understand the thermal stability and performance of a nitrite-based corrosion inhibitor at inhibiting corrosion of carbon steel at high temperature and high pressure. So, it is believed that the proposed research will be able to reveal the appropriate operating conditions, and it will reduce the economic and production losses.

Accordingly, the outcomes of this research will assist oilfield corrosion engineers to better protect production equipment from financial and environmental effects due to corrosion failures.

### **1.4 Research Methods**

#### **1.4.1 Immersion Corrosion Test**

Immersion tests were carried out using methods reported in NACE procedure NACE TM0169/G31-12a, Standard Guide for Laboratory Immersion Corrosion Testing of Metals (NACE 2012) [34], to evaluate the corrosion behavior of 316L stainless steel and carbon steel specimens when immersed in different solutions and at different conditions. The test specimens were examined periodically to monitor the corrosion as a function of time. At the end of the testing period, the specimens were removed, washed in DI water and ethanol, and then analyzed data by using different surface analysis techniques for the possibility of pitting corrosion and its extent. Weight loss is a measure of the average uniform corrosion rate over the exposure

period and is obtained by cleaning the specimen using an acid with composition under ASTM-G1-03 [35] and NACE TM0169/G31-12a [34].

#### **1.4.2 Electrochemical Test**

The corrosion behavior of 316L Stainless steel and carbon steel were evaluated for a short time by using various electrochemical techniques, such as:

##### **1.4.2.1 *Cyclic Polarization Technique***

This technique is commonly employed to determine the susceptibility to pitting corrosion of passive materials. In this test, the experiment is conducted using a conventional three-electrode test cell. A 1L Pyrex glass cell was used for the electrochemical measurements. The electrode arrangements consist of a silver/silver chloride (Ag/AgCl) reference electrode, platinum (Pt) counter electrode, and the working electrode machined from 316L Stainless steel or carbon steel specimens. A potentiostat (Gamry 600 computer controlled) will be employed and is controlled by the general purpose electrochemical software version 4.6. The exposed surface of each working electrode was wet polished with 120, 320, and 600 grit silicon carbide paper, rinsed in ultra-pure water and washed in acetone to remove any impurities that might have remained on the electrode surfaces after polishing and then put in the ultrasonic bath for 20 minutes in ethanol. The surface of each sample was investigated using an Alicona optical microscope prior to the polarization to ensure that there is no pre-existing pit on the sample surface. Working electrodes were immersed in the electrolytes for stabilization at the open-circuit potential (OCP), and the open-circuit potential was recorded after reaching the steady state conditions. A saturated silver/silver chloride electrode was connected to the test solution by a salt bridge. The potential was scanned from the OCP in a positive direction until either the resulting current suddenly increases due to the breakdown of the passive film and pitting corrosion occurs or the potential reach the pre-specified value with no sharp increase in current as no pitting takes place. Afterward, the potential was then reversed in the negative direction to determine the re-passivation potential of the materials.

##### **1.4.2.2 *Electrochemical impedance spectroscopy (EIS)***

This test was used to investigate the properties of the passivation film. The electrode potential of the specimen was measured with respect to an external saturated Ag/AgCl. A Pt mesh was

used as a large area counter electrode. The test solution was aerated by bubbling CO<sub>2</sub> through a fritted disc, and this provided a small degree of agitation of the solution.

#### 1.4.2.3 *Mott-Schottky (M-S)*

The Mott-Schottky (M-S) experiments were conducted to determine the electronic properties of the passive film of 316L SS after exposure to different conditions. M-S relation describes the potential dependence of the space charge capacity of a semiconductive electrode.

#### 1.4.3 Autoclave cell

autoclave fabricated from Hastelloy (UNSN10276) [44] was employed to investigate the influence of high temperature high pressure on the corrosion behavior of 316L Stainless steel or carbon steel samples. The autoclave design is capable of conducting electrochemical measurements. The lid of the vessel has pre-drilled ports for working electrode (316L Stainless steel or carbon steel samples), a thermocouple for temperature control, gas inlet and outlet, a pressure gauge, the HT/HP reference electrode (external pressure balanced reference probe Ag/AgCl electrode, 3 M KCl solution, Corr Instruments, LLC, USA), and the HT/HP pH electrode (ZrO<sub>2</sub>-based pH probe, Corr Instruments, LLC, USA). The body of the vessel was used as a counter electrode. A band heater was wrapped around the external body of the test vessel to increase the solution temperatures.

#### 1.4.4 Surface analysis

Different surface analysis techniques were used in these research such as optical microscopy, scanning electron microscopy, and energy X-ray spectroscopy (SEM/EDS), X-ray diffraction spectroscopy (XRD), and X-ray photoelectron microscopy (XPS).

XPS measurements were performed on a Kratos Axis Ultra DLD spectrometer using a monochromatic AlK $\alpha$  (1486.6 eV) irradiation source operated at 225 W. The vacuum pressure of the analysis chamber of the spectrometer was maintained a  $9 \times 10^{-9}$  Torr or lower throughout the analyses. The electron binding energy scale was calibrated for each sample by setting the mainline of the C<sub>1s</sub> spectrum to 284.8 eV. XPS spectra were collected with a pass energy of 160 eV for the survey spectra and 40 eV for the high-resolution spectra. Depth profiling was undertaken using an argon gas cluster ion source operating in monoatomic Ar<sup>+</sup> mode at 5 keV. A typical depth profile involved 100 survey/sputter cycles, with sputtering undertaken for 6 seconds per cycle. Data files were processed using Casa XPS software and interpreted using

relative sensitivity factors provided by the instrument manufacturer (Kratos) as a guide. Background subtractions using a Shirley background were applied to all high-resolution spectra. In the case of the Fe<sub>2p</sub>, Cr<sub>2p</sub>, and Ni<sub>2p</sub>, which are known to be complicated by complex multiplet splitting, fitting was achieved using specified empirical fitting parameters previously derived from standard samples [30, 36]. For each of the fitted species, binding energy differences and area ratios were constrained for each species, while the absolute binding energy values were allowed to vary by  $\pm 0.3$  eV to accommodate any error associated with charge referencing.

## **1.5 Outline of the thesis**

This thesis is assembled as a hybrid consisting of the published paper and submitted manuscript (in different stages of submission and review) that constitute a chapter each.

The third chapter in this thesis has been studied the relationship between the passive film properties in relatively mild CO<sub>2</sub> environments and the susceptibility to pitting corrosion by using different electrochemical techniques, such as cyclic polarization, electrochemical impedance spectroscopy, and Mott-Schottky.

The fourth chapter has involved the comparison of the corrosion behavior and passive film properties in CO<sub>2</sub> and N<sub>2</sub> environments using cyclic polarization, electrochemical impedance spectroscopy, Mott-Schottky, and x-ray photoelectron spectroscopy.

The fifth chapter was studied the impact of high temperature and high pressure and NaCl concentrations on the pitting corrosion of 316L stainless steel in a CO<sub>2</sub> environment simulating to the oil and gas production systems.

The sixth chapter has investigated the effect of different CO<sub>2</sub> partial pressure on the passive film formed on 316L stainless steel at different temperatures.

The seventh chapter involved the effect of temperature on the corrosion rate and the protective layer formed on 1018 and 1030 carbon steel at different corrosion inhibitor concentrations and evaluate of corrosion inhibitor performance.

Appendix I investigates the corrosion behavior of carbon steel in the presence and the absence of a nitrite-based corrosion inhibitor at high-temperature and high-pressure conditions simulating a heating medium circuit.

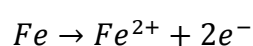
## Chapter 2: Literature Review

### 2.1 Introduction

Corrosion is the degradation of a material as a result of reaction with its environment [37] and an expected potential hazard associated with the oil and gas industry [1]. Practically any moisture environment can promote corrosion, which happens under many complex conditions in the oil and gas industry [38]. Corrosion occurs due to the presence of three main elements: an anode, cathode, and electrolyte. On the metal surface, the oxidation reaction takes place on the anode site, and the reduction reaction takes place on the cathode site while the electrolyte helps to transfer the electrons from the anode to cathode site. The corrosive media in the oil and gas industry are temperatures, carbon dioxide (CO<sub>2</sub>), hydrogen sulfide (H<sub>2</sub>S), and water, which are cause corrosion [39]. These corrosive environments lead to the destructive attack of a material by affecting the mechanical properties, which leads to material failure. Unexpected failure in the oil and gas equipment leads to serious consequences such as oil spillages, which in turn causes environmental problems on the one hand, and the loss of production on the other. Corrosion is one of the most important global problems. Reports have confirmed that the oil and gas companies lost billions of dollars every year due to corrosion. The estimated cost of the damages resulting from corrosion to be of the order of 3% to 5% of industrialized countries' gross national product [40]. For example, annually, US industries lose nearly \$170 billion due to corrosion, wherein the oil and gas industry takes more than half of these costs [41].

### 2.2 Corrosion forms

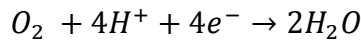
Corrosion occurs due to the contact between the metal and aqueous media [42]. When metal is exposed to a corrosive solution (the electrolyte), at the anode site, the metal atoms lose electrons, and other metal atoms then absorb these electrons at the cathode site. The cathode in contact with the anode via the electrolyte conducts this exchange in an attempt to balance their charges. The positively charged ions are released into the electrolyte, which is able to bond with other atoms that are negatively charged. This anodic reaction for iron and steel is represented in **(Equation 2.1)**



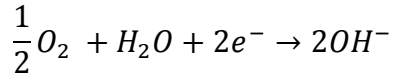
Equation 2.1

Anodic reaction

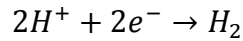
After the metal atoms at the anode site release electrons, there are four common cathode reactions, which are shown in (Equation 2.2, Equation 2.3, Equation 2.4, and Equation 2.5)[43].



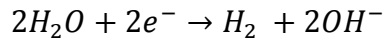
Equation 2.2  
Oxygen reduction in acidic solution



Equation 2.3  
Oxygen reduction in neutral or basic solution

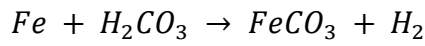


Equation 2.4  
Hydrogen evolution from acidic solution

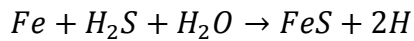


Equation 2.5  
Hydrogen evolution from neutral water

The most common gases found in the oil and gas industry are carbon dioxide (CO<sub>2</sub>) and hydrogen sulfide (H<sub>2</sub>S), and water is their catalyst for corrosion. When these gases are mixed with water, it forms the following reactions [44]



Equation 2.6



Equation 2.7

In the oil and gas industry, it is difficult to categorise the forms of corrosion uniformly. There are many forms and reasons for corrosion. The mechanism of corrosion differs according to the fluid composition, service location, geometry, and temperature. The main kinds of corrosion in the oil and gas industries involve sweet corrosion, sour corrosion, oxygen corrosion, galvanic corrosion, crevice corrosion, erosion corrosion, microbiologically induced corrosion, and stress corrosion cracking [45].

### 2.2.1 Sweet corrosion (CO<sub>2</sub> corrosion)

CO<sub>2</sub> corrosion has been known as a problem in the oil and gas industry for several years [7], and it is the most common corroding agent [46]. The dry CO<sub>2</sub> gas is noncorrosive to materials in this industry, but the dissolved CO<sub>2</sub> can encourage an electrochemical reaction between a material and the contacted aqueous phase, which leads to an increased corrosion rate [47]. CO<sub>2</sub>, when dissolved in water, will form carbonic acid, which will make the solution acidic. There

are many factors affecting the CO<sub>2</sub> corrosion such as temperature, pH, composition of the aqueous stream, flow condition, and metal characteristics [46]. When temperatures are raised, iron carbide film is formed on the pipe as a protective film, and the metal starts to corrode under these conditions. There are two types of CO<sub>2</sub> corrosion: pitting (localized attack that results in rapid penetration and removal of metal at a small discrete area) [48] and mesa attack (a form of localized CO<sub>2</sub> corrosion under medium-flow conditions) [49].

### 2.2.1.1 CO<sub>2</sub> Corrosion Mechanism

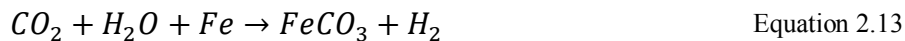
Different mechanisms have been assumed for CO<sub>2</sub> corrosion. However, all these mechanisms involve either carbonic acid or the bicarbonate ion formed on the dissolution of CO<sub>2</sub> in the aqueous phase (water). De Waard et al. [50] assumed one of the best CO<sub>2</sub> corrosion mechanism and was given as Equation 2.8



There are three cathodic reactions (Equation 2.9, Equation 2.10, and Equation 2.11) and one anodic reaction (Equation 2.12) can be recognised:



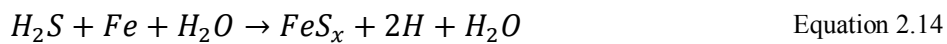
During this corrosion process, iron carbonate (FeCO<sub>3</sub>) can be formed on the metal surface according to Equation 2.13



This precipitate can act as a protective layer that reduces the general corrosion rate of the metal. However, under severe conditions, when the passive layer is destroyed, localized corrosion can occur.

### 2.2.2 Sour corrosion (H<sub>2</sub>S corrosion)

Hydrogen sulfide (H<sub>2</sub>S) represents a significant problem for the oil and gas industry. H<sub>2</sub>S is not corrosive by itself, but it turns into a strong corrosive agent in the presence of water [51], leading to form a weak acid, which is a source of hydrogen ions and is corrosive. In an H<sub>2</sub>S environment, the corrosion products are iron sulfides (FeS<sub>x</sub>) and hydrogen. Iron sulfide forms a scale that can act as a barrier to slow corrosion when temperatures are low[45]. The general equation of sour corrosion can be expressed as Equation 2.14 [52].



### 2.2.3 Oxygen corrosion

Oxygen is a strong oxidant which reacts rapidly with the metal leading to an increase in pitting and the crevice corrosion. Oxygen can damage the protective layer of metals, and oxidize dissolved ions into insoluble forms. Recently, the role of dissolved oxygen (DO) on the corrosion of carbon steel and stainless steel has been studied extensively. Baek WC et al. [53] believed that DO plays an important role in the composition of the corrosion film formed on carbon steel. In addition, the presence of oxygen increases the corrosive effects of acid gases (CO<sub>2</sub> and H<sub>2</sub>S). The types of corrosion associated with oxygen are mainly general corrosion and pitting corrosion.

### 2.2.4 Galvanic Corrosion

This type of corrosion happens when two different metallic materials (different electrochemical potential) are in contact and are exposed to an electrolytic environment, i.e., the metal with the most negative potential will be anode and starts corroding [46, 54]. The main factors affecting galvanic corrosion rates are the ratio of the cathode-to-anode area [45], the potential difference between materials, and the electrical resistance of the connection between the materials and of the electrolyte.

### 2.2.5 Crevice corrosion

Crevice corrosion is localized corrosion that happens in the narrow clearances or crevices in the metal, and the fluid is getting stagnant in the gap, which is caused as a result of concentration differences of corrodents over a metal surface [37]. The factors affecting crevice

corrosion are the type of crevice, the geometry of the crevice, the structure and composition of the alloy, and the environment (temperature, oxygen, and pH).

### **2.2.6 Erosion corrosion**

The corrosion reaction rate increased by the erosion corrosion due to removing the passive layer of corrosion products from the pipe wall. The passive layer is a thin film of corrosion products that serves to stabilize the corrosion reaction and slow it down. The turbulence and high shear stress in the line leads to remove the passive layer, which increases the corrosion rate [55]. The erosion corrosion is experienced where there is high turbulence flow with a significantly higher rate of corrosion [56] and is dependent on fluid flow rate and the density and morphology of solids present in the fluid [20]. This type of corrosion is often overlooked or recognized as being caused by wear [57].

### **2.2.7 Microbiologically induced corrosion**

Bacterial activities play the main role in this type of corrosion by producing waste products like CO<sub>2</sub>, H<sub>2</sub>S, and organic acids that corrode the pipes [58]. The microbes form colonies in a hospitable environment and promote corrosion under the colony. The neutral water promotes the formation of these colonies, especially when it is stagnant [46]. Many reports of the presence of microbes in reservoirs had been published [59-61]. Lazar et al. [60] found abundant microbial flora indigenous in oil field formation waters, which included species of Bacillus, Pseudomonas, Micrococcus, Mycobacterium, Clostridium, and Escherichia. Escherichia is reported to contain hydrogenase, an enzyme that utilizes molecular hydrogen and may be associated with cathodic hydrogen depolarization, causing corrosion of steel casings and pipes in the oil field [62].

### **2.2.8 Stress corrosion cracking**

Stress corrosion cracking (SCC) is a type of localized corrosion that produces cracks in metals from the combined influence of the corrosive environment and tensile stress. The effect of SCC on material normally falls between dry cracking and the fatigue threshold of that material [63]. The main identifying characteristic of SCC in a pipeline is the high pH of the surrounding environment, the appearance of patches, or colonies of parallel cracks on the external of the pipe.

### 2.3 Corrosion mitigation

Corrosion challenges in oil and gas are not static phenomena [38]. In the oil and gas industry, it is widely known that the effective management of corrosion will contribute towards the maintenance of asset integrity and achieve optimization of mitigation, and inspection costs [64]. Corrosion can be mitigated by using a technical approach, such as [46] :

- Material selection and design improvement
- Use of inhibitors
- Use of protective coatings and linings
- Adequate corrosion monitoring and inspection
- Anodic and cathodic protection technique

In the oil and gas industry, when it is observed that the existing materials are prone to corrosive attacks, it is normally decided to change the materials and select alternate materials to suit the specific need. Stainless steels cover a wide range of alloys, each with a particular combination of corrosion resistance and mechanical properties. Many types of stainless steel grades are used in the oil field, depending on the demands of the particular service environment. Applicable corrosion resistant alloys in the oil and gas industry proposed by Smith [65] include 13Cr, Super 13Cr, 22Cr duplex, 25Cr duplex, 28Cr stainless steel, 825 nickel alloy, 625 nickel alloy, 2550 nickel alloy, and C276 nickel alloy. The resistance to localized corrosion of the stainless steels was estimated from the composition using the pitting resistance equivalent (PRE) Equation 2.15:

$$\text{PRE} = (\%Cr) + (3.3 * \%Mo) + (16 * \%N) \quad \text{Equation 2.15}$$

### 2.4 Corrosion Inhibitors

Among the various methods to avoid or prevent destruction or degradation of a metal surface, the corrosion inhibitor is one of the best known methods of corrosion mitigation in the oil field [66]. There are many industrial systems and commercial applications that inhibitors are applicable, such as cooling water systems, refinery units, pipelines, chemical process, oil and gas production units, boilers and water treatment, paints, pigments, lubricants, etc., . Generally, inhibitors had great acceptance in industries due to excellent anti-corrosive proprieties.

#### **2.4.1 Mechanisms of action of inhibitors**

Inhibitors are substances or mixtures that in low concentration and aggressive environment inhibit, prevent, or minimize corrosion. A chemical inhibitor retards the rate of either the anodic or the cathodic reaction or both by forming a barrier at the steel surface. This adsorption restricts the electron transfer to the solution resulting in the corrosion inhibition process. Furthermore, the hydrophobic part of organic surfactants having aromatic ring and alkyl chain contacts with the hydrocarbon phase increasing the hydrophobicity of the film. The corrosive species are unable to contact the steel surface, and iron oxidation prevention occurs via this adsorption process [67]. Commonly, inhibitors are adsorbed on the carbon steel surface via either physisorption or chemisorption. Physisorption is electrostatic adsorption, which occurs by attractive forces between charged regions on inhibitor molecules and the charged sites on the steel surface [6]. While chemisorption is formed by chemical bonds from unshared electron pairs or  $\pi$  back donation to the steel surface [68].

#### **2.4.2 Inhibitors classifications**

Corrosion inhibitors can be classified as either anodic or cathodic corrosion inhibitors or mixed corrosion inhibitors. This classification is dependent on the inhibition effect on the type of the electrochemical corrosion reaction [69]. The anodic corrosion inhibitor reduces the corrosion rate by shifting the anodic potential [70]. The inhibitors react with the corrosion product, initially formed, resulting in a cohesive and insoluble film on the metal surface. For the effect of the anodic inhibitor, the inhibitor concentrations must be high enough in the solution. The inappropriate amount of the inhibitors affects the formation of film protection because it will not cover the metal surface completely, leaving sites of the metal exposed, thus causing localized corrosion. Concentrations below the critical value are worse than without inhibitors at all. In general can cause pitting, due to reduction at the anodic area relative to cathodic, or can accelerate corrosion, like generalized corrosion, due to full breakdown of the passivity. Some examples of anodic inhibitors are nitrates, molybdates, sodium chromates, phosphates, hydroxides, and silicates.

While the cathodic corrosion inhibitor shifts the cathodic potential [71], these inhibitors have metal ions able to produce a cathodic reaction due to alkalinity, thus producing insoluble compounds that precipitate selectively on cathodic sites. The cathodic inhibitors form a barrier of insoluble precipitates over the metal, covering it. Thus, restricting the metal contact with the environment, even if it is completely immersed, preventing the occurrence of the corrosion

reaction. Due to this, the cathodic inhibitor is independent of concentration, thus, they are considerably more secure than an anodic inhibitor.

Some examples of cathodic inhibitors are the ions of the magnesium, zinc, and nickel that reacts with the hydroxyl ( $\text{OH}^-$ ) of the water forming the insoluble hydroxides as ( $\text{Mg}(\text{OH})_2$ ,  $\text{Zn}(\text{OH})_2$ ,  $\text{Ni}(\text{OH})_2$ ) which are deposited on the cathodic site of the metal surface, protecting it. The mixed corrosion inhibitor acts by shifting both anodic and cathodic potential [72]. Consequently, the corrosion potential shifting inhibits the corrosion process on the metal surface.

### **2.4.3 Techniques for analysis of inhibitors**

The most useful technique to analyze the effectiveness of an inhibitor is weight loss experiment and electrochemical measurements, like the polarization curve method and the impedance measurement analysis. In addition, microscopy techniques are used to characterize the corrosion process.

### **2.4.4 Inhibitor efficiency**

The inhibitor efficiency could be measured by the following Equation 2.16

$$E_f = \frac{R_i - R_o}{R_o} \times 100 \quad \text{Equation 2.16}$$

where,  $E_f$  is inhibitor efficiency (percentage),  $R_i$  is corrosion rate of metal with inhibitor and  $R_o$  is the corrosion rate of metal without inhibitor [66].

## **2.5 Understanding Localized corrosion**

Localized corrosion is one of the biggest challenges for material selection for applications in the oil and gas industry. Unlike general corrosion, which is a slow process, localized corrosion may start and propagate rapidly leading to significant damage [73]. Generally, localized corrosion can be defined as the type of corrosion in which there is an intense attack at localized sites on the metal surface. Common forms of localized corrosion can be distinguished like pitting, crevice corrosion, and intergranular corrosion.

Several important papers on the various localized corrosion phenomena have been studied for decades. The process of localized corrosion can be divided into a sequence of steps [73]:

initiation by the breakdown of the passive film; metastable growth of small pits on the verge of stability (metastable in this context indicates that many pits cease to grow at this stage); stable growth of localized corrosion sites that can grow quite large; and finally if conditions permit repassivation or cessation of attack.

It is known that the localized corrosion initiates above a critical potential and repassivates below another, lower potential [73]. Once initiated, the attack is stabilized by the localized development of aggressive conditions as the result of metal cation hydrolysis and  $\text{Cl}^-$  ion migration. A conservative criterion for localized corrosion is the prediction that it can occur at potentials above the repassivation potential and should not occur if the corrosion potential remains below the repassivation potential by a margin of safety that should be at least 100 mV. Despite the advances and considerable understanding that has been achieved, the prediction of localized corrosion is a difficult problem for some reason. First of all, the events happen in a small area, with a passive film nanometer in thickness and initiation sites of a similar size. Once initiation, the rate of pit growth can be extremely high, even tens of  $\text{A}/\text{cm}^2$  [74]. Therefore, the situation is extremely dynamic with rapidly moving boundaries and rapidly changing chemistries. As a result, it is not possible to predict exactly when and where breakdown will occur, which makes high-resolution observation of initiation events extremely difficult. Finally, the exact susceptibility of sites for breakdown and the ability of other sites to sustain cathodic reactions depend on details of the surface film properties, such as catalytic activity, that are not well understood, difficult to measure on the scale of the sites, and change with time as the process evolves.

Different models have been developed to describe localized corrosion. The point defect model (PDM) developed by Macdonald et al. is one of the best models available for the prediction of localized corrosion susceptibility [75, 76]. The PDM considers the transport of cation vacancies in the passive film towards the film metal interface, where they can condense to form voids or nascent pits at the metal-passive film interface if the flux of vacancies arriving at the interface is greater than what can be consumed by annihilation via a metal oxidation reaction. The impact of an aggressive species, such as  $\text{Cl}^-$ , is hypothesized to alter the generation and transport of cation vacancies. The model correctly predicts the logarithmic dependency of pit initiation potential on  $\text{Cl}^-$  concentration, the effects of some alloying elements, and the effect of parameters such as scan rate on pit initiation. Furthermore, the PDM predicts the pitting potential, whereas the breakdown occurs at much lower potentials as evidenced by metastable pitting transients in the data [77]. A bilogarithmic dependence of pitting potential on  $\text{Cl}^-$  concentration is often observed but is not predicted by the PDM at present.

In recent years, Anderko et al. [78-81] have developed a different approach to modeling localized corrosion by adapting Okada's [82, 83] model and combining it with a model of thermodynamic speciation [84, 85]. This approach focuses on the repassivation potential, which is lower than the breakdown potential and, therefore, a more conservative value to use as a design parameter. As mentioned above, localized corrosion might be possible when the corrosion potential is higher than the repassivation potential and is very unlikely if the corrosion potential remains lower than the repassivation potential by a margin of 100 mV or more. The repassivation potential is the threshold condition at which pitting or crevice corrosion is stable and the effects of alloy composition and solution chemistry on this potential must be understood to predict the likelihood of localized corrosion.

## **2.6 Pitting corrosion characteristics**

### **2.6.1 Pitting potential and repassivation potential**

Several years ago, Brenner [86] introduced the concept of the pitting potential  $E_{\text{pit}}$ , and in 1963, Pourbaix et al. [87] proposed repassivation potential,  $E_{\text{rep}}$ . The two characteristics are usually determined from anodic polarisation curves;  $E_{\text{pit}}$  is represented by a sudden increase of the current, and  $E_{\text{rep}}$  is associated with a drop in current due to pit repassivation.

Several definitions have been proposed for  $E_{\text{pit}}$  such as, the potential above which stable pits propagate or a necessary potential to maintain a salt film inside a pit [88, 89], a potential at which pit solution composition is aggressive enough to keep the passive film locally unstable and thus prevent repassivation [90], or a minimum potential for metastable pits to become stable [91]. While  $E_{\text{rep}}$  was defined as the potential, below which no metastable and stable pitting occurs, and above which metastable pits can form, and already existing pits can propagate. It was also suggested that  $E_{\text{rep}}$  is the minimum required potential to maintain the critical environment inside a propagating pit [92].

Both  $E_{\text{pit}}$  and  $E_{\text{rep}}$  were found to be dependent on the method of their determination. For instance,  $E_{\text{rep}}$  depends on the concentration and combination of aggressive species [81], the scan rate [93], and decreases with increasing pit depth, and when measured on deep pits obtained values may be significantly underestimated [93].  $E_{\text{pit}}$  increases with an increase in potential scan rate [94]; depends linearly on the square root of the scan rate and is affected by the surface treatment [95]. For  $E_{\text{pit}}$  measured by potentiostatic methods, the more noble potential, the shorter was the time required for pitting initiation [96].

Scully et al. [97] showed that  $E_{\text{pit}}$  of stainless steel could be correlated with cooperative interactions between pit sites. Through the mediation of the lateral diffusion length relative to the pit defect site spacing, they could control the cooperative spreading and increase threshold ( $E_{\text{pit}}$ ) potential. Experimentally, It was found that  $E_{\text{pit}}$  depends on the concentration of aggressive species, ( $C_{\text{agg}}$ ), and inhibitors in the electrolyte, but is little influenced by pH in the case of Fe and Al. While the earlier work [98] showed that  $E_{\text{pit}}$  of Fe might be independent of pH below 10. The recent results [99] suggest pH of 8.5, which also applies to stainless steel [100]. Furthermore, Bird et al. [101] showed that  $E_{\text{pit}}$  of Fe decreases linearly with the logarithm of ( $[\text{Cl}^-]/[\text{OH}^-]$ ) in the pH range 10–14.

The fact that  $E_{\text{pit}}$  and the general corrosion resistance of metallic materials can be altered through the presence of magnetic field [102], modifications of microstructure [103, 104], surface treatments [105, 106] and irradiation is now well documented, e.g., greater  $E_{\text{pit}}$  values were reported for Zircalloy-2 [107], Ti [108], AISI 304 L and 316 L stainless steel [109] under gamma radiation, and AISI 304 stainless steel exposed to proton irradiation [110]. An increase in  $E_{\text{pit}}$  due to ultraviolet irradiation (photo-inhibition) was reported for stainless steel [111-113], Ni [114, 115], or X70 pipeline steel in  $\text{Cl}^-$  containing borate buffer [116].

Although there are various experimental techniques to determine  $E_{\text{pit}}$ , all of them depend on the development of a stable pit. The observation of the metastable pitting below  $E_{\text{pit}}$  indicates that pits might initiate, but not propagate, at more negative potentials. This contradiction is supported by the observation of micro-pits at potentials as low as 290 mV below  $E_{\text{pit}}$  of Al [117].

## **2.7 Passivity breakdown**

Passivity is an old subject. The first metal that was observed to exhibit this phenomenon was iron. It has been proposed that the breakdown of passivity is responsible for many of the localized corrosion failures in the oil field [73]. There are three mechanisms for passivity breakdown that have been raised and discussed [118]: passive film penetration, film breakdown mechanism, and the adsorption mechanism.

### 2.7.1 Passive film penetration mechanism

The mechanism of penetration involves the transfer of anions through the oxide film to the surface of a metal, where they start their specific action. Hoar et al. [119] first one discussed this mechanism and found the aggressive ions penetrated the oxide film under the influence of high electric field, following their adsorption onto the film surface.

The small diameter of the chloride ions ( $\text{Cl}^-$ ) make them more aggressive than  $\text{Br}^-$  or  $\text{I}^-$ , and subsequent ability to penetrate the oxide lattice more readily; however, it is important to note that  $\text{Br}^-$  and  $\text{I}^-$  ions were reported to be more aggressive for Ta [120] and Ti [121, 122] than  $\text{Cl}^-$ . Evans [123] presented a model, with  $\text{Cl}^-$  ions permeating through the oxide layer and the breakdown of the oxide layer occurring once they reach the underlying bare metal. This model considered the adsorption of aggressive ions on the protective oxide film as the first step towards the passivity breakdown. The localized nature of pitting was explained by easier penetration at film imperfections. The breakdown potential was that potential, at which the electric field across the film reached the value necessary for anion penetration.

Pou et al. [124] suggested a model based on the presence of a film with a hydrated polymer structure. The film is amorphous and the bound water within it plays an important binding role. In support of the penetration mechanism, the breakdown rate was found to be proportional to  $\text{Cl}^-$  ions, indicating the participation of a single  $\text{Cl}^-$  ion in the rate determining step of the breakdown process, and this step is assumed to be penetration. Contrary to this finding, Goetz et al. [125] have not detected any  $\text{Cl}^-$  incorporation into the iron oxide film by using the SIMS and Auger electron spectroscopy. McBee and Kruger [126] supported the penetration theory;  $\text{Cl}^-$  ions were found incorporated into the passive film on high purity iron. However, Foroulis [127] suggested that the measured chloride contents may be attributable to chlorides incorporated into the film during film thickening after the metal had been exposed to the electrolyte. Wood et al. [128] used secondary ion mass spectroscopy to study adsorb of  $\text{Cl}^-$  by a thin oxide film on Al in 1 M KCl. A considerable amount of  $\text{Cl}^-$  was found at the oxide-solution interface, but no  $\text{Cl}^-$  ions were detected within the oxide film itself. Similarly, Szklarska-Smialowska et al. [36] reported the presence of  $\text{Cl}^-$  ions only in the outer layers of the oxide film on samples of pure iron, which were exposed to chloride solution.

The results of Bardwell and MacDougall [129] were not consistent with the penetration model. They have demonstrated the existence of a critical charge, i.e., a critical oxide thickness, for the pitting of Fe. This charge was found to be independent of potential and associated with a transition in the growth of the passive film when a second, outer phase was first formed on top

of the inner phase. The experimentally observed dependencies of critical  $E_{\text{pit}}$  on  $\text{Cl}^-$  were consistent with this concept, and thus they concluded that the critical event in pitting is not an interaction between  $\text{Cl}^-$  ions and the bare metal surface.

### 2.7.2 Film breakdown mechanism

The film breakdown mechanism is based on the breaks within the oxide film, which lead to direct access of anions to the unprotected metal surface [20, 130, 131]. However, Galvele [132], who did not consider the model of Vetter and Strehblow [130] as realistic, Galvele predicted increasing pH for the pit solution during pit growth, while in practice the pH was found to decrease. Hoar [133] proposed that adsorption of aggressive anions decreased the surface tension of the passive film such that cracks would arise, allowing anions to reach the metal surface. Sato [20] used thermodynamics to calculate the pressure acting vertically on the film surface with contribution due to both electric fields across the film (electrostriction) and to surface tension. At some critical film thickness, the film pressure, exceeds the mechanical breakdown stress of the film and rupture occurs, leading to pit initiation. The critical thickness was shown to decrease with increasing field strength and decreasing surface tension. In common with Hoar [133], Sato supposed that adsorption of anions would decrease surface tension so that a mechanical breakdown would occur for thinner film, i.e., lower applied potentials.

Xu et al. [134] found microscopic roughness on an iron surface, with the radius of the curvature in the range of ten to a few tens of nanometres. It was postulated that the electric field was larger than average in the inner half of the concave region. According to the Sato [135] model, the passive film on the concave region of the surface is subject to a higher than average compressive electrostatic pressure during immersion in an electrolyte and is thus a preferred site for passive film rupture and micro pits formation. The role of  $\text{Cl}^-$  ions is to increase the electrostatic pressure and reduce the compressive strength of the film. The pit initiation could then be a repeated breakdown/repair process that deepens the micro pit until it reaches a critical depth.

Evans [136] provided evidence that the film on a metal containing internal stresses is constantly cracking. Galvele [132] and Videm [137] supporting this hypothesis. They believe that passivity breakdown is presumed to occur constantly even below  $E_{\text{pit}}$ . In the absence of aggressive anions, defects in the passive film are thought to be healing rapidly, while in the presence of aggressive anions and at sufficiently high potentials, the metal surface becomes activated.

Burstein and Mattin [138] suggested a model for stainless steel where pits initiate as a result of mechanical rupture of the passive film brought about by salt film formation underneath the film. The oxide was considered to grow by migration of oxygen anions towards the film–metal interface and it was suggested that simultaneous migration of  $\text{Cl}^-$  will occur in the same direction. If sufficient  $\text{Cl}^-$  ions reach the film-metal interface at one particular site (an inclusion) then metal chloride salt will form beneath the oxide film. Such salts occupy between two to eight times the volumes of the oxides or metal from which they are formed, and so the passive film above the salt must expand and eventually crack.

Rupture of the passive film and dissolution of the salt without the formation of a metastable pit was thought to be the cause of the pit nucleation events observed in the work of Burstein et al. [139], Riley et al. [140] and Suter et al. [141].

### **2.7.3 Adsorption mechanisms**

The adsorption mechanism has been discussed firstly by Kolotykin [142], Hoar, and Jacob [143] based on the adsorption of aggressive anions at the oxide film surface, which enhances the transfer of metal cations from the oxide film to the electrolyte. The model was based on the localized formation of transient complexes with metal cations creating pits. This effect leads to the thinning of the passive layer with possible final total removal and the start of intense localized dissolution.

The theory assumes that passive film is a layer of adsorbed oxygen and that pits initiate at sites where  $\text{Cl}^-$  ions displace the oxygen [144-146], lead to a surface complex with metal ions, which enhances their transfer into the electrolyte, compared to the non-complexed situation, and as a consequence, the passive film is thinned. The thinner oxide is related to a higher electrical field strength within the layer and consequently, to a migration of the metal ions. According to Heusler and Fischer [147, 148], localized adsorption of  $\text{Cl}^-$  ions leads to an enhanced oxide dissolution at these sites, thinning of the oxide film until complete film removal and active dissolution. A similar suggestion came later from Foley et al. [149, 150], claiming that the formation and existence of metal-anion complexes should be included in any mechanisms of Fe passivity or dissolution. They reported that Fe-Cl complexes that dissociate and remove Fe cations from the surface of stainless steel form in neutral chloride solutions. Khalil et al. [151] believed that the formation of soluble complexes, related to the adsorption of aggressive anions on the metal surface, initiated the dissolution of the passive film. They studied the influence of  $\text{Cl}^-$ ,  $\text{Br}^-$  and  $\text{I}^-$  ions on a passive film on Fe by X-ray photoelectron spectroscopy. The local thinning of the passive film caused an increase in the strength of the electrical field, which led

to the local dissolution. The highest reduction in thickness of the passive film was observed with  $\text{Cl}^-$  and the lowest with  $\text{I}^-$  ions.

## **Chapter 3: EIS and Mott-Schottky to Study the Passive Film Properties of 316L and its Susceptibility to Pitting Corrosion in CO<sub>2</sub> Environments**

### **3.1 Abstract**

In the production of oil and gas under anaerobic conditions at high temperature and partial pressure of CO<sub>2</sub>, the use of corrosion resistant alloys, such as 316 stainless steel, are being increasingly used to replace carbon steel with inhibition. However, stainless steel may suffer pitting corrosion. This study investigates the relationship between the passive film properties in relatively mild CO<sub>2</sub> environments and the susceptibility to pitting corrosion. Electrochemical impedance spectroscopy (EIS) and capacitance measurements (Mott-Schottky) are used to investigate the semiconductor properties of the passive films formed on 316L stainless steel in 3 wt.% NaCl aqueous solution in CO<sub>2</sub> containing environment at different temperatures (30 °C - 80 °C) as well as different NaCl concentrations (3 wt.% - 8 wt.%) at 30 °C. Its susceptibility to pitting corrosion is also studied with cyclic polarization technique. The results indicate that the pitting susceptibility of 316L stainless steel increase with increasing temperature and NaCl concentration. The properties of the passive film are influenced by temperature as well as NaCl concentration as identified by the 2 AC techniques. Bode phase plots of specimen at 30 °C and 40 °C show one time constant whereas two time constants are observed at high temperatures 60 °C and 80 °C. The two time constant feature observed at high temperature can be attributed to an inhomogeneous film consisting of a compact inner layer and a less compact (porous) outer layer. Capacitance measurements based on the Mott-Schottky relationship reveals a p-n type heterojunction in all conditions. The point defects as determined by the donor ( $N_D$ ) and acceptor ( $N_A$ ) densities increase with increasing temperature and NaCl concentrations indicating that the passive film becomes weaker and hence more prone to pitting corrosion.

**Keywords:** 316L stainless steel, pitting susceptibility, cyclic polarization, electrochemical impedance spectroscopy, Mott-Schottky analysis, donor and acceptor densities.

### **3.2 Introduction**

Stainless steel has been used for decades in several industrial sectors including oil and gas industry. The applications of stainless steel include flow lines, manifolds, heat exchangers, burners and flare systems, structural components and safety systems due to its high corrosion resistance to general corrosion [152-154]. In particular, austenitic stainless steel has been widely used because of its superior mechanical properties and corrosion resistance due to the

chromium and molybdenum addition and low carbon content [155]. The high corrosion resistance of stainless steel is primarily due to the presence of a very thin passive barrier film formed on its surface. The nature of the passive film formed in oxygen environments has undergone extensive investigation. Experiences have shown that in oxygen environments stainless steels are susceptible to localized pitting corrosion due to a breakdown in the passive film. The susceptibility to pitting corrosion generally increases with increase in temperature and the concentration of chloride ions. Despite the increasing use of stainless steel in oil and gas production where anaerobic CO<sub>2</sub> (carbonic acid) environments exist, not a great deal is known about the nature of the passive film and its protective mechanism in these environments.

Pitting corrosion of metals and alloys is one of the main causes of material failures because it is difficult to monitor and control due to its complex nature. Pitting corrosion comprises of two main processes: pit nucleation and pit growth [28, 156]. Hoar *et.al.* suggested that some anions could penetrate the passive film [157]. In particular, the effect of Cl<sup>-</sup> ion on the local breakdown of passivity and stability of surface oxide was investigated [158, 159]. On the other hand, several authors considered that the pit initiation is attributed to the breakdown of the passive film layer caused by random fluctuations at local sites [20, 134, 135].

After pit nucleates, depending upon the conditions, the pit can either repassivate or continue to grow. It is generally agreed that the nucleation and propagation of pitting corrosion are strongly related to the characteristics of the oxide film on the metal surface, mostly in the presence of chloride [160]. Therefore, the observed changes in the pitting behavior of stainless steel has often been related to changes in the composition, structure, and properties of the passive film [161, 162].

The composition and the properties of the passive film are dependent on several variables, including the composition of the alloy and the composition of the electrolyte in which the films are grown [163]. Although, there is still some controversy regarding the detail structure and composition of the passive film.

It was mentioned earlier under aerobic conditions, the characterization of passive film and investigation of corrosion mechanisms have been heavily studied aiming to explain the susceptibility to pitting corrosion [20, 164]. In addition, a modification in the protective properties of the passive films has often been suggested to be the cause of the observed changes in pitting morphology [160]. Cyclic polarization has been a common technique to evaluate the susceptibility to pitting corrosion of a passive metal [165].

On the other hand, the influence of environmental variables, such as elevated temperature and electrolyte composition on the protective properties of oxide films is still limited. Wang *et. al.* used AC impedance measurements to study the effect of temperature and chloride concentration on the protective properties of the passive films formed on 304 stainless steel [160]. They found that the charge transfer resistance decreased with increased temperature and increase in chloride concentration. Thus, the protective properties of the film were adversely affected.

Furthermore, characteristics of the passive film formed on stainless steel were investigated in alkaline media through electrochemical impedance spectroscopy (EIS) using an equivalent circuit comprising of two time constants [166, 167]. However, the physical meaning assigned to the equivalent circuit components varied. Abreu *et.al.* stated that the high frequency constant represented the charge transfer process occurring on the surface of the reinforcements [166] whereas Ping *et.al.* asserted that the charge transfer process is assigned to the low frequency constant [167]

Past investigations generally suggested that the passive film has a bilayer structure acting as barrier protecting the metal surface from the corrosive environment. This bilayer passive film is a semiconductor including cation vacancies, anion vacancies, and cation interstitials [168, 169]. The inner layer is rich with chromium oxide or hydroxide behaving as a p-type semiconductor [170-172] whereas the outer layer is composed of iron-oxide exhibiting n-type semiconductor properties [173-176]. Wijesinghe *et. al.* believed that the protectiveness of the passive film depended on the chromium content and other elements which may constitute the passive film [177]. Semiconductor behavior also depends on the point defects that can be represented by the donor density of the passive film. Oxygen vacancies and cation interstitials acting as electron donors behaving as n-type to the passive layer while cation vacancies acting as electron acceptor producing p-type [178]. Mott–Schottky analysis is a powerful method for investigating the semiconductor properties and its application in studying the passive films of stainless steel and other corrosion resistant alloys has increased over the years [179-182].

Manning *et.al.* studied the effect of temperature on the pitting susceptibility of Fe-Cr-Ni alloys by analyzing the change in the defect structure of the semiconductor using the Mott-Schottky technique [183]. The authors argued that the n-type films were more susceptible to pit initiation than p-type films due to the existence of oxygen vacancies and the enhanced diffusion of chloride ions through the oxide lattice.

This paper investigates the influences of temperature and NaCl concentrations on pitting corrosion of 316L in CO<sub>2</sub> environment simulating the oil and gas production systems using 3 electrochemical techniques; i.e. cyclic polarization, electrochemical impedance spectroscopy (EIS), and capacitance (Mott-Schottky) measurements. The semiconducting properties of the passive films are studied using the 2 latter AC techniques to further explain the pitting susceptibility determined by the conventional cyclic polarization method.

### 3.3 Experimental procedure

#### 3.3.1 Materials and specimen preparation

All specimens in this study were made from 316L stainless steel with the chemical composition depicted in Table 3.1. Specimens were machined to a flat cylinder with a height of 3 mm and diameter of 15 mm. To prevent crevice corrosion, the sample holder was designed and manufactured from an inert material (polyether ether ketone or PEEK). The area exposed to the solution was 0.96 cm<sup>2</sup>. All specimens were wet abraded from 80 to 600 SiC grit, rinsed with ethanol and ultra-pure water, and dried with N<sub>2</sub> gas.

**Table 3.1 Composition of 316L SS used in this study**

Element	C	Si	Mn	P	S	Ni	Cr	Mo	Fe
(wt. %)	0.02	0.36	1.36	0.03	0.006	10.02	16.92	2.02	Bal.

#### 3.3.2 Test solutions

The effect of temperature was studied in 3 wt.% NaCl solutions at 4 different temperatures: 30 °C, 40 °C, 60 °C, and 80 °C. In addition, a different set of experiments were conducted at a constant temperature of 30 °C but varying concentrations of NaCl; i.e. 3 wt.%, 4 wt.%, 6 wt.%, and 8 wt.%. The pH of the test solutions was adjusted to 4 by adding 1 M NaHCO<sub>3</sub>. Table 3.2 shows the summary of the test conditions.

Prior to starting the test, the test solution was sparged with CO<sub>2</sub> gas for at least 4 h to deaerate the solutions. Afterward, the solution was transferred via a peristaltic pump into another 1 L glass cell fitted with electrodes where the CO<sub>2</sub> sparging continued over the solution until the end of the tests.

**Table 3.2. Summary of test conditions**

Type of test	Variable	Conditions
Effect of temperatures	Temperature / (°C)	30, 40, 60 and 80
	NaCl / (wt.%)	3
	pH	4
Effect of NaCl concentrations	NaCl / (wt.%)	3, 4, 6 and 8
	Temperature / (°C)	30
	pH	4

### 3.3.3 Electrochemical measurements

All experiments were carried out using a classical three electrode cell of 1 L volume. 316L specimen was used as the working electrode whereas a platinum mesh and a standard silver/silver chloride (Ag / AgCl) probe connected to the cell via a Luggin probe filled with 3 M KCl were used as the counter and the reference electrode, respectively. All the electrochemical measurements of the corrosion process were performed using a potentiostat (Gamry reference 600 computer controlled).

The pitting susceptibility of 316L SS at different temperatures and NaCl concentrations were evaluated using the cyclic polarization technique in accordance with ASTM G 61 [184]. When the open circuit potential (OCP) was steady, the cyclic polarization scan was started at a scan rate 0.167 mV/s starting from the OCP. The scan was reversed back towards the OCP when the measured current exceeded 25 mA/cm<sup>2</sup>. In all cases, the tests were repeated at least two times to verify reproducibility.

To investigate the passive film properties with AC methods (EIS and Mott-Schottky), it is necessary to obtain a reproducible passive film at the electrode surface prior to the measurements. To accelerate the passive film formation in a controlled manner, the passive film was formed electrochemically. Initially, the working electrode immersed in 3 wt.% NaCl solution at 30 °C was polarized at - 0.2 V vs. OCP for 15 min to remove any air formed oxide film. Subsequently, to generate a reproducible passive film, the working electrode was then polarized to - 0.1 V vs. Ag /AgCl for 1 h. The potential at which the passive film was formed was determined from the polarization curves. To study the effect of temperature on pitting susceptibility, the solution temperature was then raised to the desired value after the film was formed. Similarly, to investigate the effect of NaCl, 3 wt.% NaCl was drained from the cell and a solution with the desired NaCl content was transferred into the cell using a peristaltic pump.

EIS was then carried out at OCP using an amplitude of 10 mV, and the frequency range from 10 kHz to 10 mHz. Subsequently, Mott – Schottky (M-S) technique was employed by sweeping the potential from -0.5 V vs. Ag/AgCl to 1 V vs. Ag/AgCl at a frequency of 3 kHz with an amplitude signal of 10 mV. The potential step was 20 mV.

### 3.4 Results and discussion

#### 3.4.1 Cyclic polarization technique

##### 3.4.1.1 *Effect of temperature*

Figure 3.1 shows the cyclic polarization curves for 316L stainless steel samples in 3% NaCl at 4 different temperatures saturated with CO<sub>2</sub> at 30 °C and pH 4. The shape of the polarization curves can indicate if the specimen is in the passive or active state. Several important parameters obtained from the polarization scans are often used to explain the susceptibility to pitting corrosion of a material; i.e. pitting potential ( $E_{pit}$ ) and repassivation potential ( $E_{rep}$ ). There is no tendency to pit if  $E_{rep}$  is more positive than  $E_{pit}$ , or the current measured from the reverse scan is smaller than that from the forward scan, i.e., negative hysteresis. On the other hand, the pitting could occur if  $E_{rep}$  is more negative than  $E_{pit}$ , i.e., positive hysteresis.

According to Figure 3.1, large positive hysteresis was evident at these conditions indicating that 316L stainless steel is prone to localized corrosion [185, 186]. The potential at which the current density suddenly increases, referred to as  $E_{pit}$ , indicates the passivation breakdown and consequently pitting corrosion.  $E_{pit}$  decreases with increasing temperatures suggesting an increased susceptibility to passive film breakdown as previously reported in the literature [187-189] albeit for oxygenated seawater environments.

The forward polarization scan was continued until the current density reached 25 mA/cm<sup>2</sup>, then the scan was reversed towards OCP. The potential where the backward scan and forward scan meet is called repassivation potential ( $E_{rep}$ ). It can be observed from Figure 3.1 that the  $E_{rep}$  decreases with an increase in temperatures. At the end of the polarization, the final potential did not reach to the OCP but stabilized at a potential more positive than the OCP for all conditions.

To determine the susceptibility of pitting corrosion, the difference between  $E_{pit}$  and OCP ( $\Delta E_{pit}$ ) is referred to pitting driving force in which the large  $\Delta E_{pit}$  is usually associated with the greater resistance to pitting corrosion [161]. Table 3.3 shows the  $\Delta E_{pit}$  obtained at different temperatures in which the largest  $\Delta E_{pit}$  was found at 30 °C. In general,  $\Delta E_{pit}$  decreases with

increasing temperatures. The adverse effect of temperature on the pitting susceptibility of 316L found in this study agreed well with the previous work in oxygenated environments [190].

Another important parameter to be considered when evaluating the pitting susceptibility is the difference between  $E_{rep}$  and OCP ( $\Delta E_{rep}$ ) is referred to repassivation driving force. The large  $\Delta E_{rep}$  is associated with a greater tendency for repassivation [161]. Table 3.3 shows the  $\Delta E_{rep}$  for 316L SS at different temperatures, and it can be seen the largest  $\Delta E_{rep}$  value was at 30 °C.

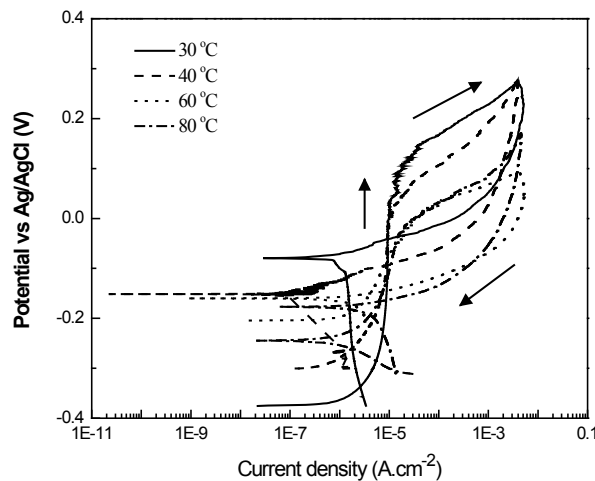


Figure 3.1 Cyclic polarization curves of 316L SS in 3% NaCl, pH 4 at different temperatures

**Table 3.3.  $\Delta E_{pit}$  and  $\Delta E_{rep}$  of 316L in 3%NaCl saturated with CO<sub>2</sub> at temperature from 30 °C to 80 °C**

Temperature / (°C)	$\Delta E_{pit}$ / (mV)	$\Delta E_{rep}$ / (mV)
30	484	336.83
40	336.56	205.83
60	191.55	55
80	180.59	46.2

#### 3.4.1.2 Effect of NaCl concentrations

Cyclic polarization curves of 316L SS as a function of NaCl concentrations are shown in Figure 3.2. It has been established that chloride ion is aggressive and can promote the passive film breakdown of stainless steel [191]. Large positive hysteresis loops exhibited at the end of the experiments confirms that 316L SS is susceptible to localized corrosion under these conditions. In addition, OCP decreases with an increase in NaCl concentrations indicating that 316L SS became more active. The current fluctuations also appeared in the passive region of the curves,

especially at high NaCl concentrations (4 wt.%, 6 wt.%, and 8 wt.%) demonstrating metastable pitting events [192].

Table 3.4 shows the  $\Delta E_{\text{pit}}$  for 316L SS at different NaCl concentrations at 30 °C and pH 4. It can be seen that 316L SS showed the largest  $\Delta E_{\text{pit}}$  value at 3 wt.% NaCl. Generally,  $\Delta E_{\text{pit}}$  decreases with the increase of NaCl concentrations. The repassivation potential cannot be obtained because the reverse scans did not meet with the forward scan. This behavior can be associated with the weakening of the passive film [193]. It has also been proposed that when OCP is higher than  $E_{\text{rep}}$ , the material is prone to stable pitting corrosion [193].

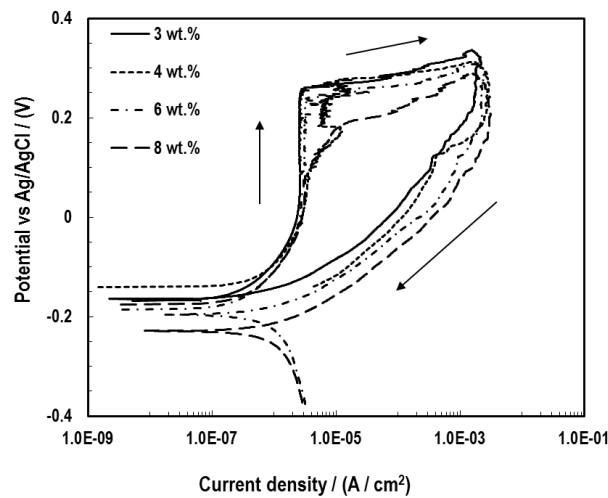


Figure 3.2 Cyclic polarization curves for 316L SS in different NaCl concentrations at 30 °C, pH 4

**Table 3.4.  $\Delta E_{\text{pit}}$  and  $\Delta E_{\text{rep}}$  of 316L in solution with varying NaCl concentration saturated with CO<sub>2</sub> at temperature at 30 °C**

NaCl (wt. %)	$\Delta E_{\text{pit}}$ (mV)	$\Delta E_{\text{rep}}$ (mV)
3	429	---
4	409	---
6	424	---
8	334	---

### 3.4.2 Electrochemical impedance spectroscopy (EIS) technique

#### 3.4.2.1 *Effect of temperature*

EIS was used to gain an insight into the influence of temperatures on the passive films of 316L SS. Figure 3.3 (A) and (B) display the Nyquist plots and the Bode phase diagrams, respectively. Nyquist plots illustrate the relationship between an in-phase (resistance) component which is described mathematically by real numbers on the x-axis and an out-of-phase (capacitance)

component described by an imaginary number on the y-axis. A similar shape of Nyquist plots was displayed for all test temperatures; i.e., the incomplete capacitive arc at the range of frequencies studied. The magnitude of the semicircles appears to be related to temperature. At a low temperature of 30 °C and 40 °C, the semicircles have a similar diameter and markedly reduced once the temperature was increased to 60 °C. From Figure 3.3A, the diameter of the depressed semicircle decreases with rising of temperatures which indicates the increased corrosion attack. In addition, the depressed semicircle implied that the surface does not behave as an ideal capacitor due to the microscopic surface roughness and the presence of a porous corrosion product film [194].

The corresponding Bode phase diagrams in Figure 3.3B presents symmetry with phase angle lower than 90° in all EIS spectra, this can be related to the deviation from ideal capacitance behavior and this characteristic, which is typical of passive behavior, can be seen in other studies on corrosion resistant alloys [195-198]. At temperatures of 60 °C and 80 °C, the phase angle in the frequency zone from about 0.1 Hz to 100 Hz increases with increasing temperatures, and the phase angle below 0.1 Hz, also increases with increased temperature. In addition, the phase diagrams in Figure 3.3B show two time constants at 60 °C and 80 °C, whereas one time constant was observed at 30 °C and 40 °C.

The one time constant shown at 30 °C can be fitted with the equivalent circuit shown in Figure 3.4A. This equivalent circuit is a modification of the Randle's cell commonly used to describe a corrosion process. It consists of a solution resistance ( $R_s$ ) in series with the parallel combination of the double layer capacitance ( $C_{dl}$ ) and charge transfer resistance ( $R_{ct}$ ). Due to the non-ideal behavior of capacitors in a corroding environment, a constant phase element (CPE) is often used to replace  $C_{dl}$  to improve the fitting. The impedance of this element is defined as shown in Equation 3.1[199]:

$$Z_{CPE} = \frac{1}{Y_o (j\omega)^\alpha} \quad \text{Equation 3.1}$$

where  $Y_o$  is CPE constant ( $\Omega^{-1}\text{cm}^{-2}\text{s}^\alpha$ ),  $\omega$  is the angular frequency (rad /s),  $j^2 = -1$  is the imaginary number and  $\alpha$  is the CPE exponent, so CPE can represent resistance if  $\alpha = 0$  and ideal capacitance if  $\alpha = 1$ .

The CPE can be calculated to pure capacitance (C) value using the correlation shown in Equation 3.2 previously proposed in the literature [198, 200, 201]

$$C = \frac{(Y_o R)^{\frac{1}{\alpha}}}{R} \quad \text{Equation 3.2}$$

where R is resistance, ( $\Omega \text{ cm}^{-2}$ ).

The two time constants shown at temperatures 60 °C and 80 °C can be explained by the presence of an inhomogeneous film consisting of a compact inner layer and a less compact outer layer, which is similar to that reported for passive alloys in other environments [195, 202, 203]. An equivalent circuit shown in Figure 3.4B has been proposed to describe this behavior [172, 179, 195, 202]. In this model, the solution resistance ( $R_s$ ) is in series with the parallel combination of the constant phase element (CPE1) and ionic path resistance ( $R_{po}$ ) of the outer porous layer (or pore resistance to the ionic current through the pores) which is in series with the parallel combination of the constant phase element (CPE) and charge transfer resistance ( $R_{ct}$ ) of the inner oxide layer.

Table 3.5 reports the EIS parameters from the fitting described above. The CPE exponents were close to 1 in all cases, confirming the suitability of CPE over capacitance.  $R_s$  decreases with increasing temperature despite a constant NaCl concentration. The increase in electrical conductivity with temperature may be associated with improved mobility of ionic species and a decrease in solution viscosity [183].  $R_{ct}$  also decreased steadily with an increase in temperature, which suggests an enhanced corrosion attack at the surface of the sample. This could be explained by an accelerated metal dissolution and the rate of chloride adsorption into the passive film. The rise in chloride ions within the passive film could increase the conductivity of the film.

As the temperature increased, the second time constant appears which corresponds to the porous layer as previously discussed. Every 20 °C increase in temperature from 40 °C to 80 °C,  $R_{po}$  decreased 1 order of magnitude. This significant reduction in  $R_{po}$  with temperature suggests that the passive film became more porous and less protective. By comparing  $R_{ct}$  and  $R_{po}$ , it is evident that  $R_{ct}$  is significantly larger than  $R_{po}$  and is not affected by temperature to the same extent as  $R_{po}$ . This observation may indicate that the corrosion protection was predominantly provided by the inner layer passive film [202, 204].

The weakening of the passive film with temperature is demonstrated by either an increased porosity of the outer layer or the enrichment of chloride ions in the inner layer as depicted by a smaller  $R_{po}$  and  $R_{ct}$ , respectively. As a result, the susceptibility to pitting corrosion increases with temperature which was shown previously using the cyclic polarization method.

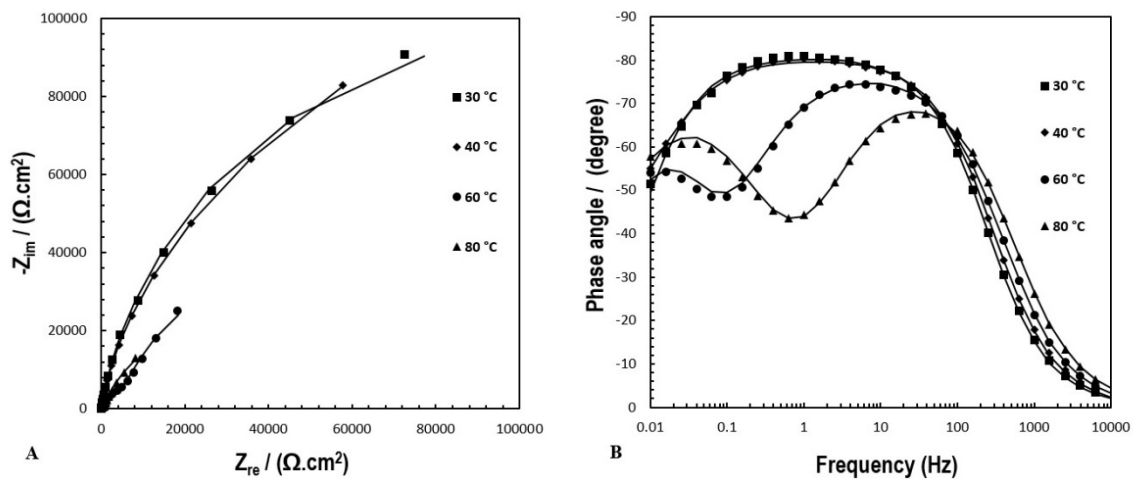


Figure 3.3 (A) Nyquist plots and (B) Bode phase diagrams for 316L SS with fitting in 3 wt.% NaCl, pH 4. Temperature was varied from 30 °C to 80 °C

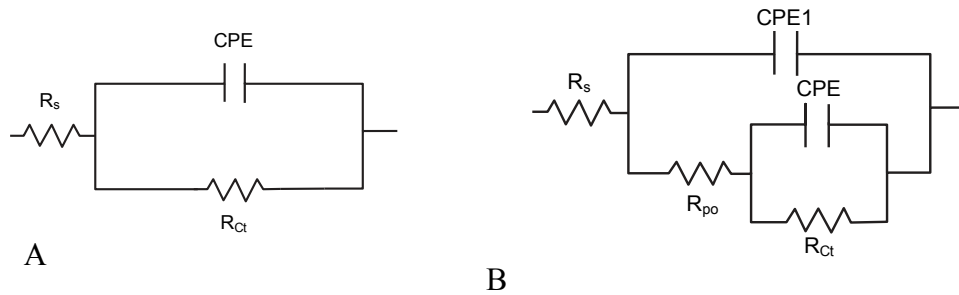


Figure 3.4 Equivalent circuit for fitting of EIS data (A) one time constant, (B) two time constant

Table 3.5. Electrical parameters obtained by fitting the EIS data for 316L SS in 3% NaCl, pH 4 at different temperatures

T (°C)	$R_s$ ( $\Omega \text{ cm}^2$ )	CPE 1 ( $\Omega^{-1} \text{ cm}^{-2} \text{ s}^{\alpha_1}$ )	$\alpha_1$	$R_{po}$ ( $\Omega \text{ cm}^2$ )	$C_1^*$ (F $\text{cm}^{-2}$ )	CPE ( $\Omega^{-1} \text{ cm}^{-2} \text{ s}^{\alpha_2}$ )	$\alpha_2$	$R_{ct}$ ( $\Omega \text{ cm}^2$ )	$C_2^*$ (F $\text{cm}^{-2}$ )	Goodness of fit
30	16.74	$7.86 \times 10^{-5}$	0.902	--	--	--	--	$2.23 \times 10^5$	$1.07 \times 10^{-4}$	$2.34 \times 10^{-4}$
40	13.23	$8.93 \times 10^{-5}$	0.895	$1.87 \times 10^5$	$1.24 \times 10^{-4}$	$2.49 \times 10^{-4}$	0.100	$7.30 \times 10^4$	$2.49 \times 10^{-4}$	$9.07 \times 10^{-5}$
60	10.45	$1.11 \times 10^{-4}$	0.868	$1.11 \times 10^4$	$1.14 \times 10^{-4}$	$3.03 \times 10^{-4}$	0.909	$7.43 \times 10^4$	$4.14 \times 10^{-4}$	$2.42 \times 10^{-4}$
80	7.779	$1.25 \times 10^{-4}$	0.865	$1.17 \times 10^3$	$9.03 \times 10^{-5}$	$4.96 \times 10^{-4}$	0.823	$5.36 \times 10^4$	$1.00 \times 10^{-3}$	$1.92 \times 10^{-4}$

\* $C_1$  and  $C_2$  were calculated from CPE and R values according to Equation 3.2.

### 3.4.2.2 Effect of NaCl concentrations

The Nyquist plots of 316L samples immersed in solutions containing different NaCl concentrations at 30 °C are shown in Figure 3.5A. In all cases, the Nyquist plots exhibit one semicircle shape with varying diameters. Bode phase diagrams are illustrated in Figure 3.5B showing three distinct zones as follows: In high frequency zone (10 kHz), the phase angle is close to zero degree indicating that the impedance is dominated by the solution resistance. In the intermediate frequency zone (1 kHz to 0.1 Hz), the phase angle varies with frequency displaying a minimum value close to 90 ° which is typical for a capacitor. In low frequency region (0.1 Hz to 0.01 Hz), the phase angle begins to increase with the frequency which can be explained by the mix influence of capacitance double layer and the charge transfer resistance. The Bode phase diagram confirms the presence of one time constant. Therefore, the equivalent circuit shown in Figure 3.4A was used to fit the experiments as described previously. The fitting parameters are reported in Table 3.6.

As a result of an increasing NaCl concentration, the solution conductivity increased as manifested by a decrease in  $R_s$ . The semicircle shape usually represents the combined effects of  $C_{dl}$  and  $R_{ct}$ , and its diameter is related to the magnitude of charge transfer resistance at the metal-solution interface.  $R_{ct}$  is only marginally influenced by NaCl concentration. This may be expected since  $R_{ct}$  is correlated to the uniform corrosion which cannot determine susceptibility to pitting corrosion. In addition, the capacitance calculated from Equation 3.2 appears to be unaffected by NaCl concentration.

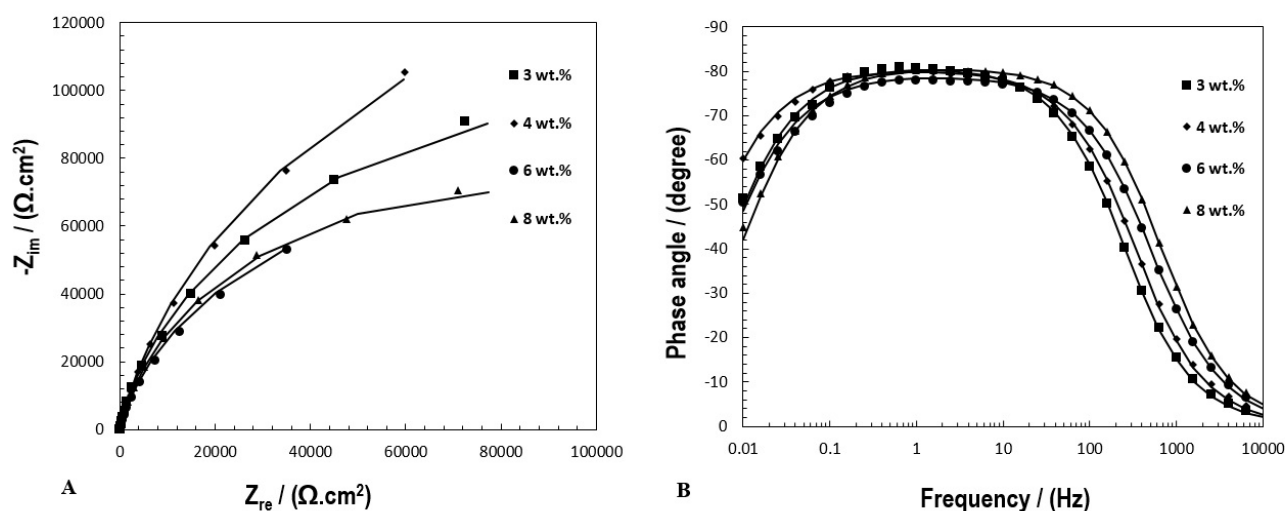


Figure 3.5 (A) Nyquist plots and (B) Bode diagrams for 316L SS with the fitting in different NaCl concentrations, at 30 °C, pH 4, at a film formation of -1 V  $_{Ag/AgCl}$

**Table 3.6. Electrical parameters obtained by fitting the EIS data for 316L SS in different NaCl concentrations, at 30 °C**

NaCl (wt.%)	R <sub>s</sub> (Ω cm <sup>2</sup> )	CPE (Ω <sup>-1</sup> cm <sup>-2</sup> s <sup>α</sup> )	α <sub>1</sub>	R <sub>ct</sub> (Ω cm <sup>2</sup> )	C (F cm <sup>-2</sup> )	Goodness of fit
3	16.74	7.86 x 10 <sup>-5</sup>	0.902	2.23 x 10 <sup>+5</sup>	1.07 x 10 <sup>-4</sup>	2.34 x 10 <sup>-4</sup>
4	12.15	8.76 x 10 <sup>-5</sup>	0.895	3.35 x 10 <sup>+5</sup>	1.30 x 10 <sup>-4</sup>	2.15 x 10 <sup>-4</sup>
6	7.890	1.03 x 10 <sup>-4</sup>	0.818	1.64 x 10 <sup>+5</sup>	1.51 x 10 <sup>-4</sup>	2.72 x 10 <sup>-4</sup>
8	7.012	7.86 x 10 <sup>-5</sup>	0.900	1.64 x 10 <sup>+5</sup>	1.04 x 10 <sup>-4</sup>	2.58 x 10 <sup>-4</sup>

### 3.4.3 Mott – Schottky

The Mott-Schottky (M-S) experiments were conducted to determine the electronic properties of the passive film of 316L SS after exposure to different conditions. M-S relation describes the potential dependence of the space charge capacity of a semi conductive electrode [205]. Based on Mott – Schottky theory [174, 205], the measured capacitance of the film/electrolyte interface can be written as Equation 3.3:

$$\frac{1}{C} = \frac{1}{C_{SC}} + \frac{1}{C_H} \quad \text{Equation 3.3}$$

where C<sub>SC</sub> and C<sub>H</sub> are the capacitance of space charge layer and capacitance of Helmholtz layer, respectively, (F/cm<sup>2</sup>).

The capacitance (C) is calculated from the measured impedance using Equation 3.4

$$C = (-Z''2\pi f)^{-1} \quad \text{Equation 3.4}$$

where Z'' is the imaginary part of the impedance and f is the frequency, Hz.

The applicability of the M–S in the passive film studies is based on the assumption that the Helmholtz layer capacitance is significantly larger than that of the space charge layer [175]. Therefore, it can be neglected, and the measured capacitance, C, reflects the space charge capacitance C<sub>sc</sub> of the passive film. According to the M-S theory, the C<sub>sc</sub> of n-type and p-type semiconductors is given by Equation 3.5 and Equation 3.6, respectively [174, 175].

$$\frac{1}{C^2} = \frac{2}{\epsilon\epsilon_0qN_D} \left[ E - E_{FB} - \frac{KT}{q} \right] \quad \begin{array}{l} \text{Equation 3.5} \\ \text{For n-type} \end{array}$$

$$\frac{1}{C^2} = -\frac{2}{\epsilon\epsilon_0qN_A} \left[ E - E_{FB} - \frac{KT}{q} \right] \quad \begin{array}{l} \text{Equation 3.6} \\ \text{For p-type} \end{array}$$

where C is the capacitance of space charge layer of the passive film, (F/cm<sup>2</sup>); E is the applied potential, (V);  $\epsilon$  is the dielectric constant of the passive film on the stainless steel having a constant value of (15.6),  $\epsilon_0$  the permittivity of free space, (8.858 x 10<sup>-14</sup> F/cm); q is the electron charge, (1.602 x 10<sup>-19</sup> C); N<sub>D</sub> and N<sub>A</sub> the charge carrier density for the donor and acceptor respectively, (cm<sup>-3</sup>); E<sub>FB</sub> is the flat band potential, (V); K is the Boltzmann constant, (1.38 x 10<sup>-23</sup> J/K); T the absolute temperature(K).

Therefore, the semiconducting behavior of passive film and the density of charge carrier can be investigated by plotting the space charge layer capacitance (1/C<sup>2</sup>) to the applied potential (E) [206, 207]. A negative slope represents the p-type semiconductor whereas a positive slope denotes the n-type. The charge carrier density can then be estimated based on the value of the slope in the linear portion of the plot.

#### 3.4.3.1 *Frequency selection*

Capacitance is usually frequency dependent [176, 205, 208]. Yet, various ranges of frequency have been used in the literature for the M-S technique without a clear explanation. Some authors used 3 kHz [172, 209], while others used 1 kHz [191]. Thus, it is necessary to determine the suitable frequency at which the capacitance becomes relatively stable across the range of potential studied and only capacitance, not resistance is measured. Figure 3.6 shows Mott-Schottky measurements performed at different frequencies, i.e., 10 Hz, 100 Hz, 1 kHz, 3 kHz, and 5 kHz. The capacitance increases with decreasing frequency. The fluctuation in the capacitance at a potential greater than 0.38 V is evident at 10 Hz. According to the results from cyclic polarization, a potential of 0.38 V is beyond the pitting potential. Therefore, it is likely that the observed fluctuation is caused by the permanent breakdown of the passive film. On the contrary, such oscillatory behavior in the capacitance does not appear at a higher frequency despite the same applied potential. The fast measurement time may not cause a disturbance at the film structure.

It can be seen from Figure 3.6 that the capacitance becomes independent of frequency at a frequency greater than 3 kHz. Therefore, a value of 3 kHz was applied in this study.

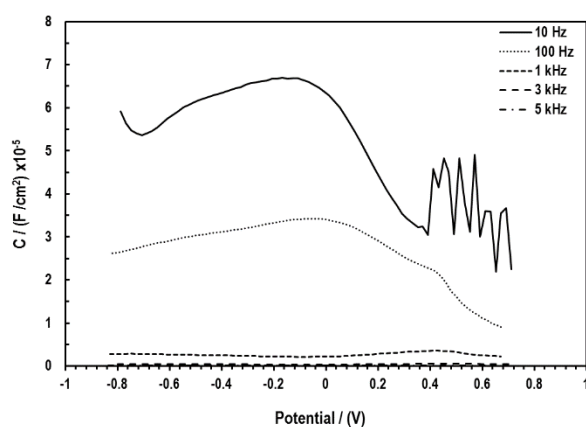


Figure 3.6 Capacitance vs. potential curves obtained at different frequencies for 316L SS in 3% NaCl, pH 4 at 30 °C

### 3.4.3.2 Effect of temperature

The Mott–Schottky (M-S) plot of the passive film formed on 316L SS at different temperatures is shown in Figure 3.7. It can be seen that the capacitance increases with increasing temperatures, which means the formation of an inversion layer as a result of an increasing holes density in the valence band due to the adsorption of anions [191]. The plots show 3 regions that exhibit a linear relationship between  $1/C^2$  and E. In the potential range between -0.5 V vs. Ag/AgCl to OCP, the slope is positive presenting an n-type semiconductor resulted from anion vacancies acting as the electron donor. This type of layer has been proposed to be enriched with iron oxide and hydroxide [207, 210]. While in the potential range from 0 V to 0.5 V vs. (Ag/AgCl), the slope is negative implying the p-type semiconductor showing electron acceptor behavior due to cation vacancies within the film [178]. Passive film exhibiting p-type layer is composed predominantly with chromium oxide [207, 210].

The final range of potential can be seen from  $E_{\text{pit}}$  to 1 V vs. Ag/AgCl which corresponds to the deep exhausting layer of electrons which results in a marked decrease in the capacitance with increasing potential [181]. The response in capacitance with the occurrence of pitting corrosion has been reported and showed that once pits initiate and grow, the capacitance decreases [211]. The variation of the slope with the applied potential is attributed to the structure and composition of the passive film on 316L SS [191].

According to Equation 3.5 and Equation 3.6,  $N_D$  and  $N_A$  can be calculated from the slope of the inverse square of space charge layer capacitance ( $1/C^2$ ) versus the applied potential and the

results are compared in Table 3.7. It can be seen that the donor and acceptor densities increase with temperature for all 3 potential regions. Generally, high donor density indicates a highly disordered character of the passive film. On the contrary, low donor and acceptor density imply an absence of these defects, hence a better corrosion resistance [181]. Therefore, the increase in  $N_D$  and  $N_A$  with temperature was due to a greater defect density within the passive film which in turn led to the weakening of the passive film.

Comparing with the results obtained from cyclic polarization and EIS, it may be deduced that the increased pitting susceptibility is due to the weakening of the passive film as illustrated by M-S measurements.

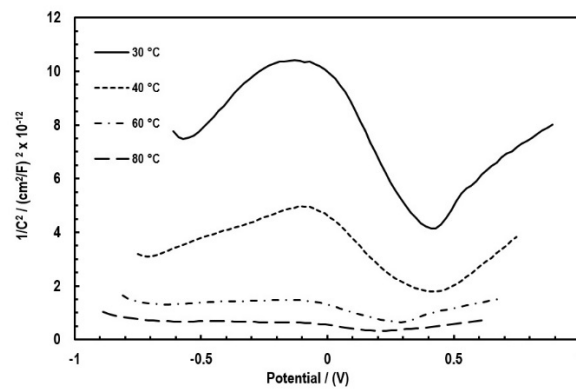


Figure 3.7 Mott-Schottky plots for 316L in 3% NaCl, pH 4 at different temperature, 3 kHz, with AC 10mV

**Table 3.7. Donor and acceptor densities of 316L in 3%NaCl, pH 4 at different temperature**

Temperature/ °C	Potential (V)	$N_D$ or $N_A$ ( $\text{cm}^{-3}$ )
30 °C	-0.50 to 0.00	$1.14 \times 10^{18}$
	0.00 to 0.50	$6.79 \times 10^{17}$
	0.50 to 1.00	$1.41 \times 10^{18}$
40 °C	-0.50 to 0.00	$2.48 \times 10^{18}$
	0.00 to 0.50	$1.04 \times 10^{18}$
	0.50 to 1.00	$2.19 \times 10^{18}$
60 °C	-0.50 to 0.00	$3.31 \times 10^{19}$
	0.00 to 0.50	$3.54 \times 10^{18}$
	0.50 to 1.00	$4.49 \times 10^{18}$
80 °C	-0.50 to 0.00	$3.22 \times 10^{19}$
	0.00 to 0.50	$7.72 \times 10^{18}$
	0.50 to 1.00	$7.23 \times 10^{18}$

### 3.4.3.3 Effect of NaCl concentrations

Figure 3.8 shows the plot of  $1/C^2$  vs.  $E$  for 316L SS in different NaCl concentrations. M-S plots reveal 3 regions exhibiting Mott-Schottky behavior similar to Figure 3.7. In the potential -0.5 V vs. Ag/AgCl to OCP, the capacitance data can be interpreted as representative of the behavior of an n-type semiconductor. In the second potential region from OCP to  $E_{pit}$ , the negative slope implies the p-type semiconductor. While at the third potential region between  $E_{pit}$  to 1 V vs. Ag/AgCl, the slope returns to positive which may be correlated with the deep exhausting layer of electrons, as mentioned before. The p-type behavior has been attributed to chromium oxides in the inner region, while n-type behavior has been attributed to iron oxides in the outer region [191].

The values of  $N_D$  and  $N_A$  calculated from M-S plots are shown in Table 3.8. Donor and acceptor densities of 316L in different NaCl concentrations at 30 °C, pH 4. As can be seen, both  $N_D$  and  $N_A$  increased with increasing NaCl concentrations. The penetration of chloride ions and their incorporation into the passive film was reported by Qiao, *et. al.* [172] with X-ray photoelectron spectrometric (XPS). A greater value of  $N_D$  and  $N_A$  is attributed to an increase of the passive film defects and an increase in the conductivity within the film which is consistent with EIS measurements. In all regions, the capacitance of the passive film increased with NaCl concentration which may be attributed to a decrease of the passive layer thickness according to the correlation given in Equation 3.7.

$$C = \frac{\epsilon \times \epsilon_0}{d} \quad \text{Equation 3.7}$$

Where  $\epsilon$  the dielectric constant of the passive film (15.6) has been reported in the literature for stainless steel [174, 177],  $\epsilon_0$  is vacuum permittivity ( $8.854 \times 10^{-14}$  F/cm), and  $d$  is the thickness of the passive film layer.

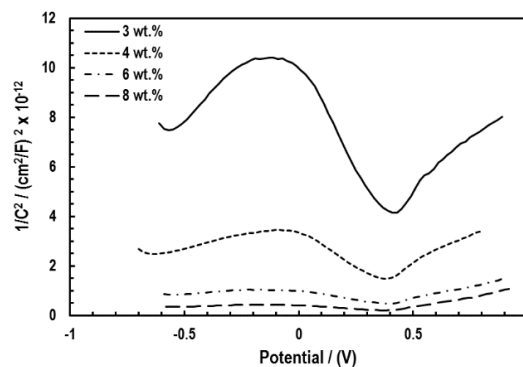


Figure 3.8 Mott-Schottky plots for 316L in different NaCl concentrations, at 30 °C pH 4, 3 kHz, with AC 10mV

**Table 3.8. Donor and acceptor densities of 316L in different NaCl concentrations at 30 °C, pH 4**

NaCl concentration/ wt. %	Potential (V)	$N_D$ or $N_A$ ( $\text{cm}^{-3}$ )
3% NaCl	- 0.50 to 0.00	$9.50 \times 10^{17}$
	0.00 to 0.50	$5.05 \times 10^{17}$
	0.50 to 1.00	$1.29 \times 10^{18}$
4% NaCl	- 0.50 to 0.00	$4.26 \times 10^{18}$
	0.00 to 0.50	$1.54 \times 10^{18}$
	0.50 to 1.00	$2.25 \times 10^{18}$
6% NaCl	- 0.50 to 0.00	$2.46 \times 10^{19}$
	0.00 to 0.50	$8.00 \times 10^{18}$
	0.50 to 1.00	$5.13 \times 10^{18}$
8% NaCl	- 0.50 to 0.00	$2.88 \times 10^{19}$
	0.00 to 0.50	$1.46 \times 10^{19}$
	0.50 to 1.00	$4.83 \times 10^{18}$

### 3.5 Conclusions

The susceptibility to pitting corrosion of 316L in an anaerobic CO<sub>2</sub> environment, as experienced in oil and gas production, was investigated with a conventional cyclic polarization method. In addition, the 2 AC techniques, i.e., electrochemical impedance spectroscopy (EIS) and Mott-Schottky were conducted to relate the characteristics of the passive film with the susceptibility to pitting corrosion. The main findings are summarized below.

1. 316L becomes more prone to pitting corrosion with increasing temperature and NaCl concentration as determined by the decrease in the difference between OCP and pitting potential ( $\Delta E_{\text{pit}}$ ).
2. EIS results provide insight into the possible change in the passive film structure as a result of an increase in temperature. Inhomogeneity in the passive film was shown by the presence of 2 time constant at a temperature greater than 40 °C.
3. Charge carrier density determined by Mott-Schottky analysis increases with increasing temperature and NaCl concentrations indicating the weakening of the passive film.

It is interesting that the results for 316L in a deoxygenated CO<sub>2</sub> environment is not dissimilar in behavior expected in oxygen rich environments which has been the focus on much more research.

## **Chapter 4: Comparison of Corrosion behavior and Passive Film Properties of 316L Austenitic Stainless Steel in CO<sub>2</sub> and N<sub>2</sub> Environments**

### **4.1 Abstract**

This study investigated the susceptibility to pitting corrosion of 316L in CO<sub>2</sub> and N<sub>2</sub> environments at temperatures from 30 °C to 80 °C in 3 wt.% NaCl at pH 4. Results from the cyclic polarization technique confirm greater pitting susceptibility of 316L in CO<sub>2</sub> environment. Electronic properties and composition of the passive film were identified by electrochemical impedance spectroscopy, Mott-Schottky, and x-ray photoelectron spectroscopy. Increasing temperature negatively affects passive film stability, and its influences are amplified in the presence of CO<sub>2</sub> as compared to N<sub>2</sub>. In CO<sub>2</sub> environment, the passive film becomes porous with increasing temperature leading to higher defects (donor/acceptor densities).

**Keywords** Pitting susceptibility, cyclic polarization, electrochemical impedance spectroscopy, Mott-Schottky analysis, x-ray photoelectron spectroscopy, donor and acceptor densities

### **4.2 Introduction**

Corrosion is acknowledged as one of the most outstanding problems causing operational, safety, and economic impacts in the oil and gas industry [212]. Carbon and low alloy steel are extensively used due to their cost, availability, and mechanical properties. Nonetheless, in an increasingly harsh environment in the oil and gas industry, its poor resistance to corrosion can lead to an increased risk of failure and high operating costs through maintenance and ongoing corrosion prevention plans. In such cases, a better performing material such as corrosion resistance alloys can be considered. In particular, stainless steel (SS) is one of the commonly used alloys due to the formation of thin passive oxide films on the surface [213-215]. Among them, 316L is used in various industry sectors, e.g., petroleum refinery [216, 217], desalination plants [218], and medical implant [219], as well as any passive alloys, are prone to localized corrosion and more specifically pitting corrosion.

Pitting corrosion is the most serious and widespread form of corrosion causing failures in various industries; e.g., petrochemical plant [220], and desalination plant [221]. The initiation of pitting corrosion has been linked to the degradation of the passive film. In another word, the integrity of the passive film determines the likelihood of pitting corrosion [222]. Over the recent years, the oxide layer and its roles on the overall corrosion process are better understood

from the use of various electrochemical techniques, such as the electrochemical impedance spectroscopy (EIS) and Mott-Schottky (M-S), to characterize the structural and electronic properties of the passive films formed on the metals and alloys [223-225]. Surface analysis techniques such as X-ray photoelectron spectroscopy (XPS) have been increasingly implemented to study film growth mechanism and to detect compositional changes with depth of the passive film. It was reported that in an aerated acidic media, the passive film formed on 316L SS is composed of iron and chromium oxide or hydroxide [226-228]. While in an aerated alkaline media, the passive film has a bilayer structure, the inner enriches chromium oxide layer, and the outer layer is composed of iron oxide with hydroxide [229-231].

The susceptibility of 316L SS to pitting corrosion depends directly on the environmental parameters. For instance, the effect of chloride ion concentration, pH, and temperature on the pitting susceptibility of 316L SS was investigated in deaerated [232] and aerated solutions [222, 233, 234]. Despite the difference in the solution aeration, literature demonstrated that the pitting susceptibility increases with chloride ion concentration, temperature, and solution acidity. In addition, sulfide ions have been shown to weaken the passive film leading to increased occurrence of localized corrosion [225].

The presence of CO<sub>2</sub> has been shown to be detrimental for various corrosion resistant alloys [235-238]. However, in neutral or alkali pH, CO<sub>2</sub> derivative species such as bicarbonate (HCO<sub>3</sub><sup>-</sup>) and carbonate ions (CO<sub>3</sub><sup>2-</sup>) become dominant. These components were described as non-aggressive anions. Lower pit density was reported with increasing HCO<sub>3</sub><sup>-</sup> concentration [239]. Nonetheless, there is still a lack of systematic study that unveils the impact of CO<sub>2</sub> on the nature of the passive film formed and the resulting susceptibility to pitting corrosion observed. The present study was undertaken to elucidate the influence of CO<sub>2</sub> and temperature on the properties of passive film formed on 316L SS and how it influences the susceptibility to pitting corrosion. Experiments were conducted using cyclic potentiodynamic polarization scans and the aforementioned EIS and Mott-Schottky techniques. Characterization of the passive film was performed using the XPS technique.

### **4.3 Experimental procedure**

#### **4.3.1 Materials and specimen preparation**

316L SS (UNS S31603), having chemical compositions of (in wt.%) 16.92 Cr, 10.02 Ni, 2.02 Mo, 0.02 C, 0.36 Si, 1.36 Mn, 0.03 P, 0.006 S and the balance Fe, was used in the present study. The samples were machined into a cylindrical shape (15 mm diameter x 3 mm

thickness). Prior to experiments, the sample was wet grounded with SiC paper from 80 to 600 grit SiC paper, rinsed with ethanol and ultrapure water, and dried with high purity N<sub>2</sub> gas (99.99%, BOC Australia). 316L SS specimen was then mounted in a polyether ether ketone (PEEK) sample holder which was manufactured according to ASTM G61 recommendation to prevent crevice formation [184]. The exposed surface area was 0.96 cm<sup>2</sup>.

### 4.3.2 Test solutions

Experiments were conducted in 3 wt.% NaCl deaerated and saturated with either CO<sub>2</sub> or N<sub>2</sub> at atmospheric pressure. The test temperature was varied from 30 °C to 80 °C. The pH of the test solutions was adjusted to 4 either by adding 1 M NaHCO<sub>3</sub> to the CO<sub>2</sub> saturated NaCl solution or 1 M HCl in the case of N<sub>2</sub>. The solution pH was measured at the end and negligible change in pH was recorded ( $\Delta \text{pH} < 0.1$ ). Test conditions are summarized in Table 4.1.

**Table 4.1 Summary of test conditions**

Parameters	Conditions
Gas (1 atmosphere)	CO <sub>2</sub> and N <sub>2</sub>
Temperature (°C)	30, 40, 60 and 80
NaCl (wt.%)	3
pH	4

### 4.3.3 Electrochemical measurements

Experiments were conducted in a 1 L test cell fitted with a 316L SS specimen mounted in the polyether ether ketone (PEEK) holder as a working electrode, a platinum mesh as a counter electrode and a silver/silver chloride (Ag/AgCl) electrode connected to the cell via a Luggin probe filled with 3 M KCl as a reference electrode. The test cell was also equipped with a temperature probe, gas inlet, and outlet.

In a separate container, the solution was sparged with the test gas for a minimum of 4 h to ensure dissolved oxygen had been removed. Subsequently, it was transferred via a peristaltic pump into the test cell which had already been sparged with the test gas for an equal amount of time to ensure an oxygen-free environment. The sparging was continued until the test was completed.

The pitting susceptibility was determined with the cyclic polarization technique in accordance with ASTM G 61- 2009 [184]. After the steady open circuit potential (OCP) was attained, the cyclic polarization was performed at a scan rate 0.167 mV/s from OCP and reversed backward

when the measured current exceeded 25 mA/cm<sup>2</sup>. For each condition, experiments were repeated at least twice to ensure reproducibility.

Electrochemical impedance spectroscopy (EIS) and Mott-Schottky (M-S) techniques were employed to gain an insight into the characteristic of the passive film which was prepared at 30 °C for all experiments. Firstly, the working electrode immersed in deoxygenated 3 % NaCl solution sparged with the test gas at 30 °C was polarized at 200 mV cathodic from OCP for 15 min to remove any air-formed oxide film. Afterward, the working electrode was potentiostatically polarized at -0.1 V<sub>Ag/AgCl</sub> for 1 h to form the passive film. Once the passive film was formed, the solution temperature was then raised to the desired values and electrochemical measurements were commenced.

EIS measurements were carried out over the frequency from 10 kHz to 10 mHz at 10 mV amplitude.

Subsequently, the M-S technique was employed by scanning a potential range from -0.5 V<sub>Ag/AgCl</sub> to 1 V<sub>Ag/AgCl</sub> with an amplitude signal of 10 mV and the potential step of 20 mV. M-S experiments were typically conducted at high frequencies to eliminate the influence of Helmholtz layer capacitance and ensure that the capacitance measured is of the space charge region [176, 205, 208]. Our previous work showed that the frequency of 3 kHz is suitable for 316L SS in the environment of this study [240]. All the electrochemical measurements were performed with a potentiostat (Gamry Reference 600) and the results were subsequently analyzed using Gamry Echem Analyst version 6.24.

#### **4.3.4 Surface characterization**

The passive film was electrochemically formed using potentiostatic polarization method at -0.1 V<sub>Ag/AgCl</sub> for 60 min in solutions sparged with test gas (either CO<sub>2</sub> or N<sub>2</sub>) for 4 h and at 2 different temperatures; i.e., 30 °C and 60 °C. Subsequently, the samples were removed from the solution, rinsed with ultrapure water, dried with N<sub>2</sub> gas, and stored in a vacuum desiccator for transportation. An unexposed sample where potentiostatic polarization was not applied was also analyzed for comparison.

*Ex-situ* XPS measurements were performed on a Kratos Axis Ultra DLD spectrometer using a monochromatic AlK $\alpha$  (1486.6 eV) irradiation source operated at 225 W. The vacuum pressure of the analysis chamber of the spectrometer was maintained a 9 $\times$ 10<sup>-9</sup> Torr or lower throughout the duration of the analyses. The electron binding energy scale was calibrated for each sample

by setting the mainline of the C<sub>1s</sub> spectrum to 284.8 eV. XPS spectra were collected with a pass energy of 160 eV for the survey spectra and 40 eV for the high-resolution spectra. Depth profiling was undertaken using an argon gas cluster ion source operating in monoatomic Ar<sup>+</sup> mode at 5 keV. A typical depth profile involved 100 survey/sputter cycles, with sputtering undertaken for 6 seconds per cycle. Data files were processed using CasaXPS software and interpreted using relative sensitivity factors provided by the instrument manufacturer (Kratos) as a guide. Shirley background subtraction was applied to all high-resolution spectra. In the case of the Fe<sub>2p</sub>, Cr<sub>2p</sub>, and Ni<sub>2p</sub> which are known to be complicated by complex multiplet splitting, fitting was achieved using specified empirical fitting parameters previously derived from standard samples [241-243]. For each of the fitted species, binding energy differences and area ratios were constrained for each species, whilst the absolute binding energy values were allowed to vary by  $\pm 0.3$  eV to accommodate any error associated with charge referencing.

## 4.4 Results and dissection

### 4.4.1 Cyclic polarization technique

After the polarisation, all samples were observed under a microscope and pits were found on the surface with no evidence of crevice corrosion. Figure 4.1a and 1b show the cyclic polarization curves for 316L SS obtained at different temperatures in 3 wt.% NaCl solutions saturated with CO<sub>2</sub> and N<sub>2</sub>, respectively. Hysteresis loops of various extent appear for all scenarios as denoted by larger current density in the reversed scan as compared to that in the forward one. The existence of these positive hysteresis loops indicates that the material is susceptible to passivation breakdown and, consequently, pitting corrosion. This behavior is expected in the presence of Cl<sup>-</sup> [187-189, 191]. In both CO<sub>2</sub> and N<sub>2</sub> environments, the pitting potential ( $E_{pit}$ ), the potential at which the sudden increase in current density takes place, decreases with increasing temperature indicating that the material becomes more prone to the breakdown of the passive film. Another important feature that can be drawn from the cyclic polarization curves is the repassivation potential ( $E_{rep}$ ) which can be determined as the potential at which the forward and backward scans meet.  $E_{rep}$  decreases with increasing temperature substantiating that susceptibility to pitting corrosion increases with temperature.

In both media, the passive current density is relatively constant with respect to temperature as illustrated in Figure 4.1 which implies that the ability of the passive film to prevent metal dissolution is independent of temperature between 30 °C to 80 °C. However, the dissolved gas plays a role because the passive current density is higher in the presence of CO<sub>2</sub> than in the N<sub>2</sub>,

i.e.,  $10 \mu\text{A cm}^{-2}$  compared to  $3 \mu\text{A cm}^{-2}$ , respectively. This result demonstrates the enhanced metal dissolution in the passive region by the dissolved  $\text{CO}_2$  and, perhaps, its derivative species. In other words, the passive film in a solution saturated with  $\text{CO}_2$  is less protective than that in its absence suggesting  $\text{CO}_2$  may alter and compromise the reliability of passive film. It should be recognized, that while observing this general trend in performance, the temperature will affect the dissolved level of  $\text{CO}_2$  present in the solutions, causing the concentration to decrease as the temperature is increased. High pressures experienced in oil and gas field environments can increase the level of dissolved  $\text{CO}_2$  to concentrations much higher than those given in this investigation. The influence of pressure and higher concentrations of dissolved  $\text{CO}_2$  will be investigated in future work.

To evaluate the susceptibility to pitting corrosion, the differences between pitting and repassivation potentials with respect to OCP; i.e.  $\Delta E_{\text{pit}}$  and  $\Delta E_{\text{rep}}$ , respectively, were used [161]. It is acknowledged that metastable pitting events occur prior to  $E_{\text{pit}}$ . Hence,  $\Delta E_{\text{rep}}$  which is associated with the repassivation tendency has been used to conservatively determine the pitting susceptibility [161, 244]. In this study,  $\Delta E_{\text{pit}}$  and  $\Delta E_{\text{rep}}$  obtained from different conditions are compared and depicted in Figure 4.2 a and b. It is apparent that both  $\Delta E_{\text{pit}}$  and  $\Delta E_{\text{rep}}$  in the presence of  $\text{CO}_2$  are lower than that in  $\text{N}_2$  environment indicating an increased vulnerability to pitting corrosion of 316L SS. At pH 4, the presence of dissolved  $\text{CO}_2$  and undissociated carbonic acid ( $\text{H}_2\text{CO}_3$ ) are the primary difference in the water chemistry of solutions saturated with  $\text{CO}_2$  and  $\text{N}_2$ . Because the pH in this study was kept constant at 4, the influence of pH on the pitting corrosion was eliminated and the observed pitting corrosion behavior was due solely to the corrosivity of  $\text{CO}_2$ .

The adverse effect of temperature on the pitting susceptibility of 316L SS in  $\text{CO}_2$  and  $\text{N}_2$  media is also shown in Figure 4.2 a and b. In  $\text{CO}_2$  environment,  $\Delta E_{\text{pit}}$  and  $\Delta E_{\text{rep}}$  decrease quite sharply with increasing temperature from  $30^\circ\text{C}$  to  $60^\circ\text{C}$ . However, increasing the temperature from  $60^\circ\text{C}$  to  $80^\circ\text{C}$  does not show a significant effect on  $\Delta E_{\text{pit}}$  and  $\Delta E_{\text{rep}}$ . This is probably related to the temperature effect on the solubility of  $\text{CO}_2$  starting to dominate over the kinetics of the reaction [245].

The cyclic polarization results presented here demonstrate the negative impacts of  $\text{CO}_2$  and temperature on pitting corrosion. The adverse effect of temperature on pitting susceptibility of stainless steel found in this study agrees well with the previous work in oxygenated environments [246].

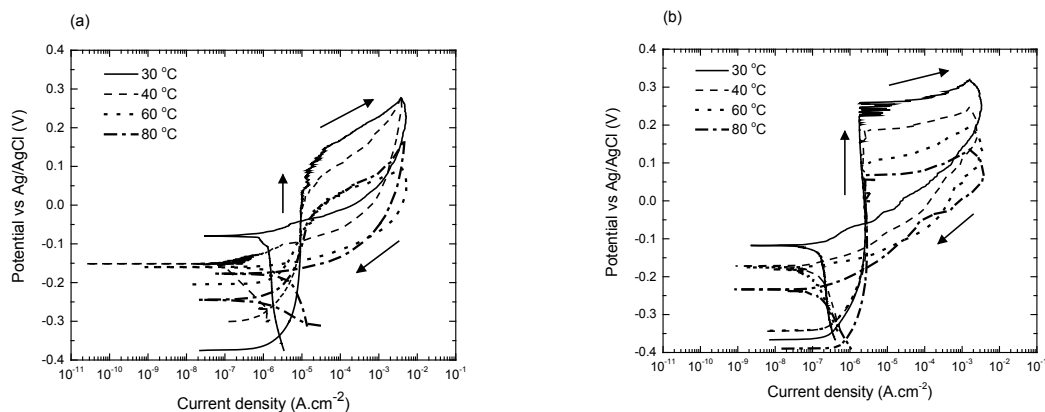


Figure 4.1 Cyclic polarization curves of 316L SS in 3wt.% NaCl, pH 4 saturated with a) CO<sub>2</sub> and b) N<sub>2</sub> at different temperatures. Arrows indicate direction of scans

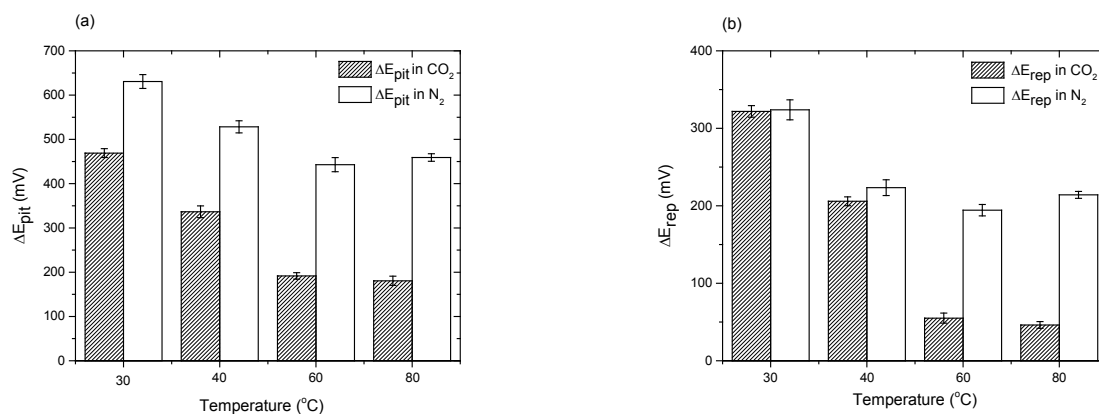


Figure 4.2 a)  $\Delta E_{pit}$ , and b)  $\Delta E_{rep}$  of 316L SS in 3wt.% NaCl, pH 4 saturated with CO<sub>2</sub> and N<sub>2</sub> at different temperatures. Error bars indicate standard deviation from multiple repeats

#### 4.4.2 Electrochemical impedance spectroscopy (EIS) technique

Electrochemical impedance measurement data is considered valid when it achieves three conditions: linearity, stability, and causality which can be independently verified through Kramers-Kronig (K-K) transforms [247]. The validation of data was performed by transforming the real axis into the imaginary axis and vice versa. K-K transforms of the data obtained in this study in both media CO<sub>2</sub> and N<sub>2</sub> for 316L SS are shown in Figure 4.3 a and b, respectively. It can be observed that the K-K transforms exactly trace the experimental values demonstrating and validating that the system was linear, causal, and stable.

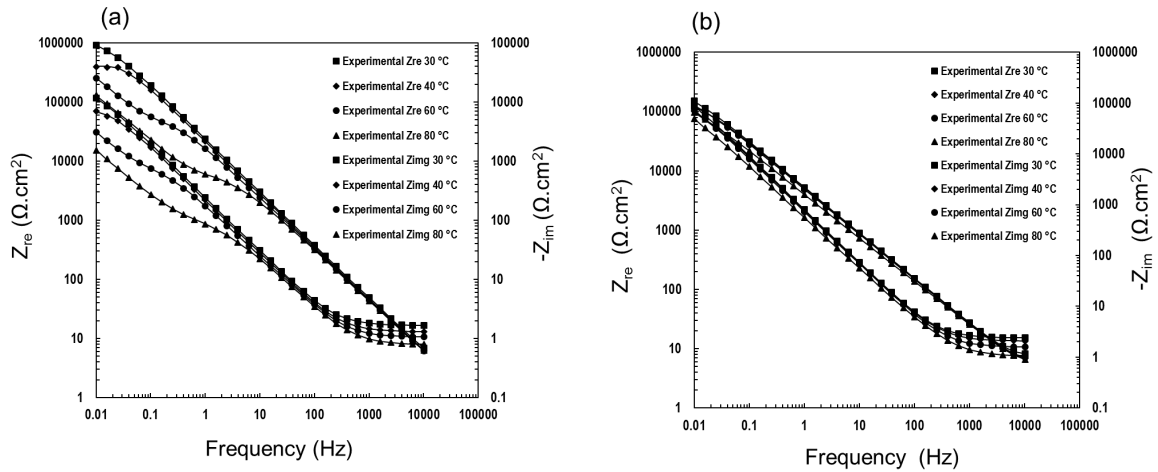


Figure 4.3 Kramer-Kronig transform of EIS data for 316L SS in 3wt.% NaCl, pH 4 saturated with a) CO<sub>2</sub> and b) N<sub>2</sub> at a different temperatures

Figure 4.4 and Figure 4.5 show the Nyquist diagrams, Bode phase angle and Bode magnitude plots of 316L SS measured in 3 wt.% NaCl solution saturated with CO<sub>2</sub> and N<sub>2</sub>, respectively, at different temperatures. The magnitude of the semicircle illustrated in the Nyquist diagrams (Figure 4.4 a and Figure 4.5 a) gives a graphical indication of the faradaic impedance values. Even at the lowest frequency of 10<sup>-2</sup> Hz, the impedance is composed of appreciable out of phase component. In the CO<sub>2</sub> environment, an abrupt decrease in the projected semicircle diameter is observed when the temperature was increased from 40 °C to 60 °C. However, in the N<sub>2</sub> environment, the projected diameter remains relatively constant with respect to temperature suggesting that the passive film remains unchanged and protective. It is also evident that 316L SS has larger impedance values in N<sub>2</sub> media than in CO<sub>2</sub> media particularly at higher temperatures of 60 °C and 80 °C.

In the N<sub>2</sub> environment, Bode phase diagrams depict one time constant for all test temperatures (Figure 4.4 b) while those in the CO<sub>2</sub> environment reveal the transformation from one time constant to two time constants (Figure 4.5 b) which manifests changes in the passive film structure. The two time constants have been associated with the presence of an inhomogeneous film consisting of a compact inner layer and a porous outer layer [195, 202, 203].

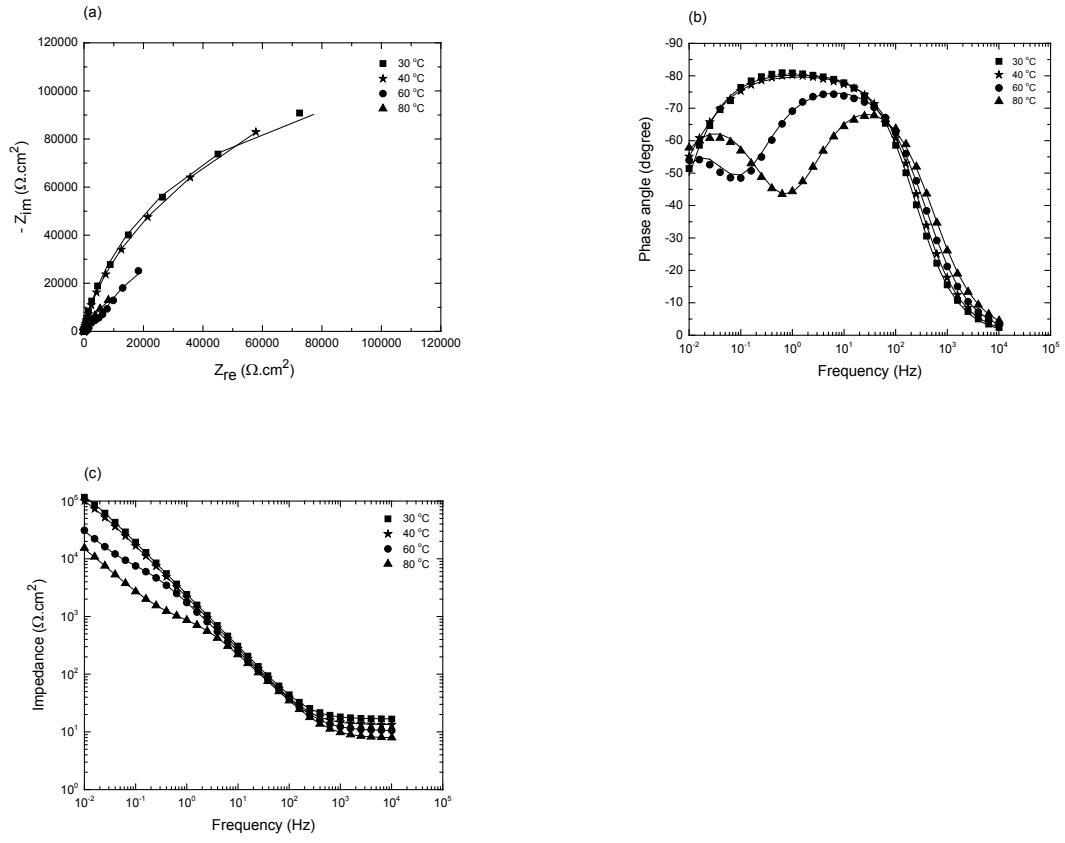
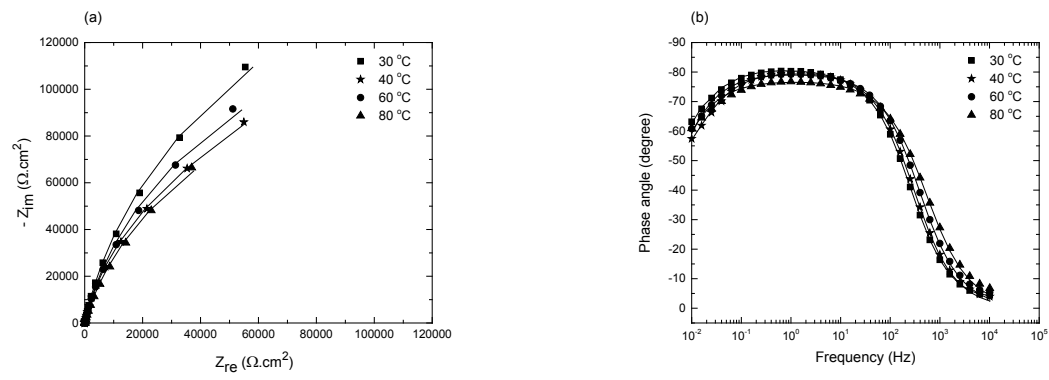


Figure 4.4 a) Nyquist, b) Bode phase angle and c) Bode magnitude diagrams of 316L SS in 3wt.% NaCl, pH 4 saturated with CO<sub>2</sub> gas at different temperatures. Lines represent the fitting with an equivalent circuit depicted in Figure 4.6



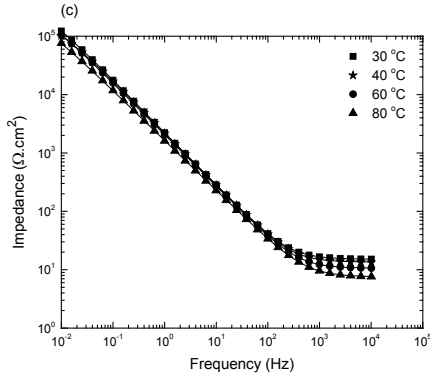


Figure 4.5 a) Nyquist diagram, b) Bode phase angle plot and c) Bode magnitude plot of 316L SS in 3wt.% NaCl, pH 4 saturated with N<sub>2</sub> gas at different temperature. Lines represent the fitting with an equivalent circuit depicted in Figure 4.6.

Hence, different equivalent electrical circuits depicted in Figure 4.6 a and b were used. Firstly, the Randle equivalent circuit (Figure 4.6 a) represents solution resistance ( $R_s$ ) in series with the parallel combination of capacitance constant phase element (CPE) and charge transfer resistance ( $R_{ct}$ ). This equivalent circuit represents a system where no porous layer appears on the sample surface and was used to fit EIS data exhibiting one time constant. Due to the non-ideal behavior of capacitors in a corroding environment, a constant phase element (CPE) is often used to replace the capacitor to improve the fitting [199]. For this particular equivalent circuit, CPE represents capacitance double layer ( $C_{dl}$ ). Though the physical meaning of CPE is unclear, and it can be converted into pure capacitance ( $C$ ) using Equation 4.1 [198, 200, 201].

$$C = \frac{(Y_o * R_{ct})^{\frac{1}{\alpha}}}{R_{ct}} \quad \text{Equation 4.1}$$

where  $R_{ct}$  is charge transfer resistance ( $\Omega.cm^2$ ),  $Y_o$  is CPE constant, ( $\Omega^{-1}.cm^{-2}.s^\alpha$ ), and  $\alpha$  is the CPE exponent which represents a resistance if  $\alpha = 0$  and an ideal capacitance if  $\alpha = 1$ .

For EIS data exhibiting two time constants, the equivalent circuit proposed for inhomogeneous passive films as shown in Figure 4.6 b was used. This circuit consists of  $R_s$  in series with the parallel combination of a CPE (CPE1) and ionic paths resistance ( $R_{po}$ ) of the outer porous layer which is in series with the parallel combination of another CPE and charge transfer resistance ( $R_{ct}$ ) of the inner oxide layer. CPE at the outer layer and the inner layer have been associated with the double layer capacitance and space charge capacitance of passive film, respectively. This circuit has been used for different kinds of metals and alloys described as having porous layer; such as titanium alloys in aerated solution at 37 °C [195], three types of SS (304, 446,

and 308) in 0.1 M Na<sub>2</sub>SO<sub>4</sub> deaerated by pure N<sub>2</sub> [202], high nitrogen SS in aerated acidic solution [172] and austenitic stainless steel containing nitrogen (ASS N25) and 316L SS in deaerated acid solution by N<sub>2</sub> [179].

The validity of the selected equivalent circuits can be seen in Figure 4.4 and Figure 4.5 where lines representing the predictions from equivalent circuits agree well with markers representing experimental values. Further, the low value of Chi-square numerically verified the goodness of fit. Table 4.2 and Table 4.3 report the EIS parameters derived from the fitting described above in N<sub>2</sub> and CO<sub>2</sub>, respectively. In the N<sub>2</sub> environment, an overall decrease in  $R_{ct}$  with increasing temperature was observed due to the enhanced kinetics of metal dissolution. Nonetheless, its high values are anticipated for materials exhibiting a low uniform corrosion rate particularly when EIS measurements were performed at OCP without any potential excitation. It can be concluded from the high projected  $R_{ct}$  the passive film prevents metal dissolution and remains protective against uniform corrosion. Similar behavior can be observed in a CO<sub>2</sub> environment where  $R_{ct}$  steadily decreases with an increase in temperature which suggests an enhanced metal dissolution rate through the passive film with increasing temperature.

In addition to the change observed in  $R_{ct}$  in CO<sub>2</sub> environment, the passive film became porous as the temperature reached 60 °C, as observed by the appearance of  $R_{po}$ .  $R_{po}$  is significantly lower than  $R_{ct}$  and is strongly influenced by temperature. Therefore, it can be stipulated that this porous structure does not contribute to corrosion protection. Instead, it was the inner layer passive film that predominantly controls corrosion activity which is in agreement with a previous observation [202, 204]. Overall, the weakening of the passive film with temperature in the CO<sub>2</sub> environment is demonstrated by an increase in the porosity of the outer layer and subsequent thinning of the protective film.

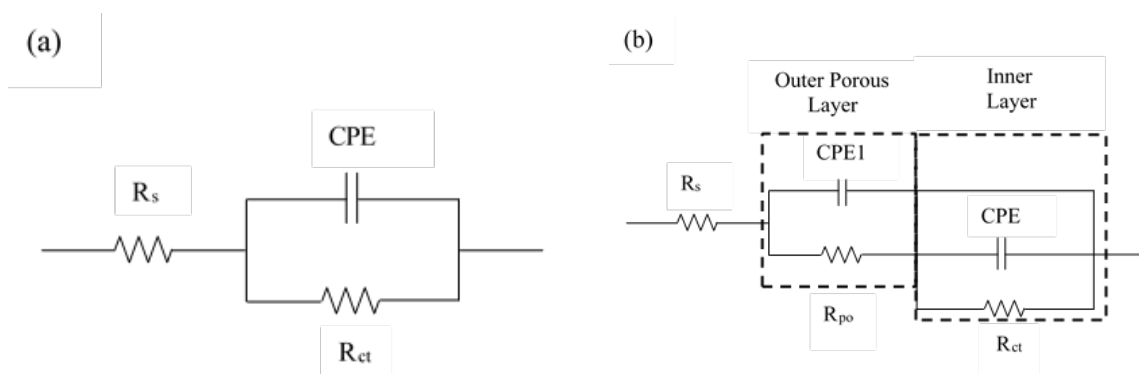


Figure 4.6 Equivalent circuits used for fitting of EIS data exhibiting a) one time constant and b) two time constant

**Table 4.2 Electrical parameters obtained by fitting the EIS data for 316L SS in 3wt.% NaCl, pH 4 saturated with N<sub>2</sub> gas at different temperatures**

T (°C)	$R_s$ ( $\Omega \text{ cm}^2$ )	CPE ( $\Omega^{-1} \text{ cm}^{-2} \text{ s}^{\alpha}$ )	$\alpha_1$	$R_{ct}$ ( $\Omega \text{ cm}^2$ )	$C^*$ ( $\text{F cm}^{-2}$ )	Chi-square
30	15.20	$8.6 \times 10^{-5}$	0.90	$3.8 \times 10^5$	$1.3 \times 10^{-4}$	$2.0 \times 10^{-4}$
40	13.42	$9.0 \times 10^{-5}$	0.89	$2.4 \times 10^5$	$1.3 \times 10^{-4}$	$3.6 \times 10^{-4}$
60	10.57	$9.5 \times 10^{-5}$	0.88	$3.0 \times 10^5$	$1.5 \times 10^{-4}$	$2.5 \times 10^{-4}$
80	7.50	$1.3 \times 10^{-4}$	0.86	$2.5 \times 10^5$	$1.5 \times 10^{-5}$	$3.1 \times 10^{-4}$

\* $C$  was calculated from CPE and  $R_{ct}$  values according to Equation 4.1

**Table 4.3 Electrical parameters obtained by fitting the EIS data for 316L SS in 3wt.% NaCl, pH 4 saturated with CO<sub>2</sub> gas at different temperatures**

T (°C)	$R_s$ ( $\Omega \text{ cm}^2$ )	CPE <sub>1</sub> ( $\Omega^{-1} \text{ cm}^{-2} \text{ s}^{\alpha}$ )	$\alpha_1$	$R_{po}$ ( $\Omega \text{ cm}^2$ )	$C_1^*$ ( $\text{F cm}^{-2}$ )	CPE ( $\Omega^{-1} \text{ cm}^{-2} \text{ s}^{\alpha}$ )	$\alpha_2$	$R_{ct}$ ( $\Omega \text{ cm}^2$ )	$C_2^*$ ( $\text{F cm}^{-2}$ )	Chi-square
30	16.74	$7.9 \times 10^{-5}$	0.90					$2.2 \times 10^5$	$1.1 \times 10^{-4}$	$2.3 \times 10^{-4}$
40	13.27	$9.1 \times 10^{-5}$	0.89					$2.2 \times 10^5$	$1.3 \times 10^{-4}$	$3.2 \times 10^{-4}$
60	10.45	$1.1 \times 10^{-4}$	0.87	$1.1 \times 10^4$	$1.1 \times 10^{-4}$	$3.0 \times 10^{-4}$	0.91	$7.4 \times 10^4$	$4.1 \times 10^{-4}$	$2.4 \times 10^{-4}$
80	7.779	$1.2 \times 10^{-4}$	0.86	$1.2 \times 10^3$	$9.0 \times 10^{-5}$	$5.0 \times 10^{-4}$	0.82	$5.4 \times 10^4$	$1.0 \times 10^{-3}$	$1.9 \times 10^{-4}$

\* $C_1$  was calculated from CPE<sub>1</sub> and  $R_{po}$  values whereas  $C_2$  was calculated from CPE and  $R_{ct}$  values according to Equation 4.1

#### 4.4.3 Mott – Schottky (M-S) technique

It has been established that passive film formed on austenitic stainless steel such as 316L SS can be envisaged as a duplex structure having semiconductor properties [230]. Hence, the Mott-Schottky technique was employed to investigate the effects of temperature, CO<sub>2</sub> and N<sub>2</sub> gas on the electronic properties of the passive film and how they correlate with film integrity. The measured capacitance is a combination of space charge and Helmholtz region, as shown in Equation 4.2 [174, 205]. Because the Helmholtz layer capacitance is generally larger than that of the space charge layer for smooth metallic/solution interface, it can be neglected and the measured capacitance, therefore, corresponds only to that of the passive layer [175].

$$\frac{1}{C} = \frac{1}{C_{SC}} + \frac{1}{C_H} \quad \text{Equation 4.2}$$

where  $C_{SC}$  and  $C_H$  are the capacitance of space charge layer and Helmholtz layer, respectively, ( $\text{F.cm}^{-2}$ ).

The Mott-Schottky behavior exhibits when there is a linear relationship between  $1/C_{SC}^2$  and applied potential ( $E$ ). A region showing a positive slope (Equation 4.3) depicts n-type semiconductor behavior whereas the negative slope (Equation 4.4) indicates p-type [175].

$$\frac{1}{C^2} = \frac{2}{\varepsilon\varepsilon_0qN_D} \left[ E - E_{FB} - \frac{KT}{q} \right] \quad \begin{array}{l} \text{Equation 4.3} \\ \text{n-type} \end{array}$$

$$\frac{1}{C^2} = -\frac{2}{\varepsilon\varepsilon_0qN_A} \left[ E - E_{FB} - \frac{KT}{q} \right] \quad \begin{array}{l} \text{Equation 4.4} \\ \text{p-type} \end{array}$$

where  $C$  is the capacitance of space charge layer of the passive film, (F/cm<sup>2</sup>),  $E$  is the applied potential, (V),  $\varepsilon$  is the dielectric constant of the passive film on the stainless steel having a constant value of (15.6),  $\varepsilon_0$  the permittivity of free space, ( $8.858 \times 10^{-14}$  F/cm),  $q$  is the electron charge, ( $1.602 \times 10^{-19}$  C),  $N_D$  and  $N_A$  the charge carrier density for the donor and acceptor respectively, (cm<sup>-3</sup>),  $E_{FB}$  is the flat band potential, (V),  $K$  is the Boltzmann constant, ( $1.38 \times 10^{-23}$  J/K),  $T$  the absolute temperature (K).

Figure 4.7 a and b shows the Mott-Schottky plots of the passive film formed on 316L SS in 3 wt.% NaCl saturated with CO<sub>2</sub> and N<sub>2</sub> gas, respectively. In all cases, similar behavior and responses to the applied potential can be observed; i.e., 3 apparent regions are showing a linear relationship. In the first region (region 1) covering the potential from -0.5 V to -0.1 V, a positive slope indicates that the passive film is an n-type semiconductor due to the oxygen vacancies or metal interstitials acting as electron donors. This layer has been associated with iron oxide and hydroxide [207, 210]. As potential increases entering region 2 (-0.1 V to 0.4 V), the slope inverts to negative presenting the p-type semiconductor which displays electron acceptor behavior due to cation vacancies within the passive film [178]. P-type behavior film has been associated with chromium oxide [207, 210]. In region 3 (0.4 V to 1.0 V), the Mott-Schottky relationship returns to the n-type semiconductor which may correspond to the composition and structure of the passive film [248].

$N_D$  and  $N_A$  density can be derived from the slopes of the linear regions according to Equation 4.3 and Equation 4.4. The results in Table 4.4 reveal that  $N_D$  and  $N_A$  in CO<sub>2</sub> media increase with temperature in all 3 potential regions. Slightly different observations can be seen in an N<sub>2</sub> environment where  $N_D$  and  $N_A$  are slightly affected by temperature up to 60 °C but sharply rises at 80 °C. It has been widely accepted that  $N_D$  and  $N_A$  are related to defect density (namely, oxygen vacancies, cation vacancies, and cation interstitials) within the passive film and are associated with the weakening of the passive film and subsequently the pitting susceptibility.

However, at the same temperature, as can be seen in Table 4.4, there is no appreciable difference in  $N_D$  and  $N_A$  in the  $\text{CO}_2$  and  $\text{N}_2$  environments. The main difference, as discussed in the previous section on EIS was the thinning of the passive film in the presence of  $\text{CO}_2$  compared to the  $\text{N}_2$  environment.

**Table 4.4 Donor and acceptor densities ( $N_D$  and  $N_A$ ) of the passive film formed on 316L SS in 3wt.% NaCl, pH 4 sparged with  $\text{CO}_2$  and  $\text{N}_2$  at different temperatures. Region 1(-0.5 V to -0.1 V), region 2 (-0.1 V to 0.4 V), and region 3 (0.4 V to 1.0 V)**

Temperature	$N_D$ or $N_A$ in $\text{CO}_2$ ( $\text{cm}^{-3}$ )			$N_D$ or $N_A$ in $\text{N}_2$ ( $\text{cm}^{-3}$ )		
	Region 1	Region 2	Region 3	Region 1	Region 2	Region 3
30 °C	$1.14 \times 10^{18}$	$6.79 \times 10^{17}$	$1.41 \times 10^{18}$	$2.50 \times 10^{18}$	$1.12 \times 10^{18}$	$2.17 \times 10^{18}$
40 °C	$2.48 \times 10^{18}$	$1.04 \times 10^{18}$	$2.19 \times 10^{18}$	$3.44 \times 10^{18}$	$1.32 \times 10^{18}$	$2.37 \times 10^{18}$
60 °C	$3.31 \times 10^{19}$	$3.54 \times 10^{18}$	$4.49 \times 10^{18}$	$5.98 \times 10^{18}$	$3.18 \times 10^{18}$	$2.43 \times 10^{18}$
80 °C	$3.22 \times 10^{19}$	$7.72 \times 10^{18}$	$7.23 \times 10^{18}$	$2.41 \times 10^{19}$	$6.99 \times 10^{18}$	$5.02 \times 10^{18}$

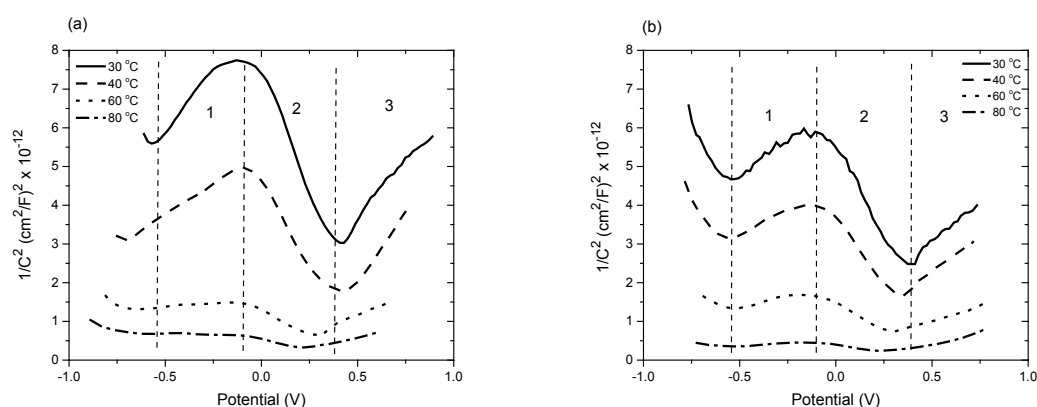


Figure 4.7 Mott-Schottky plots for 316L SS in 3wt.% NaCl, pH 4 sparged with a)  $\text{CO}_2$  and b)  $\text{N}_2$  at different temperatures

#### 4.4.4 Surface analysis by XPS

XPS measurements were used to characterize the composition of passive films formed on 316L stainless steel exposed to air and after film forming in deaerated 3 % NaCl solution with  $\text{CO}_2$  or  $\text{N}_2$  at 30 °C and 60 °C. In addition to surveying spectra, high-resolution spectra of the  $\text{Cr}_{2p}$ ,  $\text{Fe}_{2p}$ ,  $\text{Mo}_{3d}$ , and  $\text{O}_{1s}$  regions were collected for the 316L SS passive film.

According to the survey spectra presented in Figure 4.8, the passive film is composed of  $\text{C}_{1s}$ ,  $\text{O}_{1s}$ ,  $\text{Cr}_{2p}$ ,  $\text{Fe}_{2p}$ ,  $\text{Mn}_{2p}$ ,  $\text{Ni}_{2p}$ , and  $\text{Mo}_{3d}$ . The presence of carbon at the surface of the samples has been attributed to the presence of adventitious carbon due to brief exposure to air during

transportation [249, 250]. The quantitative results extracted from the survey spectra are presented in Table 4.5. Aside from carbon, the main component of the passive film electrochemically formed on 316L SS at both temperatures was Cr. The total amount of Cr was enriched compared to that exposed to air. It is also noticeable that the Cr concentration in N<sub>2</sub> is slightly higher than in CO<sub>2</sub> environment at 30 °C. The difference becomes even more apparent at 60 °C. This could be due to the destabilizing effect that CO<sub>2</sub> has on the passive layer which eventually could lead to the breakdown of the passive layer. Selective dissolution of Fe from the passive film during immersion could explain the decrease in Fe to Cr ratio compared to the specimen exposed to air.

Another notable observation from the quantitative results presented in Table 4.5 is that the concentrations of Ni and Mo in the passive film formed in both experimental conditions were slightly higher than the specimen exposed to air. Generally, the presence of Ni might effected on passivation of stainless steel by reducing the current density and increasing the pitting potential [251]. The presence of Mo tends to improve the passive film resistance to pitting corrosion by reducing the dissolution rate and decreasing the number of point defects in the passive film [252]. No apparent distinction between Ni and Mo concentrations among test conditions was observed. Therefore, the difference in corrosion behavior of 316L with respect to CO<sub>2</sub> and temperature may not be depend on Ni and Mo but more likely on Fe and Cr.

Peak fitting was performed on the high resolution spectra of Cr<sub>2p</sub>, Fe<sub>2p</sub>, Mo<sub>3d</sub>, and O<sub>1s</sub> regions and Figure 4.9 a shows representative fittings for spectra obtained in CO<sub>2</sub> environment at 60 °C. The fitting was achieved using specified empirical fitting parameters developed by Biesinger and Grosvenor. [241-243] as mentioned previously. For Cr<sub>2p</sub> spectra, the peak envelope was adequately fitted with peaks corresponding to metallic Cr, Cr<sub>2</sub>O<sub>3</sub> and Cr(OH)<sub>3</sub>. Quantitative analysis was performed and the results are reported in Table 4.6 and Table 4.7. Greater concentration of metallic Cr was founded on 316L surface in N<sub>2</sub> environment and the difference becomes more apparent particularly at 60 °C where metallic Cr concentration doubled in the presence of N<sub>2</sub> as compared to CO<sub>2</sub>. High Cr content in the passive film leads to the reduction in metal dissolution and consequently, the passive current density in agreement with polarization results. A similar trend can be observed for Cr<sub>2</sub>O<sub>3</sub> where its concentration is comparable in both environments at 30 °C but decreases when the temperature was increased to 60 °C, particularly in CO<sub>2</sub> environment. Hence, the difference becomes obvious as demonstrated in Table 4.6 and Table 4.7. It can be postulated that the inner Cr<sub>2</sub>O<sub>3</sub> converted

into outer layer  $\text{Cr}(\text{OH})_3$  as temperature increased in the  $\text{CO}_2$  environment forming a porous layer as depicted by the appearance of two time constants observed in EIS.

The  $\text{Fe}_{2p}$  spectra in Figure 4.9 b were characterized by the presence of metallic Fe and two oxide forms, namely FeO and  $\text{Fe}_3\text{O}_4$ . As can be seen in Table 4.6 and Table 4.7, the concentration of metallic Fe in the  $\text{CO}_2$  environment is less than that in the  $\text{N}_2$  environment at 2 temperatures due to enhanced selective iron dissolution by  $\text{CO}_2$ .

The deconvoluted  $\text{Mo}_{3d}$  spectra presented in Figure 4.9 c, demonstrate the existence of metallic Mo,  $\text{MoO}_2$ , and  $\text{MoO}_3$ , respectively [249, 253]. Table 4.6 and Table 4.7 demonstrates that the concentration of metallic Mo in the passive film formed in the  $\text{N}_2$  environment is slightly higher than in  $\text{CO}_2$ . The presence of Mo in the passive film promotes the resistance to the pitting corrosion susceptibility of stainless steel [254, 255] by reducing dissolution rate [54] and the number of the point defect of the passive film.

Figure 4.9 d shows that oxygen presents in the passive film in the form of an oxide ( $\text{O}^{2-}$ ), hydroxide ( $\text{OH}^-$ ) and adsorbed  $\text{H}_2\text{O}$ . According to Table 4.6 and Table 4.7, the analysis of  $\text{O}_{1s}$  spectra confirms that, as temperature increases, hydroxide species dominate the passive film corresponding with the change in Cr composition.

To provide more comprehensive information on the passive film, Figure 4.10 a to e shows the XPS depth profile of O, Fe, Cr, Ni, and Mo elements in the passive film formed upon air exposure and in 3 wt.% NaCl solutions at 30 °C and 60 °C saturated with  $\text{CO}_2$  and  $\text{N}_2$  gas, respectively. The atomic concentration of carbon sharply decreases to a constant concentration within the etch time, which is a result of the loss of the adventitious carbon contaminant. The oxygen atomic concentration is the maximum at the start of sputtering and sharply decreased to a constant value at 30 °C and 60 °C in both environments. Fe, Ni, and Mo atomic concentrations increase with the increment of etch time and then they reach a constant value. Cr concentration initially increased during the first 25 to 50 s etch time then decreased to a steady value. The results also demonstrate that the Cr atomic concentration is higher than Fe atomic concentration at the commencement of sputtering in all cases, especially in the case of  $\text{N}_2$  gas at 60 °C.

The depth profile ratio for Cr and O obtained from XPS in conjunction with EIS and M-S results suggests the passive film is made up of two layers. The external layer is largely made up of  $\text{Cr}(\text{OH})_3$ , whereas  $\text{Cr}_2\text{O}_3$  mainly resides in the inner part of the passive film. Other oxides

and hydroxide that are expected to exist within the passive film also include FeO, Cr<sub>2</sub>O<sub>3</sub>, Cr(OH)<sub>3</sub>, and MoO<sub>3</sub> at different atomic concentrations.

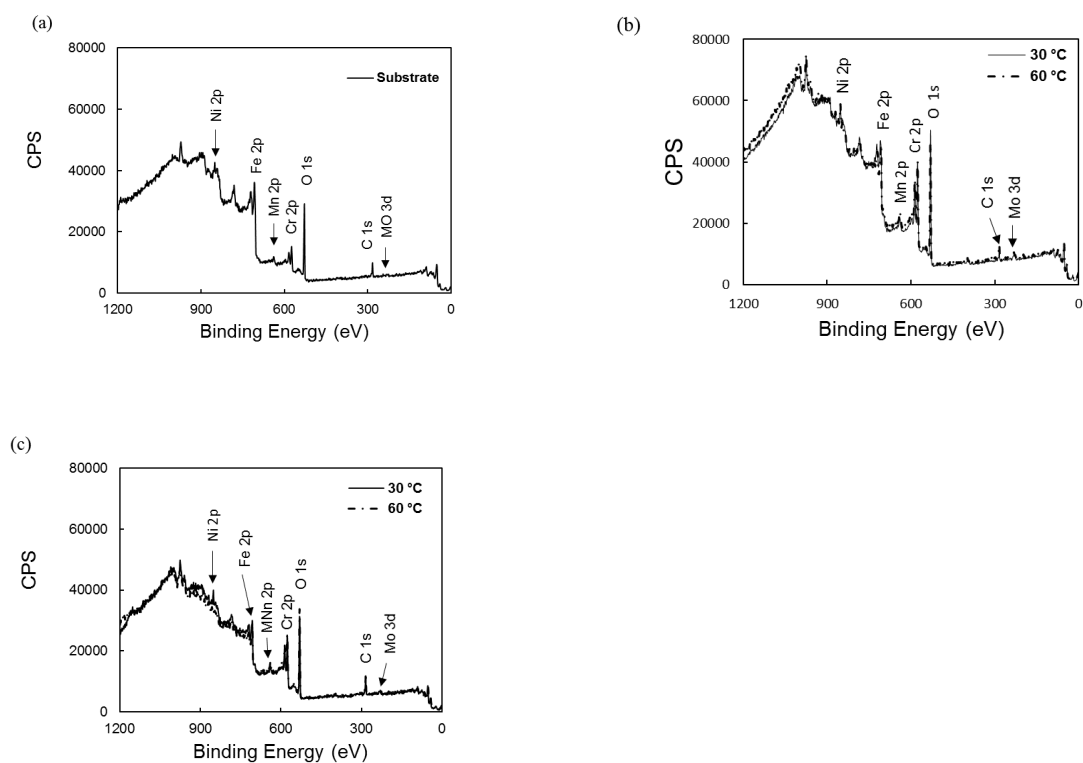


Figure 4.8 Survey XPS of the passive film formed on 316L SS a) after exposed to air and in 3wt.% NaCl pH 4 sparged with b) CO<sub>2</sub> and c) N<sub>2</sub> at 2 temperatures

**Table 4.5 Surface concentration (at%) of elements obtained from high-resolution XPS survey on the passive film formed on 316L SS exposed to air and in 3% NaCl, pH 4 at different temperatures in CO<sub>2</sub> and N<sub>2</sub> environments**

Identification	C <sub>1s</sub>		Cr <sub>2p</sub>		Fe <sub>2p</sub>		Mn <sub>2p</sub>		Mo <sub>3d</sub>		Ni <sub>2p</sub>		O <sub>1s</sub>	
	CO <sub>2</sub>	N <sub>2</sub>	CO <sub>2</sub>	N <sub>2</sub>	CO <sub>2</sub>	N <sub>2</sub>	CO <sub>2</sub>	N <sub>2</sub>	CO <sub>2</sub>	N <sub>2</sub>	CO <sub>2</sub>	N <sub>2</sub>	CO <sub>2</sub>	N <sub>2</sub>
Exposed to air	21.16		8.31		23.82		1.32		0.38		1.31		43.70	
30 °C	10.77	20.55	17.06	17.77	15.91	12.19	0.73	0.86	0.57	0.72	2.11	2.11	52.85	45.80
60 °C	15.93	24.00	15.82	18.10	12.13	8.40	1.45	1.83	0.57	0.81	2.19	1.27	51.91	45.59

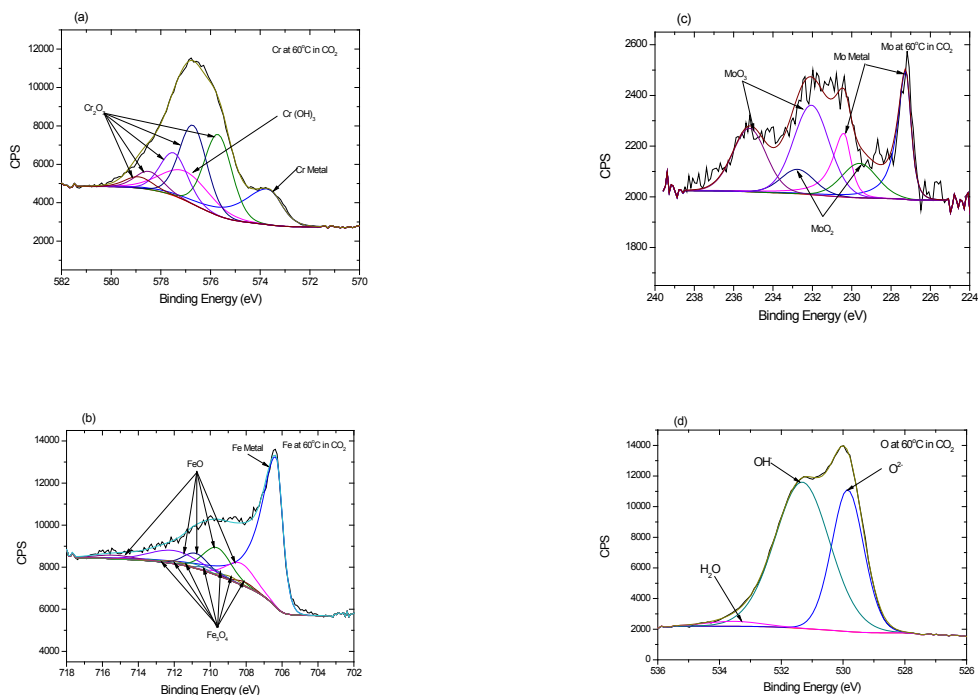


Figure 4.9 Representative high resolution XPS spectra of the passive film formed on 316L SS in CO<sub>2</sub> environment at 60 °C for a) Cr<sub>2p</sub>, b) Fe<sub>2p</sub>, C) Mo<sub>3d</sub>, and d) O<sub>1s</sub>

**Table 4.6 The detailed XPS spectra of the passive film formed on 316L SS in CO<sub>2</sub> media at 2 different temperatures**

Temperature (°C)	Cr <sub>2p</sub> (at %)			Fe <sub>2p</sub> (at %)			Mo <sub>3d</sub> (at %)			O <sub>1s</sub> (at %)		
	Cr metal	Cr <sub>2</sub> O <sub>3</sub>	Cr(OH) <sub>3</sub>	Fe metal	FeO	Fe <sub>3</sub> O <sub>4</sub>	Mo	MoO <sub>2</sub>	MoO <sub>3</sub>	O <sup>2-</sup>	OH	H <sub>2</sub> O
30	13.06	65.16	21.78	43.84	40.77	15.39	29.84	14.84	55.32	45.81	52.84	1.35
60	12.61	28.45	58.94	56.46	36.54	7.00	33.33	18.50	48.17	35.47	62.42	2.11

**Table 4.7 The detailed XPS spectra of the passive film formed on 316L SS in N<sub>2</sub> media at 2 different temperatures**

Temperature (°C)	Cr <sub>2p</sub> (at %)			Fe <sub>2p</sub> (at %)			Mo <sub>3d</sub> (at %)			O <sub>1s</sub> (at %)		
	Cr metal	Cr <sub>2</sub> O <sub>3</sub>	Cr(OH) <sub>3</sub>	Fe metal	FeO	Fe <sub>3</sub> O <sub>4</sub>	Mo	MoO <sub>2</sub>	MoO <sub>3</sub>	O <sup>2-</sup>	OH	H <sub>2</sub> O
30	19.08	67.63	13.29	54.58	26.28	19.14	33.64	14.60	51.76	30.98	66.24	2.78
60	25.64	48.72	25.64	64.95	25.33	9.72	34.62	17.74	47.63	24.67	70.37	4.96

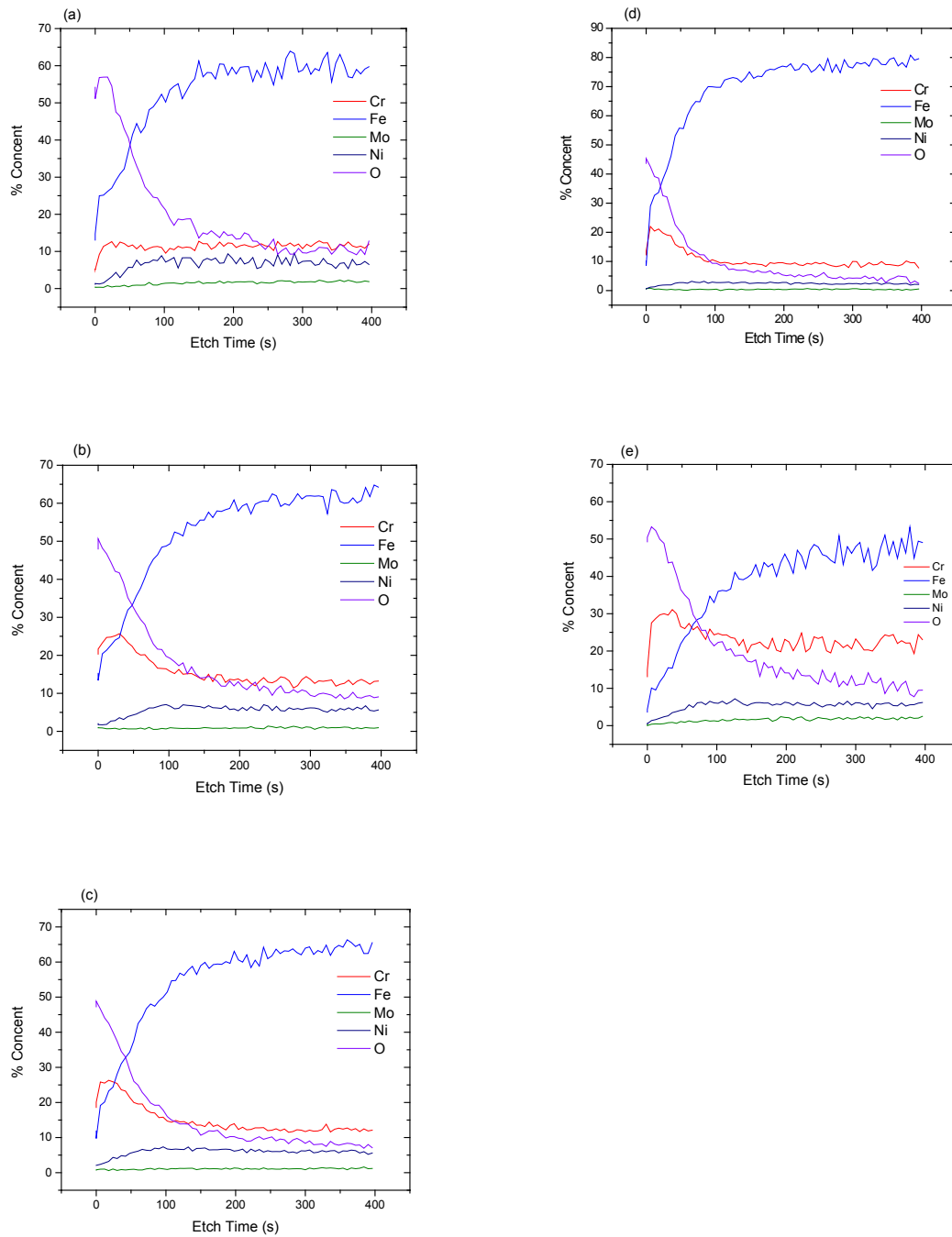


Figure 4.10 XPS depth profiles of, Cr, Fe, Mo, Ni and O elements in the passive film formed on a) 316L SS exposed to air at room temperature and that immersed in 3wt.%NaCl at b) 30 °C in CO<sub>2</sub>, c) 60 °C in CO<sub>2</sub>, d) 30 °C in N<sub>2</sub>, and e) 60 °C in N<sub>2</sub>

## 4.5 Conclusions

This study investigated the influences of CO<sub>2</sub> and temperature on the pitting susceptibility of 316L in pH 4 3wt% NaCl using electrochemical techniques and surface characterization. Based on the interpretation of combined results, the following conclusions are drawn.

1. 316L SS becomes more prone to pitting corrosion with increasing temperature. The temperature effect is magnified in the CO<sub>2</sub> environment.
2. Mott-Schottky analysis also confirms the negative impacts of temperature on pitting susceptibility due to the increase in donor ( $N_D$ ) and acceptor ( $N_A$ ) densities in both environments.
3. EIS results revealed a possible synergistic effect of temperature and CO<sub>2</sub> on the change in the passive film structure. At high temperatures 60 °C and 80 °C, a porous layer develops as indicated by the appearance of two-time constants shown in EIS results. On the other hand, this is absent in N<sub>2</sub>.
4. XPS analysis indicates that the variation in elemental composition and its speciation are in agreement with EIS results. The double layer structure is proposed where the inner layer consists of metal oxides, and the outer layer is hydroxides. A higher concentration of metal hydroxides (potentially Cr(OH)<sub>3</sub>) is observed as temperature increases particularly in the presence of CO<sub>2</sub>.

## **Chapter 5: Study the influence of high temperature and high-pressure conditions on the 316L stainless steel in CO<sub>2</sub> environment**

### **5.1 Abstract**

This study investigated the effects of temperature (30 °C, 100 °C, and 140 °C), partial pressure of CO<sub>2</sub>, and NaCl concentrations (0.05 wt.%, 3 wt.%, and 8 wt.%) on pitting corrosion behavior of UNS S31603 using cyclic polarization (CP), electrochemical impedance spectroscopy (EIS) and Mott-Schottky (MS) techniques. The CP results indicated that the pitting susceptibility of UNS S31600 increases with increasing temperature and NaCl concentration. The properties of the passive film were influenced by the temperature and NaCl concentration as identified by EIS techniques. Capacitance measurements based on the Mott-Schottky relationship revealed that the donor and acceptor densities are unaffected by increasing temperatures to the same extent as to the effect of NaCl concentration at different temperatures where the passive film has become more vulnerable with increased chloride concentrations.

**Keywords:** UNS S31603, localized corrosion, CO<sub>2</sub> environment, cyclic polarization, electrochemical impedance spectroscopy, Mott-Schottky

### **5.2 Introduction**

Stainless steels are widely used in many industries including the oil and gas industry owing to their superior corrosion resistance to general corrosion compared to mild or carbon steel [152, 213, 214]. The high corrosion resistance of stainless steel relies on the integrity of the passive film formed on its surface [256, 257]. Studies showed that the passive film of stainless steel is comprised of p-type and n-type layers, whereas the p-type represents the inner region while n-type semiconducting properties are associated with the outer region of the protective oxide film [174, 258].

Albeit the presence of such passive film, localized corrosion including pitting corrosion can occur on stainless steels in certain environments [259]. Pitting corrosion is considered a complex phenomenon and one of the important problems that are at the root of many corrosion failures. Three mechanisms, i.e., the penetration, the film breaking, and the adsorption mechanisms, have been proposed to explain the loss of passivity that leads to the initiation of localized corrosion in the form of pitting corrosion of stainless steels [118, 174, 257]. These mechanisms provided unique opportunities for understanding pitting corrosion

Environmental conditions such as water chemistry, chloride (Cl<sup>-</sup>) ion concentration, temperature, and pH [257] influence the passivation breakdown following which pitting corrosion can initiate and propagate. Moreira *et al.* noticed that the corrosion rate increased with increasing temperature from 125 °C to 175 °C under dynamic and static conditions for the 13Cr and 13Cr5Ni2Mo stainless steel [236]. Zhang *et al.* showed that the passive film formed on 13Cr stainless steel at 90 °C has a higher degree of protectiveness than that at 150 °C based on electrochemical measurements and surface analyses [235].

Furthermore, it has been reported that the pitting susceptibility of stainless steel in sodium chloride solution depends on the solution temperature. Manning *et al.* noticed that the change in the semiconductivity of the passive film formed on 304L stainless steel was related to the effect of temperature on the pitting susceptibility [260]. Carranza *et al.* found that the passive film formed on alloy 800 became more porous and less protective as the temperature was increased above 150 °C, leading to the change in the pitting morphologies based on observations and using scanning electron microscopy (SEM) and energy dispersive spectroscopy (EDS) technique [261].

There is a lack of information on the influences of high-temperature high pressure and NaCl concentrations on the pitting corrosion of UNS S31603 in the CO<sub>2</sub> environment until now. Thus, this study investigated the influences of temperature and NaCl concentrations on pitting corrosion of UNS S31603 in a constant dissolved CO<sub>2</sub> concentration using electrochemical measurements: cyclic polarization (CP), electrochemical impedance spectroscopy (EIS), and Mott-Schottky (M-S). The environment simulated that typically encountered in oil and gas production systems.

## **5.3 Experimental works**

### **5.3.1 Materials and specimen preparation**

The test specimens used in this study were machined into tube shape from UNS S31603 with the nominal chemical composition shown in Table 5.1. The specimens with an exposed ring surface of 0.22 cm<sup>2</sup> were pressed into polyether ether ketone (PEEK) to isolate them from any other electrical connections as shown in Figure 5.1. The specimens were wet ground with SiC papers from 120 to 600 grit, rinsed with ethanol (ethanol undenatured 100%, Chem-Supply Australia) and deionized (DI) water (Ibis Technology), and then dried with ultra-high purity N<sub>2</sub> gas (99.999% BOC Australia).

**Table 5.1. Chemical composition of UNS S31600 used in this study**

Element	C	Si	Mn	P	S	Ni	Cr	Mo	Fe
(wt. %)	0.02	0.36	1.36	0.03	0.006	10.02	16.92	2.02	Bal.

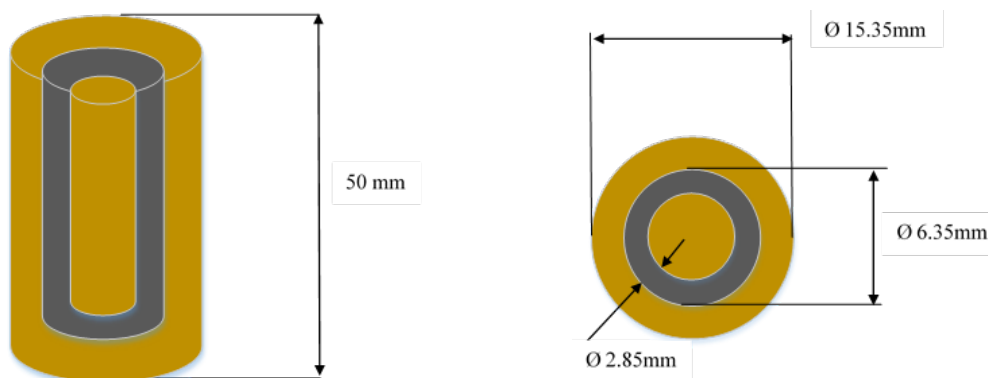


Figure 5.1 Schematic diagram to the working electrode

### 5.3.2 Test solutions

The test solutions were prepared from deionized water (Ibis Technology) and NaCl (analytical grade, Chem-Supply Australia) at various concentrations as shown in Table 5.2. Prior to a test, 1 L of the test solution was sparged with CO<sub>2</sub> (99.995%, Coregas Australia) for 4 h to remove dissolved oxygen and to saturate the solution with the test gas. The pH of the test solutions at 25 °C was adjusted to 4 with 1 M NaHCO<sub>3</sub>.

**Table 5.2. Summary of test conditions**

Variable	Conditions	Note
Temperature (°C)	30, 100, and 140	The concentration of dissolved CO <sub>2</sub> was kept constant at 0.029 kmol/m <sup>3</sup> by adjusting partial pressure of CO <sub>2</sub> .
Sodium chloride concentration (wt.%)	0.05, 3, and 8	
pH	4 @ 25 °C, 1 bar CO <sub>2</sub>	

### 5.3.3 Experimental setups

Two experimental setups were used in this study, i.e., a glass cell equipped with conventional 3-electrode for experiments at 30 °C and a high pressure/high temperature (HT/HP) test vessel for experiments at 100 and 140 °C.

The glass cell setup consisted of the platinum coated titanium mesh counter electrode (CE), the silver/silver chloride (Ag/AgCl) reference electrode (RE) in a Luggin capillary filled with 3 M KCl and a UNS S31603 specimen as the working electrode (WE). In addition to the inlet and outlet gas tube. The test cell was then placed on an electrical hot plate to maintain the test temperature at 30 °C.

The HT/HP test vessel was machined from UNS N10276. The lid of the vessel has pre-drilled ports for WE, a thermocouple for temperature control, gas inlet and outlet, a pressure gauge, the HT/HP RE (external pressure balanced reference probe Ag/AgCl electrode, 3 M KCl solution, Corr Instruments, LLC, USA), and the HT/HP pH electrode (ZrO<sub>2</sub>-based pH probe, Corr Instruments, LLC, USA). The body of the vessel was used as a counter electrode. A band heater was wrapped around the external body of the test vessel to increase the solution temperatures to 100 and 140 °C.

### 5.3.4 Experimental procedure

One litre (L) of the prepared solution was transferred using a peristaltic pump to the test vessel pre-sparged with CO<sub>2</sub>. The CO<sub>2</sub> sparging was continued until the test completion to minimise oxygen ingress and to maintain CO<sub>2</sub> saturation. The solution was then heated to the test temperature.

The cyclic polarization (CP) technique was used to determine the pitting susceptibility of UNS S31603. CP tests were performed by anodically polarizing the WE at a scan rate of 0.167 mV/s from open circuit potential ( $E_{OCP}$ ). The scan was reversed to an  $E_{OCP}$  when the measured current reached 10 mA/cm<sup>2</sup>. Tests were duplicated to verify the reproducibility of the experiments.

Prior to EIS and MS experiments at any conditions, it was important that the WE had developed reproducible passive film. This was achieved by cathodically polarizing the WE to - 0.2 V vs.  $E_{OCP}$  in the test solutions; i.e. 0.05 wt.%, 3 wt.%, and 8 wt.% NaCl at 30 °C for 15 min to remove an air formed oxide film on the surface. Subsequently, the WE was anodically polarized to - 0.1 V vs.  $E_{Ag/AgCl}$  for 1 h allowing the film to form in a controlled manner. Lastly, the solution temperature was raised to the test temperature.

EIS was then performed at  $E_{OCP}$  from 10 kHz to 10 mHz with an amplitude of 10 mV. M-S technique was then carried out by sweeping the potential from -0.5 V vs.  $E_{Ag/AgCl}$  to 1 V vs.  $E_{Ag/AgCl}$  at a frequency of 3 kHz using an amplitude signal of 10 mV and a step rate of 20 mV. All the electrochemical measurements of the corrosion process were performed using the Gamry reference 600.

## 5.4 Results and discussion

### 5.4.1 In-situ pH measurement

It has been reported that the pH value had a clear influence on the structure and the electronic property of the passive film on 316L SS [262]. Therefore, it was necessary to maintain the pH value constant during the HT/HP test.

The pH of the test solution was measured at 100 °C and 140 °C to check the change in pH by using the HT/HP pH electrode (ZrO<sub>2</sub>-based pH probe, Corr Instruments, LLC, USA). The difference in the pH ( $\Delta$ pH) was found 0.5 pH unit at 100 °C and 0.3 pH unit at 140 °C.

The amount of difference in the pH value at HT/HP is added to the required pH value which is 4 at 25 °C i.e. 4.5 pH test solution was prepared at 25 °C to conduct test at 100 °C and the pH was adjusted to 4.3 at 25 °C for test at 140 °C.

### 5.4.2 Cyclic polarization technique

The effect of temperatures on the pitting susceptibility of UNS S31603 samples immersed in 0.05 wt.%, 3 wt.%, and 8 wt.% are illustrated in Figure 5.2 a to c, respectively. The same results were rearranged and shown in Figure 5.3 a to c to demonstrate the effects of NaCl concentration at different temperatures.

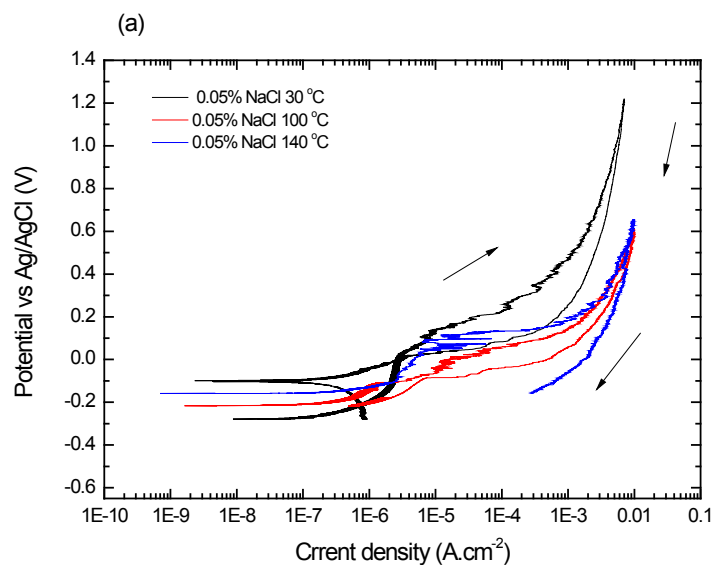
$E_{OCP}$  decreased with either increasing temperature or NaCl concentration suggesting that UNS S31603 became more active.

Pitting potential ( $E_{pit}$ ) and repassivation potential ( $E_{rep}$ ) provide information on the pitting susceptibility of metals. Materials with high  $E_{pit}$  and  $E_{rep}$  are associated with greater resistance to pitting corrosion [161]. Figure 5.2a shows that  $E_{pit}$  of 316L was not affected by temperature (up to 140 °C) when immersed in low NaCl concentration (0.05 wt.%). However, as NaCl concentration was increased to 3 and 8 wt.%,  $E_{pit}$  decreased by up to 200 and 250 mV when the temperature was increased to 100 and 140 °C, respectively. The general trend of  $E_{rep}$  also demonstrated that high temperature and chloride concentration led to decreased  $E_{rep}$ . At 140

$^{\circ}\text{C}$ ,  $E_{\text{rep}}$  was lower than  $E_{\text{OCP}}$  regardless of chloride concentrations indicating pitting corrosion initiated and propagated instantaneously on the 316L surface at  $140\text{ }^{\circ}\text{C}$  [193].

Even though  $\Delta E_{\text{pit}}$  ( $E_{\text{pit}} - E_{\text{OCP}}$ ) can be influenced by  $E_{\text{OCP}}$ , it is commonly used as another criterion to quantify the tendency for pitting corrosion. High  $\Delta E_{\text{pit}}$  is usually associated with greater resistance to pitting corrosion [161]. In addition to  $E_{\text{pit}}$  and  $\Delta E_{\text{pit}}$ , the pitting corrosion susceptibility may be visually estimated by the appearance of metastable pitting events and the magnitude of hysteresis loop from CP scans. A large hysteresis loop suggested the possibility of pitting corrosion [185, 186]. In this study, the magnitude of hysteresis loops is the greatest at  $140\text{ }^{\circ}\text{C}$  regardless of NaCl concentrations. Metastable pitting events are characterized by the current fluctuation in the passive region during the forward scan signaling the constant depassivation and passivation of the passive oxide film [263]. As 316L was polarized beyond  $E_{\text{pit}}$ , the passive film could not repassivate leading to a permanent increase in current density sustaining pit propagation. The results obtained in this study showed that at 0.05 wt.% and 3 wt.% NaCl, metastable pitting events were observed as the temperature was increased from  $30\text{ }^{\circ}\text{C}$  to  $100$  and  $140\text{ }^{\circ}\text{C}$ .

On the contrary, at high NaCl (8 wt.%), no metastable pitting event was observed at any temperatures tested in this study. Kim and Young reported that the chloride ion is aggressive and promotes the passive film breakdown of stainless steel [191]. Therefore, it is possible that the passive film could not repassivate at 8 wt.% NaCl; hence, the absence of metastable pitting events. These results are in good agreement with previous work [190, 264].



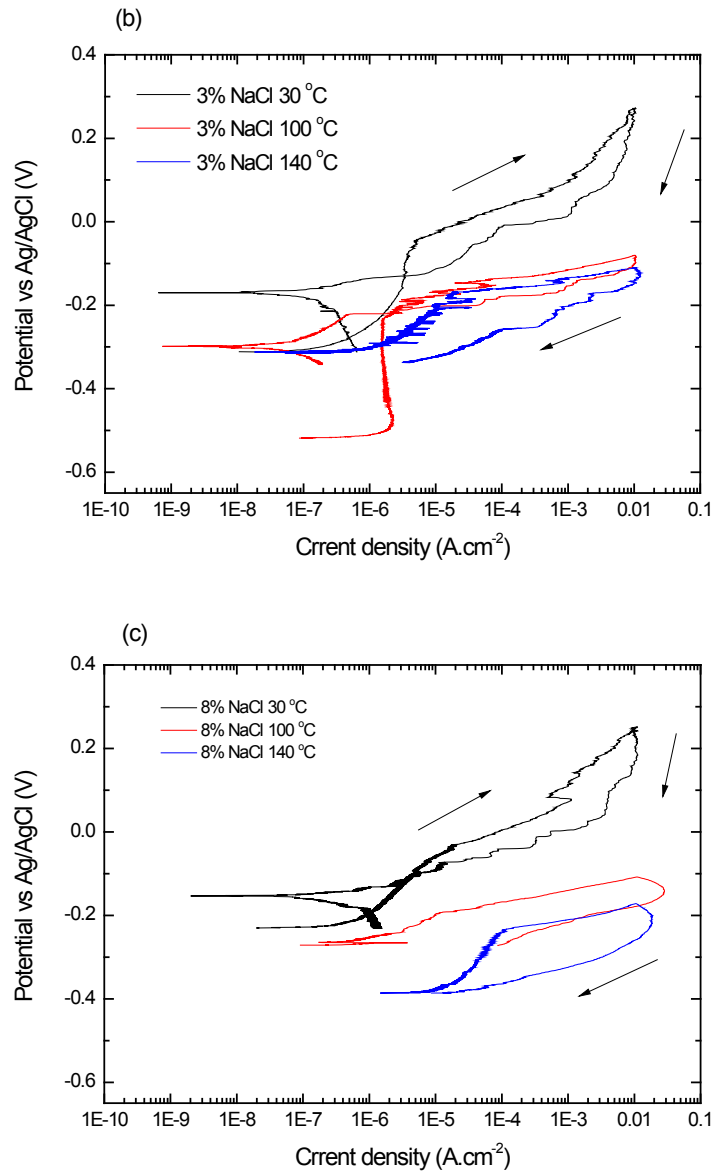


Figure 5.2 Cyclic polarization curves of UNS S31603 in a) 0.05 wt.% NaCl, b) 3 wt.% NaCl and c) 8 wt.% NaCl, pH 4 at different temperatures

To demonstrate the effects of chloride ions, the CP scans were rearranged as shown in Figure 5.3 a to c.  $E_{\text{pit}}$  decreased with increasing NaCl concentrations.

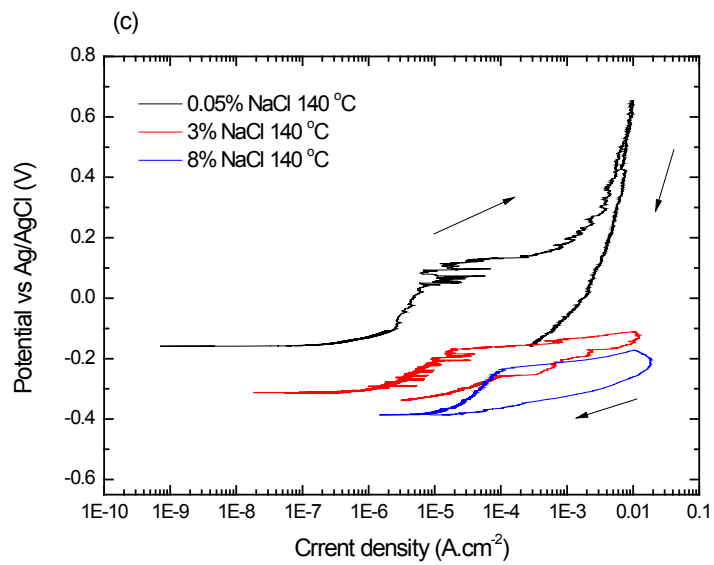
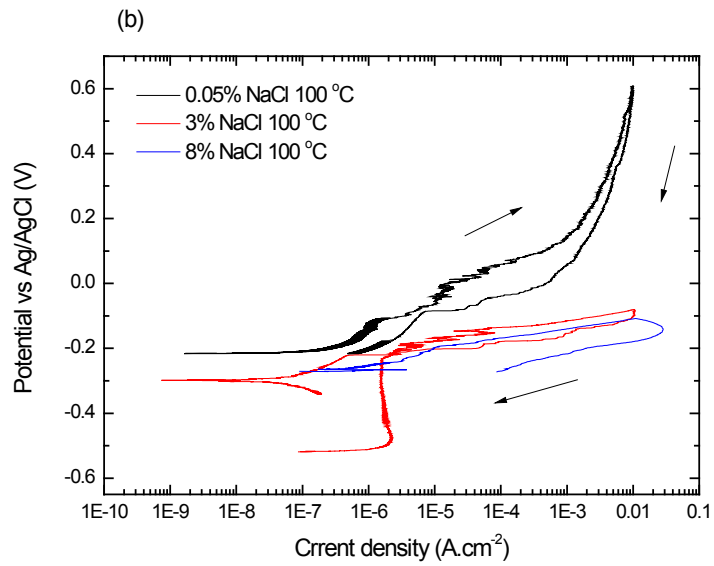
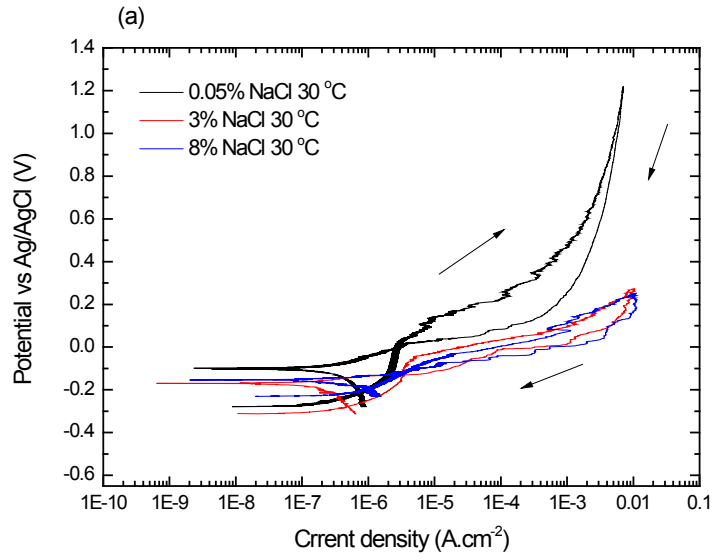


Figure 5.3 Cyclic polarization curves for UNS S31603 in different NaCl concentrations, pH 4 at a) 30 °C, b) 100 °C and c) 140 °C

### 5.4.3 Electrochemical impedance spectroscopy (EIS) technique

Figure 5.4 a to c presents the Nyquist plots and the Bode diagrams obtained on UNS S31603 at different temperatures in 0.5 wt.%, 3 wt.%, and 8 wt.% NaCl, respectively. An incomplete semicircle is a typical appearance of the Nyquist plots observed in this study. The diameter of the semicircle decreases with the increase of temperatures in every NaCl concentration suggesting an increased corrosion attack. At high temperature 140 °C in 0.05 wt.% NaCl and 3 wt.% NaCl as well as at 30 °C in 8 wt.% NaCl the shape of Nyquist plot comprises of the depressed semicircle and a diffusion tail caused by the diffusion of iron ion, which is produced by the anodic reaction. In addition, the depressed semicircle implied that the surface does not behave as an ideal capacitor due to the microscopic surface roughness and the presence of a porous corrosion product film [194].

Three equivalent circuits were used to fit EIS spectra. Spectra obtained at 30 °C and 100 °C in 0.05 wt.% NaCl and 3 wt.% NaCl (Figure 5.4 and Figure 5.5) depicts one-time constant and these spectra were fitted with the equivalent circuit shown in Figure 5.6 a. This equivalent circuit consists of the solution resistance ( $R_s$ ) between the working and reference electrodes, the double layer capacitance ( $C_{dl}$ ), and the charge transfer resistance ( $R_{ct}$ ). For account the dispersion effect caused by the roughness of the electrode interface, the constant phase element ( $CPE$ ) is used to replace the capacitance double layer ( $C_{dl}$ ) to reflect the capacitance behavior. The impedance of the CPE is defined as shown in Equation 5.1 [199].

$$Z_{CPE} = \frac{1}{Y_o (j\omega)^\alpha} \quad \text{Equation 5.1}$$

where  $Y_o$  is CPE constant ( $\Omega^{-1}\text{cm}^{-2}\text{s}^\alpha$ ),  $\omega$  is the angular frequency (rad /s),  $j^2 = -1$  is the imaginary number and  $\alpha$  is the CPE exponent, so CPE can represent resistance if  $\alpha = 0$ , ideal capacitance if  $\alpha = 1$  and Warburg element if  $\alpha = 0.5$  [265].

The impedance spectra were obtained at 140 °C in 0.05 wt.% NaCl and 3 wt.% NaCl and 30 °C in 8 wt.% NaCl were fitted with the equivalent circuit model shown in Figure 5.6 b where the Warburg impedance ( $W_s$ ) relating to ions diffusion connected in series with  $R_{ct}$ . This equivalent circuit was selected to correlate with the shape of the Nyquist plot, i.e., a depressed

semicircle and a diffusion tail caused by the diffusion of iron ion produced by the anodic reaction. The two time constants observed at 100 °C and 140 °C in 8 wt.% NaCl were often considered as the response of an inhomogeneous film, which is similar to that reported for passive alloys in other environments [195, 202, 203]. The equivalent circuit model in Figure 5.6 c [172, 179, 195, 202] was adopted to fit this behavior. In this equivalent circuit model, outer porous layer resistance ( $R_{po}$ ), the constant phase element of the porous layer (C), the charge transfer resistance of the inner layer  $R_{ct}$  and the constant phase element (C1) are introduced to the existing Figure 5.6 a model.

After the values of  $Y_o$ ,  $R$  and  $\alpha$  are deduced from the equivalent circuit, the pure capacitance (C) can be calculated using the correlation shown in Equation 5.2 previously proposed in the literature [198, 200, 201]

$$C = \frac{(Y_o R)^\frac{1}{\alpha}}{R} \quad \text{Equation 5.2}$$

where  $R$  is resistance, ( $\Omega \text{ cm}^2$ ).

Table 5.3 reports the EIS parameters from the fitting data described above.  $R_{ct}$  decreased with the increasing temperatures and NaCl concentrations suggesting an enhanced corrosion attack on the electrode surface due to accelerated metal dissolution and the rate of chloride adsorption into the passive film.  $R_{po}$  values have a small magnitude compared with  $R_{ct}$ . The probable reason is that the corrosion protection was provided by the inner layer passive film [202, 204]. In addition,  $R_s$  values decrease with increasing temperature and NaCl concentration due to increased dissolution and ionic transport which is improved by the decrease of solution viscosity and by greater diffusion [183]. As the temperature was increased in high NaCl solution, the second time constant appears which corresponds to the porous layer as previously discussed.

As a result, increasing temperatures lead to increase in the susceptibility to film breakdown, which was shown previously using the cyclic polarization technique.

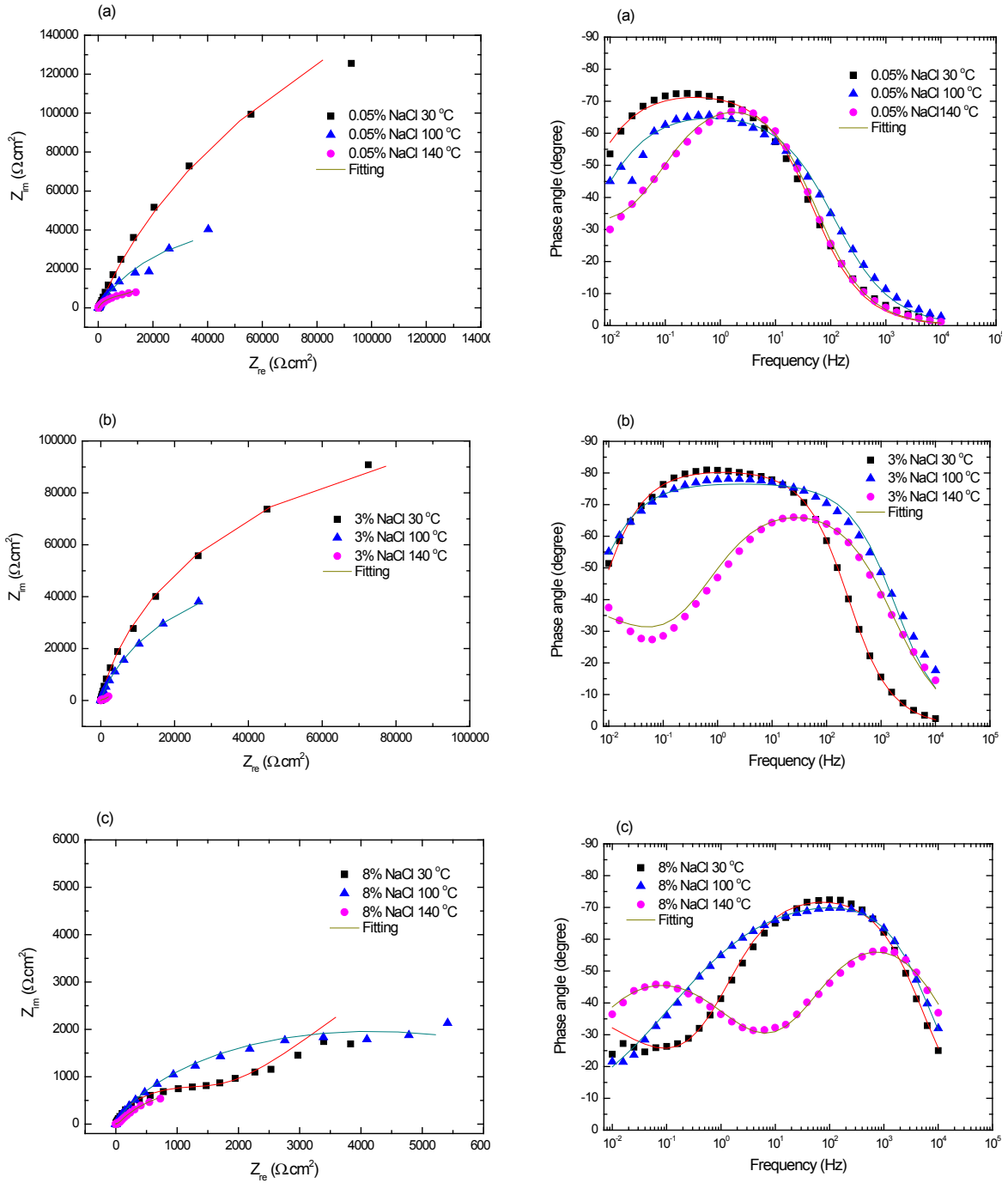


Figure 5.4 Nyquist plots (left) and Bode phase diagrams (right) of UNS S31603 in a) 0.05 wt.% NaCl, b) 3 wt.% NaCl and c) 8 wt.% NaCl, pH 4 at different temperatures

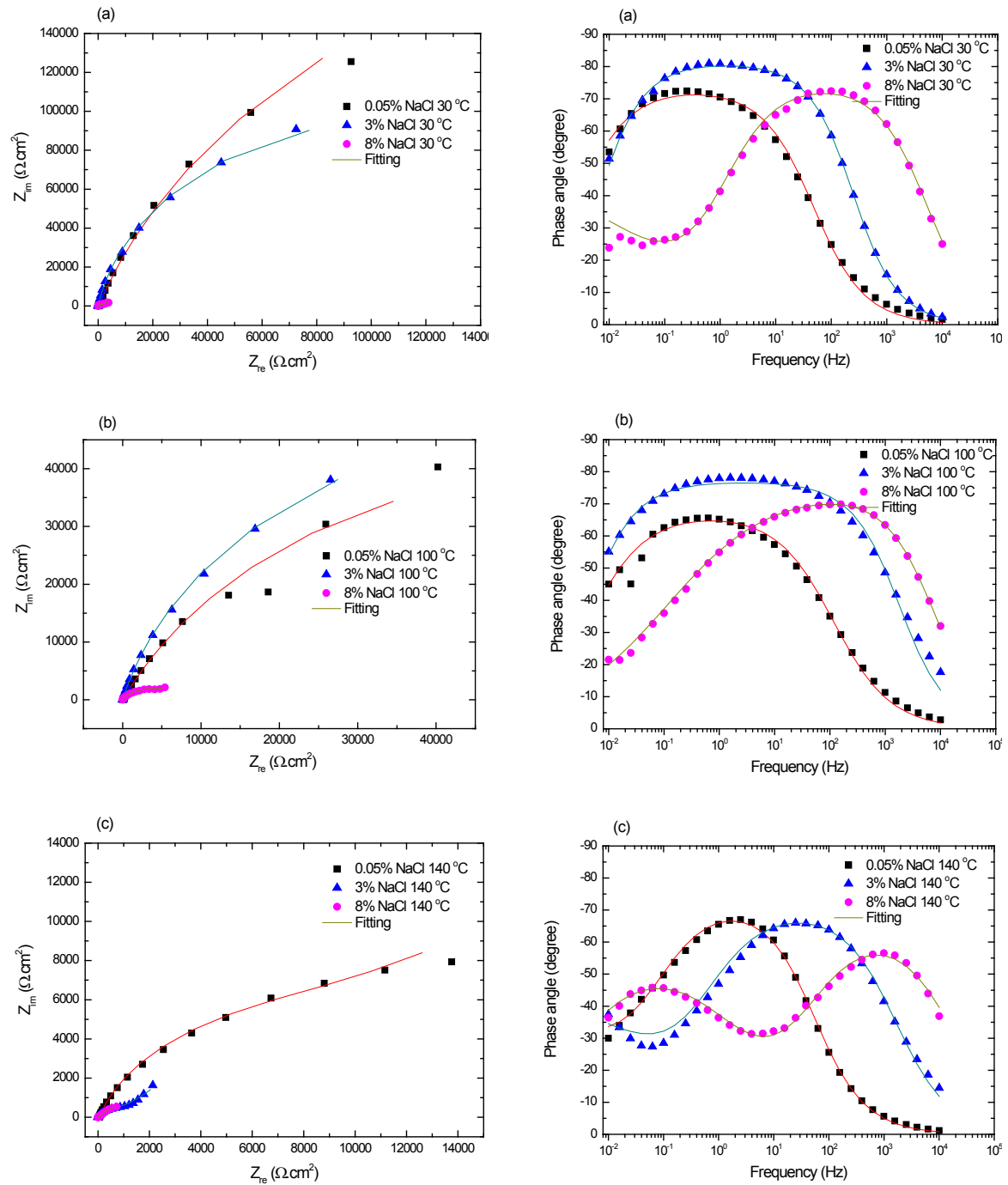


Figure 5.5 Nyquist plots (left) and Bode phase diagrams (right) of UNS S31603 in different NaCl concentrations, at a) 30 °C, b) 100 °C and c) 140 °C, pH 4

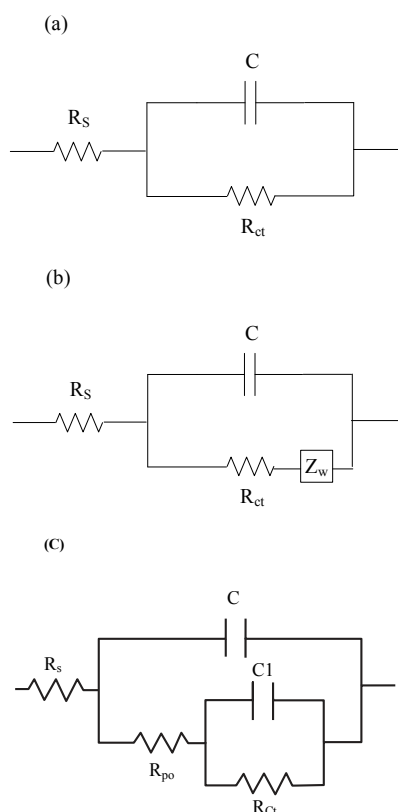


Figure 5.6 Equivalent circuit for fitting of EIS data a) one time constant, b) one time constant with diffusion and c) two time constant

**Table 5.3. Electrical parameters obtained by fitting the EIS data for 316L SS in a) 0.05 wt.% NaCl, b) 3 wt.% NaCl and c) 8 wt.% NaCl, pH 4 at different temperatures**

(a)	NaCl Concentration 0.05 wt.%					
T (°C)	$R_s$ ( $\Omega \text{ cm}^2$ )	CPE ( $\Omega^{-1} \text{ cm}^{-2} \text{ s}^{\alpha}$ )	$\alpha$	$R_{ct}$ ( $\Omega \text{ cm}^2$ )	C ( $\text{F cm}^{-2}$ )	Wd ( $\Omega^{-1} \text{ cm}^{-2} \text{ s}^{0.5}$ )
30	175.10	$5.51 \times 10^{-5}$	0.81	$5.26 \times 10^5$	$1.19 \times 10^{-4}$	-
100	59.51	$1.24 \times 10^{-4}$	0.75	$1.19 \times 10^4$	$3.11 \times 10^{-4}$	-
140	46.11	$1.87 \times 10^{-4}$	0.81	$1.14 \times 10^4$	$2.22 \times 10^{-4}$	$4.34 \times 10^{-4}$

(b)	NaCl Concentration 3 wt.%					
T (°C)	$R_s$ ( $\Omega \text{ cm}^2$ )	CPE ( $\Omega^{-1} \text{ cm}^{-2} \text{ s}^{\alpha}$ )	$\alpha$	$R_{ct}$ ( $\Omega \text{ cm}^2$ )	C ( $\text{F cm}^{-2}$ )	Wd ( $\Omega^{-1} \text{ cm}^{-2} \text{ s}^{0.5}$ )
30	16.74	$7.86 \times 10^{-5}$	0.90	$2.23 \times 10^5$	$1.07 \times 10^{-4}$	-
100	1.81	$1.89 \times 10^{-4}$	0.85	$1.18 \times 10^4$	$3.22 \times 10^{-4}$	-
140	1.77	$4.11 \times 10^{-4}$	0.78	981.10	$3.19 \times 10^{-4}$	$2.06 \times 10^{-3}$

(c)	NaCl Concentration 8 wt.%									
T (°C)	$R_s$ ( $\Omega \text{ cm}^2$ )	CPE <sub>1</sub> ( $\Omega^{-1} \text{ cm}^{-2} \text{ s}^{\alpha_1}$ )	$\alpha_1$	$R_{po}$ ( $\Omega \text{ cm}^2$ )	C ( $\text{F cm}^{-2}$ )	CPE ( $\Omega^{-1} \text{ cm}^{-2} \text{ s}^{\alpha_2}$ )	$\alpha_2$	$R_{ct}$ ( $\Omega \text{ cm}^2$ )	C1 ( $\text{F cm}^{-2}$ )	Wd ( $\Omega^{-1} \text{ cm}^{-2} \text{ s}^{0.5}$ )
30	1.41	$1.26 \times 10^{-4}$	0.83	-	$9.13 \times 10^{-5}$	-	-	$1.61 \times 10^3$	-	$1.28 \times 10^{-3}$
100	$8.22 \times 10^{-1}$	$1.63 \times 10^{-4}$	0.83	$5.70 \times 10^{-1}$	$2.43 \times 10^{-5}$	$2.35 \times 10^{-4}$	0.40	$9.80 \times 10^3$	$8.30 \times 10^{-4}$	-
140	$4.50 \times 10^{-1}$	$4.52 \times 10^{-4}$	0.73	$4.40 \times 10^1$	$1.08 \times 10^{-4}$	$4.80 \times 10^{-3}$	0.61	$2.59 \times 10^3$	$2.37 \times 10^{-2}$	-

\*C and C1 were calculated from CPE and R values according to Equation 3.2

#### 5.4.4 Mott – Schottky

Before discussing the effect of different conditions (temperatures and NaCl concentrations) on the semiconducting properties of the passive film formed on 316L SS, it is important to select a suitable frequency to measure the Mott-Schottky plot. It is known that the capacitances are frequency dependent [176, 205, 208]. Therefore, the frequency of 3 kHz is used as the applied frequency in this study to eliminate the capacitance dependence on the frequency [240].

For Mott–Schottky analysis, the imaginary part of the impedance ( $Z''$ ) was measured as a function of applied potential, and then the capacitance of the passive film ( $C$ ) was calculated from the measured impedance using Equation 5.3.

$$C = (-Z''2\pi f)^{-1} \quad \text{Equation 5.3}$$

Where  $Z''$  is the imaginary part of the impedance, and  $f$  is the frequency, (Hz).

Depending on Mott–Schottky theory [174, 205], the measured capacitance of the film/electrolyte interface consists of the capacitance of the space charge layer ( $C_{SC}$ ) and capacitance of Helmholtz layer ( $C_H$ ). It can be written by Equation 5.4

$$\frac{1}{C} = \frac{1}{C_{SC}} + \frac{1}{C_H} \quad \text{Equation 5.4}$$

where  $C_{SC}$  and  $C_H$  are the capacitance of the space charge layer and capacitance of the Helmholtz layer, respectively, (F/cm<sup>2</sup>).

Assuming that the capacitance of the space charge layer is smaller than the Helmholtz layer capacitance [175]. Therefore, the capacitance determined reflects the space charge capacitance  $C_{sc}$  of the passive film.

The Mott–Schottky relations for n-type and p-type semiconductors are expressed by Equation 5.5 and Equation 5.6 respectively [174, 175].

$$\frac{1}{C^2} = \frac{2}{\epsilon\epsilon_0qN_D} \left[ E - E_{FB} - \frac{KT}{q} \right] \quad \begin{array}{l} \text{Equation 5.5} \\ \text{For n- type} \end{array}$$

$$\frac{1}{C^2} = -\frac{2}{\epsilon\epsilon_0qN_A} \left[ E - E_{FB} - \frac{KT}{q} \right] \quad \begin{array}{l} \text{Equation 5.6} \\ \text{For p- type} \end{array}$$

where  $C$  is the capacitance of the space charge layer of the passive film ( $\text{F}/\text{cm}^2$ ),  $\epsilon$  is the dielectric constant of the passive film (15.6) for stainless steel,  $\epsilon_0$  is the vacuum permittivity ( $8.854 \times 10^{-14} \text{ F}/\text{cm}$ ),  $q$  is the electron charge ( $1.602 \times 10^{-19} \text{ C}$ ),  $K$  is the Boltzmann constant ( $1.38 \times 10^{-23} \text{ J}/\text{K}$ ),  $E$  is the applied potential (V),  $E_{FB}$  is the flat band potential,  $N_A$  is the acceptor density, and  $N_D$  is the donor density,  $T$  is the absolute temperature (K).

Figure 5.7 and Figure 5.8 shows Mott–Schottky plots of the passive film formed on UNS S31603 at different temperatures and different NaCl concentrations, respectively. It can be seen as temperatures increased the slopes of the linear region decreased indicating an increment of a defect in the passive film (Figure 5.7). M-S plots reveal 3 regions showing a linear relationship between  $1/C^2$  and  $E$  in 0.05 wt.% NaCl at different temperatures and in 3 wt.% NaCl at 30 °C. While it shows 2 regions in 3 wt.% NaCl at high temperatures 100 °C and 140 °C and in 8 wt.% NaCl at different temperatures, it should be noted that the change of the slope shape with potential is related to the structure and composition of the passive film formed on UNS S31603 [191]. It is important to focus on the potential range of around between -0.35V to 0.2V, which exhibits the passive range according to the cyclic polarization technique. Generally, the positive slopes indicate that the passive film formed on UNS S31603 is n-type semiconductor results from anion diffusion towards the metal acting as an electron donor. It has been reported that this type of layer is enriched with iron oxide and hydroxide [207, 210]. While the passive film with an excess of cation vacancies or shortage of metal ion behaves as p-type semiconductor showing electron acceptor [178]. The donor density  $N_D$  and the acceptor density  $N_A$  of the passive film formed on UNS S31603 were calculated from Equation 5.5 and Equation 5.6. The results show that the donor and acceptor densities increased with temperature and NaCl concentration suggesting a highly disordered character of the passive film [181]. These results are in good agreement with EIS measurements and cyclic polarization.

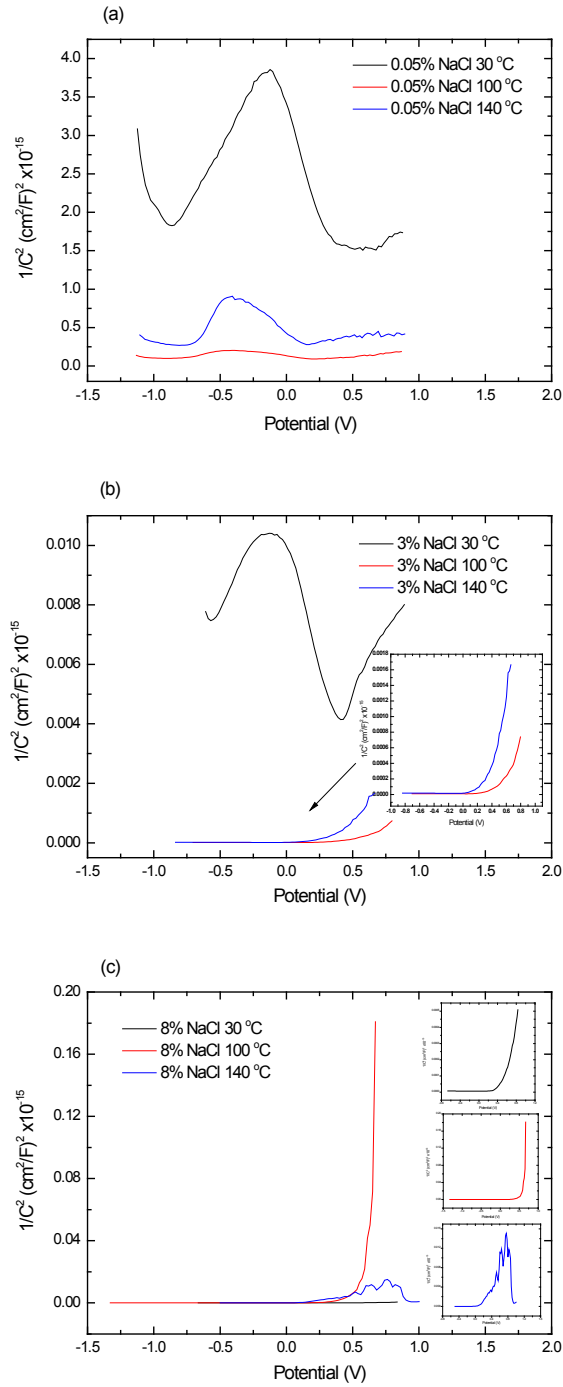


Figure 5.7 Mott-Schottky plots for UNS S31603 in a) 0.05 wt.% NaCl, b) 3 wt.% NaCl and c) 8 wt.% NaCl, pH 4 at different temperature, 3 kHz, with AC 10 mV

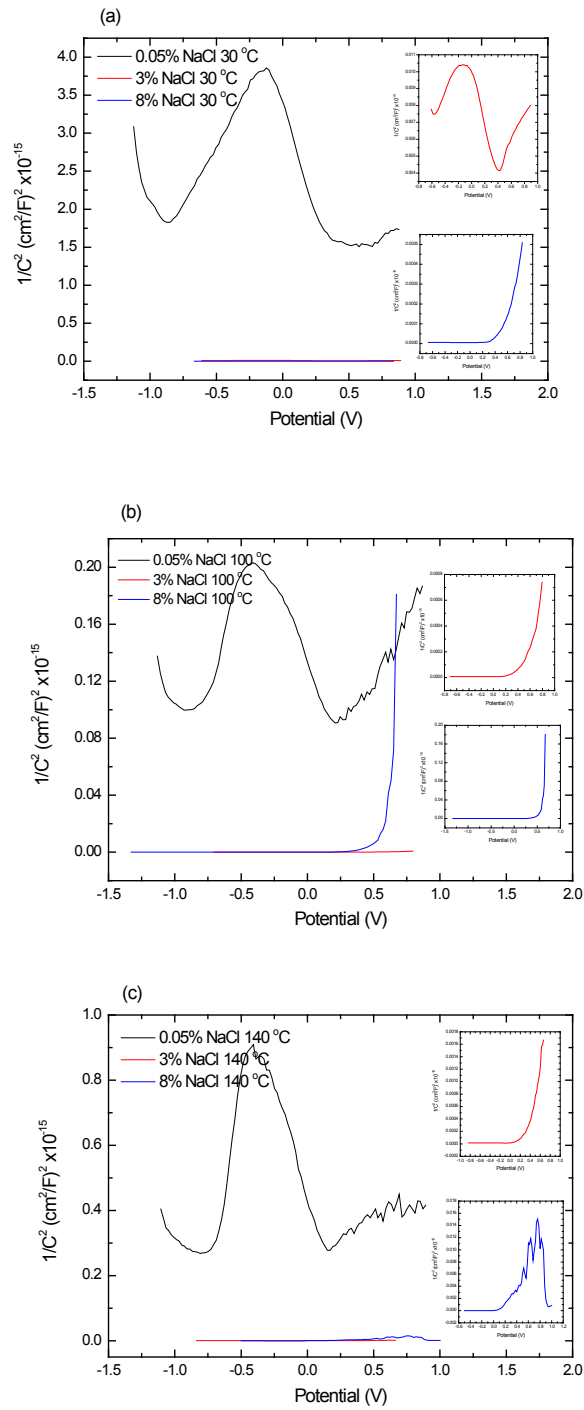


Figure 5.8 Mott-Schottky plots for UNS S31603 in different NaCl concentrations, at a) 30 °C, b) 100 °C and c) 140 °C, pH 4, 3 kHz, with AC 10 mV

## 5.5 Conclusions

- 1- The increased temperature and NaCl concentration can enhance the pitting susceptibility of UNS S31603 as determined by the parameters that were obtained from the cyclic polarization.
- 2- The electrochemical impedance spectroscopy results have revealed the change in the passive film formed on UNS S31603 at different temperatures and NaCl concentrations. The high temperatures increase the defects on the passive film and make it more heterogeneous. In addition, this harmful effect is intensified at higher NaCl concentrations. Therefore, the combined effect of these two factors decreases the protectiveness of the passive film formed on UNS S31603.
- 3- Mott-Schottky analysis results have shown that the donor and acceptor densities ( $N_D$  and  $N_A$ ) appear to be unaffected by the increasing temperatures to the same extent as increased NaCl concentration indicating the weakening of the passive film with increased solution concentration.

## **Chapter 6: Effect of CO<sub>2</sub> partial pressure on the pitting susceptibility of UNS S31603 at different temperatures**

### **6.1 Abstract**

The influence of CO<sub>2</sub> partial pressure on the corrosion behaviour of UNS S31603 stainless steels (SS316L) in 3wt.% NaCl at various temperatures were investigated by open circuit potential (OCP), cyclic polarization techniques (CP). Electrochemical impedance spectroscopy technique (EIS). CO<sub>2</sub>, NaCl, and temperatures were found to decrease the corrosion resistance of SS316L. The results showed that OCP was shifted to more negative values when the CO<sub>2</sub> partial pressure was increased from 2.6 to 10.3 bar at 100 °C as well as from 6.7 to 10.1 at 140 °C. Results from CP technique confirm greater pitting susceptibility of SS316 with increasing CO<sub>2</sub> partial pressure at different temperatures.

**Keywords:** CO<sub>2</sub> partial pressure, UNS S31603 stainless steel, open circuit potential, cyclic polarization techniques, electrochemical impedance spectroscopy technique

### **6.2 Introduction**

Carbon dioxide corrosion (CO<sub>2</sub> corrosion) is a very serious problem in the oil and gas industry and often results in severe damage by affecting the materials used in production and processing facilities [5, 266-271]. The crude oil and natural gas from the oil reservoir/gas wells usually contains some level of CO<sub>2</sub>. CO<sub>2</sub> corrosion was reported as early as 1940 [272]. The mechanism of corrosion of ferrous alloys in media containing CO<sub>2</sub> is complex, and depending on the prevailing conditions, it may lead to general or localized corrosion and corrosion cracking. Therefore, a better understanding of CO<sub>2</sub> corrosion will help identify measures to mitigate corrosion and avoid unexpected damage and production loss.

The possible CO<sub>2</sub> corrosion mechanisms and the various steps in the CO<sub>2</sub> corrosion process are widely discussed in the literature [46, 50, 273, 274]. The overall corrosion process can be divided into four major steps. The first step is the dissolution of CO<sub>2</sub> in the aqueous solution to form the various reactive species which take part in the CO<sub>2</sub> corrosion reaction. The second step is the transportation of these reactants to the surface of the metal. The third step involves the electrochemical reactions (cathodic and anodic) taking place at the metal surface. The fourth step involves the transportation of the products of the corrosion reaction to the solution.

It was proposed that three species present in a CO<sub>2</sub> containing aqueous solution, namely H<sub>2</sub>CO<sub>3</sub>, HCO<sub>3</sub><sup>-</sup>, and H<sup>+</sup>, take part in the electrochemical cathodic reduction reactions in the CO<sub>2</sub> corrosion process. The contributions to corrosion by the individual cathodic reactions of H<sub>2</sub>CO<sub>3</sub>, HCO<sub>3</sub><sup>-</sup>, and H<sup>+</sup> and their kinetics are very important. These three species have different mass transfer and reaction kinetics and contribute to different corrosivity. The direct reduction of H<sub>2</sub>CO<sub>3</sub> as an additional cathodic reaction was proposed in early literature [275, 276]. However, a recent study suggested another mechanism called “buffering effect” illustrating that dissolved CO<sub>2</sub> and their derivative species including H<sub>2</sub>CO<sub>3</sub> act as a buffer source for the reduction of H<sup>+</sup> [277]. Tran et al. [278] found that the presence of H<sub>2</sub>CO<sub>3</sub> only affects the cathodic limiting current due to the ability of carbonic acid to provide H<sup>+</sup> by dissociation which are the dominant cathodic reactants reduced at the surface of the metal.

Iron alloys in the presence of solutions containing dissolved carbon dioxide present higher corrosion rates than in the presence of strong acid solutions at the same pH [275, 279]. CO<sub>2</sub> corrosion is sensitively dependent on alloy composition, environmental conditions such as temperature, CO<sub>2</sub> partial pressure, flow conditions, and protective corrosion scales [280-284]. CO<sub>2</sub> partial pressure and protective scale considerably affect corrosion rate. Many studies demonstrated that the CO<sub>2</sub> corrosion rate of steel increases with increasing CO<sub>2</sub> pressure [285-287]. The concentration of carbonic acid increases as CO<sub>2</sub> partial pressure increases, which accelerates the cathodic reactions and increases the corrosion rate [288-291]. CO<sub>2</sub> partial pressure affects the protective properties and components of the corrosion product layer by changing the pH of the system. Many studies [290-295] indicated that FeCO<sub>3</sub> is the main composition in the corrosion product layer that is formed on corroded carbon steel surface exposed to CO<sub>2</sub> environment. Mustafa et al. showed that the corrosion product film of X52 steel is inhomogeneous and porous in CO<sub>2</sub> formation water at different CO<sub>2</sub> pressures (10, 40, and 60 bar) and 60 °C, and the corrosion product layer is mainly composed of FeCO<sub>3</sub> and Fe<sub>3</sub>C [292]. However, increasing CO<sub>2</sub> partial pressure does not often accelerate corrosion. Choi et al. reported that the corrosion rates of carbon steel measured in CO<sub>2</sub> saturated water show no significant difference (19.5-20.1 mm/y) with pressure (40, 60, and 80 bar) at 50 °C [294].

Lim et al. [296] found that the corrosion rates of SS316L and 310S stainless steels depend significantly on the partial pressure of CO<sub>2</sub> but very little on the partial pressure of O<sub>2</sub>. Combined temperature and the presence of dissolved CO<sub>2</sub> are reported to have an important effect on the chloride pitting corrosion behavior and mechanism, leading to increased attack

with temperature [297]. Numerous studies mainly focused on the influences of CO<sub>2</sub> partial pressure on the corrosion of carbon steel. However, information about the influence of CO<sub>2</sub> partial pressure on corrosion of stainless steel is rather scarce. Thus, understanding the effect of CO<sub>2</sub> partial pressure on the corrosion behavior of SS316L in 3wt.% NaCl at various temperatures is important.

In this study, the effects of CO<sub>2</sub> partial pressures on the corrosion properties of UNS S31603 stainless steels in 3wt.% NaCl at various temperatures were investigated by using electrochemical techniques such as OCP, CP, and EIS techniques in order to gain a better understanding of the material behaviour.

### 6.3 Experimental procedure

#### 6.3.1 Materials and specimen preparation

SS316L with the chemical composition shown in Table 6.1 was in the present study. The specimens were tube-shaped, with an exposed ring surface of 0.22 cm<sup>2</sup> pressed into polyether ether ketone (PEEK) to isolate them from any other electrical connections. The specimens were wet ground with a series of SiC papers to 600 grit, then rinsed with ethanol (AR 100%, Chem-Supply Australia) and deionized (DI) water (Ibis Technology), and then dried with ultrahigh purity N<sub>2</sub> gas (99.999%, BOC Australia).

**Table 6.1. Chemical composition of UNS S31603 stainless steel**

Element	C	Si	Mn	P	S	Ni	Cr	Mo	Fe
(wt. %)	0.02	0.36	1.36	0.03	0.006	10.02	16.92	2.02	Bal.

#### 6.3.2 In-situ pH measurement

The solution pH is an important factor which may influence the structure and the electronic property of the passive film on UNS S31603 stainless steels [262]. It is also widely known that the presence of CO<sub>2</sub> can affect the solution pH. Therefore, in this work, a high temperature and high pressure (HT/HP) pH electrode (ZrO<sub>2</sub>-based pH probe, Corr Instruments, USA) connected with a HT/HP Ag/AgCl external reference electrode (external pressure balanced reference probe Ag/AgCl electrode, 3M KCl solution, Corr Instruments, USA), was used.

#### 6.3.3 Test solutions

The effect of CO<sub>2</sub> partial pressure was studied in 3 wt.% NaCl solutions at 2 different temperatures: 100 °C, and 140 °C. The solution was prepared with DI water and NaCl (AR,

Chem-Supply Australia). The pH of the test solutions was adjusted at room temperatures by adding 1 M NaHCO<sub>3</sub>. Table 6.2 shows the summary of the test conditions. Prior to a test, 1 L of the test solution was sparged with CO<sub>2</sub> (99.995%, Coregas Australia) for 4 h to remove dissolved oxygen and to saturate the solution with the test gas. The prepared deaerated solution was then transferred into the HT/HP test vessel via a peristaltic pump. The solution was heated to and maintained at the desired temperature with a band heater attached to the body of the test vessel, external temperature controller, and an in-situ thermocouple.

**Table 6.2. Summary of test conditions**

Variables		Conditions				Units
CO <sub>2</sub> partial pressure ( $P_{CO_2}$ )	100 °C	2.1	5.1	7.7	10.3	bar
	140 °C	6.7		10.1		
Dissolved CO <sub>2</sub> Concentration*	100 °C	0.029	0.058	0.087	0.116	kmol/m <sup>3</sup>
	140 °C	0.058		0.087		
Temperature		100, and 140				°C
NaCl concentration		3				Wt.%
pH at the test temperature		4				
Note*: The dissolved CO <sub>2</sub> concentration was calculated as outlined in [298].						

### 6.3.4 Experimental setup

All experiments were carried out in the HT/HP test vessel constructed from UNS N10276. The lid of the vessel has pre-drilled ports for a working electrode (WE), a thermocouple for temperature control, gas inlet and outlet, a pressure gauge, the HT/HP reference electrode (RE), and the HT/HP pH electrode. The body of the vessel was used as a counter electrode (CE). A band heater was wrapped around the external body of the test vessel to increase the solution temperatures to 100 and 140 °C. All the electrochemical measurements of the corrosion process were performed using a computer controlled potentiostat (Gamry reference 600).

### 6.3.5 Electrochemical measurements

The corrosion behavior of UNS S31603 stainless steels was evaluated using electrochemical techniques. Firstly, OCP of the WE immersed in the test solution was recorded for 3 h. The pitting susceptibility of UNS S31603 stainless steels at different  $P_{CO_2}$  and different temperatures were performed using CP technique in accordance with ASTM G61-86 [184]. The potential was scanned from the OCP in a positive direction at a scan rate 0.167 mV/s until either the resulting current suddenly increased and exceeded 5 mA/cm<sup>2</sup> due to the breakdown of passive film and pitting corrosion occurred or the potential reach the pre-specified value with no sharp increase in current as no pitting took place. Afterward, the potential scan was

reversed in the negative direction to OCP to determine the repassivation potential of the materials. In addition, the passive film properties formed on UNS S31603 stainless steels were studied by the electrochemical impedance spectroscopy technique (EIS). The EIS technique was conducted in the frequency range from 10 kHz to 10 mHz with voltage amplitude of 10 mV.

## 6.4 Results and discussion

### 6.4.1 Open circuit potential measurements

The open circuit potentials of UNS S31603 stainless steels in 3 wt.% NaCl at different  $P_{\text{CO}_2}$  are depicted in Figure 6.1, as a function of time. The steady state potential was obtained after 3 h. At 100 °C and 2.6 bar  $P_{\text{CO}_2}$ , potential oscillation was evident during the first 2 h of immersion. Subsequently, steady OCP with a final potential of approximately -215 mV vs. Ag/AgCl was measured at 3 h. Increasing  $P_{\text{CO}_2}$  to 5 and 7 bar resulted in a reduced OCP but no potential oscillation was observed. At  $P_{\text{CO}_2}$  of 10.3 bar, the starting potential oscillated between -200 to -250 mV vs. Ag/AgCl which later markedly decreased to a steady value of about -413 mV vs. Ag/AgCl. High  $P_{\text{CO}_2}$  at a constant temperature of 100°C appears to decrease the OCP observed over the periods of 3 h exposure.

At 140 °C, the initial OCP shifted to a more negative value especially at 10.1 bar  $P_{\text{CO}_2}$  (Figure 6.2). OCP gradually rose in the first 1-1.5 h to reach steady values of -270 and -360 mV vs. Ag/AgCl for 6.7 and 10.1 bar  $P_{\text{CO}_2}$  conditions, respectively. Similar to what was observed at 100 °C, increasing  $P_{\text{CO}_2}$  and the corresponding dissolved  $\text{CO}_2$  led to a reduction in OCP.

The effect of  $P_{\text{CO}_2}$  on OCP in chloride containing solutions is consistent with the results reported for super-martensitic and duplex stainless steel alloys [299, 300]. Anselmo et al. have reported that the changes in corrosion potential of stainless steel alloys in the presence of  $\text{CO}_2$  is related to changes in passive film composition [299]. The destabilizing effect of  $\text{CO}_2$  on the passive film has been explained by the dehydroxylation of the outer part of the oxide film by the carbonic acid and an increase in ionic conductivity of the passive film. X-ray photoelectron spectroscopy (XPS) analysis of stainless steel passive film exposed to  $\text{CO}_2$  environment revealed that the surface film morphology contains many defects which act on blocking the diffusion process of the corrosive environment [17].

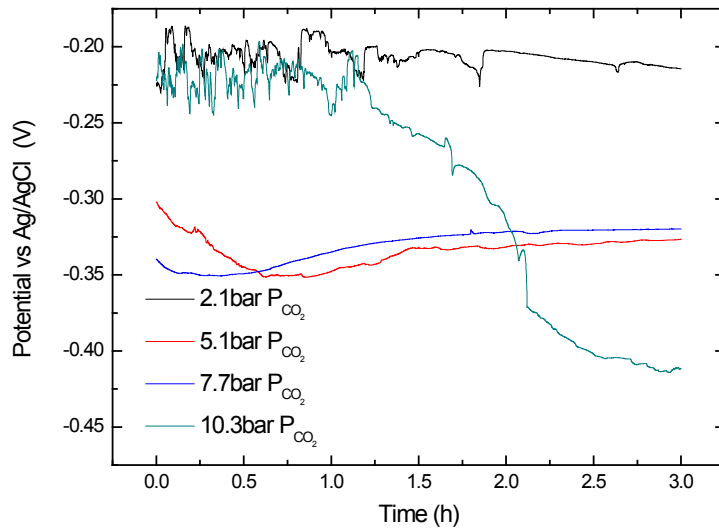


Figure 6.1 Open circuit potential of UNS S31603 stainless steels in 3wt.% NaCl at different CO<sub>2</sub> partial pressure at 100 °C

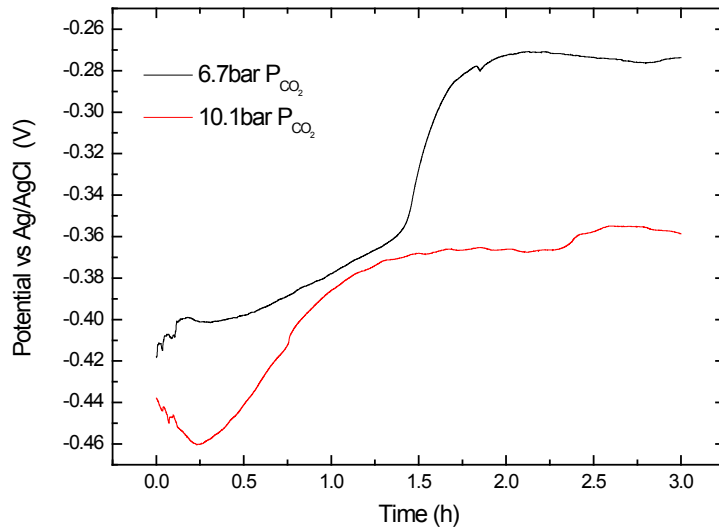


Figure 6.2 Open circuit potential of UNS S31603 stainless steels in 3wt.% NaCl at different CO<sub>2</sub> partial pressure at 140 °C

#### 6.4.2 Cyclic polarization technique

Figure 6.3 and Figure 6.4 show the cyclic polarization curves for UNS S31603 stainless steels in 3wt.% NaCl at different CO<sub>2</sub> partial pressure at 100 °C and 140 °C, respectively.

Hysteresis loops of various extents appear for all scenarios as denoted by larger current density in the reversed scan as compared to that in the forward one. The existence of these positive hysteresis loops indicates that the material was susceptible to passivation breakdown and, consequently, pitting corrosion [185].

At 100 °C, the pitting potential ( $E_{\text{pit}}$ ), the potential at which the sudden increase in current density takes place, decreases with increasing  $P_{\text{CO}_2}$  indicating that the material becomes more prone to the breakdown of the passive film, as shown in Figure 6.3. Another important feature that can be drawn from the cyclic polarisation curves is the repassivation potential ( $E_{\text{rep}}$ ) which can be determined as the potential at which the forward and backward scans meet. It is visible, particularly at 5.1 and 7.7 bar  $P_{\text{CO}_2}$ , that  $E_{\text{rep}}$  decreased with increasing  $P_{\text{CO}_2}$  substantiating that susceptibility to pitting corrosion increases with temperature. In addition, the passive current density increased with increasing  $P_{\text{CO}_2}$  as illustrated in Figure 6.3. This result demonstrates the enhanced metal dissolution suggesting that the passive film was less protective when  $P_{\text{CO}_2}$  was increased. The influence of  $P_{\text{CO}_2}$  on the pitting of SS316L in chloride solution has been related to the acceleration of cathodic reaction due to the high concentration of carbonic acid which could cause instability in the passive film [232, 299].

A similar observation was found at 140 °C. Passive current density increased with increasing  $P_{\text{CO}_2}$ . However, the difference in  $E_{\text{pit}}$  was minimal; i.e., -0.185 mV at 6.7 and -0.207 mV at 10.1 bar  $P_{\text{CO}_2}$ .

At pH 4, the presence of dissolved  $\text{CO}_2$  and undissociated carbonic acid ( $\text{H}_2\text{CO}_3$ ) are the primary change in the water chemistry of solutions saturated with  $\text{CO}_2$ . Because the pH in this study was kept constant at 4, the influence of pH on the pitting corrosion could be eliminated, and the observed pitting corrosion behavior was due to the effect of  $P_{\text{CO}_2}$  and temperatures. The cyclic polarization results presented here demonstrate the negative impacts of  $\text{CO}_2$  partial pressure and temperature on pitting susceptibility of stainless steel.

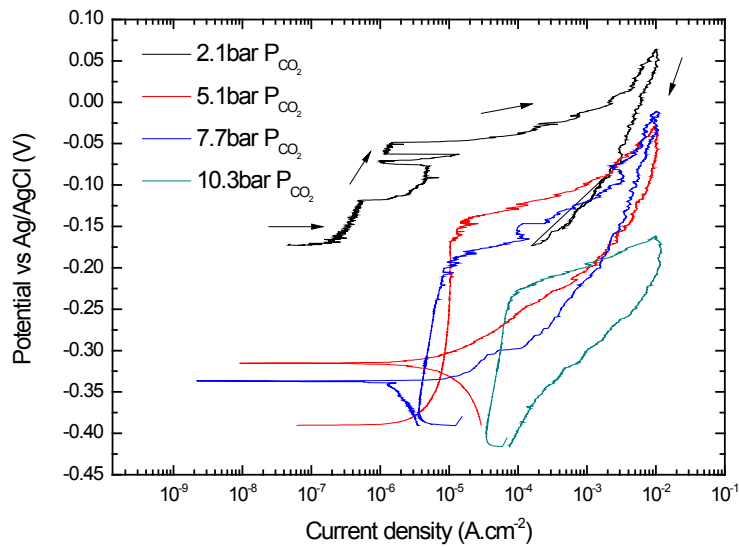


Figure 6.3 Cyclic polarization curves of UNS S31603 stainless steel in 3wt.% NaCl at different CO<sub>2</sub> partial pressure at 100 °C

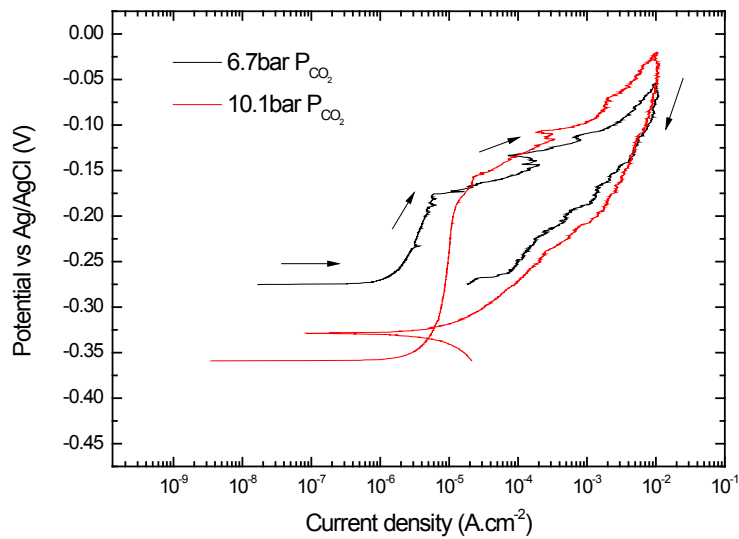


Figure 6.4 Cyclic polarization curves of UNS S31603 stainless steel in 3wt.% NaCl at different CO<sub>2</sub> partial pressure at 140 °C

### 6.4.3 Electrochemical impedance spectroscopy (EIS) technique

Figure 6.5 and Figure 6.6 shows the effects of  $P_{CO_2}$  on the Nyquist plots and the Bode plots for the passive films formed on UNS S31603 stainless steel at 100 and 140 °C, respectively. As shown in Figure 6.5 a, the Nyquist plots, composed of capacitive arcs with different radius in all different  $P_{CO_2}$ . As the previous study reported that as for corrosion resistance steel or alloys,

the radius of the semi-circular arc is related to the polarization resistance of the passive film [301]. It shows that the diameters of the capacitive loop decreased as the increasing of  $P_{CO_2}$  values particularly at 10.1 bar  $P_{CO_2}$ , indicating that the corrosion resistance of stainless steel decreased at high  $P_{CO_2}$  value. However, this effect is not clearly visible at 140 °C (Figure 6.6 a). The Bode plots clearly demonstrated two time constants and also agreed that modulus values and phase angles are strongly dependent on the  $P_{CO_2}$  values.

To quantify the changes in the passive film properties and corrosion behaviour of UNS S31603 stainless steel, the obtained EIS spectra were fitted with the selected electrical equivalent circuit shown in Figure 6.7. This model consists of a solution resistance ( $R_s$ ) connected in series with a parallel combination of ionic path resistance ( $R_{po}$ ) and a constant phase element ( $Z_{CPE}$ ) in parallel combination with charge transfer resistance ( $R_{ct}$ ) and a constant phase element ( $Z_{CPE1}$ ). This model considered that the passive film of stainless steel was already formed, and it could undergo changes in the microstructural and electrical properties [302, 303]. In addition, it assumed that the passive film was a homogeneous layer but rather as a defective layer.

In this equivalent circuit, the constant phase element (CPE) was used for the description of a non-ideal capacitance with varying  $\alpha$ . The impedance of the CPE is given by Equation 6.1

$$Z_{CPE} = Y_o \cdot (j\omega)^{-\alpha} \quad \text{Equation 6.1}$$

The factor  $\alpha$ , which is defined as a CPE power, always lies from 0 to 1. When  $\alpha = 1$ , the CPE describes an ideal capacitance. For  $0.5 < \alpha < 1$ , the CPE represents the distribution of the dielectric relaxation times in the frequency space, CPE represents a Warburg impedance ( $\alpha = 0.5$ ) and it also can represent resistance ( $\alpha = 0$ ). Previous literature reported that the CPE has been widely used for modeling frequency dispersion behaviour corresponding to different physical phenomena [304, 305].

After the values of  $Y_o$ ,  $R$  and  $\alpha$  are deduced from the equivalent circuit, the capacitance ( $C$ ) was calculated using the correlation shown in Equation 6.2 [201, 306].

$$C = \frac{(Y_o R)^{\frac{1}{\alpha}}}{R} \quad \text{Equation 6.2}$$

where  $R$  is resistance, ( $\Omega \text{ cm}^2$ ).

The selected model provided good fittings with the experimental data. Table 6.3 and Table 6.4 describe the fitting parameters based on the equivalent circuit showed in Figure 6.7. The value of CPE at both temperatures decreases when the  $P_{CO_2}$  value increases, suggesting an increase of defects in the passive film. The charge transfer resistance  $R_{ct}$  also decreased as  $P_{CO_2}$  changes from 2.1 to 10.3 bar at 100 °C and from 6.7 to 10.1 bar at 140 °C which reflected the reduction in the protectiveness of passive film at higher  $P_{CO_2}$ . The values of  $R_{po}$  obtained at 100 °C increased about 3 times when  $P_{CO_2}$  was increased from 2.1 to 10.3 bar. However, the values of  $R_{po}$  obtained at different temperatures are significantly smaller than  $R_{ct}$  values suggesting that the corrosion protection was predominantly provided by the inner layer passive film [204, 307]. As a result, increasing  $P_{CO_2}$  led to an increased susceptibility to film breakdown, which was shown previously using the cyclic polarization technique.

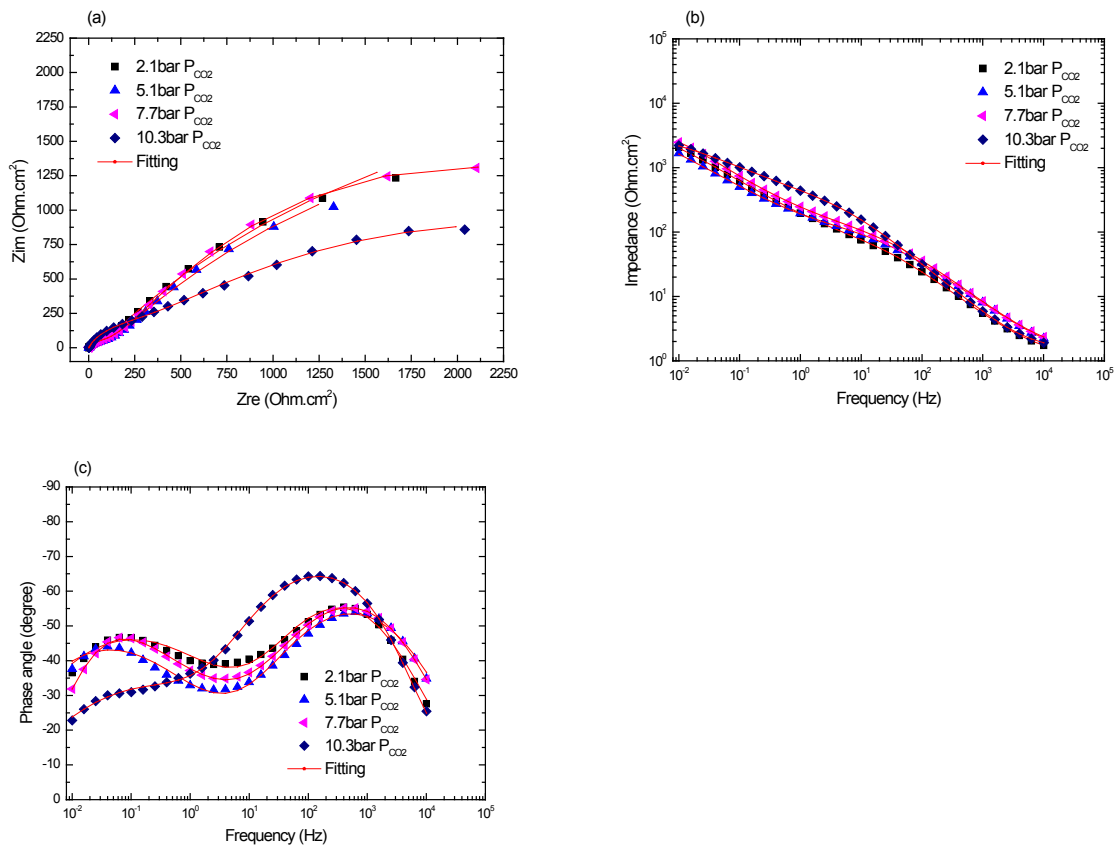


Figure 6.5 a) Nyquist plots and Bode diagrams b) variation of the impedance, and c) variation of the phase angle with the frequency of UNS S31603 stainless steel in 3wt.% NaCl and different  $P_{CO_2}$  at 100 °C.

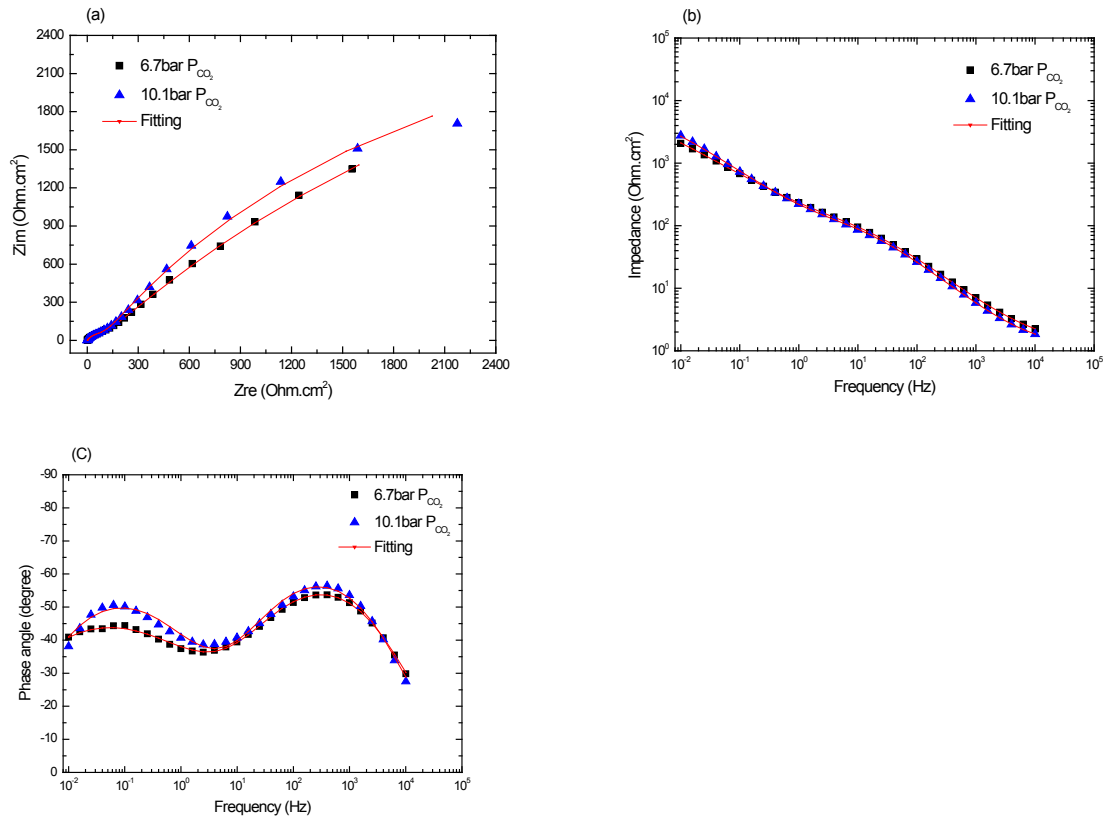


Figure 6.6 a) Nyquist plots and Bode diagrams b) variation of the impedance, and c) variation of the phase angle with the frequency of UNS S31603 stainless steel in 3wt.% NaCl and different  $P_{CO_2}$  at 140 °C.

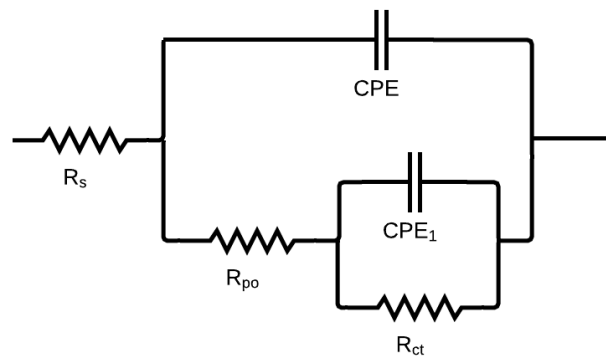


Figure 6.7 Two-time constant equivalent circuit for the fitting of EIS data

**Table 6.3 Electrical parameters obtained by fitting the EIS data for UNS S31603 stainless steel in 3wt.% NaCl and different  $P_{CO_2}$  at 100 °C.**

$P_{CO_2}$ (bar)	$R_s$ ( $\Omega\text{ cm}^2$ )	CPE ( $\Omega^{-1}\text{cm}^{-2}\text{s}^a$ )	$\alpha_1$	$R_{po}$ ( $\Omega\text{ cm}^2$ )	$C$ ( $\text{F cm}^{-2}$ )	$CPE_1$ ( $\Omega^{-1}\text{cm}^{-2}\text{s}^a$ )	$\alpha_2$	$R_{ct}$ ( $\Omega\text{ cm}^2$ )	$C_1$ ( $\text{F cm}^{-2}$ )
2.1	1.13	$3.37 \times 10^{-4}$	0.73	95.76	$9.46 \times 10^{-5}$	$1.87 \times 10^{-3}$	0.59	$6.67 \times 10^3$	$1.10 \times 10^{-2}$
5.1	1.09	$3.03 \times 10^{-4}$	0.70	122.50	$7.09 \times 10^{-5}$	$4.09 \times 10^{-3}$	0.64	$6.01 \times 10^3$	$2.56 \times 10^{-2}$
7.7	1.19	$2.76 \times 10^{-4}$	0.70	160.70	$7.31 \times 10^{-5}$	$1.58 \times 10^{-3}$	0.65	$5.13 \times 10^3$	$4.85 \times 10^{-3}$
10.3	1.45	$1.93 \times 10^{-4}$	0.78	348.60	$9.34 \times 10^{-5}$	$1.27 \times 10^{-3}$	0.51	$4.05 \times 10^3$	$6.32 \times 10^{-3}$

**Table 6.4 Electrical parameters obtained by fitting the EIS data for UNS S31603 stainless steel in 3wt.% NaCl and different  $P_{CO_2}$  at 140 °C.**

$P_{CO_2}$ (bar)	$R_s$ ( $\Omega\text{ cm}^2$ )	CPE ( $\Omega^{-1}\text{cm}^{-2}\text{s}^a$ )	$\alpha_1$	$R_{po}$ ( $\Omega\text{ cm}^2$ )	$C$ ( $\text{F cm}^{-2}$ )	$CPE_1$ ( $\Omega^{-1}\text{cm}^{-2}\text{s}^a$ )	$\alpha_2$	$R_{ct}$ ( $\Omega\text{ cm}^2$ )	$C_1$ ( $\text{F cm}^{-2}$ )
6.7	1.36	$3.36 \times 10^{-4}$	0.70	136.50	$9.08 \times 10^{-5}$	$4.78 \times 10^{-3}$	0.66	$8.74 \times 10^3$	$3.21 \times 10^{-2}$
10.3	1.20	$3.33 \times 10^{-4}$	0.73	138.50	$1.04 \times 10^{-4}$	$1.57 \times 10^{-3}$	0.60	$7.51 \times 10^3$	$2.6 \times 10^{-2}$

\* $C$  and  $C_1$  were calculated from CPE and  $R$  values according to Equation 6.2

## 6.5 Conclusions

The influences of  $P_{CO_2}$  on the corrosion properties of UNS S31603 stainless steel in 3wt.% NaCl at various temperatures were investigated by OCP, CP, and EIS. The main conclusions can be drawn below.

- 1- Increasing  $P_{CO_2}$  decreased the corrosion potential of UNS S31603 stainless steel at 100 and 140 °C.
- 2- UNS S31603 stainless steel became more prone to pitting corrosion and passive film breakdown with increasing  $P_{CO_2}$  as determined by the decrease in  $E_{pit}$  particularly at 100 °C.
- 3- The electrochemical impedance spectroscopy results revealed the change in the passive film formed on UNS S31603 stainless steel at different  $P_{CO_2}$  and temperatures. In addition, this harmful effect is intensified at higher temperatures. Therefore, the combined effect of these two factors decreased the protectiveness of the passive film formed on UNS S31603 stainless steel.

## Chapter 7: Electrochemical investigation of nitrite ions as a corrosion inhibitor at elevated temperature

### 7.1 Abstract

The ability of nitrite ( $\text{NO}_2^-$ ) corrosion inhibitors to protect carbon steel against corrosion in aerated conditions at high temperatures was investigated using weight loss measurements, cyclic polarization, and electrochemical impedance spectroscopy. The effects of chloride ions on nitrite inhibition were also investigated. The pH of the inhibited solutions was measured in-situ at high temperatures. The results showed that the corrosion resistance of carbon steel was improved by the addition of  $\text{NO}_2^-$  as evident by the reduction in weight loss corrosion rate and the combined results from electrochemical measurements. Further, the presence of 500 ppm chloride ion increased the susceptibility to localized corrosion in the form of pits, which was mitigated by the addition of 500 ppm  $\text{NO}_2^-$ .

**Keywords:** corrosion inhibitors, nitrite, carbon steel, Weight loss, cyclic polarization, electrochemical impedance spectroscopy

### 7.2 Introduction

In the oil and gas industry, corrosion represents a large portion of the total costs for companies every year worldwide [1]. In some cases, it can lead to recurrent partial and even total process shutdown. General and localized corrosion are the most common types of corrosion. The appropriate approach to corrosion control can avoid many potential disasters that can cause serious issues. Corrosion inhibitors are widely implemented as a corrosion prevention approach, and significant research activities have been conducted in this area [66, 308, 309]. Corrosion inhibitors are substances that, when introduced into a corrosive environment, reduce the corrosion rate of a metallic substrate [310].

Nitrite ( $\text{NO}_2^-$ ) is part of many commercially available inhibitor formulations used for corrosion protection of carbon steels in industrial applications [310, 311].  $\text{NO}_2^-$  has been widely applied to inhibit the localized corrosion of carbon steels [312]. The mechanism of the corrosion protection of  $\text{NO}_2^-$  is based on the formation of a protective (passive) surface film [313-315]. It is known that  $\text{NO}_2^-$  is equally effective in both aerated and deaerated aqueous environments [313]. The main effect of nitrite ions is to oxidize  $\text{Fe}^{2+}$  into  $\text{Fe}^{3+}$ . Its oxidizing action upon  $\text{Fe}^{2+}$  cations promotes the formation of maghemite ( $\gamma - \text{Fe}_2\text{O}_3$ ). Passivation of steel originates from

the oxidation of  $\text{Fe}^{2+}$  ions adsorbed on the surface. This leads to  $\text{Fe}^{3+}$  cations bound to the surface.

A variety of studies have been published addressing the inhibition effects of nitrite in chloride-free or in low chloride neutral or alkaline aqueous media conditions [315-319]. Dong et al. studied the effect of nitrite concentration on the corrosion behaviour of carbon steel pipelines in synthetic tap water and reported that the corrosion resistance was improved by adding nitrite as evidenced an increase in the corrosion potential ( $E_{\text{Corr}}$ ) and a decreased in the corrosion rate from 0.171 to 0.00171 mm/y. The authors suggested that nitrites improved corrosion resistance by forming a protective passive film [320]. Tosun mentioned that a 95% inhibition efficiency was achieved with 50 ppm nitrite in natural aqueous media containing 100 ppm NaCl [321]. Vazquez et al. studied the effects of  $\text{NO}_2^-$  on the passivation behaviour of steel in solutions containing  $\text{Cl}^-$  and reported that  $\text{NO}_2^-$  could inhibit the initiation and growth of pitting corrosion and accelerate repassivation of the steel surface [322]. Cohen suggested that in the presence of sodium chloride and sodium nitrite, corrosion products formed consisted of  $\gamma - \text{FeOOH}$  rather than  $\gamma - \text{Fe}_2\text{O}_3$  [323]. Competitive adsorption between chloride and hydroxyl ions was associated with poorly protective films.

Although nitrite ions are well known to be an effective corrosion inhibitor in a wide range of applications, the understanding of their inhibition behaviour at high temperatures and elevated pressures is still limited. The objectives of this study were, thus, to evaluate the protection of carbon steel by  $\text{NO}_2^-$  at different concentrations at high temperature conditions in the absence and presence of chloride. The effect of chloride ions on inhibition efficacy was evaluated using cyclic polarization (CP) and electrochemical impedance spectroscopy (EIS).

## 7.3 Experimental

### 7.3.1 Materials and specimen preparation

Two types of carbon steels were used in this study; UNS G101800 obtained from the field in a limited quantity and UNS G10300. The nominal compositions of both materials are shown in Table 7.1. As seen in Table 1, both materials differ mainly in their carbon content, but they were in a similar metallurgical condition.

#### 7.3.1.1 *Weight loss experiments*

Test specimens were prepared from a UNS G101800 cylinder shape (15 mm diameter by 3 mm thickness) with an exposed surface area of 1.7  $\text{cm}^2$ . The samples wet ground with sequentially

finer SiC papers from 120 to 600 grit, rinsed with ethanol (ethanol undenatured 100%, Chem-Supply Australia) and deionized (DI) water (Ibis Technology), and then dried with ultra-high purity N<sub>2</sub> gas (99.999% BOC Australia).

### 7.3.1.2 *Electrochemical experiments*

To perform the electrochemical experiments at 115 °C, a UNS G10300 tube-shape with an exposed ring surface of 0.22 cm<sup>2</sup> was pressed into polyether ether ketone (PEEK) to isolate them from any other electrical connections. All specimens were wet ground from 120 to 600 SiC grit and finally cleaned with ethanol, rinsed with DI water, and dried with high purity N<sub>2</sub>.

**Table 7.1. Nominal composition of UNS G101800 and UNS G10300 carbon steel used in this study**

Element	C	Si	Mn	P	S	Fe
UNS G101800 (wt. %)	0.17	0.23	0.85	0.01	0.02	Bal.
UNS G10300 (wt. %)	0.30	0.25	0.75	0.04	0.04	Bal.

### 7.3.2 Test solutions

The test solutions for both the weight loss experiments and electrochemical experiments were prepared from deionized (DI) water (Ibis solution resistivity 18 MΩ) and a nitrite based commercial corrosion inhibitor, which also contained a pH buffering agent. Zero grade compressed air (both supplied by BOC Australia). Table 7.2 summarizes all test conditions.

**Table 7.2. Summary of the test conditions**

Parameter	Weight loss corrosion tests	Electrochemical tests
Temperature (°C)	115	115
NO <sub>2</sub> <sup>-</sup> concentration (ppm)	0, and 700	0, 500, and 1100
NaCl concentration (ppm)	0	0 and 500
Total pressure (bar)	3.4 at 115 °C	3.4 at 115 °C

### 7.3.3 In-situ pH measurement

Figure 7.1 shows the UNS N10276 high pressure/ high temperature (HP/HT) Ag/AgCl reference electrode and the HP/HT ZrO<sub>2</sub> based pH electrode (Corr Instruments) used to measure the solution pH in-situ. A heating band connected to a controller and a thermocouple were used to heat and maintain the solution temperature in the vessel. 1 L of test solutions with varying concentrations of NO<sub>2</sub><sup>-</sup> was transferred to the pressure vessel. After the pressure vessel was sealed, the temperature of the solution was gradually raised the test temperature, after which the solution pH was checked and recorded.



Figure 7.1 a) High-Pressure Ag/AgCl reference electrode and b) High-Temperature and High- pressure ZrO<sub>2</sub> based pH electrodes

### 7.3.4 Experimental setups

Figure 7.2 shows the two types of pressure vessels used in this study; i.e., Figure 7.2 a illustrates the autoclaves used for immersion testing (Parr Instrument) for the weight loss analysis and Figure 7.2 b HP/HT electrochemical test cell. The Parr autoclave setup consisted of a thermocouple for temperature control, gas inlet, and outlet, a pressure gauge, and a rotating shaft with an internal volume of 2 L. The HT/HP cell used for electrochemical measurements was made of UNS N10276. The lid of the vessel had pre-set ports for the working electrode (WE), the HT/HP reference electrode (RE) (external pressure balanced reference probe Ag/AgCl electrode, 3 M KCl solution, Corr Instruments, LLC, USA) a thermocouple for temperature control, gas inlet and outlet, a pressure gauge, and the HT/HP pH electrode (ZrO<sub>2</sub>-based pH probe, Corr Instruments, LLC, USA). The body of the vessel was used as a counter electrode (CE). A band heater was wrapped around the external body of the test vessel to raise the solution temperatures to 115 °C.

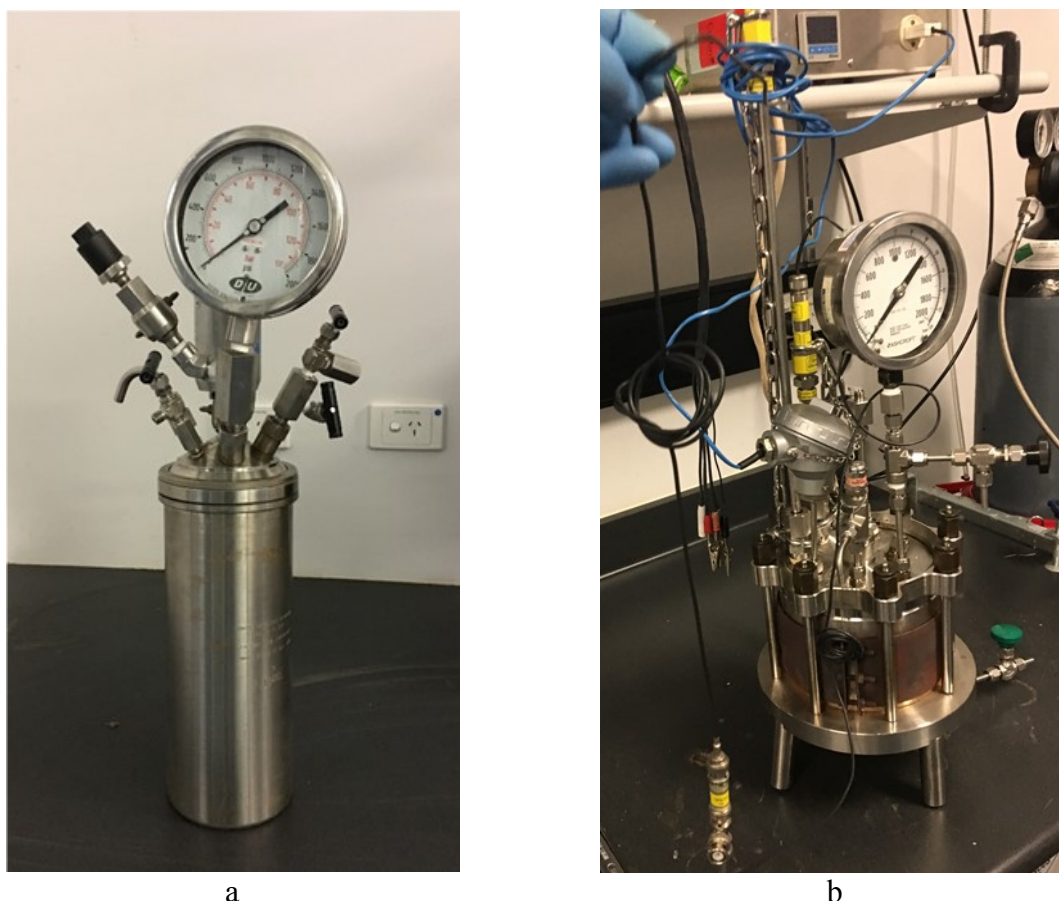


Figure 7.2 The experimental setup for a) immersion tests and b) electrochemical tests

### 7.3.5 Experimental procedure

For the weight loss measurements, three samples were weighed in an analytical balance and placed in the inert dish and, then, immersed in each solution of interest for 30 days. Right before testing, 1.5 L of the prepared solution was transferred using a peristaltic pump to the autoclave pre-sparged with the test gas for 6 h, and the pH recorded. The autoclaves were pressurized with the test gas to reach 3.4 bar at 115 °C. An impeller connected to the magnetic drive was rotated at 300 rpm for all tests.

After 30 days, the autoclaves were let cool down to room temperature before removing the samples. To determine the weight loss corrosion rate, Clarke's solution was used to remove adherent corrosion products according to the procedure described in ASTM G1[324]. Corrosion rates were calculated from the average weight loss of the samples in each solution. The samples were inspected using a surface profilometer ( Alicona G4) for evidence of localized corrosion.

For the electrochemical study, experiments were conducted at 115 °C in the HT/HP electrochemical cell. Immediately before testing, 1.5 L of the prepared solution was transferred

using a peristaltic pump to the pressure vessel pre-sparged with air. The solution was, then, heated to the test temperature of 115 °C with a total pressure 3.4 bar. After the test temperature was attained,  $E_{\text{Corr}}$  was monitored for 24 h. EIS was, then, performed from 10 kHz to 10 mHz with an amplitude of 10 mV. Finally, cyclic potentiodynamic polarization (CPP) was performed to determine the pitting susceptibility of UNS G10300 carbon steel under the test conditions using ASTM G61 as a guide [184]. CPP tests were performed by anodically polarizing the WE at a scan rate of 0.167 mV/s from  $E_{\text{Corr}}$ . The scan was reversed when the current density reached 10 mA/cm<sup>2</sup> and the test stopped at the cross-over potential or when attaining a new  $E_{\text{Corr}}$ . A computer-controlled potentiostat (Gamry reference 600) was used to acquire all the electrochemical data. All experiments were performed in duplicate.

## 7.4 Results and discussion

### 7.4.1 HP/HT pH measurements

Table 7.3 summarizes the variation of in-situ solution pH with  $\text{NO}_2^-$  concentration ( $c_{\text{NO}_2^-}$ ) at 115 °C. The solution pH increased with increasing corrosion inhibitor concentrations but decreased with increasing temperature. At 115 °C, the addition of 500 ppm  $\text{NO}_2^-$  increased the solution pH from 5.82 to 9.24. Further, increase  $c_{\text{NO}_2^-}$  to 1100 ppm resulted in a minor increase in pH to 9.58. At the same  $c_{\text{NO}_2^-}$ , the solution pH decreased with increasing temperature.

**Table 7.3 In-situ pH measurements at 115 °C**

$c_{\text{NO}_2^-}$ (ppm)	pH at 25 °C	pH at 115 °C
0	6.49	5.82
500	10.96	9.24
700	11.21	9.39
1100	11.76	9.58
1100 + 500 ppm NaCl	11.63	9.50

### 7.4.2 Weight loss measurements

Table 7.4 shows the effect of  $c_{\text{NO}_2^-}$  on the corrosion rate of UNS G101800 carbon steel after 30 days of immersion at 115 °C. The corrosion rate was the highest in the inhibitor-free case, which was, on average, 2.27 mm/y. Figure 7.3 a shows a photo of a UNS G101800 sample immersed in the baseline solution (0 ppm  $\text{NO}_2^-$ ) for 30 days. As seen in Figure 7.3 a, a thick and darkish-brown deposit covered most of the surface. After cleaning the samples with Clarke's solution, severe surface roughening due to metal dissolution was visible, Figure 7.3 b.

The dominant corrosion products at the current condition (115°C) was suggested to be ferric hydroxide  $\text{Fe}(\text{OH})_3$  or  $\text{Fe}_2\text{O}_3 \cdot n\text{H}_2\text{O}$ , which was non-protective [325]. Bornak also indicated that the transition from hydroxide to a protective form of oxide (magnetite,  $\text{Fe}_3\text{O}_4$ ) occurred at 121 °C (250 °F). Several studies have shown that magnetite ( $\text{Fe}_3\text{O}_4$ ) is a thermodynamically stable corrosion product at a temperature range greater than the current study [325-327].

In the presence of the corrosion inhibitor, the weight loss corrosion rate was greatly reduced to 0.002 mm/y. Figure 7.4 show optical microscopic images of the samples immersed in 700 ppm  $c_{\text{NO}_2^-}$  at 115 °C. It was clear from the appearance of the surface after exposure that  $\text{NO}_2^-$  effectively inhibited uniform and localized corrosion of carbon steel at the high temperature of the tests. This behaviour was attributed to the tendency of  $\text{NO}_2^-$  to promote surface passivation which is a characteristic of an anodic inhibition [310, 313].

**Table 7.4 the effect of different nitrite concentrations on the corrosion rate of UNS G101800 carbon steel after 30 days immersion at 115 °C**

Temperatures (°C)	$c_{\text{NO}_2^-}$ (ppm)	Weight loss corrosion rate (mm/y)
115	0	2.27
	700	0.002



a



b

Figure 7.3 UNS G101800 (a) before and (b) after corrosion product removal. The samples were immersed in the baseline solution (0 ppm  $\text{NO}_2^-$ ) at 115 °C for 30 days

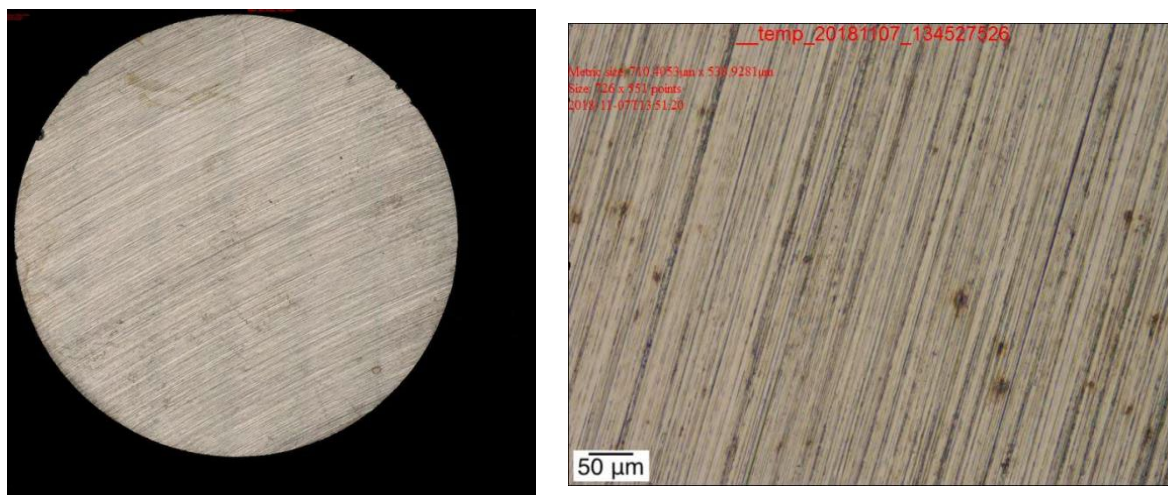


Figure 7.4 Microscope image of a sample UNS G101800 immersed in 700 ppm  $\text{NO}_2^-$  solution at 115 °C for 30 days after cleaning with Clarke solution

### 7.4.3 Electrochemical measurements

#### 7.4.3.1 Chloride-free solutions

The effects of  $c_{\text{NO}_2^-}$  on the inhibition performance were further evaluated using CPP testing performed on UNS G10300 samples after 24 h immersion. Figure 7.5 a shows cyclic potentiodynamic polarization curves at three  $\text{NO}_2^-$  concentrations (i.e., 0, 500, and 1100 ppm) at 115 °C. In the absence of  $\text{NO}_2^-$ , a negative hysteresis loop was obtained, suggesting the absence of localized corrosion, in agreement with the uniform corrosion observed in the 4-week immersion experiments (Figure 7.4). The in-situ pH was measured to be 5.82. In the presence of a nitrite-based corrosion inhibitor equivalent to 500 and 1100 ppm  $\text{NO}_2^-$ , a negative hysteresis loop was also obtained, but there was a sharp increase in current density at a potential range between 0 to 0.2  $\text{V}_{\text{Ag}/\text{AgCl}}$ . The greater current density was measured in the case with  $\text{NO}_2^-$  present. The appearance of active/passive region may imply the electrochemical reaction of passive film formation,[314] which could be associated with the action by  $\text{NO}_2^-$  or by a rise in pH. The resistance to pitting attack as determined from the CPP curves is supported by the lack of localised corrosion evidenced from the optical images shown in Figure 7.5 b to d.

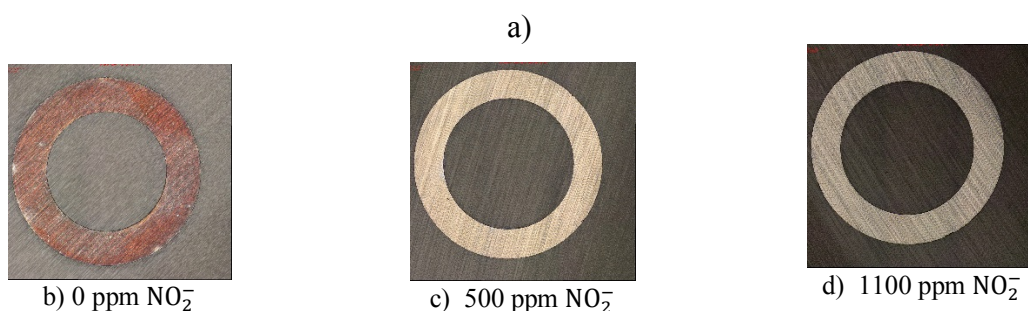
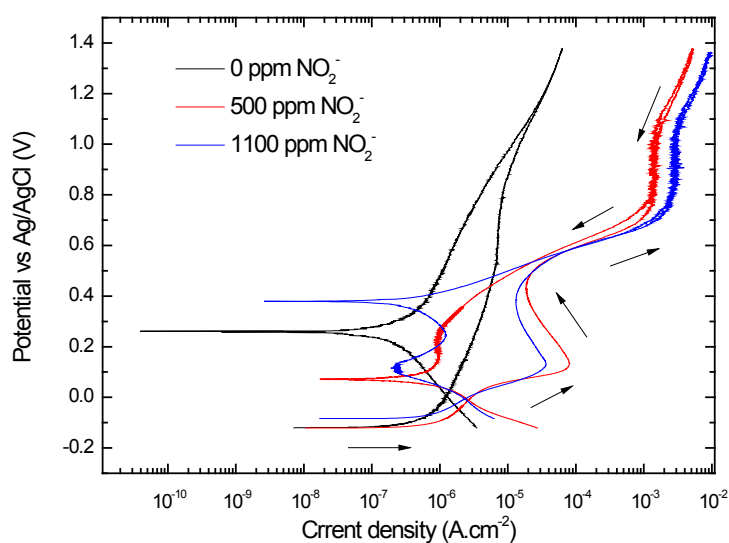


Figure 7.5 a) Cyclic polarization curves and b) to d) optical microscopic images of UNS G10300 samples in solutions with varying concentrations of  $\text{NO}_2^-$  after cyclic polarisation experiments at 115 °C.

### 7.4.3.2 Chloride-containing solutions

#### 7.4.3.2.1 Corrosion potential measurements

Figure 7.6 shows the time evolution of  $E_{\text{Corr}}$  of UNS G10300 samples in solutions containing 0, 500, and 1100 ppm  $\text{NO}_2^-$  and 500 ppm NaCl at 115 °C.  $E_{\text{Corr}}$  initially increased with time and reached steady values after approximately 5 h. In the absence of  $\text{NO}_2^-$ , the steady-state  $E_{\text{Corr}}$  was  $-58 \text{ mV}_{\text{Ag}/\text{AgCl}}$ . The addition of 500 ppm  $\text{NO}_2^-$  shifted  $E_{\text{Corr}}$  to  $-8 \text{ mV}_{\text{Ag}/\text{AgCl}}$ . However,  $E_{\text{Corr}}$  decreased to  $-78 \text{ mV}_{\text{Ag}/\text{AgCl}}$  when increasing  $c_{\text{NO}_2^-}$  to 1100 ppm.

The reduction in  $E_{\text{Corr}}$  appears to be contradictory to previously published studies. Khani measured approximately 100 mV and 200 mV increase in  $E_{\text{Corr}}$  following a 1 mM (46 ppm) and 9 mM (414 ppm)  $\text{NO}_2^-$  addition at 25 °C [328]. Mohana et al. also observed a gradual increase in  $E_{\text{Corr}}$  with respect to  $\text{NO}_2^-$  at 30 to 55 °C. The authors associated this behaviour with the formation of passive film promoted by  $\text{NO}_2^-$  [329].

The lack of OCP trend with respect to  $c_{\text{NO}_2^-}$  observed in this study might be associated with high temperature conditions and at high pH that could also promote the formation of the surface film [330, 331].

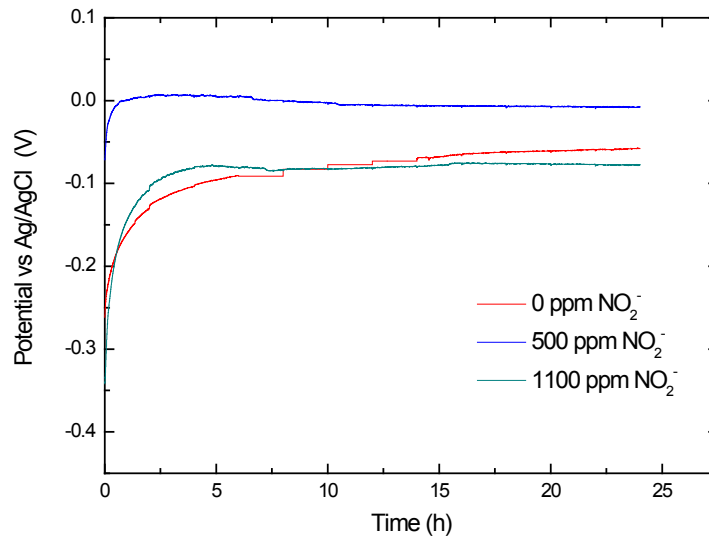


Figure 7.6 Open circuit potential of UNS G10300 samples in solutions containing 0, 500, and 1100 ppm  $\text{NO}_2^-$  and 500 ppm NaCl at 115 °C

#### 7.4.3.2.2 Cyclic polarization

It has been discussed in the previous section that the addition of  $\text{NO}_2^-$  corrosion inhibitor led to an increase in pH and passive film formation. Both of which affected the corrosion behaviour of UNS G10300. Therefore, it was necessary to distinguish between these effects. Figure 7.7 a shows cyclic potentiodynamic polarization curves of UNS G10300 in inhibitor-free solutions containing 500 ppm NaCl at 115 °C with and without pH adjustments, as indicated. 1 M NaOH was used to adjust the solution pH to 11 at room temperature. It can be seen that the polarization curves exhibited a positive hysteresis loop in both pH values. Nonetheless, without the pH adjustment, the anodic scan did not exhibit an active/passive transition. Current density abruptly increased marking the pitting potential to be +0.6  $V_{\text{Ag}/\text{AgCl}}$ . At pH 11, the active/passive transition was visible. The drop in current density observed between 0.2 to 0.6  $V_{\text{Ag}/\text{AgCl}}$  could be attributed to the electrochemical reaction associated with the oxide formation at high temperatures. The positive hysteresis evident in the reverse scan indicated that the oxide film formed at high pH conditions but in the absence of  $\text{NO}_2^-$  was not protective. Localized corrosion (pitting and crevice) attack can be seen from the optical micrographs shown in Figure 7.7 b and c.

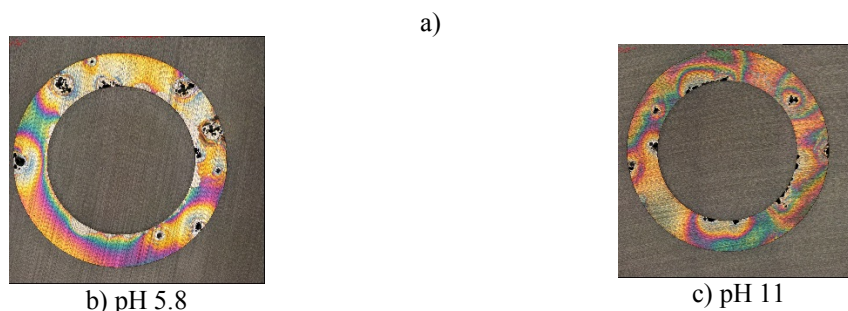
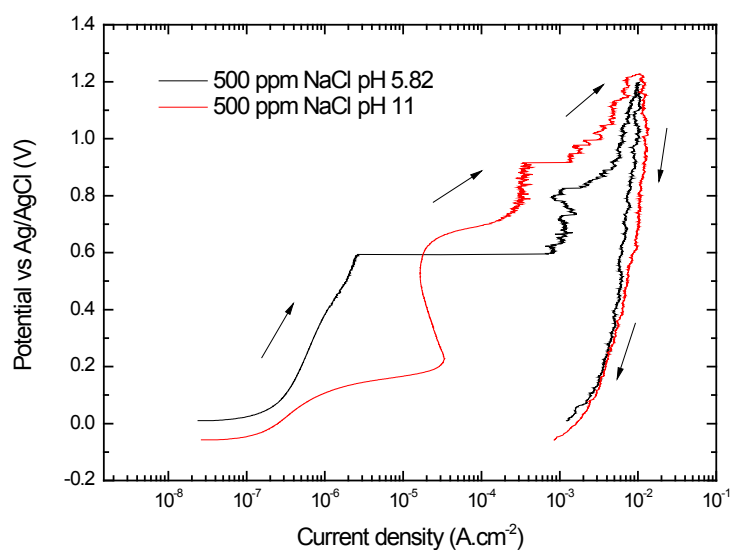


Figure 7.7 UNS G103000 a) Cyclic polarization curves and b) & c) light optical micrographs in a solution containing 500 ppm NaCl at 115 °C at different pH values.

Figure 7.8 a shows the CP curves of UNS G10300 samples in solutions containing 0, 500, and 1100 ppm  $\text{NO}_2^-$  and 500 ppm NaCl at 115 °C. In the case of the uninhibited solution (0 ppm  $\text{NO}_2^-$  with 500 ppm NaCl, pH adjusted 11 with NaOH), it can be seen that the curve exhibited a positive hysteresis loop. The pitting potential was +0.92  $V_{\text{Ag}/\text{AgCl}}$  and the repassivation potential was lower than the initial  $E_{\text{Corr}}$ , indicating that UNS G10300 was prone to localized corrosion at 115 °C. The large hysteresis loop indicated that the formed pits could not repassivate after scan reversal [332]. When 500 ppm and 1100 ppm nitrite ions were added, the curves showed negative hysteresis loops, which can be attributed to the propensity of nitrite ions to promote a protective oxide film that suppressed pitting attack. Therefore, the results showed that the passive film formed on UNS G10300 promoted by  $\text{NO}_2^-$  became more resistant to localized corrosion when nitrite ions were added to the solution. The critical inhibitor concentration was 500 ppm.

The ratio between  $\text{NO}_2^-$  and chloride concentration investigated in this study was 1:1 and 2.2:1 by ppm or 0.77:1 and 1.70:1 by mol/L. The inhibition against pitting corrosion could be achieved at the  $[\text{NO}_2^-]/[\text{Cl}^-]$  of 1:1 by ppm.

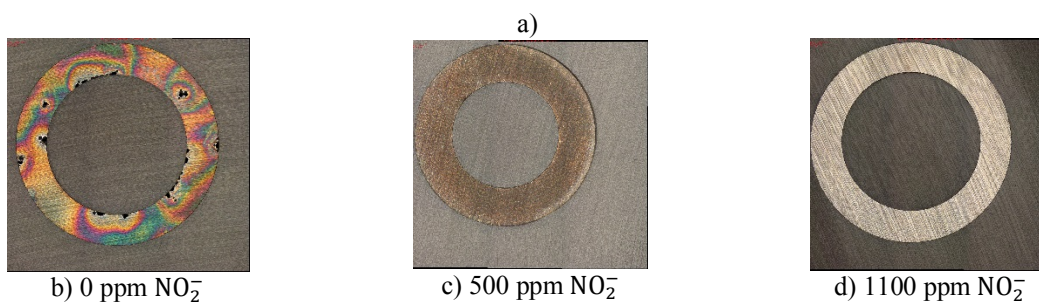
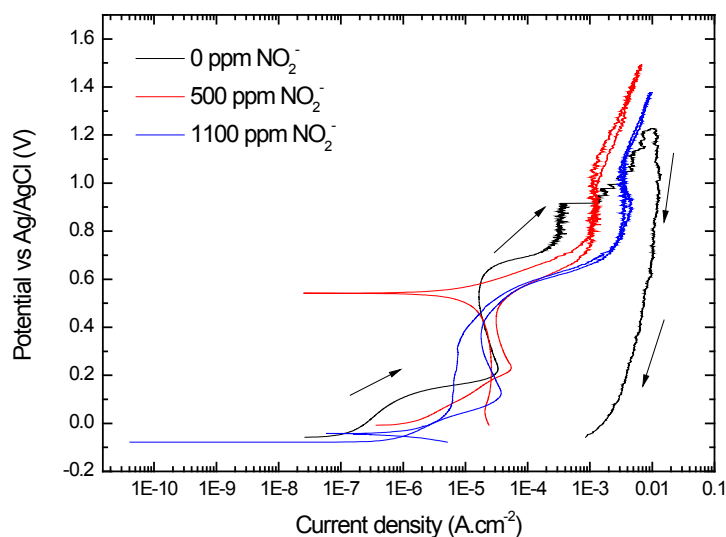


Figure 7.8 a) Cyclic polarization curves and b) to d) optical microscopic images of UNS G10300 samples in a solution containing different  $\text{NO}_2^-$  concentrations with 500 ppm NaCl at 115 °C.

#### 7.4.3.2.3 Electrochemical impedance spectroscopy

Figure 7.9 presents the Nyquist and Bode plots obtained on UNS G10300 at 115 °C in different  $c_{\text{NO}_2^-}$ , as indicated. The Nyquist plots in Figure 7.9a showed incomplete semicircles with their magnitudes graphically indicate the faradaic impedance values [333]. The depression observed in the Nyquist plots was associated with the non-ideal behavior of capacitors in a corroding environment [334].

In Bode plots, electrochemical behavior with respect to frequency could be revealed. The Bode phase plots shown in Figure 7.9 c showed two time constants. The high frequency time constant was associated with the defects in the oxide film while that at low frequency was attributed to the electrochemical processes occurring at the metal/electrolyte interface [334].

The equivalent circuit consisting of two-time constants as shown in Figure 7.10 was used to fit EIS spectra obtained in this study. This equivalent circuit consists of solution resistance ( $R_s$ ) is in series with the parallel combination of the dielectric strength of the oxide film and the adsorbed water ( $C$ ) and ionic paths resistance ( $R_{po}$ ) of the oxide film which is in series with the parallel combination of the capacitance developed by the electrical double layer at the metal/electrolyte interface ( $C_l$ ) and charge transfer resistance ( $R_{ct}$ ) of the. Due to the non-ideal behavior of capacitors resulted in the depressed semicircles, a constant phase element (CPE) is often used to replace the capacitor to improve the fitting. The impedance of this element is defined as shown in Equation 7.1 [335-337].

$$Z_{CPE} = \frac{1}{Y_o (j\omega)^\alpha} \quad \text{Equation 7.1}$$

where  $Y_o$  is CPE constant ( $\Omega^{-1}\text{cm}^{-2}\text{s}^\alpha$ ),  $\omega$  is the angular frequency (rad /s),  $j^2 = -1$  is the imaginary number and  $\alpha$  is the CPE exponent, so CPE can represent resistance if  $\alpha = 0$ , ideal capacitance if  $\alpha = 1$  [265] .

The CPE was converted into capacitance ( $C$ ) using the correlation shown in Equation 7.2 previously proposed in the literature [201].

$$C = \frac{(Y_o R)^\frac{1}{\alpha}}{R} \quad \text{Equation 7.2}$$

where  $R$  is resistance ( $\Omega \text{ cm}^{-2}$ ).

The validity of the selected equivalent circuits can be seen in Figure 7.9 where lines representing the predictions from equivalent circuits agree well with markers representing experimental values. Table 7.5 reports the EIS parameters from the fitting data described above.  $R_s$  values decreased with the increase  $c_{NO_2^-}$  due to increased concentration of ionic species and consequently, solution conductivity.  $R_{po}$  increased by an order of magnitude ( $10^2$  to  $10^3 \text{ ohm.cm}^2$ ) when  $NO_2^-$  was present indicating that protectiveness of the oxide film induced by  $NO_2^-$  was superior to the native oxide formed naturally at high temperature and high pH. This could explain the localized corrosion behaviour observed in the cyclic polarization tests.  $R_{ct}$  values have the same order of magnitude regardless of  $c_{NO_2^-}$  suggesting the passive film remains protective.  $R_{po}$  values have a small magnitude compared with  $R_{ct}$  implying that the corrosion protection was provided by the inner layer passive film.

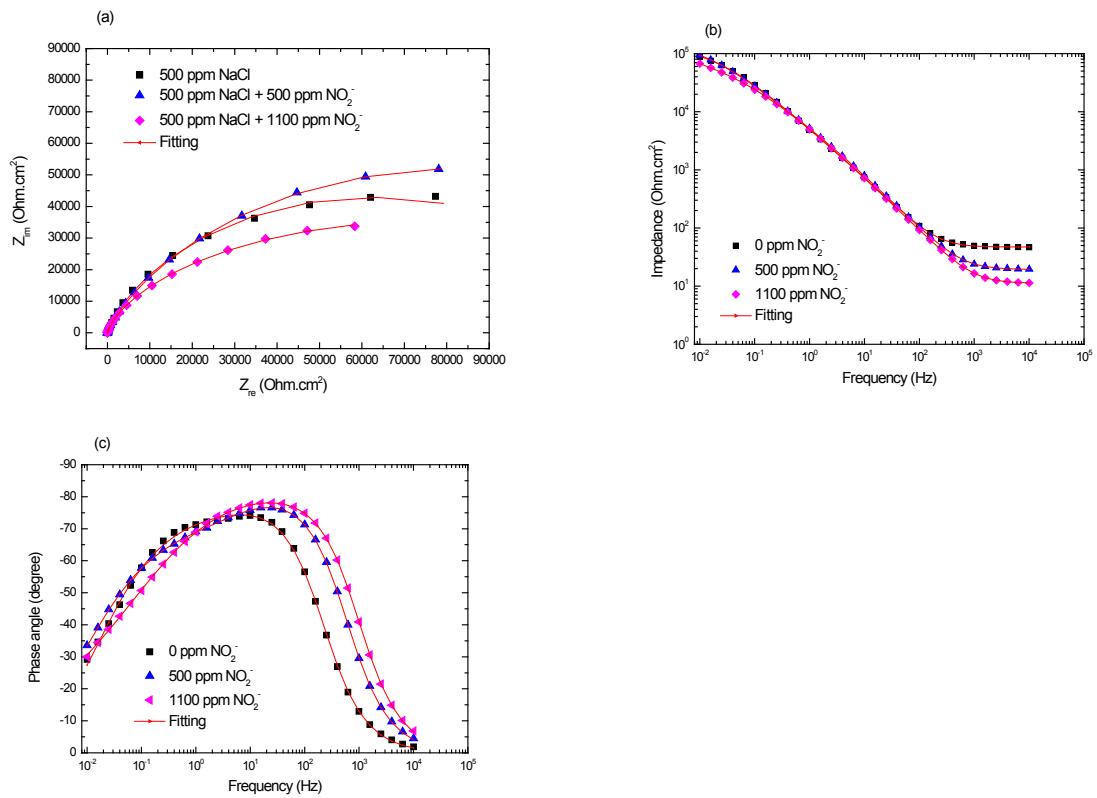


Figure 7.9 a) Nyquist, b) Bode impedance, and c) Bode phase angle plots of UNS G10300 samples in 500 ppm NaCl and different  $\text{NO}_2^-$  concentrations at 115 °C. Initial solution pH was 11.

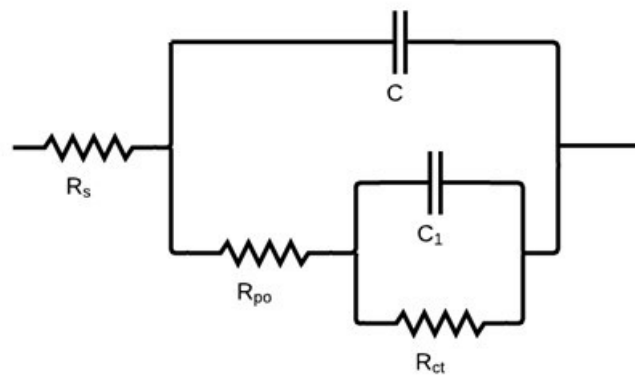


Figure 7.10 Two-time constant equivalent circuit for the fitting of EIS data

Table 7.5. Electrical parameters obtained by fitting the EIS data for UNS G10300 samples in 500 ppm NaCl and different NO<sub>2</sub><sup>-</sup> concentrations at 115 °C, pH 11

$c_{\text{NO}_2^-}$ (ppm)	$R_s$ ( $\Omega \text{ cm}^2$ )	$\text{CPE}_1$ ( $\Omega^{-1} \text{ cm}^{-2} \text{ s}^\alpha$ )	$\alpha_1$	$R_{po}$ ( $\Omega \text{ cm}^2$ )	$C$ ( $\text{F cm}^{-2}$ )	$\text{CPE}$ ( $\Omega^{-1} \text{ cm}^{-2} \text{ s}^\alpha$ )	$\alpha_2$	$R_{ct}$ ( $\Omega \text{ cm}^2$ )	$C_1$ ( $\text{F cm}^{-2}$ )
0, pH 11	47.16	$2.09 \times 10^{-5}$	0.96	617	$1.74 \times 10^{-5}$	$2.68 \times 10^{-5}$	0.65	$1.32 \times 10^5$	$5.29 \times 10^{-5}$
500	19.27	$2.76 \times 10^{-5}$	0.92	$5.87 \times 10^3$	$2.36 \times 10^{-5}$	$2.62 \times 10^{-5}$	0.60	$1.67 \times 10^5$	$7.01 \times 10^{-5}$
1100	11.17	$2.84 \times 10^{-5}$	0.92	$1.19 \times 10^3$	$2.12 \times 10^{-5}$	$2.90 \times 10^{-5}$	0.42	$1.77 \times 10^5$	$2.78 \times 10^{-4}$

\*C and C<sub>1</sub> were calculated from CPE and R values according to Equation 7.2

## 7.5 Conclusions

The present study investigated the effects of nitrite ions on the corrosion inhibition of carbon steel in the absence and presence of chloride solution at high temperature; i.e. 115 °C. The conclusions below were drawn from results obtained from weight loss measurements and electrochemical methods.

- 1- In the absence of NO<sub>2</sub><sup>-</sup>, carbon steel suffered severe uniform corrosion. The average weight loss corrosion rate was 2.27 mm/y, which is excessively high.
- 2- Corrosion rates of carbon steel significantly decreased from 2.27 to 0.005 mm/y with the presence of NO<sub>2</sub><sup>-</sup> concentrations.
- 3- Negative hysteresis loops indicated that passive film formed on UNS G10300 became more resistant to localised corrosion when nitrite ions were added to the solution as determined by the cyclic polarization.
- 4- In the absence of chloride ions and both in the presence and the absence of nitrite, corrosion proceeded uniformly. However, the tendency for localized corrosion increased with the presence of 500 ppm chloride ions as determined from cyclic polarization tests and visual inspection.
- 5- Pitting corrosion was mitigated by the addition of 500 ppm NO<sub>2</sub><sup>-</sup>.

## Chapter 8: Conclusions and Recommendations

### 8.1 Conclusion

Based on the experimental results reporting in this thesis, the following conclusions were made; regarding the study of the relationship between the passive film properties formed on UNS S31600 Stainless steel in relatively mild CO<sub>2</sub> environments and the susceptibility to pitting corrosion at different temperatures (30 °C - 80 °C) as well as different NaCl concentrations (3 wt.% - 8 wt.%) at 30 °C, the results revealed that the pitting susceptibility of UNS S31600 stainless steel increases with increasing temperature and NaCl concentration. In addition, the passive film properties are influenced by temperature as well as NaCl concentration as identified by EIS technique. Inhomogeneity in the passive film was shown by the presence of 2 time constant at a temperature greater than 40 °C and charge carrier density determined by Mott-Schottky analysis which increases with increasing temperature and NaCl concentrations indicating the weakening of the passive film.

To compare the corrosion behavior and passive film properties formed on UNS S31600 Stainless steel in CO<sub>2</sub> and N<sub>2</sub> environments and how it influences the susceptibility to pitting corrosion. The results have shown that the passive film formed on UNS S31600 consists of 2 layers in both environments. The outer passive layer becomes porous as temperature increases in the presence of CO<sub>2</sub>. No porous layer was found on the passive film formed in N<sub>2</sub> environment for the temperatures tested. CO<sub>2</sub> and temperature synergistically increase the pitting susceptibility of UNS S31600 stainless steel. In addition, x-ray photoelectron spectroscopy analysis indicates that the variation in the elemental composition of the passive films, and a higher concentration of metal hydroxides (potentially Cr(OH)<sub>3</sub>) is observed as temperature increases particularly in the presence of CO<sub>2</sub>.

To elucidate the influence of high-temperature high pressure and NaCl concentrations on pitting corrosion of UNS S31600 stainless steel in a CO<sub>2</sub> environment simulating to the oil and gas production systems. Results reveal a synergistic effect of high temperatures and high NaCl concentration on the change in the passive layer structure. As the temperature increases, the defects in the passive film formed on the UNS S31600 stainless steel increase and make it more heterogeneous. In addition, this harmful effect is intensified at higher NaCl concentrations. Therefore, the combined effect of these factors decreases the protectiveness of the passive film. Whereas, Mott-Schottky results have shown that the donor and acceptor densities appear to be unaffected by the increasing temperatures to the same extent as increased NaCl concentrations.

To highlight the effect of different CO<sub>2</sub> partial pressure on the passive film formed on UNS S31600 stainless steel at different temperatures. The coexistence of CO<sub>2</sub>, NaCl, and temperatures can decrease the corrosion resistance of UNS S31600 stainless steel. Results show that the CO<sub>2</sub> partial pressure significantly decreases the corrosion potential, indicating that CO<sub>2</sub> partial pressure plays an indisputably major role in the stability of the metal surfaces in chloride environments. The cyclic polarization technique confirms greater pitting susceptibility of UNS S31600 stainless steel with increasing CO<sub>2</sub> partial pressure at different temperatures. The increment of CO<sub>2</sub> partial pressure increases the defects on the passive film and makes it more heterogeneous. In addition, this harmful effect is intensified at higher temperatures. Therefore, the combined effect of these two factors decreases the protectiveness of the passive film formed on UNS S31600 stainless steel.

In connection with the investigation of the corrosion behavior and passive film properties formed on UNS S31600 Stainless steel in different environmental condition and how it influences the susceptibility to pitting corrosion compared with the effect of temperature on the corrosion rate and the protective layer formed on carbon steel at different corrosion inhibitor concentrations. Results reveal that the carbon steel suffered severe uniform corrosion in the absence of corrosion inhibitor (NO<sub>2</sub><sup>-</sup>). The immersion test results indicate that the corrosion rate of carbon steel decreases with increasing the inhibitor concentration. In addition, the inhibition activity increases with the increase of nitrite concentration. The action of nitrite based corrosion inhibitor is due to the oxidation of iron ion to form Fe<sub>2</sub>O<sub>3</sub> on the carbon steel surface. In the presence and the absence of nitrite and absence of chloride ions, corrosion proceeded uniformly. However, the tendency for localized corrosion increased with the presence of 500 ppm chloride ions as determined from cyclic polarization tests and visual inspection.

Finally, it can be concluded from the research presented in this thesis that the results of UNS S31600 Stainless steel in a deoxygenated CO<sub>2</sub> environment are not dissimilar in behavior expected in the oxygen-rich environments. Moreover, there is a synergistic effect of temperature and CO<sub>2</sub> on the change in the passive film structure formed on UNS S31600 Stainless steel especially at high temperatures as well as at high NaCl Concentrations. The corrosion rates of UNS S31600 Stainless steel depend significantly on the partial pressure of CO<sub>2</sub>. Furthermore, the corrosion rates of carbon steel decrease with increasing the inhibitor concentration due to the oxidation of iron ion to form Fe<sub>2</sub>O<sub>3</sub> on the carbon steel surface.

## **8.2 Recommendations for future work**

The following suggestions can be considered or to be examined for future work:

- 1- It is interesting that the results for UNS S31600 stainless steel in a deoxygenated CO<sub>2</sub> environment are not dissimilar in behavior expected in oxygen rich environments which has been the focus on much more research.
- 2- Studying the localized corrosion behavior of UNS S31600 stainless steel by using different electrochemical techniques and investigate the best stability of the passive film that will be formed on UNS S31600 stainless steel for different parameters.
- 3- Studying the characteristics of the passive film formed on the surface of UNS S31600 stainless steel and carbon steel at different stages of exposure, as well as the re-passivation kinetics.
- 4- Studying the influence of flow rate on the characterization and mechanisms of corrosion product layers from CO<sub>2</sub> corrosion of UNS S31600 stainless steel in simulated oilfield solution.

## **Appendix 1: High temperature corrosion inhibition performance and thermal stability of nitrite-based corrosion inhibitor**

### **1 Abstract**

The thermal stability and performance of a nitrite-based corrosion inhibitor at inhibiting corrosion of carbon steel UNS G10180 were investigated at high temperature (i.e., up to 230 °C) and high pressure (i.e., 27 barg). Four-week immersion tests were conducted to evaluate the influences of temperature, inhibitor concentrations, and oxygen partial pressure. The nitrite corrosion inhibition mechanism and its performance were assessed using gravimetric analysis, optical microscopy, scanning electron microscopy, and energy X-ray spectroscopy (SEM/EDS), X-ray diffraction spectroscopy (XRD), and X-ray photoelectron microscopy (XPS). The inhibition performance was affected by the temperature and the reduction in residual nitrite concentration associated with thermal degradation. XRD and XPS results showed that the surface film primarily consisted of Fe<sub>3</sub>O<sub>4</sub> and, to a lesser extent, Fe<sub>2</sub>O<sub>3</sub> and oxyhydroxide FeOOH.

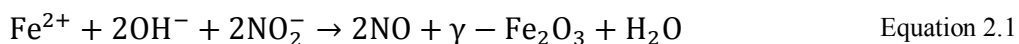
**Keywords:** carbon steel, corrosion inhibitor, nitrite, high temperature

### **2 Introduction**

Monoethylene glycol (MEG) is widely used as a thermodynamic hydrate inhibitor for natural gas production and transportation due to its low toxicity, low flammability, and its ability to be regenerated, which results in a long-term economic advantage over other hydrate inhibitors [308, 338]. The regeneration process involves the removal of excess water by means of water evaporation to achieve MEG concentration in a range of 80-90%. The heat supplied to MEG recovery units comes from a closed-loop heating medium system, which generally operates at a temperature between 120–160 °C [339]. The closed-loop heating medium system is constructed of carbon steel through which deionized water is circulated. Hence, the system can be prone to corrosion. Corrosion risks of the heating medium loop are managed by suppressing the concentration of dissolved oxygen and chloride ions together with the addition of a corrosion inhibitor.

In this case, a nitrite-based corrosion inhibitor was selected for the heating medium system. Nitrite is an effective inorganic corrosion inhibitor that has a wide range of applications, i.e., closed loop water circulation [328, 340, 341], concrete admixture [342-344], etc. It has been

proposed that nitrite ions convert ferrous to ferric ions which then facilitates the formation of passive film on carbon steel. In alkaline solutions, nitrites promote the formation of a stable passive film promoted by the reaction shown in Equation 2.1[328]. This passive film has been characterized to be a combination of magnetite ( $\text{Fe}_3\text{O}_4$ ) and maghemite ( $\gamma - \text{Fe}_2\text{O}_3$ ). The passive film has been shown to be approximately 2 nm thick [345].



Khani studied the effect of nitrite concentration and temperature [328]. The author found that at 25 °C, the optimum nitrite concentration was 9 mM (302 mg/L) in a solution containing 5 mM chloride (172.5 mg/L). The performance of nitrite ions is reduced in the presence of chloride. It was proposed that competitive adsorption between chloride and hydroxyl group at the metal surface led to the formation of soluble iron (II)chloride. Cohen reported that, in the presence of chloride,  $\gamma - \text{FeOOH}$  is formed rather than magnetite [323].

The efficiency of nitrite at reducing the corrosion rate can be improved by the presence of coinhibitors such as molybdate ion. Mustafa and Dulal reported that nitrite promoted the formation of an oxide layer where molybdate can preferentially adsorb. This created a negatively charged surface which, according to the authors, prevented the deleterious effect by aggressive anions in the solutions [318]. A synergistic effect between nitrite and borax has also been reported [329].

Despite their high inhibition efficiency, localized corrosion is the main risk associated with anodic corrosion inhibitors, which can occur when the inhibitor concentration falls below a critical value. Lee et al. showed pitting corrosion when the nitrite concentration was reduced from 200 ppm to 100 ppm at 50 °C [320]. A further reduction in nitrite concentration resulted in uniform corrosion.

A reduction in the inhibitor concentration could arise due to the thermal oxidation and loss in the process. The residual nitrite concentration could decrease over time as nitrite is used to sustain passivity (Equation 2.1). Limited information is available regarding nitrite degradation. Rey suggested that in the presence of air ingress, nitrite could oxidize to form nitrate [340]. Thermal decomposition of the molten sodium nitrite was studied. No by-product from the decomposition process could be detected at 260 °C and below [346]. Nitrite was found to be stable in water at temperatures up to 150 °C [347]. Nitrite degradation was promoted when the

medium contained monoethylene glycol (MEG). Madera speculated that the glycol degradation products as those of volatile fatty acids aid nitrite degradation [347].

At present, corrosion studies have focused on temperatures below 100 °C. Information related to nitrite corrosion inhibition performance and the degradation behavior at high temperatures is still lacking. Therefore, the purposes of this work were to investigate the corrosion behavior of carbon steel in the presence and the absence of a nitrite-based corrosion inhibitor at high-temperature and high-pressure conditions simulating a heating medium circuit. The possible corrosion inhibition mechanisms were evaluated by a combination of immersion tests and surface characterization techniques. Characterization techniques included scanning electron microscopy and energy dispersive X-ray spectroscopy (SEM/EDS), X-ray diffraction spectroscopy (XRD), and X-ray photoelectron spectroscopy (XPS). Finally, laboratory results were validated with the field data.

### **3 Experimental procedure**

#### **3.1 Materials and solution**

UNS G101800 carbon steel rods were machined into 3 mm thick coin-shape specimens with a 15 mm diameter.

Test solutions consisted of deionized (DI) water (Ibis solution resistivity 18 M $\Omega$ ) and NO<sub>2</sub><sup>-</sup> containing a commercial corrosion inhibitor to achieve 0, 500, 700, and 1100 ppm NO<sub>2</sub><sup>-</sup> concentrations. Zero grade compressed air (both supplied by BOC Australia) was used in this study. A 500 ppm aliquot of analytical grade citric acid (C<sub>6</sub>H<sub>8</sub>O<sub>7</sub>) which is used as cleaning in place solution for the close-loop heating circuit pipes was added into the test solutions to evaluate its effect on NO<sub>2</sub><sup>-</sup> degradation and corrosion inhibition performance.

#### **3.2 Immersion tests**

Four-week immersion tests were conducted in 2-L Parr autoclaves fitted with a rotating shaft and an impeller for agitation, a gas sparging tube, a thermowell (for inserting a thermocouple), a gas outlet, and a liquid sampling port.

Three carbon steel samples were wet ground with SiC paper to 600 US-grit, rinsed with ethanol, and dried with high purity N<sub>2</sub>. Samples were weighed in an analytical balance to a 0.1 mg readability and subsequently placed in a non-metallic and inert dish (polyether ether ketone –

PEEK), which was then positioned at the bottom of the autoclave. The test solution (1.5 L) was purged with the test gas for a minimum of 6 h and subsequently transferred to an autoclave, which was continuously purged with the test gas, with a peristaltic pump to avoid disturbance to the samples.

The autoclave was, then, tightened and pressurized with the test gas to a total pressure of approximately 3 bar prior to heating up to the desired test temperature. The selected test temperature mimicked 2 heating loops operating at 115 and 230 °C. After the test temperature was attained, the total pressure at 115 and 230 °C was adjusted to 3.4 bar and 28 bar, respectively. The dissolved oxygen concentration was calculated to be 9.65 ppm (5.4 μM) at 115 °C, 3.4 bar total pressure and 5.96 ppm (3.35 μM) at 230 °C, 28 bar total pressure [348]. The rotational speed was set to 300 rpm for all tests.

### **3.3 Post-test analysis**

#### **3.3.1 Water analysis**

After 2 weeks, an aliquot of approximately 300 mL of the test solution was drawn from each autoclave to measure pH ex-situ and analyze for  $\text{NO}_2^-$  and  $\text{NO}_3^-$  concentration using the calorimetric method.

#### **3.3.2 Weight loss and localized corrosion**

Two carbon steel samples were cleaned using Clarkes solution (20 g  $\text{Sb}_2\text{O}_3$ , 50 g  $\text{SnCl}_2$ , and 1 L conc. HCl as described in ASTM G1 [349]) and visually inspected using a surface profilometer and a light optical microscope for evidence of pitting corrosion.

#### **3.3.3 Surface characterization**

One carbon steel sample for each condition was kept for the following surface characterization:

Field emission scanning electron microscope (FESEM), Mira-3.

X-ray Diffraction spectroscopy (XRD), Bruker D8 Discover XRD.

X-ray photoelectron spectroscopy (XPS), Kratos AXIS Ultra DLD - system.

## 4 Results and discussion

### 4.1 Immersion tests

Table 6 presents weight loss corrosion rates and photographs of carbon steel samples exposed to various  $\text{NO}_2^-$  concentrations at 115 and 230 °C. Maximum pit depths are reported where localized corrosion was observed.

In the absence of the corrosion inhibitor, the baseline corrosion rates were 2.27 and 0.047 mm/y at 115 and 230 °C, respectively. The corrosion product layer appeared thicker on the samples exposed to 115 °C than those formed at 230 °C. However, the corrosion product formed without the corrosion inhibitor provided no corrosion protection to the underlying steel substrates. At 115 °C, severe uniform corrosion was evident, while at 230 °C pitting corrosion was found (Figure 11a and b).

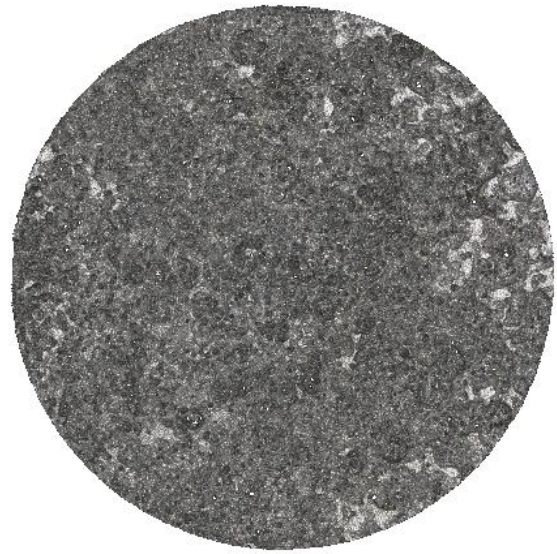
In the presence of the corrosion inhibitor, weight loss corrosion rate decreased to below 0.01 mm/y except in the experiment with non-neutralized citric acid where corrosion rate was 0.05 mm/y. No visible oxide film could be detected. The surface discoloration was observed on samples exposed to 230 °C. Pitting corrosion was not apparent, i.e., pit depth was not quantifiable by profilometry and light optical microscopy (LOM) (Figure 12). It can be deduced from the immersion tests that the nitrite-based corrosion inhibitor at the concentrations used provided effective corrosion protection at both 115 °C and 230 °C.

**Table 6 Weight loss corrosion rates, pit depth (if found and quantifiable), and photographs of carbon steel samples after immersion tests**

Test No.	Temperature (°C)	Test gas	NO <sub>2</sub> <sup>-</sup> (ppm)	Citric acid (ppm)	Weight loss corrosion rate (mm/y)	Pit depth (μm)	Photographs of carbon steel samples after tests.
1	230 °C	Air	0	0	0.047	32	
2			700		0.005	ND	
3			700	500 <sup>(1)</sup>	0.003	ND	
4			1100	0	0.001	ND	
5	115 °C	Air	0	0	2.27	ND	
6			700		0.002	ND	
7			700	500 <sup>(1)</sup>	0.001	ND	
8			700	500 <sup>(2)</sup>	0.05	8	
Note 1: neutralized with NaOH. Note 2: non-neutralized.							



a)



b)

Figure 11 LOM images of samples exposed to DI water at a) 230 °C and b) 115 °C after cleaning with Clarke solution

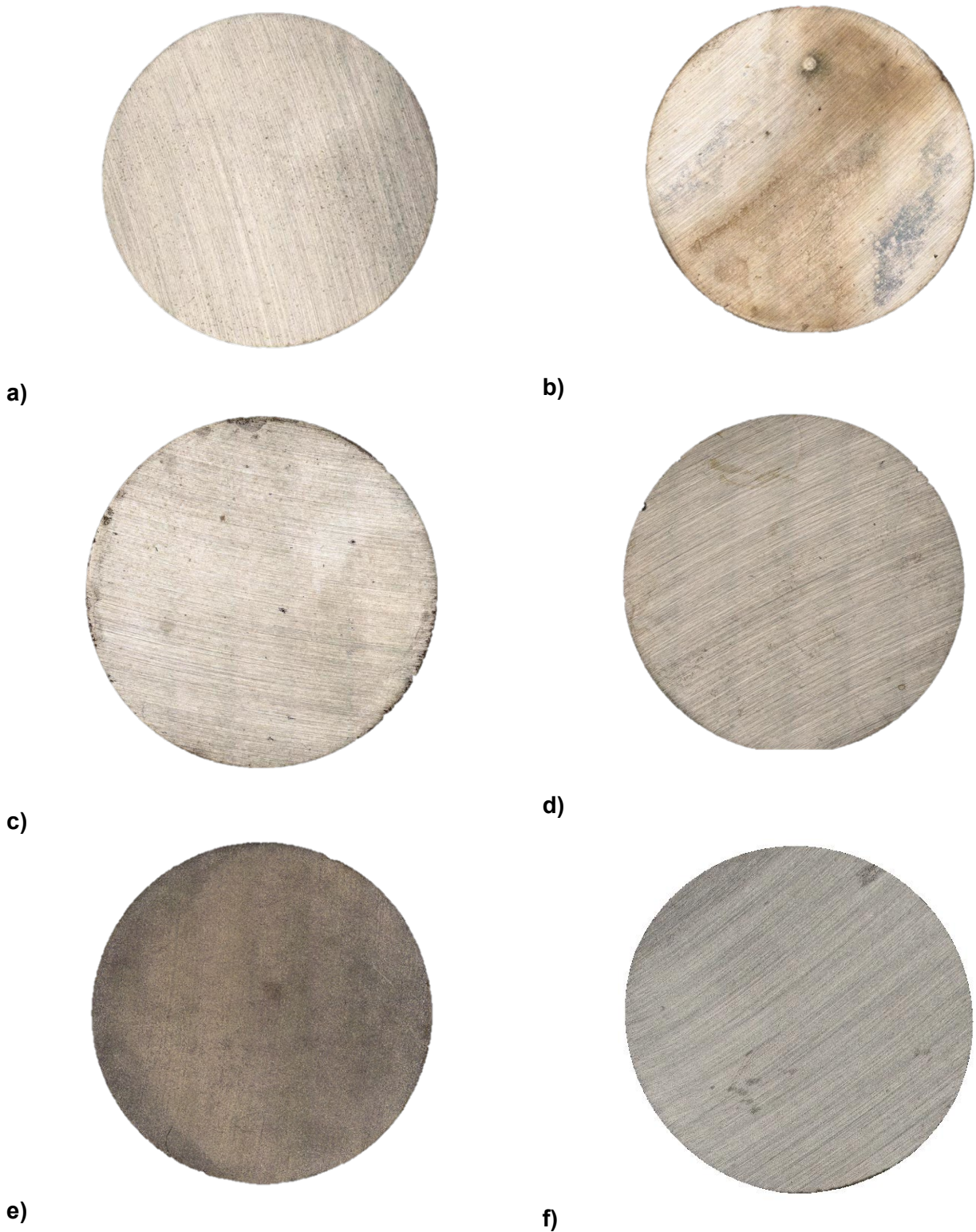


Figure 12 LOM images of samples exposed to inhibited-DI water at a) 230 °C, 700 ppm  $\text{NO}_2^-$ ; b) 230 °C, 700 ppm  $\text{NO}_2^-$  with neutralized citric acid, c) 230 °C, 1100 ppm  $\text{NO}_2^-$ , d) 115 °C 700 ppm  $\text{NO}_2^-$ ; e) 115 °C, 700 ppm  $\text{NO}_2^-$ , with non-neutralized citric acid after cleaning with Clarke solution

## 4.2 Water analysis

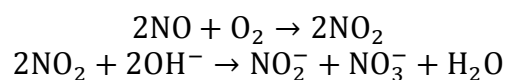
The changes in solution chemistries after the exposure are reported in Table 7. Except Test 8 where non-neutralized citric acid was used, pH decreased after the initial 2-week exposure. The decrease in pH may be due to the formation of magnetite and maghemite at high temperatures. Tomlinson proposed a series of electrochemical steps associated with magnetite formation at the oxide/water interface [350]. The process involved the diffusion of  $\text{Fe}^{2+}$  through the oxide layer to form intermediate species (namely  $\text{Fe}(\text{OH})_2$  and  $\text{FeOH}^+$ , which then further hydrolyze to form magnetite and hydrogen ions. In addition, the formation of a passive film induced by  $\text{NO}_2^-$  appears to involve the consumption of hydroxyl ions, which could also lead to the reduction in pH (Equation 2.1).

$\text{NO}_2^-$ , and  $\text{NO}_3^-$  concentrations before and after exposure are also reported in Table 7. The  $\text{NO}_2^-$  concentration decreased in all test scenarios. The decrease in  $\text{NO}_2^-$  concentration from 2 to 4 weeks seemed to slow down from its initial drop. The reduction in  $\text{NO}_2^-$  concentration could be partly explained by the passive film formation (Equation 2.1) leading to a decrease in the bulk  $\text{NO}_2^-$ . Cohen detected the reduction in  $\text{NO}_2^-$  anions only in the experiments containing steel, while the  $\text{NO}_2^-$  concentration remained unchanged in the control experiment without a steel [351].

Additionally, since  $\text{NO}_3^-$  was detected in the solution, the oxidation of  $\text{NO}_2^-$  (Equation 4.1) may have occurred. The  $\text{NO}_2^-$  oxidation reaction was found to be a function of the solution pH. Significant degradation occurred at strong acidic condition (pH 1) whereas in an alkaline condition (pH 13), no evidence of  $\text{NO}_2^-$  oxidation was found [344]. In the current study, the pH of the solutions varied from 8 to 10 (Table 7). Therefore,  $\text{NO}_2^-$  oxidation might not be significant in the current conditions.



Other potential reactions that could take place in the presence of dissolved oxygen are Equation 4.2 and Equation 4.3 [344]. The NO byproduct from the passive film formation (Equation 2.1) reacts with the dissolved oxygen to form  $\text{NO}_2$  that further reacts with  $\text{OH}^-$  to form  $\text{NO}_2^-$  and  $\text{NO}_3^-$ .



Equation 4.2

Equation 4.3

Regardless of the reaction pathways, the residual  $\text{NO}_2^-$  concentration was sufficient to provide corrosion protection to carbon steel.

**Table 7 pH,  $\text{NO}_2^-$ , and  $\text{NO}_3^-$  concentrations analysis of test solutions before and after exposure**

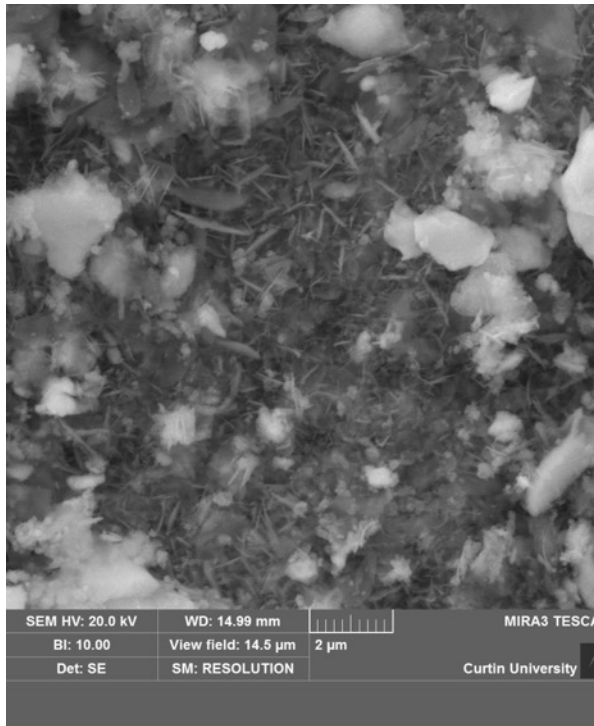
Test No.	Temp. (°C)	Test gas	$\text{NO}_2^-$ (ppm)	Citric acid (ppm)	pH			$\text{NO}_2^-$ (ppm)		$\text{NO}_3^-$ (ppm)	
					Initial	2 wk	4 wk	2 wk	4 wk	2 wk	4 wk
1	230	Air	0	0	6.66	4.32	4.51	-	-	-	-
2			700	0	11.43	7.37	8.63	395	265	130	160
3			700	500 <sup>(1)</sup>	11	8.81	9.05	265	175	62	110
4			1100	0	11.66	8.81	8.6	430	450	250	390
5	115	Air	0	0	6.45	-	-	-	-	-	-
6			700	0	11.35	10.67	10.63	660	620	60	30
7			700	500 <sup>(1)</sup>	11	9.32	9.11	365	435	100	190
8			700	500 <sup>(2)</sup>	5.25	6.95	7.15	590	560	100	160

Note 1: neutralized with NaOH.  
Note 2: non-neutralized.

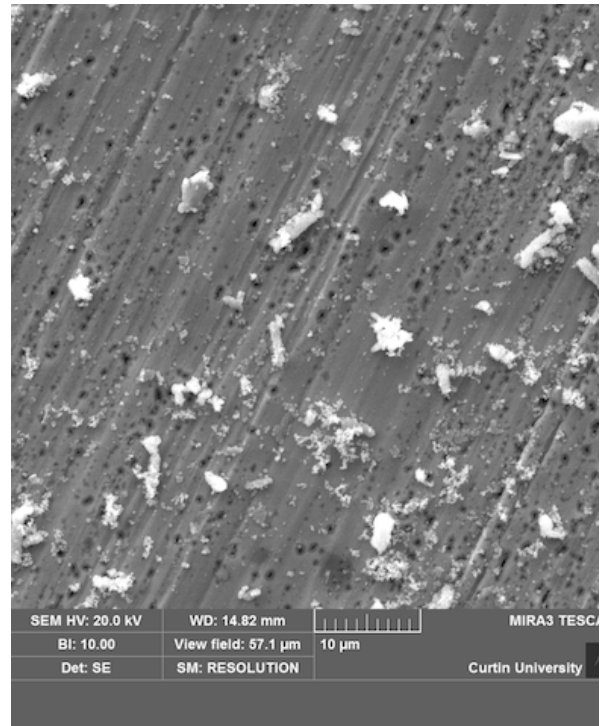
## 5 Corrosion product characterization

### 5.1 Scanning Electron Microscopy (SEM)

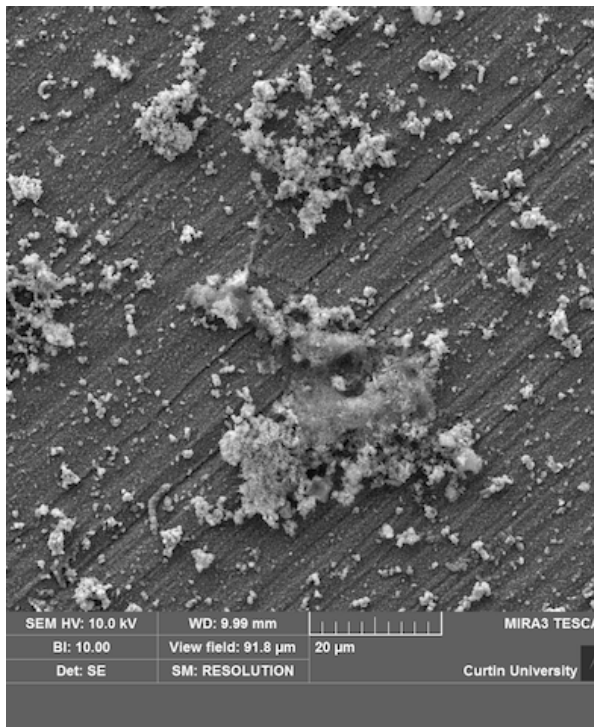
SEM images from samples exposed to 230 and 115 °C are shown in Figure 13 and Figure 14, respectively. In the absence of the corrosion inhibitor, surface precipitates were visible. At 230 °C and in the presence of the corrosion inhibitor, surface films were not found and polishing marks remained visible. A similar surface appearance, i.e., visible polishing marks, was observed in the presence of 700 ppm  $\text{NO}_2^-$  with and without citric acid. Increasing the corrosion inhibitor further to 1100 ppm  $\text{NO}_2^-$  appeared to facilitate plate-like surface film formation. At 115 °C, samples exposed to the inhibited solution had similar appearances, i.e., no visible corrosion products and clear polishing marks.



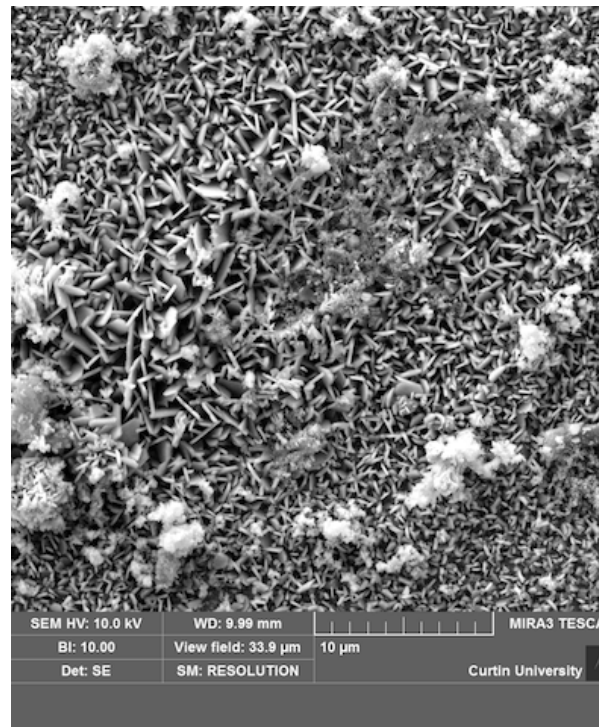
a) Baseline (0 ppm)



b) 700 ppm  $\text{NO}_2^-$

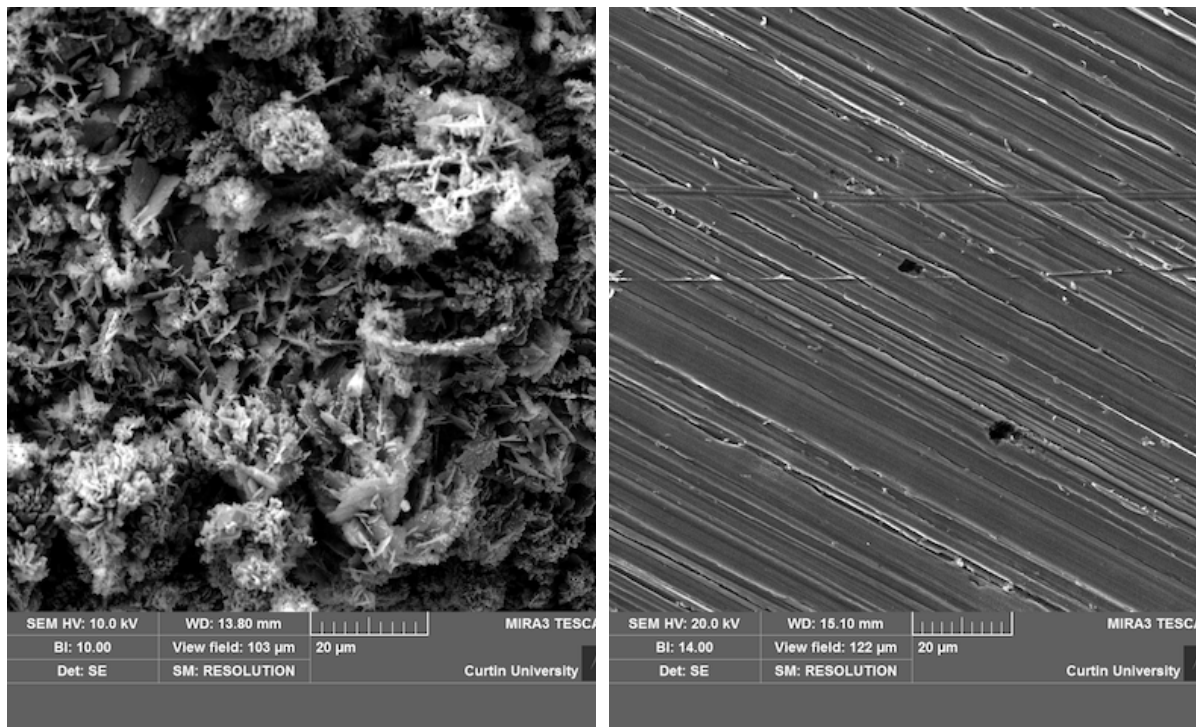


c) 700 ppm  $\text{NO}_2^-$  (with citric acid) neutralised



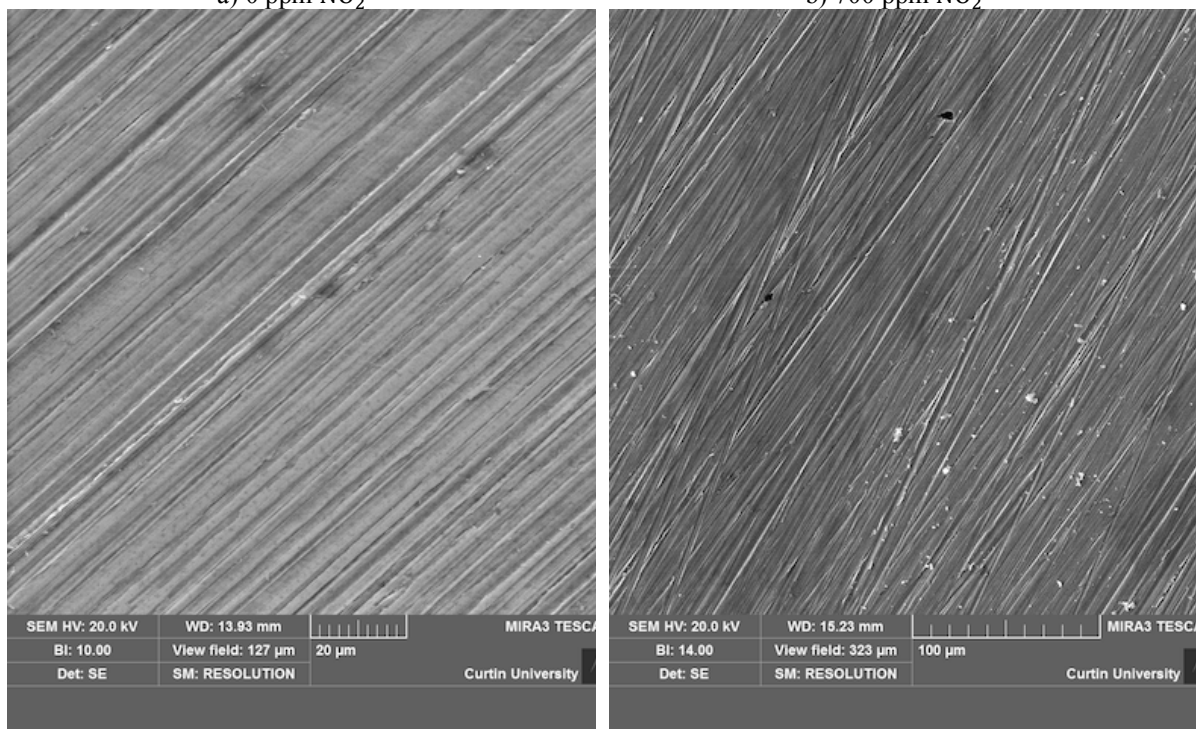
d) 1100 ppm  $\text{NO}_2^-$

Figure 13 Secondary Electron (SE) SEM images of carbon steel UNS G10180 samples after a 4-week exposure in DI-water containing various corrosion inhibitor concentrations at 230 °C



a) 0 ppm  $\text{NO}_2^-$

b) 700 ppm  $\text{NO}_2^-$



c) 700 ppm  $\text{NO}_2^-$  + 500 ppm citric acid (non-neutralised)

d) 700 ppm  $\text{NO}_2^-$  + 500 ppm citric acid (neutralised).

Figure 14 Secondary Electron (SE) SEM images of carbon steel UNS G10180 samples after 4-week exposure in deionized water containing various corrosion inhibitor concentrations at 115 °C

## 5.2 X-ray diffraction

X-ray diffraction patterns of corrosion products formed on carbon steel surfaces exposed to selected conditions are presented in Figure 15.

At 230 °C and 115 °C, without the corrosion inhibitor, the surface film primarily consisted of magnetite ( $\text{Fe}_3\text{O}_4$ ). Corrosion behavior of carbon steel in the temperature range experienced in high temperature aqueous systems has been reported [325, 331]. Corrosion product mainly observed is magnetite ( $\text{Fe}_3\text{O}_4$ ). Bornak proposed that under aerated conditions at high temperatures ferric hydroxide forms, which further dehydrated to ferric oxide [325]. On the other hand, magnetite precipitates under deaerated conditions, leading to localized corrosion where the magnetite layer is locally damaged. In this study, the corrosion products formed at 230 °C were more protective than those formed at 115 °C according to weigh loss corrosion rates (Table 6). The formation of protective  $\text{Fe}_3\text{O}_4$  was facilitated at high temperatures, which provided corrosion protection against uniform corrosion. However, it is widely accepted that imperfect passivity often leads to localized corrosion [352]. This correlates well with the surface profile of samples after the removal of corrosion products.

The addition of 700 ppm  $\text{NO}_2^-$  at 230 °C yielded similar diffraction patterns, which were identified as  $\text{Fe}_3\text{O}_4$  (or  $\gamma - \text{Fe}_2\text{O}_3$ ) as the dominant oxide phase.  $\alpha - \text{Fe}_2\text{O}_3$  was detected with an increased  $\text{NO}_2^-$  concentration of 1100 ppm.

No oxide film could be detected in the following conditions; 700 ppm with neutralized citric acid at 230 °C and all conditions at 115 °C, where the only identified phase was metallic iron (Fe). The absence of oxides/hydroxides peaks could be due to insufficient surface film thickness. Therefore, XPS, an appropriate technique for thin-film characterization, was used, and the results are described in the following section.

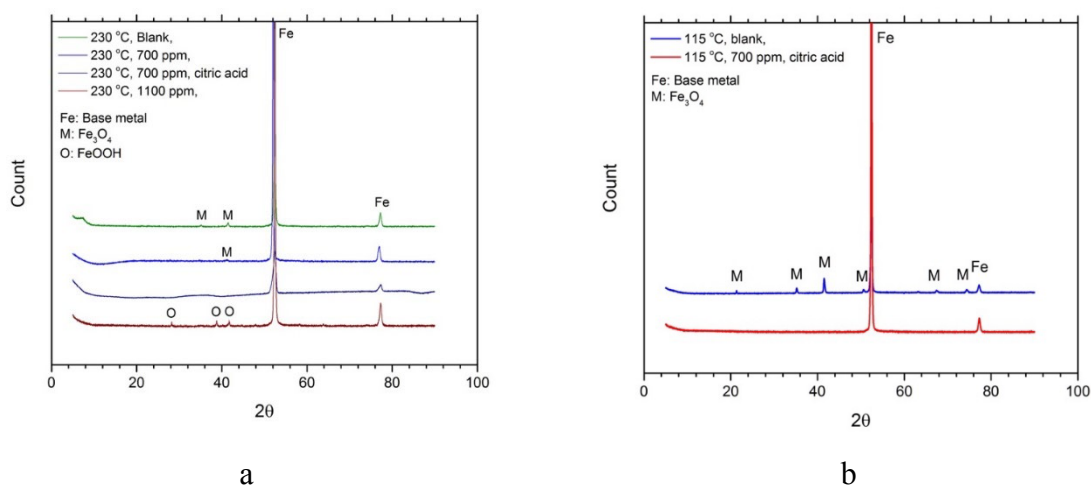


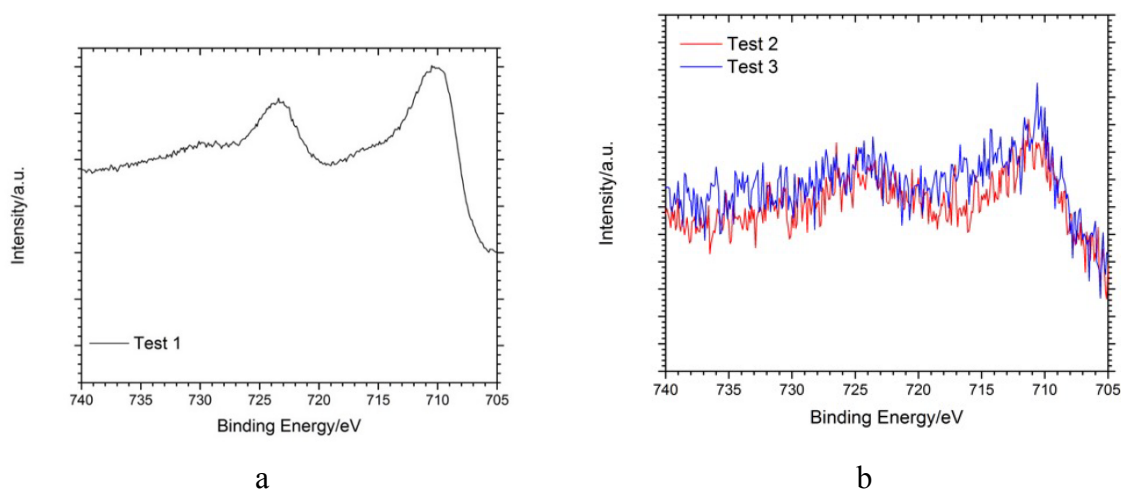
Figure 15 Overlaid X-Ray diffraction patterns of samples exposed to a) 230 °C and b) 115 °C

### 5.3 X-ray photoelectron spectroscopy

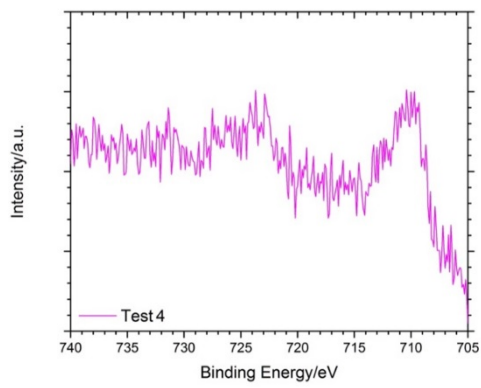
Figure 16 and Figure 17 are high-resolution XPS spectra of Fe and O obtained from the carbon steel surface exposed to the primary loop (230 °C) and secondary loop (115 °C) conditions, respectively. In all test conditions, the prominent Fe 2p peaks appeared at approximately 712 eV, which are typically associated with oxide or hydroxide species. This also included those samples that XRD did not detect oxide layers, confirming that the oxide films formed were approximately 2-5 nm and below the XRD detection limit. O 1s peaks support the presence of oxide and hydroxide species.

Examples of XPS curve fittings<sup>1</sup> are presented in Figure 18. Fe<sub>3</sub>O<sub>4</sub> was the dominant corrosion product film formed on the carbon steel surface in the absence of a corrosion inhibitor. In the presence of NO<sub>2</sub><sup>-</sup>, the corrosion product film appeared to be more complex as not only Fe<sub>3</sub>O<sub>4</sub> but also Fe<sub>2</sub>O<sub>3</sub> and FeOOH were identified.

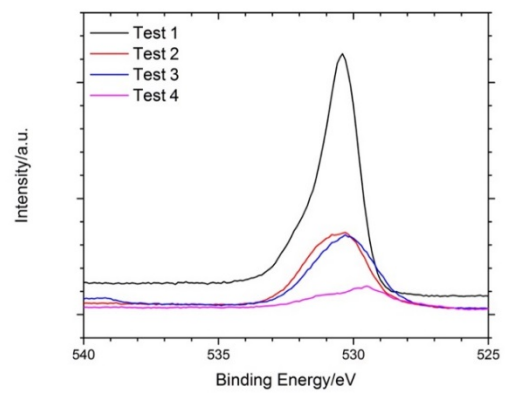
At low concentrations of nitrite (i.e., at an ineffective concentration range), corrosion products consisted of goethite and lepidocrocite and magnetite [320].



<sup>1</sup> The fitting was performed according to fitting parameters (binding energy, FWHM, and multiplet splittings) outlined in <http://www.xpsfitting.com/2012/01/iron.html>.

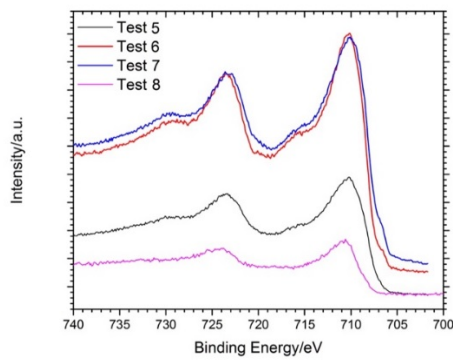


c

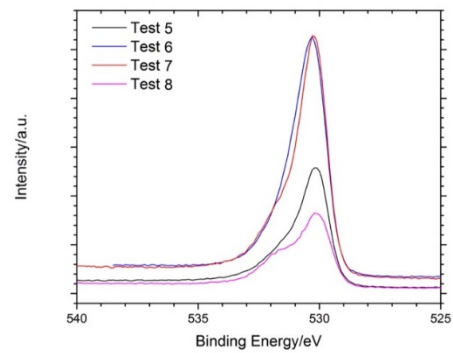


d

Figure 16 XPS of Fe 2p (a to c) and of O 1s (d) at the primary loop conditions (230 °C)

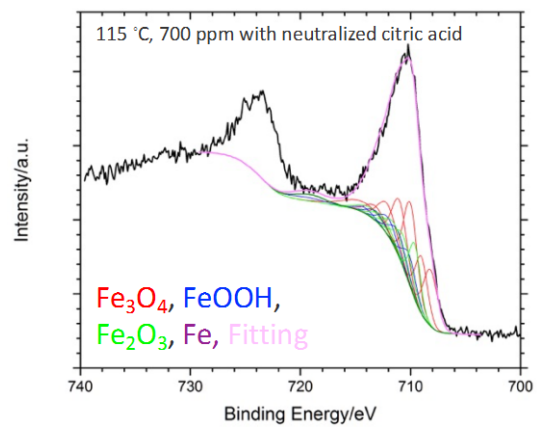
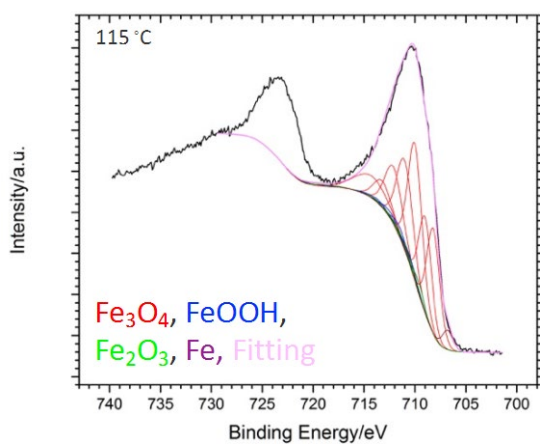


a



b

Figure 17 XPS of a) Fe 2p and b) O 1s at the secondary loop conditions (115 °C)



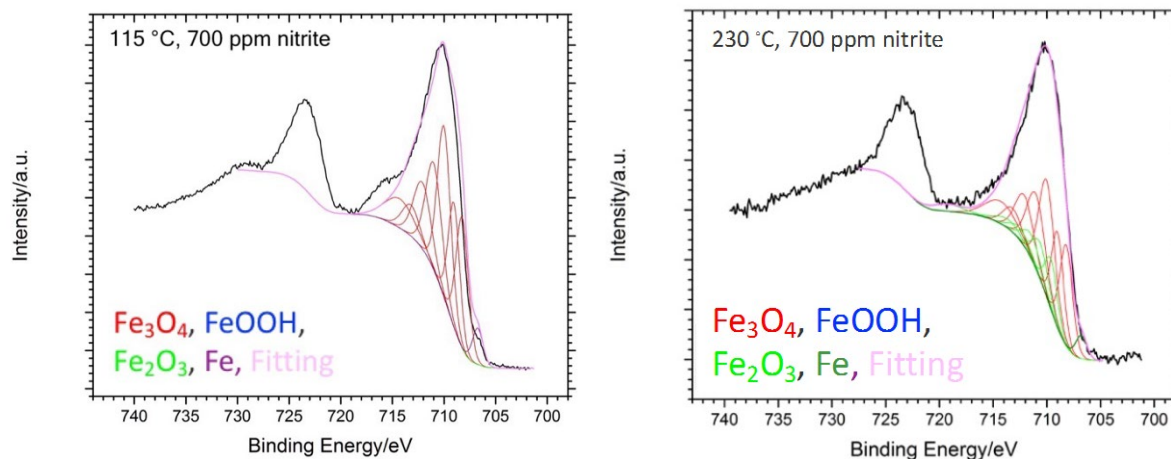


Figure 18 Examples of X-Ray Photoelectron spectroscopy curve fittings

## 6 Conclusion

The performance of the  $\text{NO}_2^-$  containing corrosion inhibitor was evaluated in conditions simulating heating circuit loops operating at temperatures up to 230 °C. The study consisted of 4-week immersion tests, surface characterization, and a comparison between laboratory and field coupon exposure. The following conclusions were drawn based on the findings:

1. In the absence of the corrosion inhibitor, uniform corrosion with a corrosion rate of 2.27 mm/y was observed at 115 °C, whereas pitting corrosion was found at 230 °C. The maximum pit depth was 32  $\mu\text{m}$  and the weight loss corrosion rate 0.047 mm/y.
2. Corrosion rates of less than 0.01 mm/y were measured by weight loss in all inhibited conditions including those with neutralized citric acid—after a 4-week exposure at both primary and secondary loop conditions.
3. The presence of citric acid (after neutralization) had no negative effects on the performance of the nitrite-based corrosion inhibitor, while the non-neutralized citric acid reduced the inhibition efficiency of nitrite as corrosion rates determined by weight loss increased from 0.002 to 0.05 mm/y at 115°C.
4. The decrease in  $\text{NO}_2^-$  concentration with exposure time is measured. After 30 days, at 700 ppm  $\text{NO}_2^-$ ,  $\text{NO}_2^-$  concentration was reduced by 62% and 38% at 230 °C and 115 °C, respectively.
5. The oxide film induced by  $\text{NO}_2^-$  was detectable by XPS. At 230 °C, the dominant oxides were  $\text{Fe}_2\text{O}_3$  and  $\text{Fe}_3\text{O}_4$  while at 115 °C  $\text{FeOOH}$  was also detected.

## References

1. Kermani, M. and D. Harrop, *The impact of corrosion on oil and gas industry*. SPE Production & Facilities, 1996. **11**(03): p. 186-190.
2. Attwood, P., et al. *The development of a corrosion management system as a means of achieving cost control in oil production operations*. in *7th Middle East Corrosion Conference, NACE, Bahrain*. 1996.
3. Heidersbach, R., *Metallurgy and corrosion control in oil and gas production*. 2018: John Wiley & Sons.
4. Song, F., *A comprehensive model for predicting CO<sub>2</sub> corrosion rate in oil and gas production and transportation systems*. Electrochimica Acta, 2010. **55**(3): p. 689-700.
5. Kermani, M. and A. Morshed, *Carbon dioxide corrosion in oil and gas production—a compendium*. Corrosion, 2003. **59**(8): p. 659-683.
6. El-Lateef, H.A., et al., *Corrosion protection of steel pipelines against CO<sub>2</sub> corrosion—a review*. Chem. J, 2012. **2**(2): p. 52-63.
7. Kermani, B. and L.M. Smith, *A working party report on CO<sub>2</sub> corrosion control in oil and gas production: design considerations*. Vol. 688. 1997: Maney Pub.
8. Zhou, X. and W. Jepson, *Corrosion in three-phase oil/water/gas slug flow in horizontal pipes*. 1994, NACE International, Houston, TX (United States).
9. Berry, W. *Effect of CO<sub>2</sub> on corrosion of pipeline*. in *Proc. AGA Transmission Conference, Chicago*. 1982.
10. Ikeda, A., S. Mukai, and M. Ueda, *Corrosion behavior of 9 to 25% Cr steels in wet CO<sub>2</sub> environments*. Corrosion, 1985. **41**(4): p. 185-192.
11. Ikeda, A., *CO<sub>2</sub> Corrosion Behavior and Mechanism of Carbon and Alloy Steel*. CORROSION/83, 1983. **45**.
12. Kane, R.D., *Corrosion in petroleum production operations*. Metals Handbook, 2006. **13**: p. 922-966.
13. Craig, B.D. and L. Smith, *Corrosion Resistant Alloys (CRAs) in the oil and gas industry*. Nickel Institute Technical Series, 2011. **1**: p. 0073.
14. Heubner, U., *Corrosion resistant alloys in oil and gas production*. Hrsg. von J. Kolts und SW Ciaraldi, 2 Bände, 1135 Seiten, NACE International, Houston, Texas 1996, 237.00(List), 177.00 (NACE Member), ISBN 1-877914-92-4. Materials and Corrosion, 1997. **48**(2): p. 134-135.
15. Groysman, A., *Corrosion problems and solutions in oil refining and petrochemical industry*. 2017: Springer.
16. Dillon, C., *Materials selection for the chemical process industries*. 1992: McGraw-Hill Companies.
17. Zhang, H., Y. Zhao, and Z. Jiang, *Effects of temperature on the corrosion behavior of 13Cr martensitic stainless steel during exposure to CO<sub>2</sub> and Cl<sup>-</sup> environment*. Materials Letters, 2005. **59**(27): p. 3370-3374.
18. Ikeda, A., *Recent progress in tubular products for oil and gas production*. A. Ikeda, et. al. Sumitomo Search, 1989(37): p. 43-64.
19. Hoffmeister, H. *Modeling of H<sub>2</sub>S-Corrosion by Coupling of Phase and Polarization Behavior*. in *CORROSION 2005*. 2005. NACE International.
20. Sato, N., *A theory for breakdown of anodic oxide films on metals*. Electrochimica Acta, 1971. **16**(10): p. 1683-1692.
21. Fontana, M.G., *Corrosion engineering*. 2005: Tata McGraw-Hill Education.
22. Marcus, P., *Surface science approach of corrosion phenomena*. Electrochimica Acta, 1998. **43**(1-2): p. 109-118.
23. Marcus, P., V. Maurice, and H.-H. Strehblow, *Localized corrosion (pitting): A model of passivity breakdown including the role of the oxide layer nanostructure*. Corrosion Science, 2008. **50**(9): p. 2698-2704.
24. Marcus, P., *Sulfur-assisted corrosion mechanisms and the role of alloyed elements*, in *Corrosion Mechanisms in Theory and Practice*. 2002, CRC Press. p. 287-310.
25. Banaś, J., et al., *Effect of CO<sub>2</sub> and H<sub>2</sub>S on the composition and stability of passive film on iron alloys in geothermal water*. Electrochimica Acta, 2007. **52**(18): p. 5704-5714.
26. Banaś, J., et al., *The Effect of CO<sub>2</sub> and H<sub>2</sub>S on the passivation of chromium and stainless steels in aqueous solutions at elevated temperature and under high pressure*, in *Passivation of Metals and Semiconductors, and Properties of Thin Oxide Layers*. 2006, Elsevier. p. 417-423.
27. Brown, M., W. DeLong, and J. Auld, *Corrosion by chlorine and by hydrogen chloride at high temperatures*. Industrial & Engineering Chemistry, 1947. **39**(7): p. 839-844.
28. Dawson, J. and M. Ferreira, *Electrochemical studies of the pitting of austenitic stainless steel*. Corrosion Science, 1986. **26**(12): p. 1009-1026.
29. Szklarska-Smialowska, Z., *Pitting Corrosion of Metals (NACE, Houston, 1986)*. Critical local volume strain. **43**: p. 44-46.

30. Oldfield, J. and W. Sutton, *New technique for predicting the performance of stainless steels in sea water and other chloride-containing environments*. British Corrosion Journal, 1980. **15**(1): p. 31-34.
31. Kain, R.M. and T.S. Lee, *Recent developments in test methods for investigating crevice corrosion*, in *Laboratory corrosion tests and standards*. 1985, ASTM International.
32. Oldfield, J. and W. Sutton, *Crevice corrosion of stainless steels: i. a mathematical model*. British corrosion journal, 1978. **13**(1): p. 13-22.
33. Betts, A. and L. Boulton, *Crevice corrosion: review of mechanisms, modelling, and mitigation*. British corrosion journal, 1993. **28**(4): p. 279-296.
34. TM, N., *G31-12a*, “. Standard guide for laboratory immersion corrosion testing of metals,” ASTM Int, 2012: p. 1-10.
35. Standard, A., *G1-03*. Standard practice for preparing, cleaning and evaluating corrosion test specimens", American Society for Testing and Materials, 2003.
36. Szklarska-Smialowska, Z., H. Viehhaus, and M. Janik-Czachor, *Electron spectroscopy analysis of in-depth profiles of passive films formed on iron in Cl<sup>-</sup>/sup<sup>-</sup>-containing solutions*. 1976.
37. Roberge, P.R., *Handbook of Corrosion Engineering* McGraw-Hill. New York, NY, 2000.
38. Popoola, L.T., et al., *Corrosion problems during oil and gas production and its mitigation*. International Journal of Industrial Chemistry, 2013. **4**(1): p. 35.
39. Lusk, D., et al., *Armoured against corrosion*. Hydrocarbon engineering, 2008. **13**(11).
40. Uhlig, H.H., *The cost of corrosion to the United States*. Chemical and Engineering News, 1949. **27**: p. 2764.
41. Tuttle, R., *Corrosion in oil and gas production*. Journal of petroleum technology, 1987. **39**(07): p. 756-762.
42. Corbin, D. and E. Willson. *New technology for real-time corrosion detection*. in *Tri-service corrosion conference, Denver, CO*. 2007.
43. Nimmo, B. and G. Hinds, *Beginners guide to corrosion*. NPL, Teddington, 2003.
44. Dean, F. and S. Powell. *Hydrogen flux and high temperature acid corrosion*. in *CORROSION 2006*. 2006. NACE International.
45. Brondel, D., et al., *Corrosion in the oil industry*. Oilfield review, 1994. **6**(2): p. 4-18.
46. Nalli, K., *Corrosion and its mitigation in the oil and gas industry*. An overview. PM-Pipeliners report, 2010.
47. Dugstad, A., *The importance of FeCO<sub>3</sub> supersaturation on the CO<sub>2</sub> corrosion of carbon steels, corrosion '92, paper 14*. NACE, Houston, 1992.
48. Schmitt, G., *Fundamental aspects of CO<sub>2</sub> corrosion*. G. Schmitt, Technical Univ. of Aachen, Warrinjer Weg 1, D-5100 Aachen, West Germany, Corrosion 83/43, NACE, Houston, Tx., Per Copy,\$ 3. 00, 1984.
49. Dunlop, A., H. Hassell, and P. Rhodes, *Fundamental considerations in sweet gas well corrosion*, in *Corrosion 83*. 1983. p. 461-4624.
50. De Waard, C., U. Lotz, and D. Williams, *Predictive model for CO<sub>2</sub> corrosion engineering in wet natural gas pipelines*. Corrosion, 1991. **47**(12): p. 976-985.
51. Ray, J., B. Randall, and J. Parker. *Use of reactive iron oxide to remove H<sub>2</sub>S from drilling fluid*. 53rd Annu. in *Fall Tech. Conf. of AIME, Houston*. 1978.
52. Chilingar, G. and C. Beeson, *Surface operations in petroleum production* New York. 1969, American Elsevier p.
53. Baek, W.-C., et al., *In situ surface enhanced Raman spectroscopic study on the effect of dissolved oxygen on the corrosion film on low carbon steel in 0.01 M NaCl solution*. Electrochimica acta, 2001. **46**(15): p. 2321-2325.
54. Martin, R. *Use of electrochemical methods to evaluate corrosion inhibitors under laboratory and field condition*. in *UMIST conference of electrochemical techniques, Manchester*. 1982.
55. Hassani, S., et al., *Flow loop study of NaCl concentration effect on erosion, corrosion, and erosion-corrosion of carbon steel in CO<sub>2</sub>-saturated systems*. Corrosion, The Journal of Science and Engineering, 2012. **68**(2): p. 026001-1-026001-9.
56. Sami, A. and A. Mohammed, *Study synergy effect on erosion-corrosion in oil and gas pipelines*. Engineering and Technology, 2008. **26**(9).
57. Bertness, T., *Reduction of failures caused by corrosion in pumping wells*. API Dril Prod Pract, 1957. **37**: p. 129-135.
58. Ossai, C.I., *Advances in asset management techniques: An overview of corrosion mechanisms and mitigation strategies for oil and gas pipelines*. ISRN Corrosion, 2012. **2012**.
59. Crawford, P.B. *Possible reservoir damage from microbial enhanced oil recovery*. in *Proceedings of the 1982 International Conference on Microbial Enhancement of Oil Recovery*''(EC Donaldson and JB Clark, Eds.). 1983.

60. Lazar, I. and P. Constantinescu, *Field trials results of microbial enhanced oil recovery*. Microbes and oil recovery, 1985. **1**: p. 122-143.
61. Moses, V., *Microbes and oil recovery*. Microbiological sciences, 1987. **4**(10): p. 306-309.
62. Gates, G. and C. Parent, *Water quality control presents challenge in giant Wilmington Field*. Oil Gas J, 1976. **74**(33): p. 115-126.
63. Wilhelm, S. and D. Currie, *Relationship of localized corrosion and SCC in oil and gas production environments*, in *Slow Strain Rate Testing for the Evaluation of Environmentally Induced Cracking: Research and Engineering Applications*. 1993, ASTM International.
64. Kermani, B., *Recommended Practice for Corrosion Management of Pipelines in Oil & Gas Production and Transportation*. 2017: CRC Press.
65. Smith, L., *Control of corrosion in oil and gas production tubing*. British Corrosion Journal, 1999. **34**(4): p. 247-253.
66. Al-Otaibi, M., et al., *Corrosion inhibitory action of some plant extracts on the corrosion of mild steel in acidic media*. Arabian Journal of Chemistry, 2014. **7**(3): p. 340-346.
67. De Marco, R., et al., *Persistence of carbon dioxide corrosion inhibitors*. Corrosion, 2002. **58**(4): p. 354-363.
68. Durnie, W., et al., *Predicting the adsorption properties of carbon dioxide corrosion inhibitors using a structure-activity relationship*. Journal of The Electrochemical Society, 2005. **152**(1): p. B1-B11.
69. Srisuwan, N., et al., *Variation of carbon steel corrosion rate with flow conditions in the presence of an inhibitive formulation*. Corrosion Science, 2008. **50**(5): p. 1245-1250.
70. Zhang, X., et al., *Study of the inhibition mechanism of imidazoline amide on CO<sub>2</sub> corrosion of Armco iron*. Corrosion Science, 2001. **43**(8): p. 1417-1431.
71. Finšgar, M., et al., *Polyethyleneimine as a corrosion inhibitor for ASTM 420 stainless steel in near-neutral saline media*. Corrosion Science, 2009. **51**(3): p. 525-533.
72. Badiea, A. and K. Mohana, *Effect of temperature and fluid velocity on corrosion mechanism of low carbon steel in presence of 2-hydrazino-4, 7-dimethylbenzothiazole in industrial water medium*. Corrosion Science, 2009. **51**(9): p. 2231-2241.
73. Frankel, G., *Pitting corrosion of metals a review of the critical factors*. Journal of the Electrochemical society, 1998. **145**(6): p. 2186-2198.
74. Frankel, G., *The growth of 2-D pits in thin film aluminum*. Corrosion Science, 1990. **30**(12): p. 1203-1218.
75. Lin, L., C. Chao, and D. Macdonald, *A point defect model for anodic passive films II. Chemical breakdown and pit initiation*. Journal of the Electrochemical Society, 1981. **128**(6): p. 1194-1198.
76. Macdonald, D.D., *On the existence of our metals-based civilization I. Phase-space analysis*. Journal of the Electrochemical Society, 2006. **153**(7): p. B213-B224.
77. Yang, S. and D.D. Macdonald, *Theoretical and experimental studies of the pitting of type 316L stainless steel in borate buffer solution containing nitrate ion*. Electrochimica Acta, 2007. **52**(5): p. 1871-1879.
78. Anderko, A., C. Brossia, and N. Sridhar, *Prediction of Corrosion of Nickel-Base Alloys and Stainless Steels in Oxidizing Environments Using Thermodynamic and Electrochemical Models*. CORROSION 2005, 2005.
79. Anderko, A.M., et al. *Modeling Localized Corrosion in Complex Process Environments in the Presence of Inhibitors*. in *CORROSION 2006*. 2006. NACE International.
80. Anderko, A.M., et al., *A Computational Approach to Predicting the Occurrence of Localized Corrosion in Multicomponent Aqueous Solutions*. CORROSION 2004, 2004.
81. Anderko, A., N. Sridhar, and D. Dunn, *A general model for the repassivation potential as a function of multiple aqueous solution species*. Corrosion Science, 2004. **46**(7): p. 1583-1612.
82. Okada, T., *Halide nuclei theory of pit initiation in passive metals*. journal of the Electrochemical Society, 1984. **131**(2): p. 241-247.
83. Okada, T., *Considerations of the stability of pit repassivation during pitting corrosion of passive metals*. Journal of the Electrochemical Society, 1984. **131**(5): p. 1026-1032.
84. Anderko, A., P. McKenzie, and R.D. Young, *Computation of rates of general corrosion using electrochemical and thermodynamic models*. Corrosion, 2001. **57**(3): p. 202-213.
85. Anderko, A., P. Wang, and M. Rafal, *Electrolyte solutions: from thermodynamic and transport property models to the simulation of industrial processes*. Fluid Phase Equilibria, 2002. **194**: p. 123-142.
86. Brennert, S., *Method for testing the resistance of stainless steels to local corrosive attack*. J. Iron Steel Inst.(London), 1937. **135**: p. 101.
87. Pourbaix, M., et al., *Potentiokinetic and corrosimetric investigations of the corrosion behaviour of alloy steels*. Corrosion Science, 1963. **3**(4): p. 239-259.
88. Laycock, N. and R. Newman, *Localised dissolution kinetics, salt films and pitting potentials*. Corrosion science, 1997. **39**(10-11): p. 1771-1790.

89. Laycock, N. and R. Newman, *Temperature dependence of pitting potentials for austenitic stainless steels above their critical pitting temperature*. Corrosion science, 1998. **40**(6): p. 887-902.
90. Inturi, R.B. and Z. Szklarska-Smialowska, *The pitting corrosion of sputtered Fe base alloy films*. Corrosion science, 1993. **34**(12): p. 1973-1989.
91. Sasaki, K. and G. Burstein, *The generation of surface roughness during slurry erosion-corrosion and its effect on the pitting potential*. Corrosion Science, 1996. **38**(12): p. 2111-2120.
92. Frankel, G., et al., *On the Pitting Resistance of Sputter-Deposited Aluminum Alloys*. Journal of the Electrochemical Society, 1993. **140**(8): p. 2192-2197.
93. Wilde, B. and E. Williams, *The relevance of accelerated electrochemical pitting tests to the long-term pitting and crevice corrosion behavior of stainless steels in marine environments*. Journal of the Electrochemical Society, 1971. **118**(7): p. 1057-1062.
94. Bond, A. and E. Lizlovs, *Anodic polarization of austenitic stainless steels in chloride media*. Journal of The Electrochemical Society, 1968. **115**(11): p. 1130-1135.
95. Shibata, T. and T. Takeyama, *Stochastic theory of pitting corrosion*. Corrosion, 1977. **33**(7): p. 243-251.
96. Schwenk, W., *Theory of stainless steel pitting*. Corrosion, 1964. **20**(4): p. 129t-137t.
97. Scully, J.R., et al., *An alternate explanation for the abrupt current increase at the pitting potential*. Corrosion Science, 2008. **50**(2): p. 316-324.
98. Janik-Czachor, M., *An assessment of the processes leading to pit nucleation on iron*. Journal of The Electrochemical Society, 1981. **128**(12): p. 513C-519C.
99. Boucherit, M. and D. Tebib, *A study of carbon steels in basic pitting environments*. Anti-Corrosion Methods and Materials, 2005. **52**(6): p. 365-370.
100. Tzaneva, B., *EFFECT OF pH ON THE CORROSION BEHAVIOUR OF HIGH NITROGEN STAINLESS STEEL IN CHLORIDE MEDIUM*. Journal of Chemical Technology & Metallurgy, 2013. **48**(4).
101. Bird, H., B. Pearson, and P. Brook, *The breakdown of passive films on iron*. Corrosion science, 1988. **28**(1): p. 81-86.
102. Tang, Y.C. and A.J. Davenport, *Magnetic field effects on the corrosion of artificial pit electrodes and pits in thin films*. Journal of the Electrochemical Society, 2007. **154**(7): p. C362-C370.
103. Ralston, K., et al., *Role of nanostructure in pitting of Al-Cu-Mg alloys*. Electrochimica Acta, 2010. **55**(27): p. 7834-7842.
104. Zheng, Z., et al., *Corrosion behaviour of nanocrystalline 304 stainless steel prepared by equal channel angular pressing*. Corrosion Science, 2012. **54**: p. 60-67.
105. Chateauminois, A., *ASM Handbook: Surface Engineering (Vol 5): ASM International, 1999, pp. 1039, ISBN 0-87170-384-X, £ 143 hardback*. 2000, Elsevier.
106. Meng, G., et al., *Effect of microcrystallization on pitting corrosion of pure aluminium*. Corrosion Science, 2009. **51**(9): p. 2151-2157.
107. Motooka, T., et al., *Pitting potential of Zircaloy-2 in artificial seawater under gamma-ray irradiation*. ECS Transactions, 2013. **53**(21): p. 25-32.
108. Kim, Y. and R. Oriani, *Brine radiolysis and its effect on the corrosion of Grade 12 titanium*. Corrosion, 1987. **43**(2): p. 92-97.
109. Glass, R.S., et al., *Gamma radiation effects on corrosion—I. Electrochemical mechanisms for the aqueous corrosion processes of austenitic stainless steels relevant to nuclear waste disposal in tuff*. Corrosion Science, 1986. **26**(8): p. 577-590.
110. Lillard, R. and G. Vasquez, *The inhibition of pitting corrosion in stainless steel 304 L during proton irradiation*. Journal of The Electrochemical Society, 2008. **155**(4): p. C162-C168.
111. Fujimoto, S., T. Yamada, and T. Shibata, *Improvement of pitting corrosion resistance of type 304 stainless steel by modification of passive film with ultraviolet light irradiation*. Journal of the Electrochemical Society, 1998. **145**(5): p. L79-L81.
112. Macdonald, D.D. and D.F. Heaney, *Effect of variable intensity ultraviolet radiation on passivity breakdown of AISI Type 304 stainless steel*. Corrosion science, 2000. **42**(10): p. 1779-1799.
113. Breslin, C.B., et al., *Photo-inhibition of pitting corrosion on types 304 and 316 stainless steels in chloride-containing solutions*. Electrochimica acta, 1997. **42**(1): p. 137-144.
114. Lenhart, S., M. Urquidi-Macdonald, and D. Macdonald, *Photo-inhibition of passivity breakdown on nickel*. Electrochimica Acta, 1987. **32**(12): p. 1739-1741.
115. Macdonald, D., et al., *Photoinhibition of pitting on nickel and alloy CDA 715 in buffered chloride-containing solutions*. Corrosion, 1999. **55**(4): p. 343-354.
116. Zhu, W., et al., *Decreasing pitting susceptibility of passive films on X70 pipeline steel in NaCl solutions by illumination*. Acta Metallurgica Sinica (English Letters), 2006. **19**(2): p. 91-97.
117. Baumgärtner, M. and H. Kaesche, *The nature of crevice corrosion of aluminum in chloride solutions*. Materials and Corrosion, 1988. **39**(3): p. 129-135.
118. Böhni, H., *Breakdown of passivity and localized corrosion processes*. Langmuir, 1987. **3**(6): p. 924-930.

119. Hoar, T., D. Mears, and G. Rothwell, *The relationships between anodic passivity, brightening and pitting*. Corrosion Science, 1965. **5**(4): p. 279-289.
120. Hoch, G., et al., *Localized Corrosion, NACE-3*. 1974, NACE International, Houston.
121. Raetzer-Scheibe, H.-J., *The Relationship Between Repassivation Behavior and Pitting Corrosion for Ti and Ti6Al4V*. Corrosion, 1978. **34**(12): p. 437-442.
122. Basame, S.B. and H.S. White, *Pitting corrosion of titanium the relationship between pitting potential and competitive anion adsorption at the oxide film/electrolyte interface*. Journal of the Electrochemical Society, 2000. **147**(4): p. 1376.
123. Evans, U.R., *CXL.—The passivity of metals. Part I. The isolation of the protective film*. Journal of the Chemical Society (Resumed), 1927: p. 1020-1040.
124. Pou, T.E., et al., *Passive films on iron: the mechanism of breakdown in chloride containing solutions*. Journal of the Electrochemical Society, 1984. **131**(6): p. 1243-1251.
125. Goetz, R., B. MacDougall, and M. Graham, *An AES and SIMS study of the influence of chloride on the passive oxide film on iron*. Electrochimica Acta, 1986. **31**(10): p. 1299-1303.
126. McBee, C. and J. Kruger, *Localized corrosion*. by RW Staehle et al, 1974: p. 252.
127. Foroulis, Z. and M. Thubrikar, *On the kinetics of the breakdown of passivity of preanodized aluminum by chloride ions*. Journal of the Electrochemical Society, 1975. **122**(10): p. 1296-1301.
128. Wood, G., et al. *Passivity of metals*. in *Proceedings of the Fourth International Symposium on Passivity, The Electrochem. Soc., Pennington, NJ*. 1978.
129. Bardwell, J.A. and B. MacDougall, *Pitting of Iron by Chloride in Borate Buffer Solution Role of the Anodic Oxide Film*. Journal of the Electrochemical Society, 1988. **135**(9): p. 2157-2161.
130. Vetter, K. and H.H. Strehblow, *Entstehung und Gestalt von Korrosionslöchern bei Lochfraß an Eisen und theoretische Folgerungen zur Lochfraßkorrosion*. Berichte der Bunsengesellschaft für physikalische Chemie, 1970. **74**(10): p. 1024-1035.
131. Sato, N., K. Kudo, and T. Noda, *The anodic oxide film on iron in neutral solution*. Electrochimica Acta, 1971. **16**(11): p. 1909-1921.
132. Galvele, J.R., *Transport processes and the mechanism of pitting of metals*. Journal of The Electrochemical Society, 1976. **123**(4): p. 464-474.
133. Hoar, T., *The production and breakdown of the passivity of metals*. Corrosion Science, 1967. **7**(6): p. 341-355.
134. Xu, Y., M. Wang, and H. Pickering, *On electric field induced breakdown of passive films and the mechanism of pitting corrosion*. Journal of the Electrochemical Society, 1993. **140**(12): p. 3448-3457.
135. Sato, N., *Anodic breakdown of passive films on metals*. Journal of The Electrochemical Society, 1982. **129**(2): p. 255.
136. Evans, U.R. and C. King, *The corrosion and oxidation of metals*. Journal of The Electrochemical Society, 1961. **108**(4): p. 94C-95C.
137. Videm, K., *The electrochemistry of uniform corrosion and pitting of aluminium*. 1974.
138. Burstein, G., et al., *The nucleation and early stages of growth of corrosion pits*. Critical Factors in Localised Corrosion II, 1996: p. 1-14.
139. Burstein, G., P. Pistorius, and S. Mattin, *The nucleation and growth of corrosion pits on stainless steel*. Corrosion Science, 1993. **35**(1-4): p. 57-62.
140. Riley, A., D. Wells, and D. Williams, *Initiation events for pitting corrosion of stainless steel?* Corrosion science, 1991. **32**(12): p. 1307-1313.
141. Suter, T., T. Peter, and H. Böhni. *Microelectrochemical investigations of MnS inclusions*. in *Materials Science Forum*. 1995. Trans Tech Publ.
142. Kolotyrkin, J.M., *Pitting corrosion of metals*. Corrosion, 1963. **19**(8): p. 261t-268t.
143. Hoar, T. and W. Jacob, *Breakdown of passivity of stainless steel by halide ions*. Nature, 1967. **216**(5122): p. 1299-1301.
144. Uhlig, H.H., *Adsorbed and Reaction-Product Films on Metals*. Journal of the Electrochemical Society, 1950. **97**(11): p. 215C.
145. Kolotyrkin, J.M., *Effects of anions on the dissolution kinetics of metals*. Journal of the Electrochemical Society, 1961. **108**(3): p. 209.
146. Uhlig, H. and J. Gilman, *Pitting of 18-8 stainless steel in ferric chloride inhibited by nitrates*. Corrosion, 1964. **20**(9): p. 289t-292t.
147. Heusler, K. and L. Fischer, *Kinetics of pit initiation at passive iron*. Materials and Corrosion, 1976. **27**(8): p. 551-556.
148. Heusler, K. and L. Fischer, *Kinetics of pit initiation at the alloy Fe5Cr*. Materials and Corrosion, 1976. **27**(11): p. 788-791.
149. Trautenberg, S. and R. Foley, *The influence of chloride and sulfate ions on the corrosion of iron in sulfuric acid*. Journal of the Electrochemical Society, 1971. **118**(7): p. 1066.

150. Staehle, R.W. and H. Okada, *Passivity and Its Breakdown on Iron and Iron Base Alloys*. National Assoc. of Corrosion Engineers, Houston, Tex. 1976, 194 p, 1976.
151. Khalil, W., S. Haupt, and H.H. Strehblow, *The thinning of the passive layer of iron by halides*. Materials and Corrosion, 1985. **36**(1): p. 16-21.
152. Lu, B.T., et al., *Pitting and stress corrosion cracking behavior in welded austenitic stainless steel*. Electrochimica Acta, 2005. **50**(6): p. 1391-1403.
153. Lo, K.H., C.H. Shek, and J.K.L. Lai, *Recent developments in stainless steels*. Materials Science and Engineering: R: Reports, 2009. **65**(4–6): p. 39-104.
154. Davison, R.M., et al., *A review of worldwide developments in stainless steels*. Materials & Design, 1986. **7**(3): p. 111-119.
155. Oñoro, J., *Corrosion fatigue behaviour of 317LN austenitic stainless steel in phosphoric acid*. International Journal of Pressure Vessels and Piping, 2009. **86**(10): p. 656-660.
156. Frankel, G. and N. Sridhar, *Understanding localized corrosion*. Materials Today, 2008. **11**(10): p. 38-44.
157. Hoar, T.P., D.C. Mears, and G.P. Rothwell, *The relationships between anodic passivity, brightening and pitting*. Corrosion Science, 1965. **5**(4): p. 279-289.
158. Marcus, P., *Surface science approach of corrosion phenomena*. Electrochimica Acta, 1998. **43**(1–2): p. 109-118.
159. Marcus, P., V. Maurice, and H.H. Strehblow, *Localized corrosion (pitting): A model of passivity breakdown including the role of the oxide layer nanostructure*. Corrosion Science, 2008. **50**(9): p. 2698-2704.
160. Wang, J., C. Su, and Z. Szklarska-Smialowska, *Effects of Cl-concentration and temperature on pitting of AISI 304 stainless steel*. Corrosion, 1988. **44**(10): p. 732-737.
161. Zatkalíková, V. and T. Liptáková, *Pitting corrosion of stainless steel at the various surface treatment*. Materials Engineering-Materiálové inžinierstvo (MEMI), 2011. **18**(4): p. 115-120.
162. Burstein, G. and P. Pistorius, *Surface roughness and the metastable pitting of stainless steel in chloride solutions*. Corrosion, 1995. **51**(5): p. 380-385.
163. Olsson, C.O.A. and D. Landolt, *Passive films on stainless steels—chemistry, structure and growth*. Electrochimica Acta, 2003. **48**(9): p. 1093-1104.
164. Fontana, M.G., *Corrosion Engineering*, 1986. McGraw-Hill, Inc., New York, NY 0.8■—Thickness. 1: p. 0.1-0.1.
165. Sobral, A.V., et al., *Potentiodynamic tests and electrochemical impedance spectroscopy of injection molded 316L steel in NaCl solution*. Corrosion Science, 2001. **43**(6): p. 1019-1030.
166. Abreu, C.M., et al., *High frequency impedance spectroscopy study of passive films formed on AISI 316 stainless steel in alkaline medium*. Journal of Electroanalytical Chemistry, 2004. **572**(2): p. 335-345.
167. Ping, G., et al., *Corrosion resistance of stainless steel in chloride contaminated concrete*. Cement and Concrete Research, 1996. **26**(8): p. 1151-1156.
168. Hakiki, N.E., et al., *Semiconducting properties of thermally grown oxide films on AISI 304 stainless steel*. Corrosion Science, 2000. **42**(4): p. 687-702.
169. Carmezim, M.J., et al., *Electrochemical behaviour of thermally treated Cr-oxide films deposited on stainless steel*. Corrosion Science, 2002. **44**(3): p. 451-465.
170. Gaben, F., B. Vuillemin, and R. Oltra, *Influence of the chemical composition and electronic structure of passive films grown on 316L SS on their transient electrochemical behavior*. Journal of the Electrochemical Society, 2004. **151**(11): p. B595-B604.
171. Ha, H., et al., *Effects of nitrogen on the passivity of Fe–20Cr alloy*. Corrosion Science, 2009. **51**(1): p. 48-53.
172. Qiao, Y.X., et al., *Electrochemical behaviour of high nitrogen stainless steel in acidic solutions*. Corrosion Science, 2009. **51**(5): p. 979-986.
173. Carmezim, M.J., et al., *Capacitance behaviour of passive films on ferritic and austenitic stainless steel*. Corrosion Science, 2005. **47**(3): p. 581-591.
174. Hakiki, N.B., et al., *The electronic structure of passive films formed on stainless steels*. Corrosion Science, 1995. **37**(11): p. 1809-1822.
175. Hakiki, N., et al., *Semiconducting properties of passive films formed on stainless steels influence of the alloying elements*. Journal of the Electrochemical Society, 1998. **145**(11): p. 3821-3829.
176. Da Cunha Belo, M., N.E. Hakiki, and M.G.S. Ferreira, *Semiconducting properties of passive films formed on nickel–base alloys type Alloy 600: influence of the alloying elements*. Electrochimica Acta, 1999. **44**(14): p. 2473-2481.
177. Wijesinghe, T.L.S.L. and D.J. Blackwood, *Photocurrent and capacitance investigations into the nature of the passive films on austenitic stainless steels*. Corrosion Science, 2008. **50**(1): p. 23-34.

178. Macdonald, D.D., *The point defect model for the passive state*. Journal of the Electrochemical Society, 1992. **139**(12): p. 3434.
179. Metikoš-Huković, M., et al., *High corrosion resistance of austenitic stainless steel alloyed with nitrogen in an acid solution*. Corrosion Science, 2011. **53**(6): p. 2176-2183.
180. Fattah-alhosseini, A., et al., *Effect of solution concentration on semiconducting properties of passive films formed on austenitic stainless steels*. Corrosion Science, 2010. **52**(1): p. 205-209.
181. Fattah-alhosseini, A., et al., *The semiconducting properties of passive films formed on AISI 316 L and AISI 321 stainless steels: A test of the point defect model (PDM)*. Corrosion Science, 2011. **53**(10): p. 3186-3192.
182. Paredes, E.C., et al., *Influence of the forming process of corrugated stainless steels on their corrosion behaviour in simulated pore solutions*. Corrosion Science, 2012. **58**: p. 52-61.
183. Manning, P.E. and J. Duquette, *The effect of temperature (25°–289°C) on pit initiation in single phase and duplex 304L stainless steels in 100 ppm Cl<sup>-</sup> solution*. Corrosion Science, 1980. **20**(4): p. 597-609.
184. Standard, A., *G61-86*. Standard test method for conducting cyclic potentiodynamic polarization measurements for localized corrosion susceptibility of iron-, nickel-, or cobalt-based alloys, ASTM standards, ASTM, Philadelphia, PA, USA, 2009.
185. Davis, J.R., *Corrosion: understanding the basics*. 2000: ASM International.
186. Perez, N., *Electrochemistry and Corrosion Science*. 2004. Kluwer Academic.
187. Wika, S.F., *Pitting and Crevice Corrosion of Stainless Steel under Offshore Conditions*. 2012.
188. Malik, A.U., et al., *Corrosion behavior of steels in Gulf seawater environment*. Desalination, 1999. **123**(2): p. 205-213.
189. Neville, A. and T. Hodgkiess, *An assessment of the corrosion behaviour of high-grade alloys in seawater at elevated temperature and under a high velocity impinging flow*. Corrosion Science, 1996. **38**(6): p. 927-956.
190. Meguid, E.A.E., V. Gouda, and N. Mahmoud, *Pitting corrosion behaviour of type SUS904L and SUS316L stainless steels in chloride solutions*. Materials Transactions, JIM, 1994. **35**(10): p. 699-702.
191. Kim, J.J. and Y.M. Young, *Study on the passive film of type 316 stainless steel*. Int. J. Electrochem. Sci, 2013. **8**(10): p. 11847-11859.
192. Newman, R., *2001 WR Whitney Award Lecture: Understanding the Corrosion of Stainless Steel*. Corrosion, 2001. **57**(12): p. 1030-1041.
193. Huang, J. *Study of Pitting Corrosion of Corrosion Resistant Alloys at Extreme High Temperature Using Electrochemical Measurements*. in *CORROSION 2015*. 2015. NACE International.
194. Touzet, M., et al., *An EIS study and auger analysis on 304L stainless steel in hot chloride media before and after a sample straining*. Corrosion Science, 1993. **34**(7): p. 1187-1196.
195. Assis, S.L.d., S. Wolyneć, and I. Costa, *Corrosion characterization of titanium alloys by electrochemical techniques*. Electrochimica Acta, 2006. **51**(8–9): p. 1815-1819.
196. Pan, J., D. Thierry, and C. Leygraf, *Electrochemical impedance spectroscopy study of the passive oxide film on titanium for implant application*. Electrochimica Acta, 1996. **41**(7–8): p. 1143-1153.
197. Fernández-Domene, R.M., et al., *Passive and transpassive behaviour of Alloy 31 in a heavy brine LiBr solution*. Electrochimica Acta, 2013. **95**: p. 1-11.
198. Valero Vidal, C. and A. Igual Muñoz, *Study of the adsorption process of bovine serum albumin on passivated surfaces of CoCrMo biomedical alloy*. Electrochimica Acta, 2010. **55**(28): p. 8445-8452.
199. Evgenij, B. and J.R. Macdonald, *Impedance Spectroscopy: Theory. Experiment and Applications*, West Sussex, UK, 2005.
200. Brug, G.J., et al., *The analysis of electrode impedances complicated by the presence of a constant phase element*. Journal of Electroanalytical Chemistry and Interfacial Electrochemistry, 1984. **176**(1): p. 275-295.
201. Hirschorn, B., et al., *Determination of effective capacitance and film thickness from constant-phase-element parameters*. Electrochimica Acta, 2010. **55**(21): p. 6218-6227.
202. Pan, J., et al., *Characterization of High-Temperature Oxide Films on Stainless Steels by Electrochemical-Impedance Spectroscopy*. Oxidation of Metals, 1998. **50**(5): p. 431-455.
203. Yagi, S., et al., *Surface modification of ACM522 magnesium alloy by plasma electrolytic oxidation in phosphate electrolyte*. Corrosion Science, 2012. **57**: p. 74-80.
204. Fernández-Domene, R.M., et al., *Thermogalvanic corrosion of Alloy 31 in different heavy brine LiBr solutions*. Corrosion Science, 2012. **55**: p. 40-53.
205. Paola, A.D., *Semiconducting properties of passive films on stainless steels*. Electrochimica Acta, 1989. **34**(2): p. 203-210.
206. Macdonald, D.D., et al., *An electrochemical impedance study of Alloy-22 in NaCl brine at elevated temperature: II. Reaction mechanism analysis*. Journal of Electroanalytical Chemistry, 2004. **572**(2): p. 421-431.

207. Ningshen, S., et al., *Semiconducting and passive film properties of nitrogen-containing type 316LN stainless steels*. Corrosion Science, 2007. **49**(2): p. 481-496.
208. Amri, J., et al., *Effect of the final annealing of cold rolled stainless steels sheets on the electronic properties and pit nucleation resistance of passive films*. Corrosion Science, 2008. **50**(2): p. 431-435.
209. De Gryse, R., et al., *On the Interpretation of Mott-Schottky Plots Determined at Semiconductor/Electrolyte Systems*. Journal of the Electrochemical Society, 1975. **122**(5): p. 711-712.
210. Goodlet, G., et al., *The electronic properties of sputtered chromium and iron oxide films*. Corrosion Science, 2004. **46**(6): p. 1479-1499.
211. Fujimoto, S. and H. Tsuchiya, *Semiconductor Property of Passive Films and Corrosion Behavior of Fe-Cr Alloys*, in *Characterization of Corrosion Products on Steel Surfaces*. 2006, Springer. p. 33-49.
212. Kermani, M. and D. Harr. *The impact of corrosion on oil and gas industry*. in *Giornata di studio IGF S. Donato Milanese 1996*. 2008.
213. Davison, R., et al., *A review of worldwide developments in stainless steels*. Materials & design, 1986. **7**(3): p. 111-119.
214. Lo, K.H., C.H. Shek, and J. Lai, *Recent developments in stainless steels*. Materials Science and Engineering: R: Reports, 2009. **65**(4): p. 39-104.
215. Callaghan, B., *The performance of a 12% chromium steel in concrete in severe marine environments*. Corrosion science, 1993. **35**(5-8): p. 1535-1541.
216. Silva, C.C., J.P. Farias, and H.B. de Sant'Ana, *Evaluation of AISI 316L stainless steel welded plates in heavy petroleum environment*. Materials & Design, 2009. **30**(5): p. 1581-1587.
217. Silva, C.C., et al., *Microstructure, hardness and petroleum corrosion evaluation of 316L/AWS E309MoL-16 weld metal*. Materials Characterization, 2009. **60**(4): p. 346-352.
218. Olsson, J., *Stainless steels for desalination plants*. Desalination, 2005. **183**(1-3): p. 217-225.
219. Olivares, R., S. Rodil, and H. Arzate, *In vitro studies of the biomineralization in amorphous carbon films*. Surface and Coatings Technology, 2004. **177**: p. 758-764.
220. Zahrani, E.M., A. Saatchi, and A. Alfantazi, *Pitting of 316L stainless steel in flare piping of a petrochemical plant*. Engineering Failure Analysis, 2010. **17**(4): p. 810-817.
221. Saricimen, H., et al., *Performance of austenitic stainless steels in MSF desalination plant flash chambers in the arabian gulf*. Desalination, 1990. **78**(3): p. 327-341.
222. Malik, A., et al., *The influence of pH and chloride concentration on the corrosion behaviour of AISI 316L steel in aqueous solutions*. Corrosion science, 1992. **33**(11): p. 1809-1827.
223. Bastidas, J., et al., *A study on the stability of AISI 316L stainless steel pitting corrosion through its transfer function*. Corrosion science, 2001. **43**(2): p. 269-281.
224. Jia, Z.-j., et al., *Study on pitting process of 316L stainless steel by means of staircase potential electrochemical impedance spectroscopy*. International Journal of Minerals, Metallurgy, and Materials, 2011. **18**(1): p. 48-52.
225. Li, D., et al., *Influences of pH value, temperature, chloride ions and sulfide ions on the corrosion behaviors of 316L stainless steel in the simulated cathodic environment of proton exchange membrane fuel cell*. Journal of Power Sources, 2014. **272**: p. 448-456.
226. Olefjord, I., *The passive state of stainless steels*. Materials Science and Engineering, 1980. **42**: p. 161-171.
227. Liu, J., et al., *Effect of pitting nucleation on critical pitting temperature of 316L stainless steel by nitric acid passivation*. Corrosion Science, 2015. **91**: p. 232-244.
228. Li, T., et al., *Passive behavior of a bulk nanostructured 316L austenitic stainless steel consisting of nanometer-sized grains with embedded nano-twin bundles*. Corrosion Science, 2014. **85**: p. 331-342.
229. Fredriksson, W., et al., *Full depth profile of passive films on 316L stainless steel based on high resolution HAXPES in combination with ARXPS*. Applied Surface Science, 2012. **258**(15): p. 5790-5797.
230. Montemor, M., et al., *Chemical composition and electronic structure of the oxide films formed on 316L stainless steel and nickel based alloys in high temperature aqueous environments*. Corrosion Science, 2000. **42**(9): p. 1635-1650.
231. Mesquita, T.J., et al., *A XPS study of the Mo effect on passivation behaviors for highly controlled stainless steels in neutral and alkaline conditions*. Applied surface science, 2013. **270**: p. 90-97.
232. Ramana, K., et al., *Effect of different environmental parameters on pitting behavior of AISI type 316L stainless steel: Experimental studies and neural network modeling*. Materials & Design, 2009. **30**(9): p. 3770-3775.
233. Yang, Y., L. Guo, and H. Liu, *The effect of temperature on corrosion behavior of SS316L in the cathode environment of proton exchange membrane fuel cells*. Journal of Power Sources, 2011. **196**(13): p. 5503-5510.
234. MEGUID, E.A.E., N. Mahmoud, and V. Gouda, *Pitting corrosion behaviour of AISI 316L steel in chloride containing solutions*. British corrosion journal, 1998. **33**(1): p. 42-48.

235. Zhang, H., Y. Zhao, and Z. Jiang, *Effects of temperature on the corrosion behavior of 13Cr martensitic stainless steel during exposure to CO<sub>2</sub> and Cl<sup>-</sup> environment*. *Materials Letters*, 2005. **59**(27): p. 3370-3374.
236. Moreira, R., et al., *The effects of temperature and hydrodynamics on the CO<sub>2</sub> corrosion of 13Cr and 13Cr5Ni2Mo stainless steels in the presence of free acetic acid*. *Corrosion Science*, 2004. **46**(12): p. 2987-3003.
237. Ezuber, H.M., *Corrosion behavior of heat-treated duplex stainless steels in saturated carbon dioxide-chloride solutions*. *Journal of ASTM International*, 2005. **2**(5): p. 1-11.
238. Anselmo, N., et al., *Corrosion behavior of supermartensitic stainless steel in aerated and CO<sub>2</sub>-saturated synthetic seawater*. *Materials Science and Engineering: A*, 2006. **428**(1): p. 73-79.
239. Park, J.-J., et al., *Effect of bicarbonate ion additives on pitting corrosion of type 316L stainless steel in aqueous 0.5 M sodium chloride solution*. *Corrosion*, 1999. **55**(4): p. 380-387.
240. Y. Abdulwahhab1, T.P., A. Barifcani1, M. Tadel1, B. Kinsella1, *EIS and Mott-Schottky to Study the Passive Film Properties of 316L and its Susceptibility to Pitting Corrosion*. 2016.
241. Biesinger, M.C., et al., *Resolving surface chemical states in XPS analysis of first row transition metals, oxides and hydroxides: Cr, Mn, Fe, Co and Ni*. *Applied Surface Science*, 2011. **257**(7): p. 2717-2730.
242. Biesinger, M.C., et al., *X-ray photoelectron spectroscopic chemical state quantification of mixed nickel metal, oxide and hydroxide systems*. *Surface and Interface Analysis*, 2009. **41**(4): p. 324-332.
243. Grosvenor, A.P., et al., *New interpretations of XPS spectra of nickel metal and oxides*. *Surface Science*, 2006. **600**(9): p. 1771-1779.
244. Mundhenk, N., et al., *Electrochemical study of the corrosion of different alloys exposed to deaerated 80° C geothermal brines containing CO<sub>2</sub>*. *Corrosion Science*, 2014. **84**: p. 180-188.
245. Li, D. and Z. Duan, *The speciation equilibrium coupling with phase equilibrium in the H<sub>2</sub>O-CO<sub>2</sub>-NaCl system from 0 to 250 C, from 0 to 1000 bar, and from 0 to 5 molality of NaCl*. *Chemical Geology*, 2007. **244**(3): p. 730-751.
246. El Meguid, E.A., V. Gouda, and N. Mahmoud, *Pitting corrosion behaviour of type SUS904L and SUS316L stainless steels in chloride solutions*. *Materials Transactions, JIM*, 1994. **35**(10): p. 699-702.
247. Boukamp, B.A., *A Linear Kronig-Kramers Transform Test for Immittance Data Validation*. *Journal of the electrochemical society*, 1995. **142**(6): p. 1885-1894.
248. Feng, Z., et al., *Passivity of 316L stainless steel in borate buffer solution studied by Mott-Schottky analysis, atomic absorption spectrometry and X-ray photoelectron spectroscopy*. *Corrosion Science*, 2010. **52**(11): p. 3646-3653.
249. Bastidas, J., et al., *Influence of molybdenum on passivation of polarised stainless steels in a chloride environment*. *Corrosion Science*, 2002. **44**(3): p. 625-633.
250. Karimi, S., T. Nickchi, and A.M. Alfantazi, *Long-term corrosion investigation of AISI 316L, Co-28Cr-6Mo, and Ti-6Al-4V alloys in simulated body solutions*. *Applied Surface Science*, 2012. **258**(16): p. 6087-6096.
251. Jang, H. and H. Kwon, *In situ study on the effects of Ni and Mo on the passive film formed on Fe-20Cr alloys by photoelectrochemical and Mott-Schottky techniques*. *Journal of Electroanalytical Chemistry*, 2006. **590**(2): p. 120-125.
252. Marcus, P., V. Maurice, and M. Schutze, *Corrosion and environmental degradation*. *Materials Science and Technology*, vol, 2000. **19**: p. 131-169.
253. Xu, H., et al., *The passive oxide films growth on 316L stainless steel in borate buffer solution measured by real-time spectroscopic ellipsometry*. *Applied Surface Science*, 2015. **351**: p. 367-373.
254. Hashimoto, K., K. Asami, and K. Teramoto, *An X-ray photo-electron spectroscopic study on the role of molybdenum in increasing the corrosion resistance of ferritic stainless steels in HCl*. *Corrosion Science*, 1979. **19**(1): p. 3-14.
255. Sedriks, A.J., *Corrosion of stainless steel, 2nd Edition, Wiley-Interscience, New York*. 1996.
256. Sikora, E. and D.D. Macdonald, *Defining the passive state*. *Solid State Ionics*, 1997. **94**(1): p. 141-150.
257. Frankel, G.S., *Pitting Corrosion of Metals*. *Journal of The Electrochemical Society*, 1998. **145**(6): p. 2186.
258. Montemor, M.F., et al., *Chemical composition and electronic structure of the oxide films formed on 316L stainless steel and nickel based alloys in high temperature aqueous environments*. *Corrosion Science*, 2000. **42**(9): p. 1635-1650.
259. Shatak, H. and R. Baldev, *Corrosion of austenitic stainless steel*. 2002, Narosa Publishing House, London.
260. Manning, P. and J. Duquette, *The effect of temperature (25-289 C) on pit initiation in single phase and duplex 304L stainless steels in 100 ppm Cl<sup>-</sup> solution*. *Corrosion Science*, 1980. **20**(4): p. 597-609.
261. Carranza, R. and M. Alvarez, *The effect of temperature on the passive film properties and pitting behaviour of a Fe- Cr- Ni alloy*. *Corrosion Science*, 1996. **38**(6): p. 909-925.

262. Li, D.G., et al., *Influences of pH value, temperature, chloride ions and sulfide ions on the corrosion behaviors of 316L stainless steel in the simulated cathodic environment of proton exchange membrane fuel cell*. Journal of Power Sources, 2014. **272**: p. 448-456.
263. Newman, R., *2001 W.R. Whitney Award Lecture: Understanding the corrosion of stainless steel*. Corrosion, 2001. **57**(12): p. 1030.
264. Abdulwahhab, Y., et al., *EIS and Mott-Schottky to study the passive film properties of 316L and its susceptibility to pitting corrosion in CO<sub>2</sub> environments*. 2016.
265. JP Diard, B.L.G., C Montella *Handbook of electrochemical impedance spectroscopy*. 2012.
266. Moiseeva, L. and O. Kuksina, *Predicting the corrosion aggressiveness of CO<sub>2</sub>-containing media in oil and gas wells*. Chemical and petroleum engineering, 2000. **36**(5): p. 307-311.
267. Nešić, S., *Key issues related to modelling of internal corrosion of oil and gas pipelines—A review*. Corrosion science, 2007. **49**(12): p. 4308-4338.
268. Drugli, J., et al., *The effect of buffered solutions in corrosion testing of alloyed 13% Cr martensitic steels for mildly sour applications*. Proceedings of Corrosion/99, NACE International, Houston, TX, 1999: p. 99-586.
269. Carvalho, D., C. Joia, and O. Mattos, *Corrosion rate of iron and iron–chromium alloys in CO<sub>2</sub> medium*. Corrosion Science, 2005. **47**(12): p. 2974-2986.
270. Seiersten, M. *Materials selection for separation, transportation and disposal of CO<sub>2</sub>*. in *CORROSION 2001*. 2001. NACE International.
271. Nyborg, R., *Controlling internal corrosion in oil and gas pipelines*. business briefing: exploration & production: the oil & gas review, 2005. **2**: p. 70-74.
272. Ikeda, A., M. Ueda, and S. Mukai, *CO<sub>2</sub> Corrosion Behavior and Mechanism of Carbon Steel and Alloy Steel*, *Corrosion/83*. 1983, NACE International, Houston, TX.
273. Sun, W., *Kinetics of iron carbonate and iron sulfide scale formation in CO<sub>2</sub>/H<sub>2</sub>S corrosion*. 2006, Ohio University.
274. Dugstad, A., *Fundamental aspects of CO<sub>2</sub> metal loss corrosion-part 1: mechanism*. CORROSION 2006, 2006.
275. De Waard, C. and D. Milliams, *Carbonic acid corrosion of steel*. Corrosion, 1975. **31**(5): p. 177-181.
276. Nescic, S., J. Postlethwaite, and S. Olsen, *An electrochemical model for prediction of corrosion of mild steel in aqueous carbon dioxide solutions*. Corrosion, 1996. **52**(4): p. 280-294.
277. Hurlen, T., et al., *Effects of carbon dioxide on reactions at iron electrodes in aqueous salt solutions*. Journal of electroanalytical chemistry and interfacial electrochemistry, 1984. **180**(1-2): p. 511-526.
278. Tran, T., B. Brown, and S. Nescic, *Corrosion of mild steel in an aqueous CO<sub>2</sub> environment—basic electrochemical mechanisms revisited*. CORROSION/2015, 2015.
279. Linter, B. and G. Burstein, *Reactions of pipeline steels in carbon dioxide solutions*. Corrosion science, 1999. **41**(1): p. 117-139.
280. Lopez, D., T. Perez, and S. Simison, *The influence of microstructure and chemical composition of carbon and low alloy steels in CO<sub>2</sub> corrosion. A state-of-the-art appraisal*. Materials & Design, 2003. **24**(8): p. 561-575.
281. Kemp, M., A. Van Bennekom, and F. Robinson, *Evaluation of the corrosion and mechanical properties of a range of experimental Cr- Mn stainless steels*. Materials Science and Engineering: A, 1995. **199**(2): p. 183-194.
282. Tahara, A. and T. Shinohara, *Influence of the alloy element on corrosion morphology of the low alloy steels exposed to the atmospheric environments*. Corrosion Science, 2005. **47**(10): p. 2589-2598.
283. Moreira, R., et al., *The effects of temperature and hydrodynamics on the CO<sub>2</sub> corrosion of 13Cr and 13Cr5Ni2Mo stainless steels in the presence of free acetic acid*. Corrosion Science, 2004. **46**(12): p. 2987-3003.
284. Ueda, M. and A. Ikeda. *Effect of microstructure and Cr content in steel on CO<sub>2</sub> corrosion*. in *CORROSION 96*. 1996. NACE International.
285. Wei, L., X. Pang, and K. Gao. *Effects of Crude Oil on Corrosion Behavior of Pipeline Steel Under Wet CO<sub>2</sub> Condition*. in *CORROSION 2014*. 2014. NACE International.
286. Efirid, K. and R. Jasinski, *Effect of the crude oil on corrosion of steel in crude oil/brine production*. Corrosion, 1989. **45**(2): p. 165-171.
287. Lin, G., et al., *Effect of temperature and pressure on the morphology of carbon dioxide corrosion scales*. Corrosion, 2006. **62**(6): p. 501-507.
288. Zhang, G., et al., *Corrosion behaviour of N80 carbon steel in formation water under dynamic supercritical CO<sub>2</sub> condition*. Corrosion Science, 2017. **120**: p. 107-120.
289. Zhang, Y., et al., *The relationship between fracture toughness of CO<sub>2</sub> corrosion scale and corrosion rate of X65 pipeline steel under supercritical CO<sub>2</sub> condition*. International Journal of Greenhouse Gas Control, 2011. **5**(6): p. 1643-1650.

290. Zhang, Y., et al., *Discussion of the CO<sub>2</sub> corrosion mechanism between low partial pressure and supercritical condition*. Corrosion Science, 2012. **59**: p. 186-197.
291. Cui, Z., et al., *Corrosion behavior of oil tube steels under conditions of multiphase flow saturated with super-critical carbon dioxide*. Materials letters, 2004. **58**(6): p. 1035-1040.
292. Mustafa, A., B. Ari-Wahjoedi, and M. Ismail, *Inhibition of CO<sub>2</sub> corrosion of X52 steel by imidazoline-based inhibitor in high pressure CO<sub>2</sub>-water environment*. Journal of materials engineering and performance, 2013. **22**(6): p. 1748-1755.
293. Choi, Y.-S., et al., *Corrosion behavior of deep water oil production tubing material under supercritical CO<sub>2</sub> environment: part I—effect of pressure and temperature*. Corrosion, 2013. **70**(1): p. 38-47.
294. Choi, Y.-S. and S. Nešić, *Determining the corrosive potential of CO<sub>2</sub> transport pipeline in high pCO<sub>2</sub>-water environments*. International Journal of Greenhouse Gas Control, 2011. **5**(4): p. 788-797.
295. Nesic, S., *Effects of multiphase flow on internal CO<sub>2</sub> corrosion of mild steel pipelines*. Energy & Fuels, 2012. **26**(7): p. 4098-4111.
296. Lim, T.-H., et al., *Effects of temperature and partial pressure of CO<sub>2</sub>/O<sub>2</sub> on corrosion behaviour of stainless-steel in molten Li/Na carbonate salt*. Journal of power sources, 2000. **89**(1): p. 1-6.
297. Yin, Z., et al., *Pitting corrosion behaviour of 316L stainless steel in chloride solution with acetic acid and CO<sub>2</sub>*. Corrosion Engineering, Science and Technology, 2011. **46**(1): p. 56-63.
298. Nesic, S. and W. Sun, *Corrosion in acid gas solutions*. 2010. 1270-1298.
299. Anselmo, N., et al., *Corrosion behavior of supermartensitic stainless steel in aerated and CO<sub>2</sub>-saturated synthetic seawater*. Materials Science and Engineering: A, 2006. **428**(1-2): p. 73-79.
300. Ezuber, H., *Metallurgical and environmental factors affecting the pitting behavior of UNS S 32205 duplex stainless steel in chloride solutions*. Materials and Corrosion, 2012. **63**(2): p. 111-118.
301. Liu, C., et al., *An electrochemical impedance spectroscopy study of the corrosion behaviour of PVD coated steels in 0.5 N NaCl aqueous solution: Part II.: EIS interpretation of corrosion behaviour*. Corrosion Science, 2003. **45**(6): p. 1257-1273.
302. Kocijan, A., D.K. Merl, and M. Jenko, *The corrosion behaviour of austenitic and duplex stainless steels in artificial saliva with the addition of fluoride*. Corrosion Science, 2011. **53**(2): p. 776-783.
303. Macdonald, D.D., *The point defect model for the passive state*. Journal of the Electrochemical Society, 1992. **139**(12).
304. Rammelt, U. and G. Reinhard, *The influence of surface roughness on the impedance data for iron electrodes in acid solutions*. Corrosion science, 1987. **27**(4): p. 373-382.
305. Diard, J., B. Le Gorrec, and C. Montella, *Handbook of electrochemical impedance spectroscopy. Diffusion Impedances*. www. bio-logic. info/potentiostat/notes. html, 2012.
306. Brug, G., et al., *The analysis of electrode impedances complicated by the presence of a constant phase element*. Journal of electroanalytical chemistry and interfacial electrochemistry, 1984. **176**(1-2): p. 275-295.
307. Pan, J., et al., *Characterization of high-temperature oxide films on stainless steels by electrochemical-impedance spectroscopy*. Oxidation of Metals, 1998. **50**(5-6): p. 431-455.
308. Kelland, M.A., *Production chemicals for the oil and gas industry*. 2014: CRC press.
309. Finšgar, M. and J. Jackson, *Application of corrosion inhibitors for steels in acidic media for the oil and gas industry: a review*. Corrosion science, 2014. **86**: p. 17-41.
310. Rozenfel'd, I.L.v., *Corrosion inhibitors*. 1981: McGraw-Hill Companies.
311. Sastri, V.S., *Corrosion inhibitors: principles and applications*. 1998.
312. Söylev, T.A. and M. Richardson, *Corrosion inhibitors for steel in concrete: State-of-the-art report*. Construction and Building Materials, 2008. **22**(4): p. 609-622.
313. Pryor, M. and M. Cohen, *The inhibition of the corrosion of iron by some anodic inhibitors*. Journal of the Electrochemical Society, 1953. **100**(5): p. 203-215.
314. Legault, R. and M. Walker, *Sodium nitrite as a corrosion inhibitor for mild steel*. Corrosion, 1964. **20**(9): p. 282t-288t.
315. Mercer, A., I. Jenkins, and J. Rhoades-Brown, *Comparative Study of Factors Influencing the Action of Corrosion Inhibitors for Mild Steel in Neutral Solution: III. Sodium Nitrite*. British Corrosion Journal, 1968. **3**(3): p. 136-144.
316. Ramasubramanian, M., et al., *Inhibiting action of calcium nitrite on carbon steel rebars*. Journal of Materials in Civil Engineering, 2001. **13**(1): p. 10-17.
317. Mustafa, C. and S. Shahinoor Islam Dulal, *Molybdate and nitrite as corrosion inhibitors for copper-coupled steel in simulated cooling water*. Corrosion, 1996. **52**(1): p. 16-22.
318. Mustafa, C., S. Shahinoor, and I. Dulal, *Corrosion behaviour of mild steel in moderately alkaline to acidic simulated cooling water containing molybdate and nitrite*. British Corrosion Journal, 1997. **32**(9): p. 133-137.

319. Karim, S., et al., *Effect of nitrate ion on corrosion inhibition of mild steel in simulated cooling water*. Chemical Engineering Research Bulletin, 2010. **14**(2): p. 87-91.
320. Lee, D.Y., W.C. Kim, and J.G. Kim, *Effect of nitrite concentration on the corrosion behaviour of carbon steel pipelines in synthetic tap water*. Corrosion science, 2012. **64**: p. 105-114.
321. Tosun, A. and M. Ergun, *Protection of corrosion of carbon steel by inhibitors in chloride containing solutions*. Gazi University Journal of Science, 2006. **19**(3): p. 149-154.
322. Valcarce, M.B. and M. Vázquez, *Carbon steel passivity examined in alkaline solutions: the effect of chloride and nitrite ions*. Electrochimica Acta, 2008. **53**(15): p. 5007-5015.
323. Cohen, M., *The breakdown and repair of inhibitive films in neutral solution*. Corrosion, 1976. **32**(12): p. 461-465.
324. Standard, A., *Standard practice for preparing, cleaning, and evaluating corrosion test specimens*. American Society for Testing and Materials G1-03, 2011.
325. Bornak, W., *Chemistry of iron and its corrosion products in boiler systems*. Corrosion, 1988. **44**(3): p. 154-158.
326. Rocchini, G., *Magnetite stability in aqueous solutions as a function of temperature*. Corrosion science, 1994. **36**(12): p. 2043-2061.
327. Young, D.J., *High temperature oxidation and corrosion of metals*. Vol. 1. 2008: Elsevier.
328. Khani, H. and R. Arefinia, *Inhibition mechanism of nitrite on the corrosion of carbon steel in simulated cooling water systems*. Materials and Corrosion, 2018. **69**(3): p. 337-347.
329. Mohana, K. and A. Badiea, *Effect of sodium nitrite–borax blend on the corrosion rate of low carbon steel in industrial water medium*. Corrosion Science, 2008. **50**(10): p. 2939-2947.
330. Beverskog, B. and I. Puigdomenech, *Revised Pourbaix diagrams for iron at 25–300 C*. Corrosion Science, 1996. **38**(12): p. 2121-2135.
331. Park, J.-R. and D. Macdonald, *The fast-growth mechanism of magnetite on carbon steel in oxidizing high-temperature aqueous solutions*. Corrosion, 1989. **45**(7): p. 563-571.
332. Jafarian, M., et al., *Electrochemical studies of the pitting corrosion of tin in citric acid solution containing Cl<sup>-</sup>*. Electrochimica Acta, 2008. **53**(13): p. 4528-4536.
333. Orazem, M.E. and B. Tribollet, *Electrochemical impedance spectroscopy*. 2017: John Wiley & Sons.
334. Lasia, A., *Electrochemical impedance spectroscopy and its applications*, in *Modern aspects of electrochemistry*. 2002, Springer. p. 143-248.
335. Popova, A., M. Christov, and A. Vasilev, *Inhibitive properties of quaternary ammonium bromides of N-containing heterocycles on acid mild steel corrosion. Part II: EIS results*. Corrosion Science, 2007. **49**(8): p. 3290-3302.
336. Hsu, C. and F. Mansfeld, *Concerning the conversion of the constant phase element parameter Y0 into a capacitance*. Corrosion, 2001. **57**(9): p. 747-748.
337. Bentiss, F., et al., *Improvement of corrosion resistance of carbon steel in hydrochloric acid medium by 3, 6-bis (3-pyridyl) pyridazine*. Int. J. Electrochem. Sci, 2012. **7**: p. 1699-1723.
338. Son, K.V. and C. Wallace, *Reclamation/regeneration of glycols used for hydrate inhibition*. Deep Offshore Technology, 2000.
339. Zaboon, S., et al., *Recovery of mono-ethylene glycol by distillation and the impact of dissolved salts evaluated through simulation of field data*. Journal of Natural Gas Science and Engineering, 2017. **44**: p. 214-232.
340. Rey, S. and G. Reggiani. *Molybdate and non-molybdate options for closed systems–Part II*. in *AWT annual convention (Palm Springs: Cooling Water Subcommittee of the AWT Technical Committee)*. 2005.
341. Kadnar, R., M. Madera, and R. Schlifke, *Determination of inorganic corrosion inhibitors in heat transfer systems by ion chromatography*. Journal of Chromatography A, 2003. **997**(1-2): p. 285-290.
342. Raja, P.B., et al., *Reviews on corrosion inhibitors: a short view*. Chemical Engineering Communications, 2016. **203**(9): p. 1145-1156.
343. Li, L., A.A. Sagüés, and N. Poor, *In situ leaching investigation of pH and nitrite concentration in concrete pore solution*. Cement and Concrete Research, 1999. **29**(3): p. 315-321.
344. Gaidis, J.M., *Chemistry of corrosion inhibitors*. Cement and Concrete Composites, 2004. **26**(3): p. 181-189.
345. Hayyan, M., et al., *Utilizing of sodium nitrite as inhibitor for protection of carbon steel in salt solution*. International Journal of Electrochemical Science, 2012. **7**(8): p. 6941-6950.
346. Fei, Z., et al., *Probing thermal decomposition mechanism of molten nitrite/nitrates salt by time of flight mass spectrometry*. Solar Energy, 2019. **183**: p. 823-828.
347. Madera, M., et al., *Reduction of nitrite in aged heat transfer media at elevated temperatures*. Materials and Corrosion, 2004. **55**(1): p. 43-45.

348. Fernández-Prini, R., J.L. Alvarez, and A.H. Harvey, *Henry's constants and vapor-liquid distribution constants for gaseous solutes in H<sub>2</sub>O and D<sub>2</sub>O at high temperatures*. Journal of Physical and Chemical Reference Data, 2003. **32**(2): p. 903-916.
349. ASTM, G., *G1-90-Standard Practice for Preparing, Cleaning, and Evaluating Corrosion Test Specimens*, 1999.
350. Tomlinson, L., *Mechanism of corrosion of carbon and low alloy ferritic steels by high temperature water*. Corrosion, 1981. **37**(10): p. 591-596.
351. Pyke, R. and M. Cohen, *Rate of breakdown and mechanism of nitrite inhibition of steel corrosion*. Journal of the Electrochemical Society, 1948. **93**(3): p. 63-78.
352. Heyes, A., *Oxygen pitting failure of a bagasse boiler tube*. Engineering Failure Analysis, 2001. **8**(2): p. 123-131.

*Every reasonable effort has been made to acknowledge the owners of copyright material. I would be pleased to hear from any copyright owner who has been omitted or incorrectly acknowledged.*

## **Appendix 2: Written Statements of co-authors**

The written statements of co-authors about the contribution of the candidate on each publication that forming individual chapter of this thesis are given are given in the subsequent pages.

**To whom it may concern,**

I, Yousuf Abdulwahhab, as the first author of the publication entitled “*EIS and Mott-Schottky to Study the Passive Film Properties of 316L and its Susceptibility to Pitting Corrosion in CO<sub>2</sub> Environments*” was primarily involved in planning and conducting the experiments, data analysis and interpretation of the findings and manuscript preparation.

---

**First author signature**

I, as a co-author, endorse that this level of contribution by the first author indicated above is appropriate.

Thunyaluk Pojtanabuntoeng

**Full name of co-author 1**

Ahmed Barifcani

**Full name of co-author 2**

Moses Tade

**Full name of co-author 3**

Brian Kinsella

**Full name of co-author 4**

**To whom it may concern,**

I, Yousuf Abdulwahhab, as the first author of the publication entitled “*Comparison of Corrosion behavior and Passive Film Properties of 316L Austenitic Stainless Steel in CO<sub>2</sub> and N<sub>2</sub> Environments*” was primarily involved in planning and conducting the experiments, data analysis and interpretation of the findings and manuscript preparation.

---

**First author signature**

I, as a co-author, endorse that this level of contribution by the first author indicated above is appropriate.

Thunyaluk Pojtanabuntoeng

**Full name of co-author 1**

Brian Kinsella

**Full name of co-author 2**

Jean-Pierre Veder

**Full name of co-author 3**

Ahmed Barifceni

**Full name of co-author 4**

**To whom it may concern,**

I, Yousuf Abdulwahhab, as the first author of the publication entitled “*Study the influence of high temperature and high-pressure conditions on the 316L stainless steel in CO<sub>2</sub> environment*” was primarily involved in planning and conducting the experiments, data analysis and interpretation of the findings and manuscript preparation.

---

**First author signature**

I, as a co-author, endorse that this level of contribution by the first author indicated above is appropriate.

Thunyaluk Pojtanabuntoeng

**Full name of co-author 1**

Brian Kinsella

**Full name of co-author 2**

Ahmed Barifcani

**Full name of co-author 3**

**To whom it may concern,**

I, Yousuf Abdulwahhab, as the first author of the publication entitled *“Effect of CO<sub>2</sub> partial pressure on the pitting susceptibility of UNS S31603 at different temperatures”* was primarily involved in planning and conducting the experiments, data analysis and interpretation of the findings and manuscript preparation.

---

**First author signature**

I, as a co-author, endorse that this level of contribution by the first author indicated above is appropriate.

Thunyaluk Pojtanabuntoeng

**Full name of co-author 1**

Ahmed Barifcani

**Full name of co-author 2**

### Appendix 3: Copyright Statements

I acknowledged that I have obtained the approval from the copyright owners to use my published work as conference paper (Chapter 3) and journal paper (Chapter 4) for this thesis where the ownership is held by Australasian Corrosion Association and Taylor and Francis Group. The permission to utilise the published material by the author has been stated in the email and copyright link below:

- <https://membership.corrosion.com.au/blog/aca-conference-proceedings/>.  
Lucy Krelle AIMM, Australasian Corrosion Association [lkrelle@corrosion.com.au](mailto:lkrelle@corrosion.com.au)
- <https://authorservices.taylorandfrancis.com/publishing-your-research/moving-through-production/copyright-for-journal-authors/>.

Yousuf Abdulwahhab